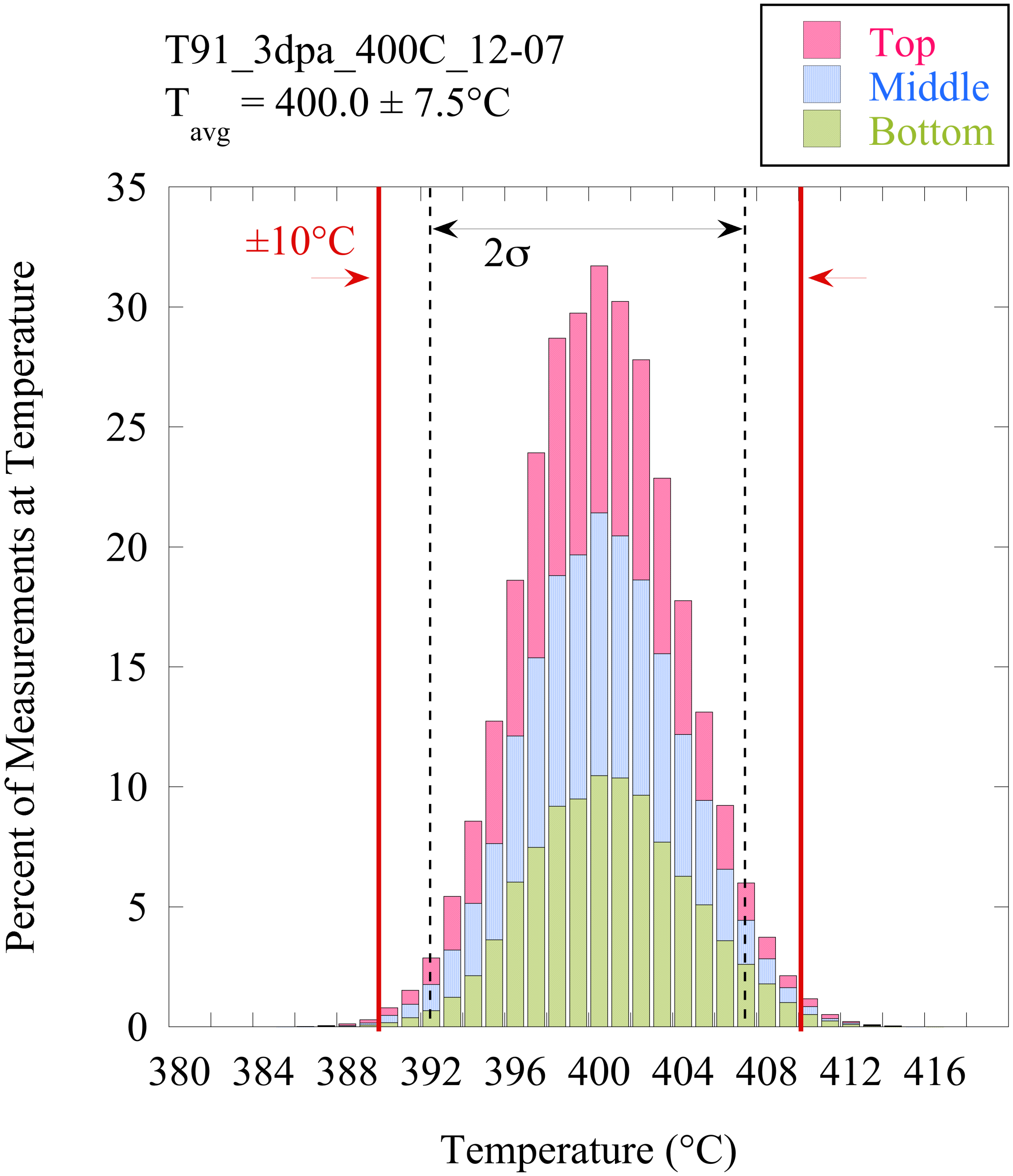

Figure 5.1. Example temperature histogram from proton irradiation of specimen T91_3dpa_400C_12-07, showing normal temperature distribution of all three (top, middle, bottom) areas of interest on the specimen and having 2σ within ±10°C of the target temperature.

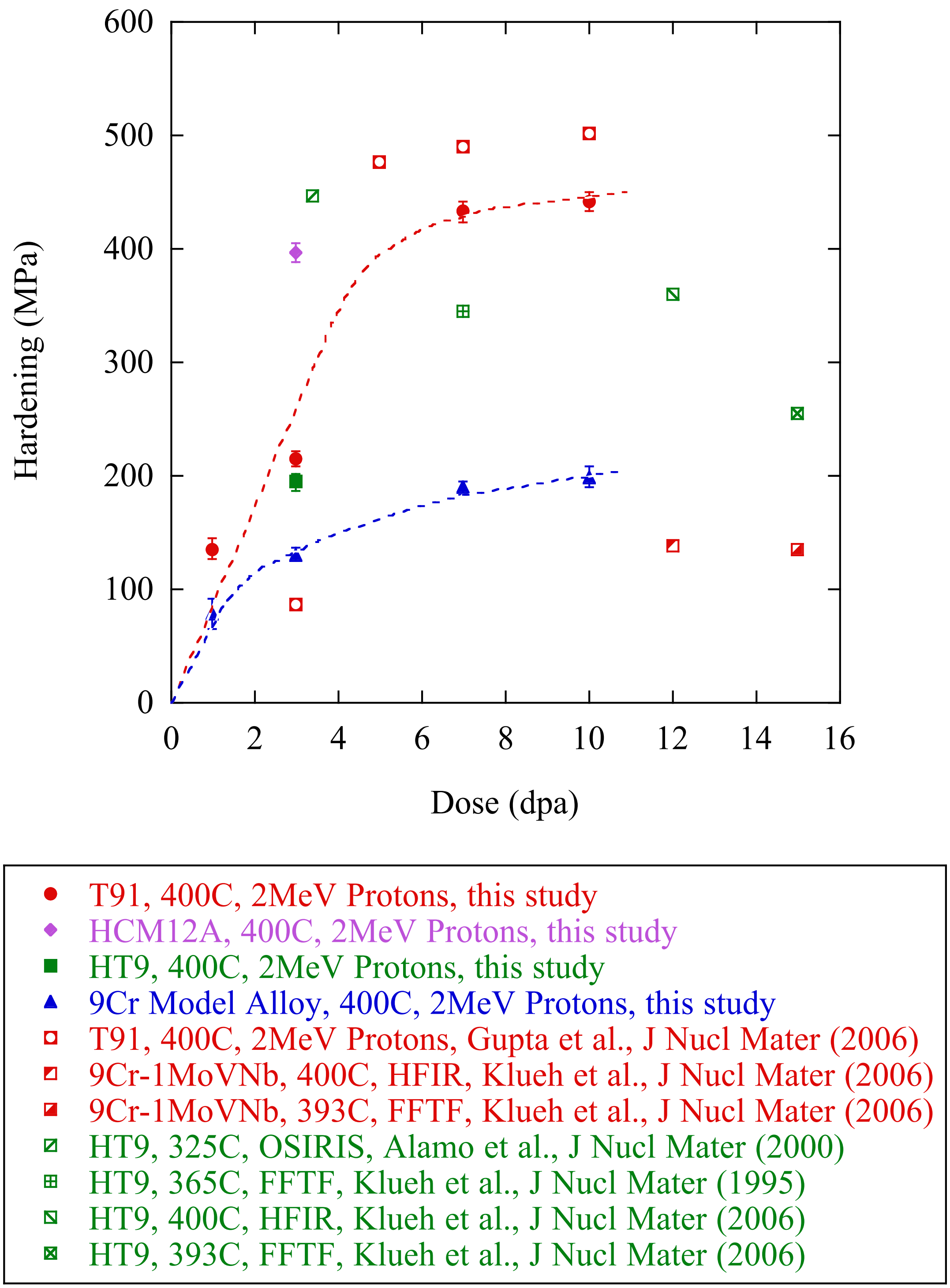

Figure 5.2. Irradiation hardening at 400°C as a function of dose for proton-irradiated T91, 9Cr model alloy, HCM12A, and HT9 from this study, as compared to hardening data from literature at or near 400°C.

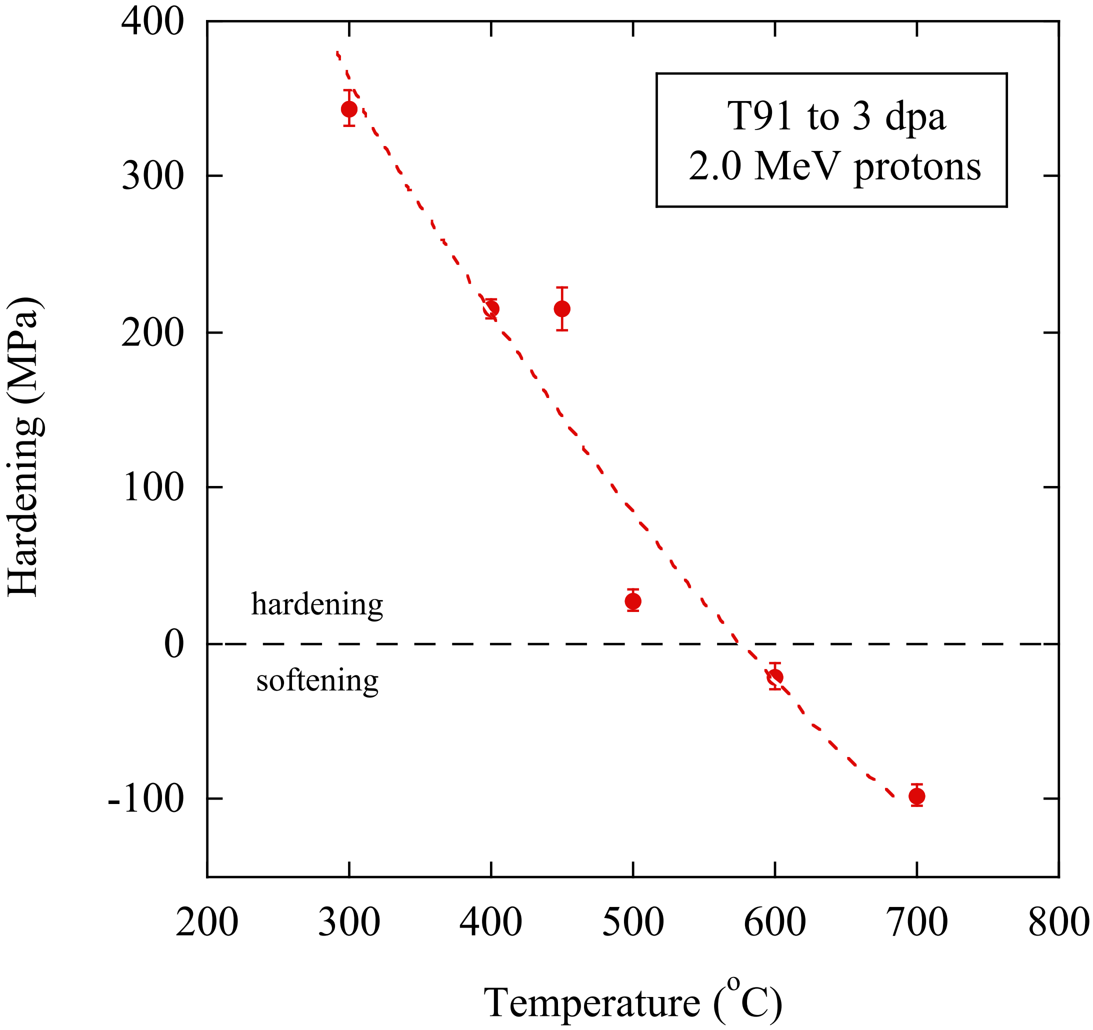

Figure 5.3. Irradiation hardening at 3 dpa as a function of temperature for proton-irradiated T91.

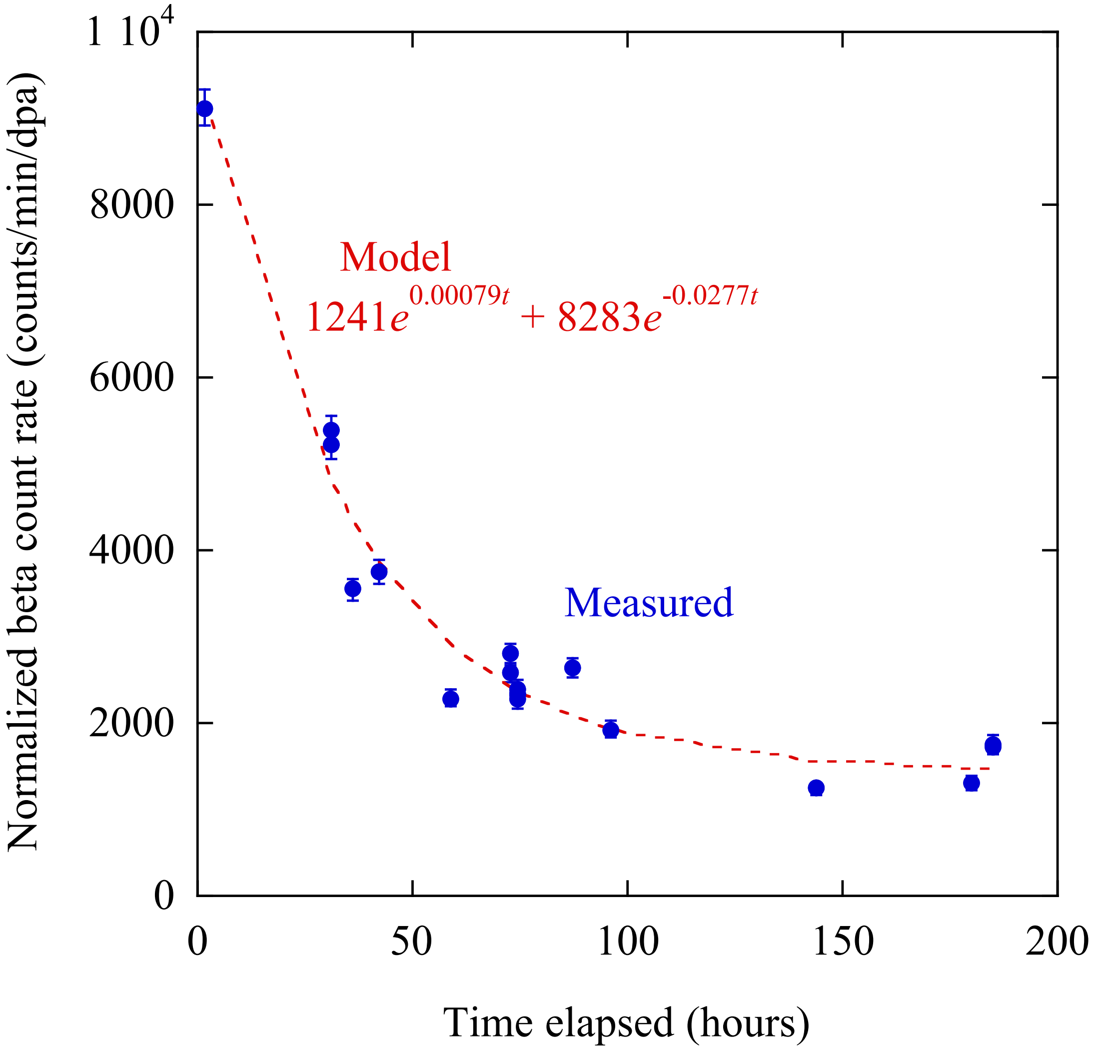

Figure 5.4. Post-irradiation beta activity measurements with model fit.

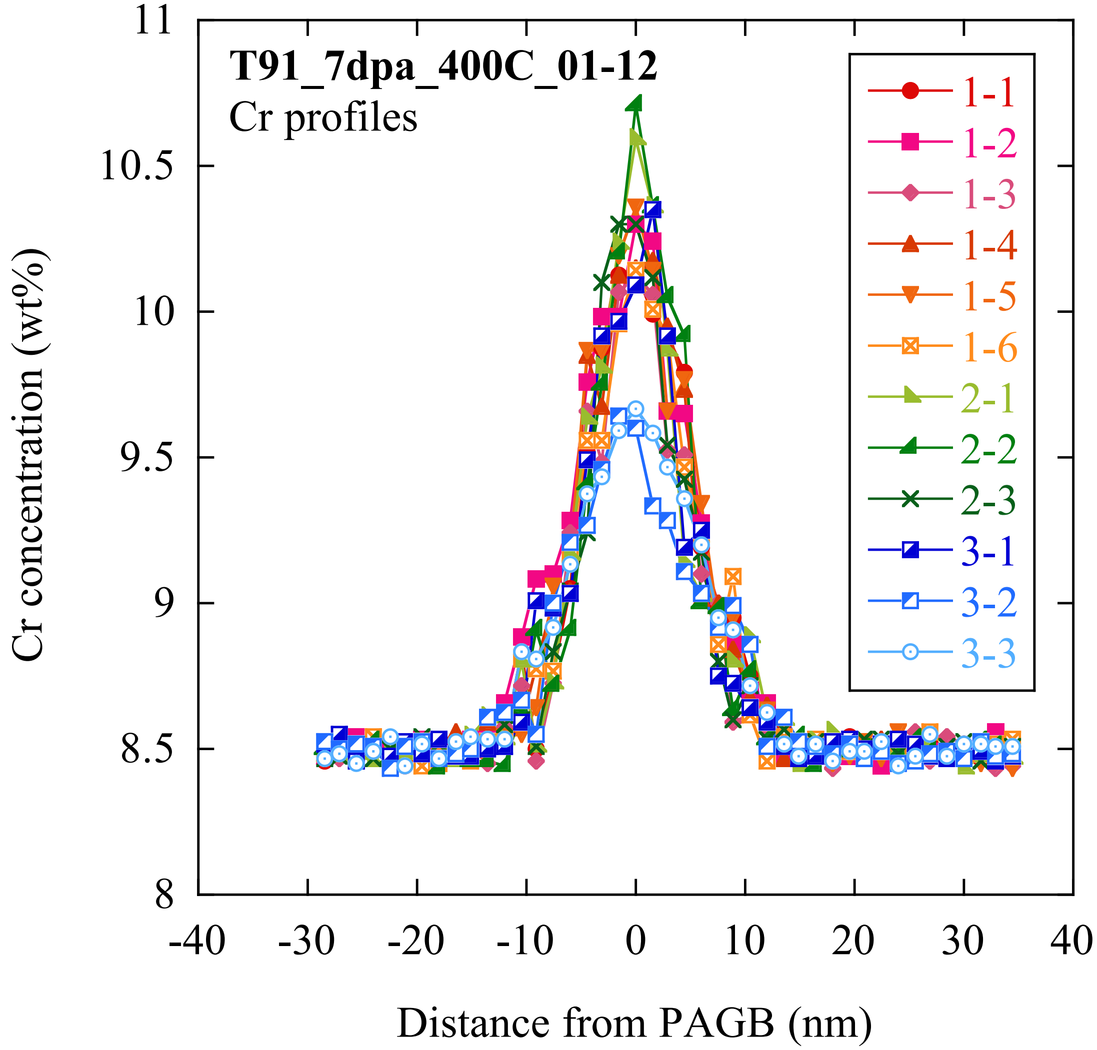

Figure 5.5. All Cr concentration profiles from T91_7dpa_400C_01-12, overlaid upon one another.

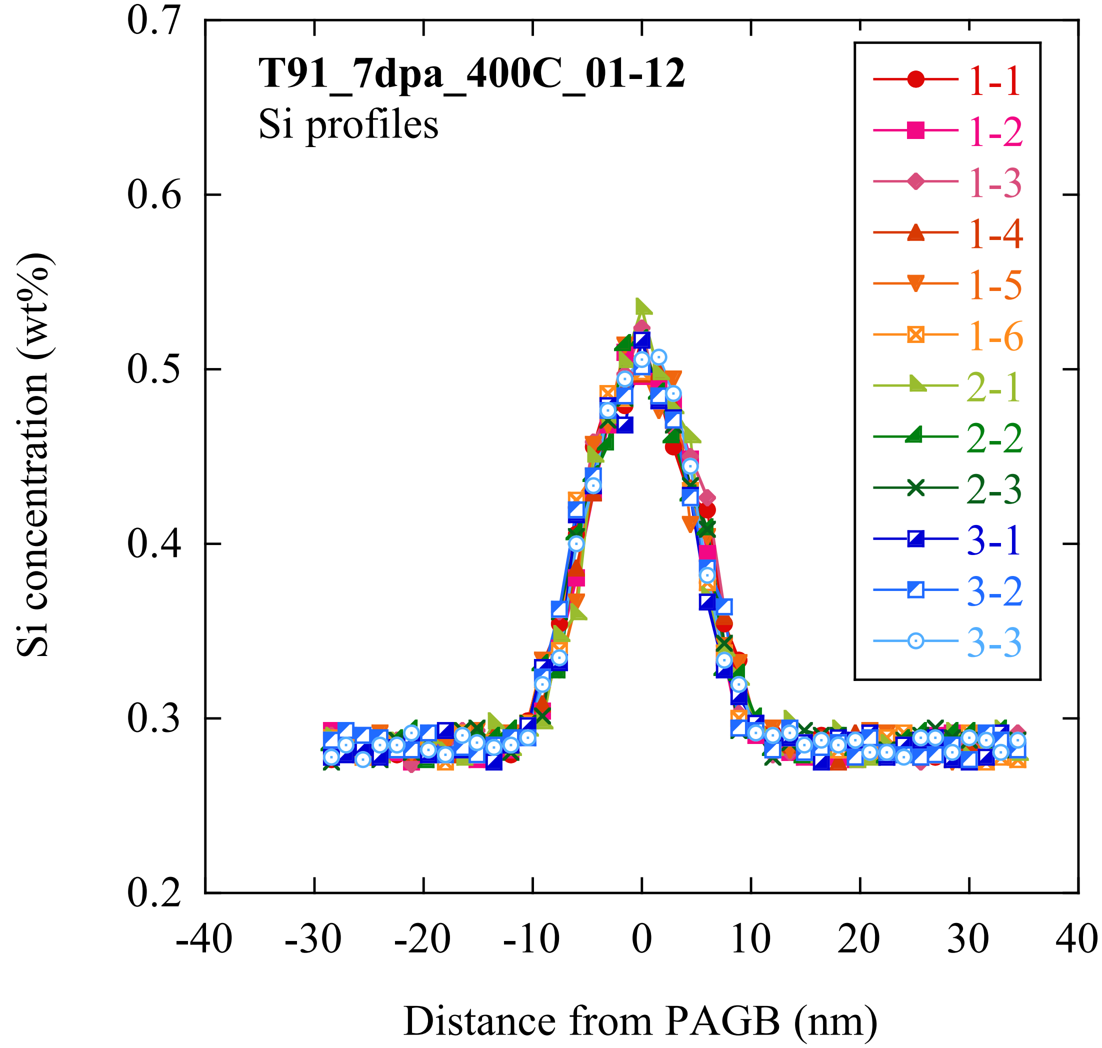

Figure 5.6. All Si concentration profiles from T91_7dpa_400C_01-12, overlaid upon one another.

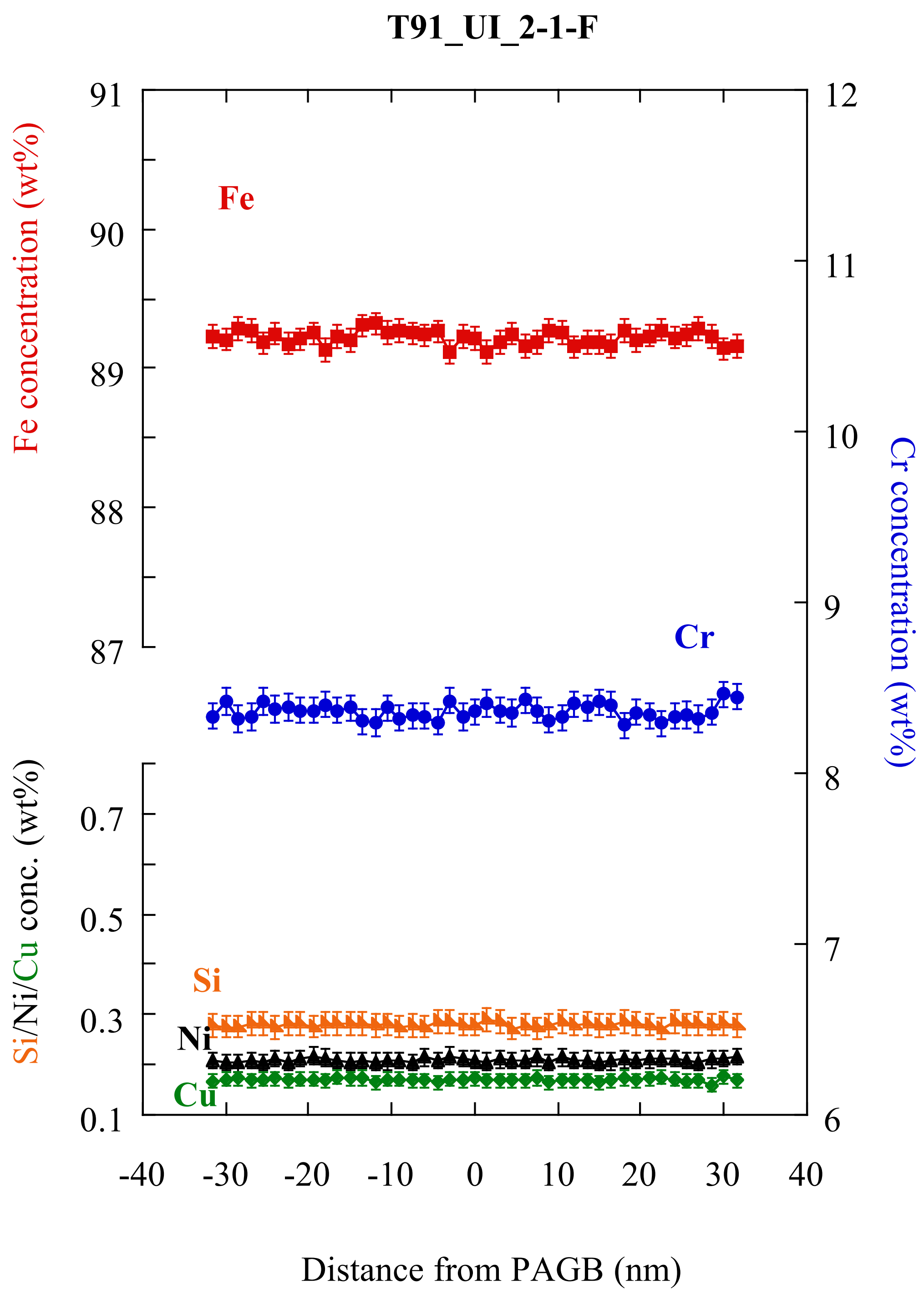

Figure 5.7. Representative concentration profile from as-received T91, T91_UI_2-1-F.

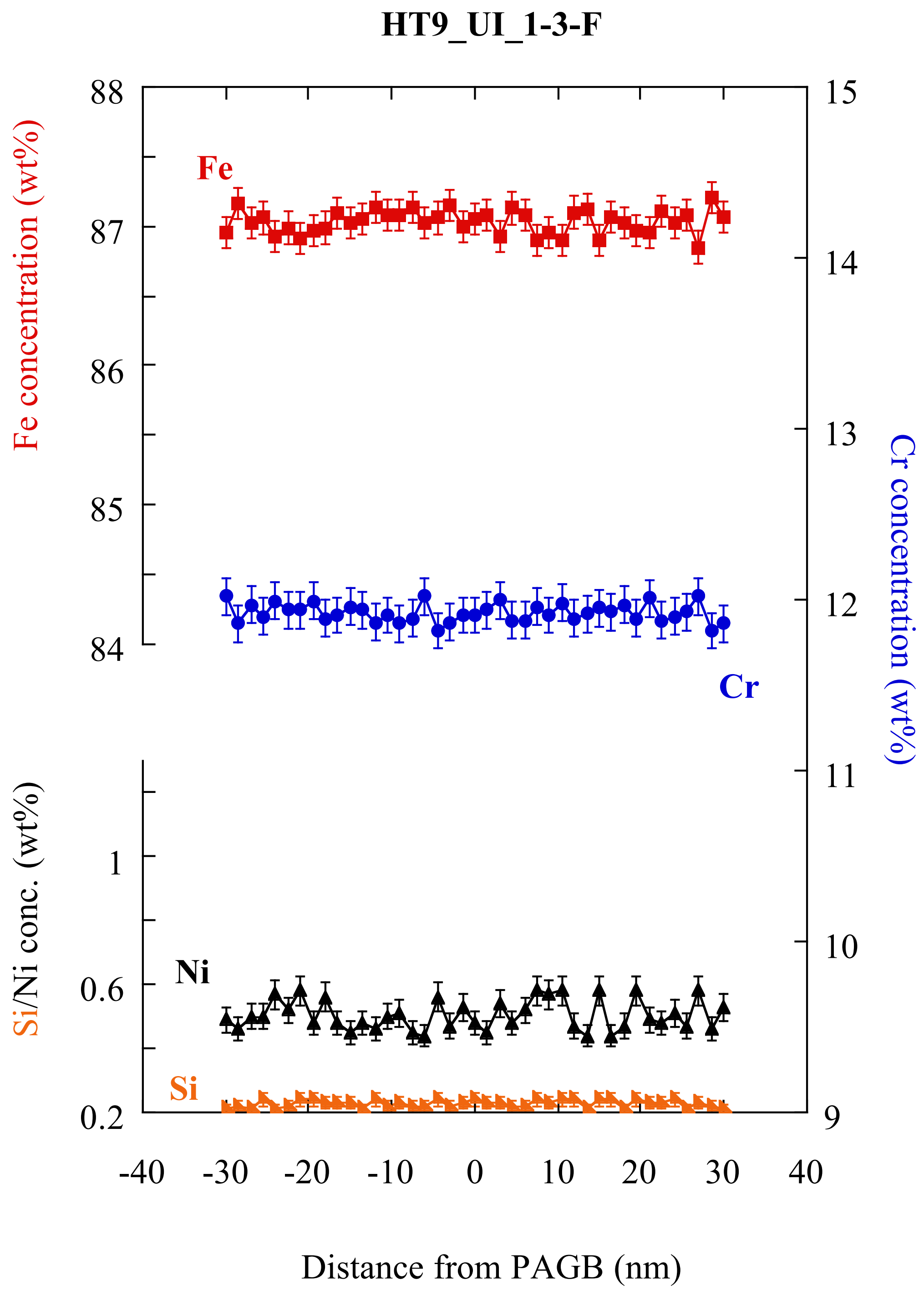

Figure 5.8. Representative concentration profile from as-received HT9, HT9_UI_1-3-F.

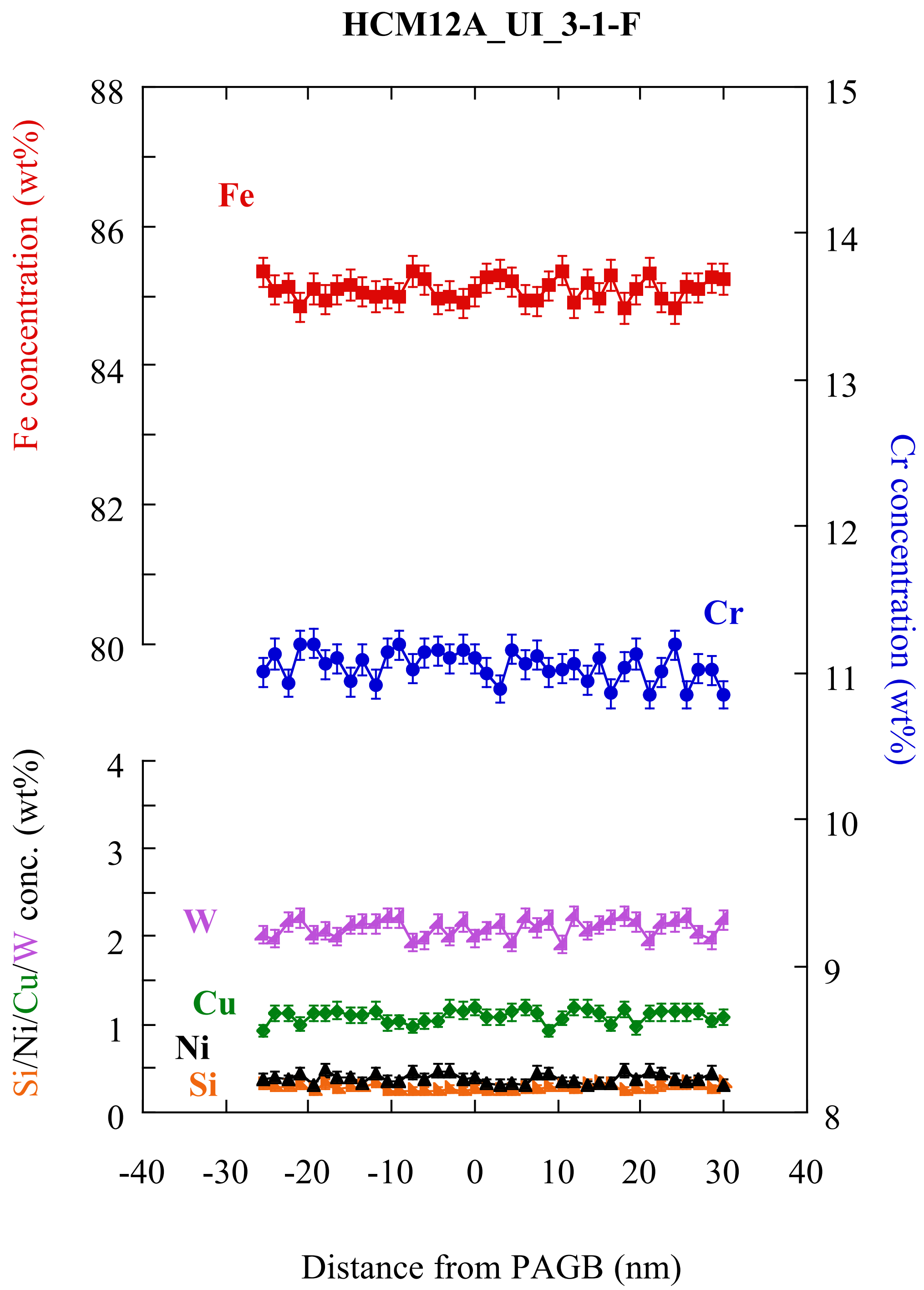

Figure 5.9. Representative concentration profile from as-received HCM12A, HCM12A_UI_3-1-F.

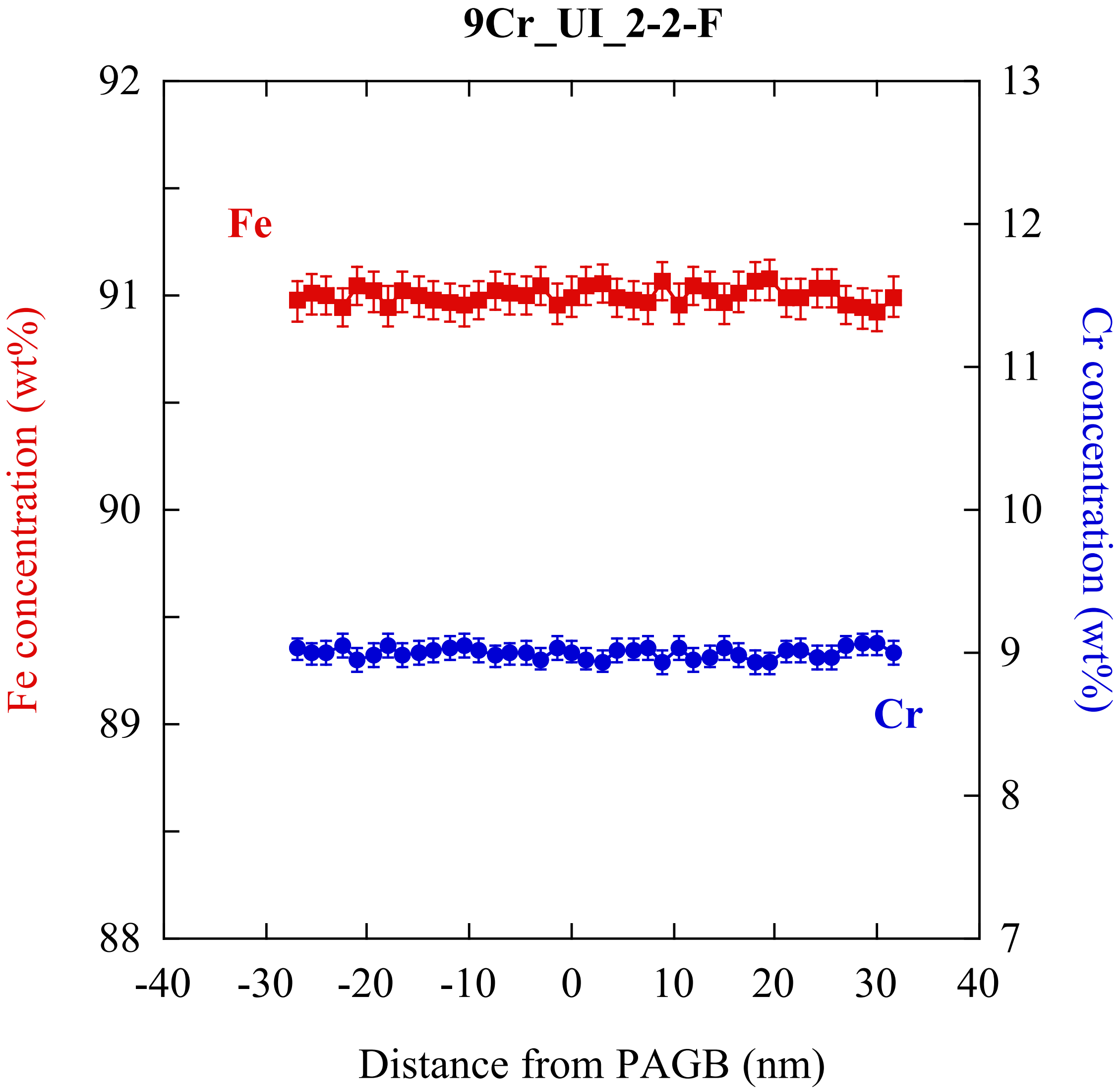

Figure 5.10. Representative concentration profile from as-received 9Cr model alloy, 9Cr_UI_2-2-F.

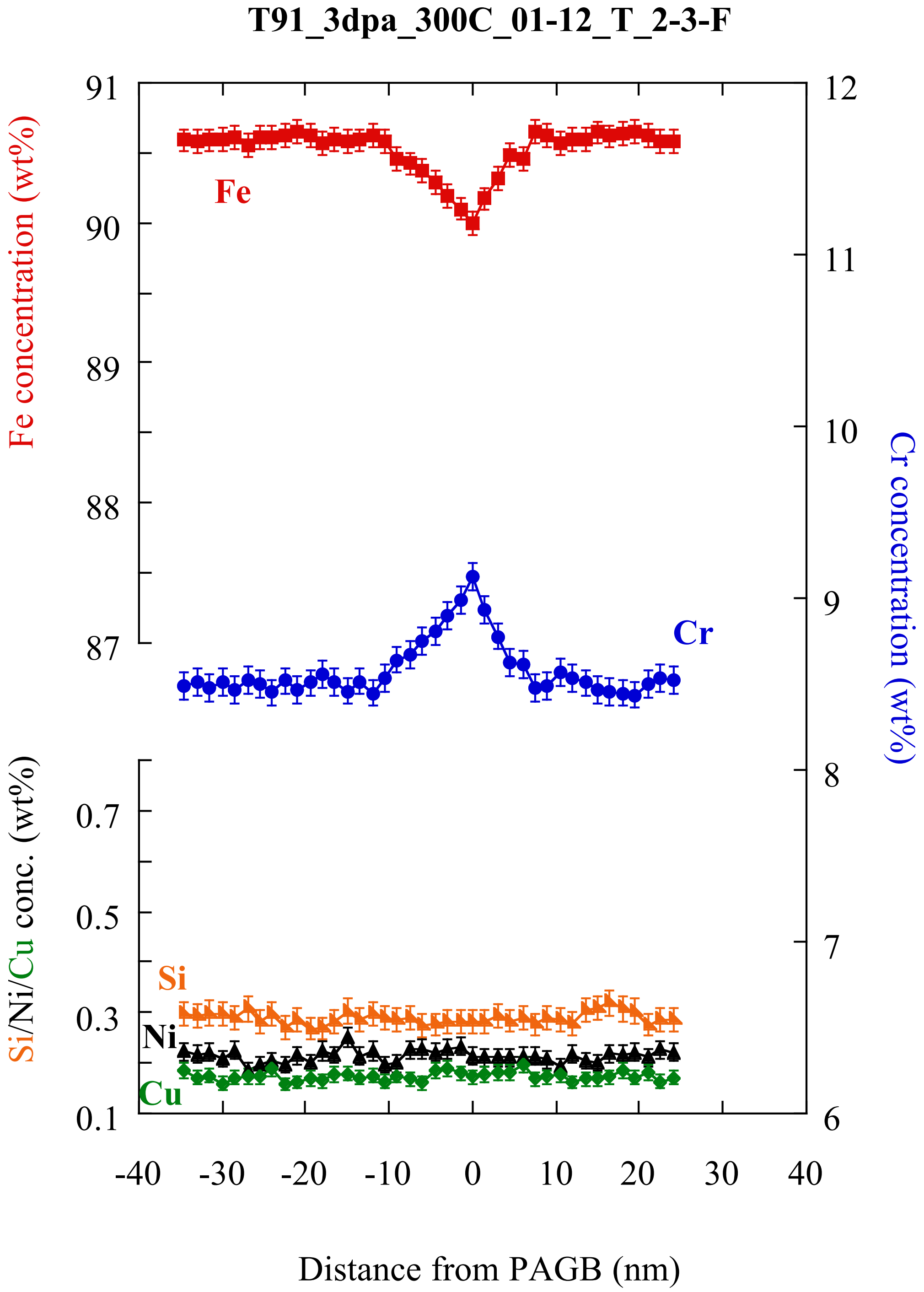

Figure 5.11. Representative concentration profile from T91 irradiated to 3 dpa at 300°C, T91_3dpa_300C_01-12_T_2-3-F.

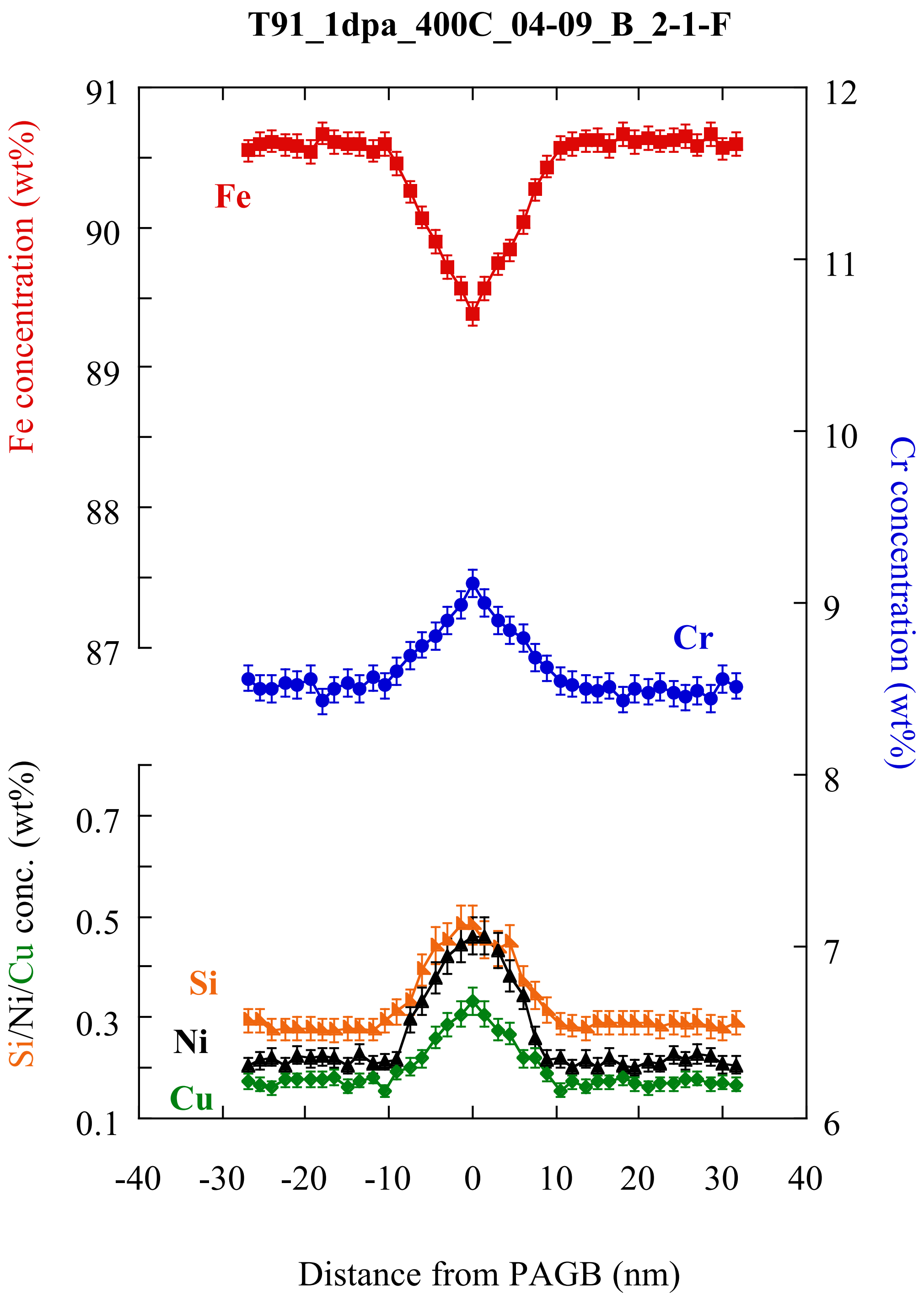

Figure 5.12. Representative concentration profile from T91 irradiated to 1 dpa at 400°C, T91_1dpa_400C_04-09_B_2-1-F.

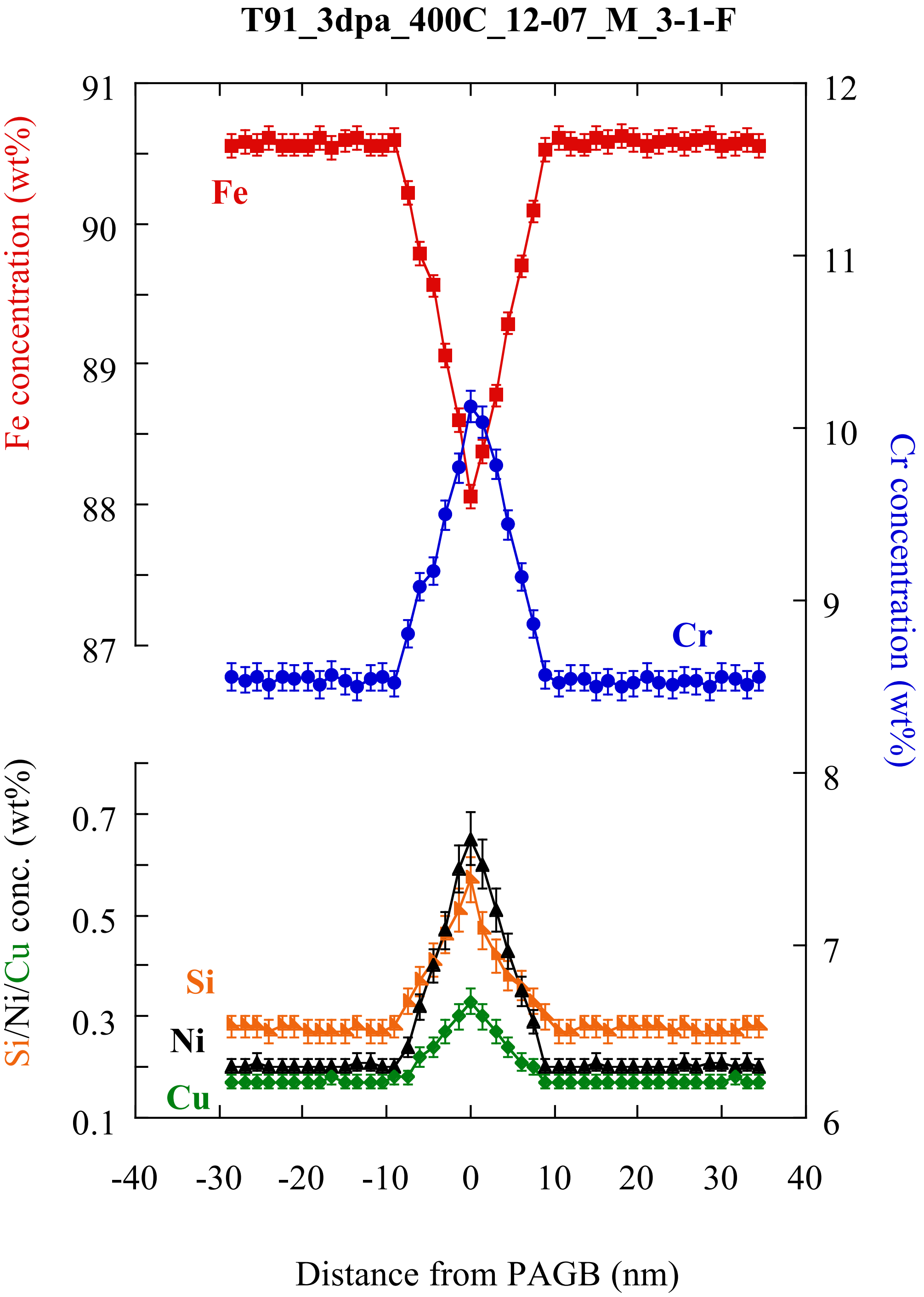

Figure 5.13. Representative concentration profile from T91 irradiated to 3 dpa at 400°C, T91_3dpa_400C_12-07_M_3-1-F.

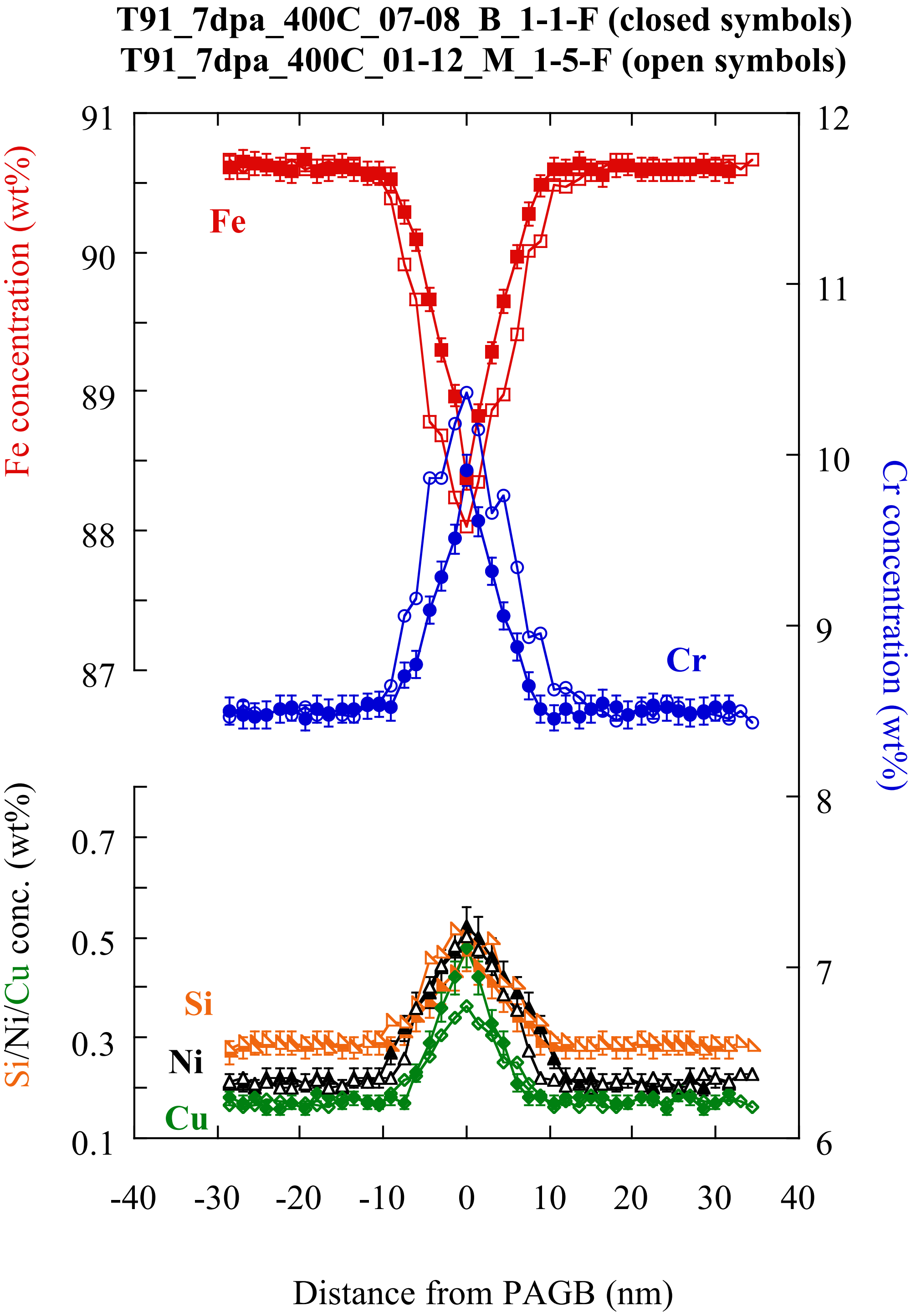

Figure 5.14. Representative concentration profiles from the two T91 irradiations to 7 dpa at 400°C. Profile from first irradiation, T91_7dpa_400C_07-08_B_1-1-F, is shown in closed symbols. Profile from second irradiation, T91_7dpa_400C_01-12_M_1-5-F, is shown in open symbols.

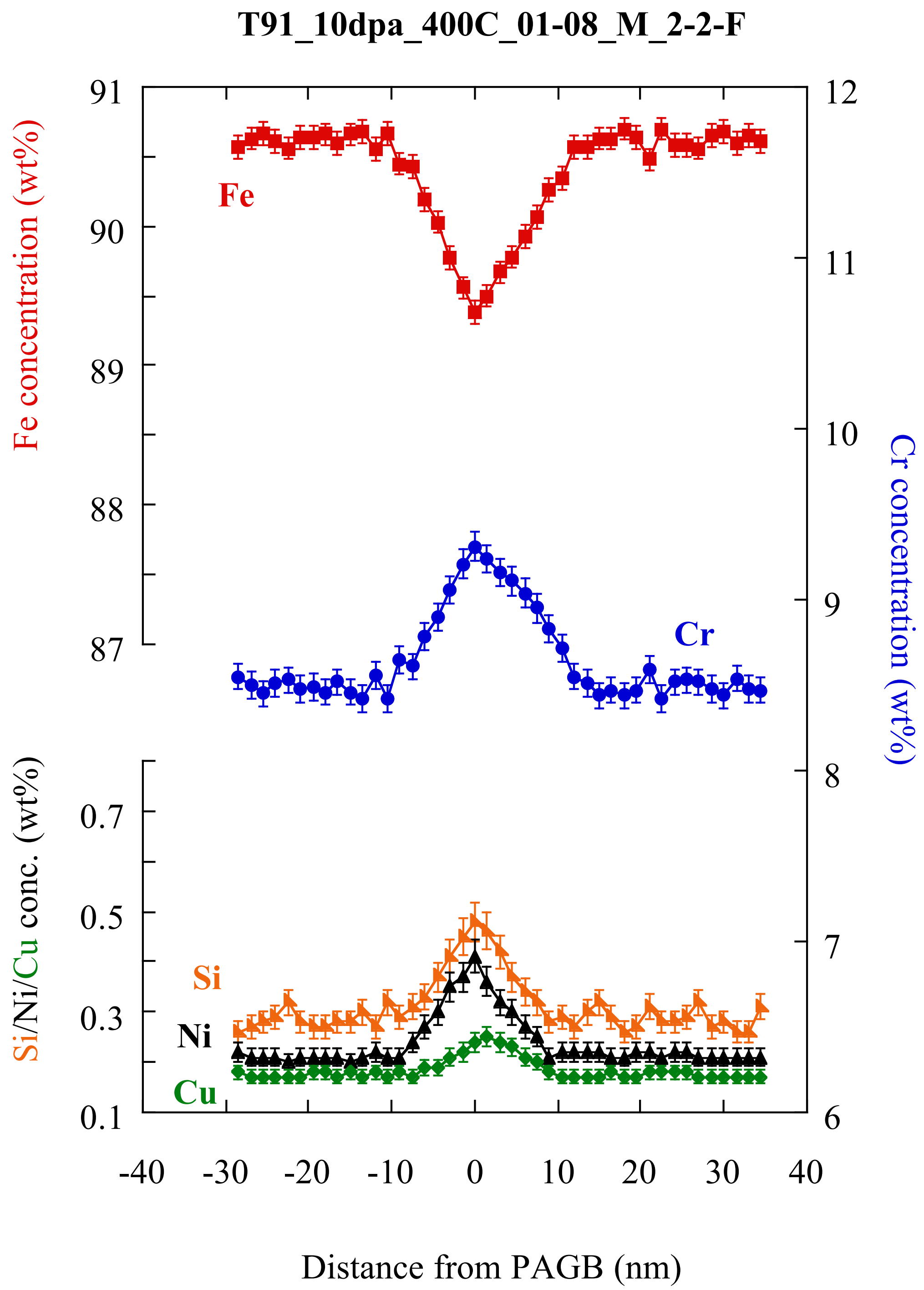

Figure 5.15. Representative concentration profile from T91 irradiated to 10 dpa at 400°C, T91_10dpa_400C_01-08_M_2-2-F.

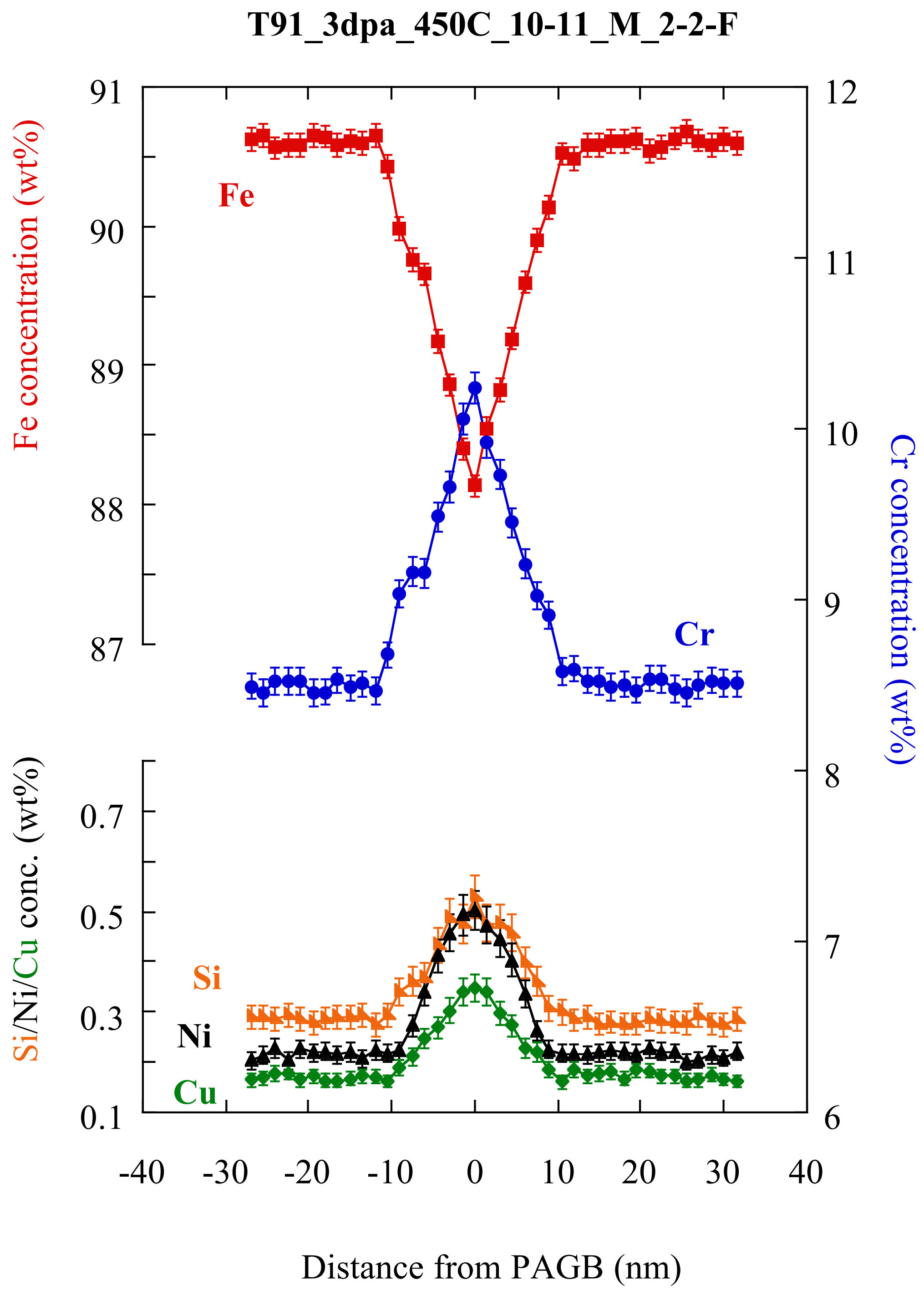

Figure 5.16. Representative concentration profile from T91 irradiated to 3 dpa at 450°C, T91_3dpa_450C_10-11_M_2-2-F.

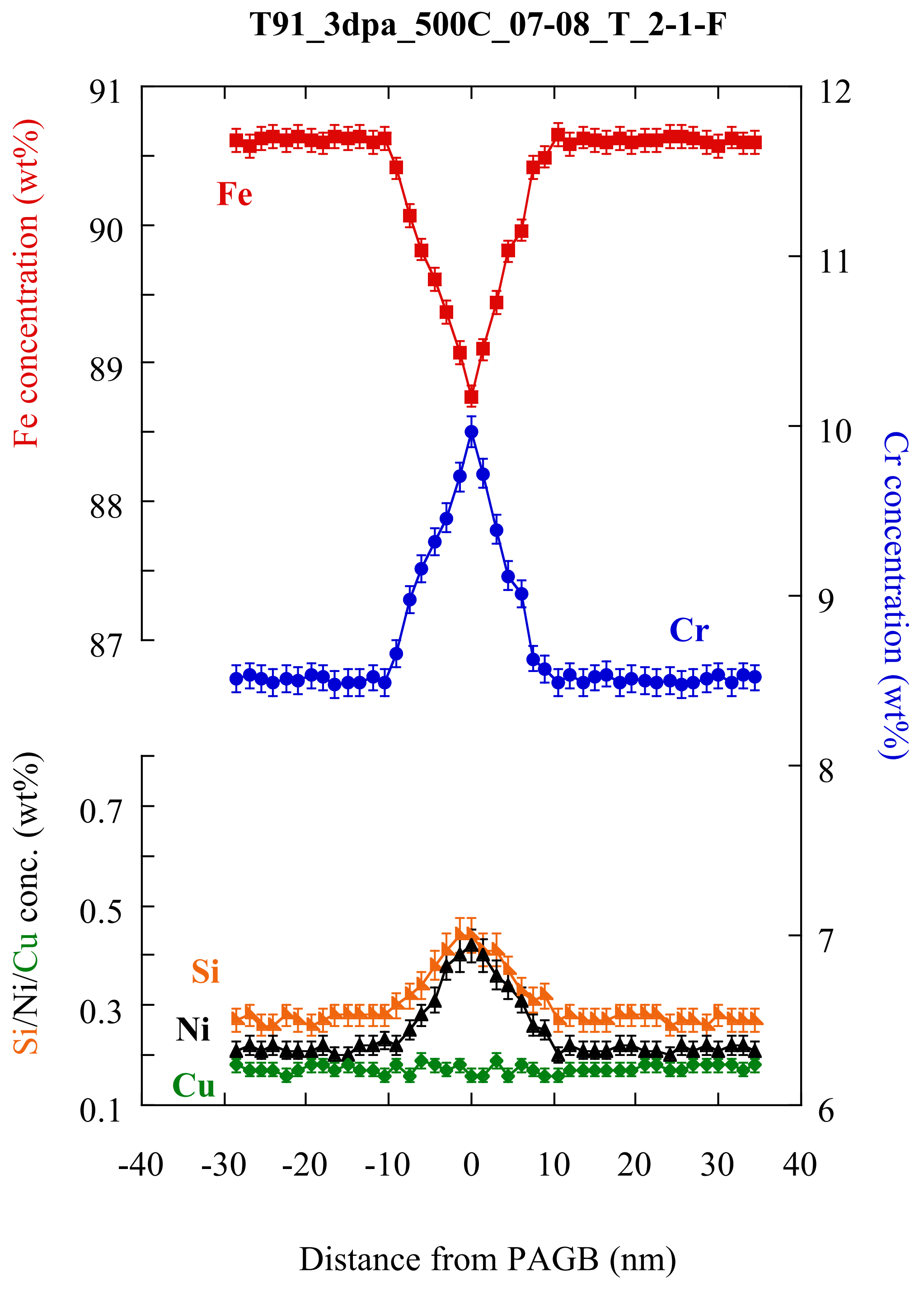

Figure 5.17. Representative concentration profile from T91 irradiated to 3 dpa at 500°C, T91_3dpa_500C_07-08_T_2-1-F.

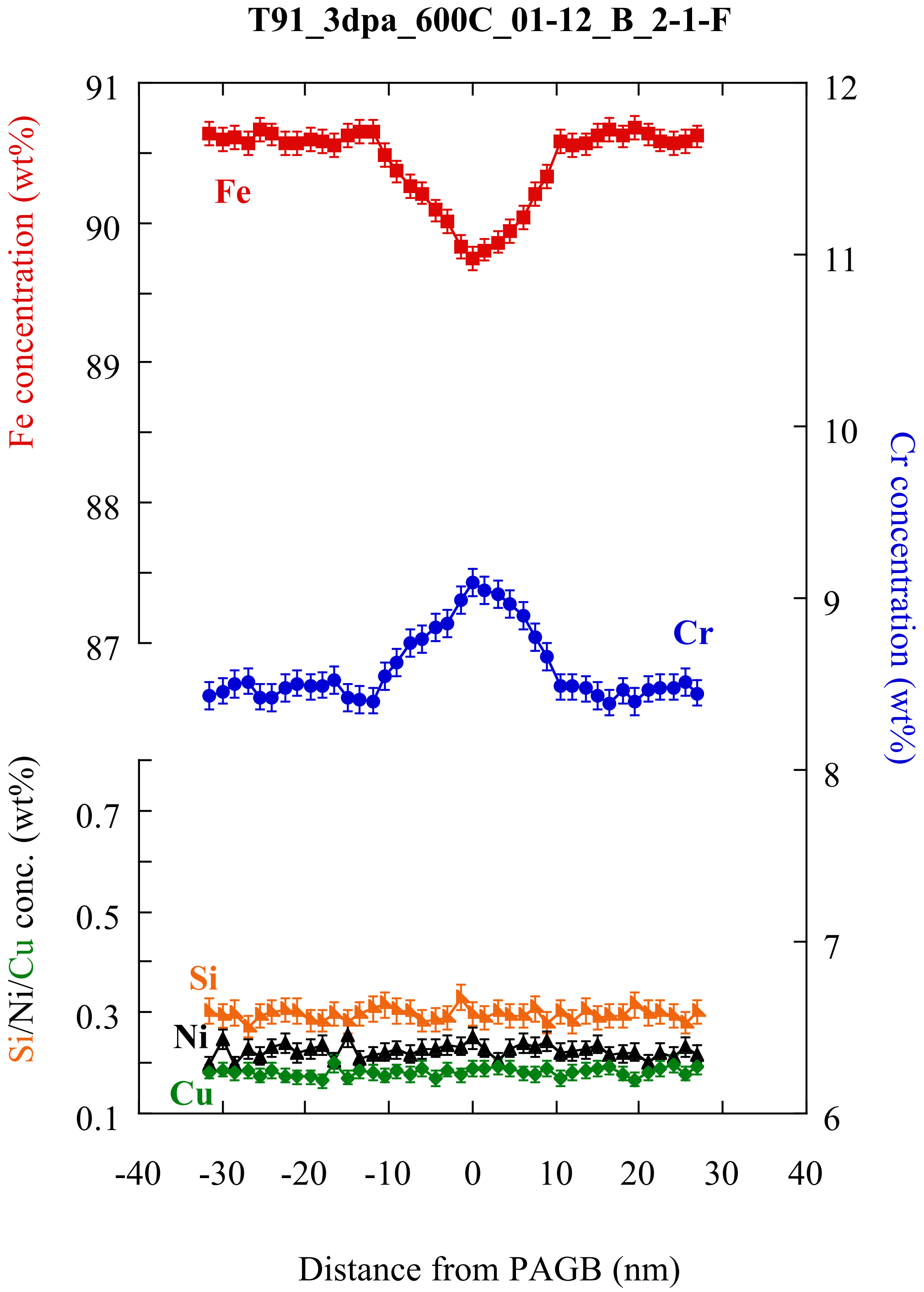

Figure 5.18. Representative concentration profile from T91 irradiated to 3 dpa at 600°C, T91_3dpa_600C_01-12_B_2-1-F.

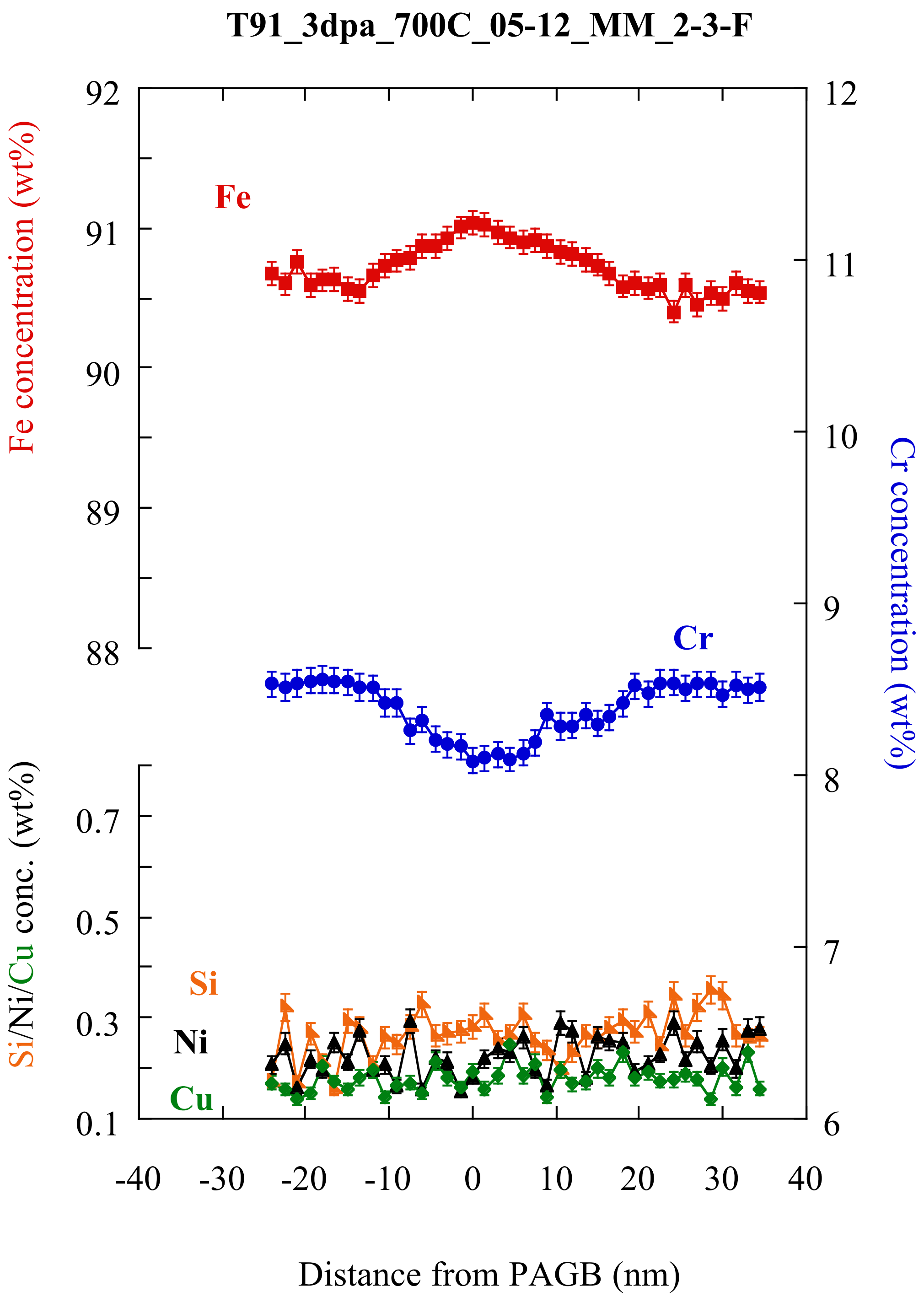

Figure 5.19. Representative concentration profile from T91 irradiated to 3 dpa at 700°C, T91_3dpa_700C_05-12_MM_2-3-F.

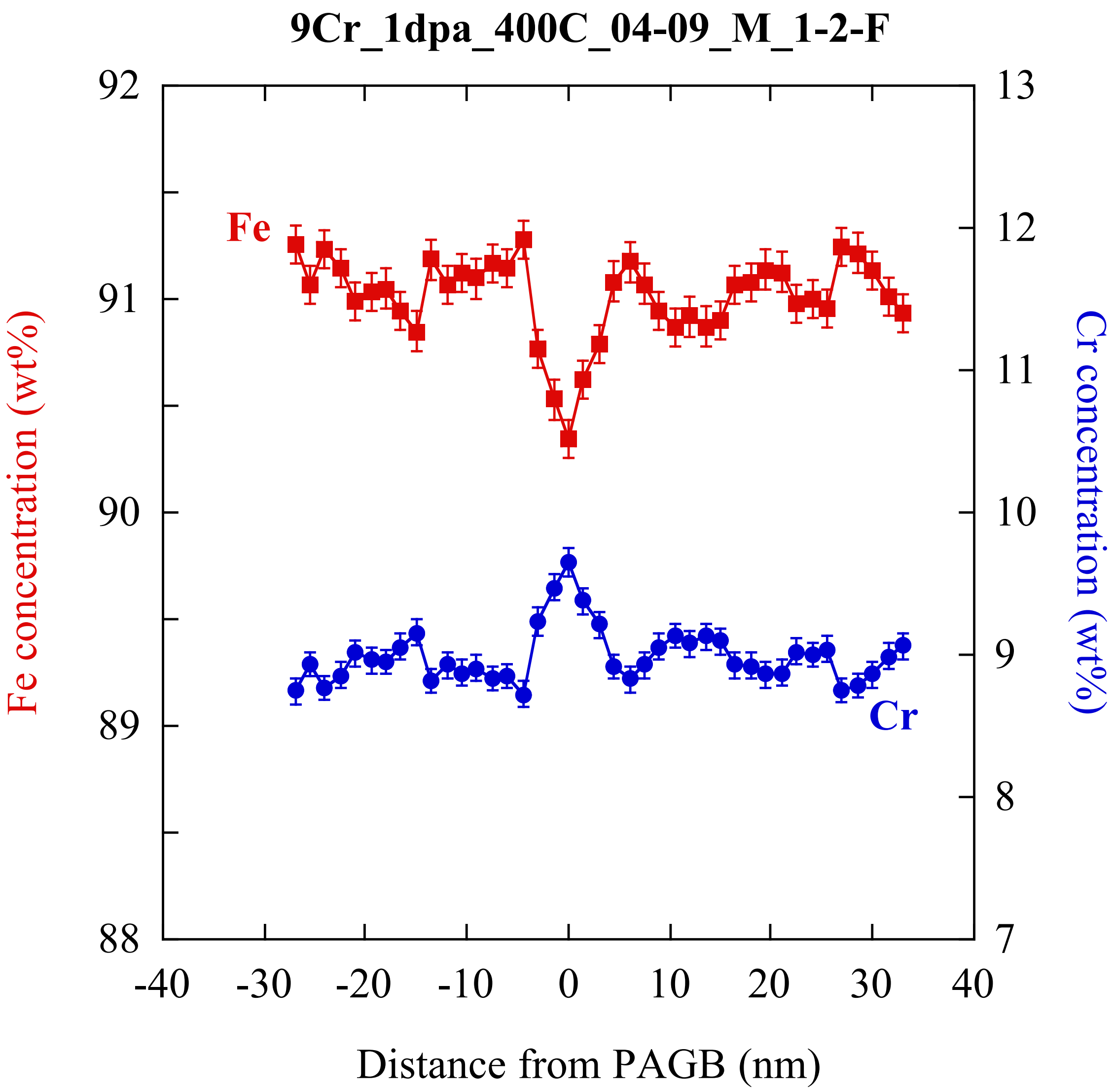

Figure 5.20. Representative concentration profile from 9Cr model alloy irradiated to 1 dpa at 400°C, 9Cr_1dpa_400C_04-09_M_1-2-F.

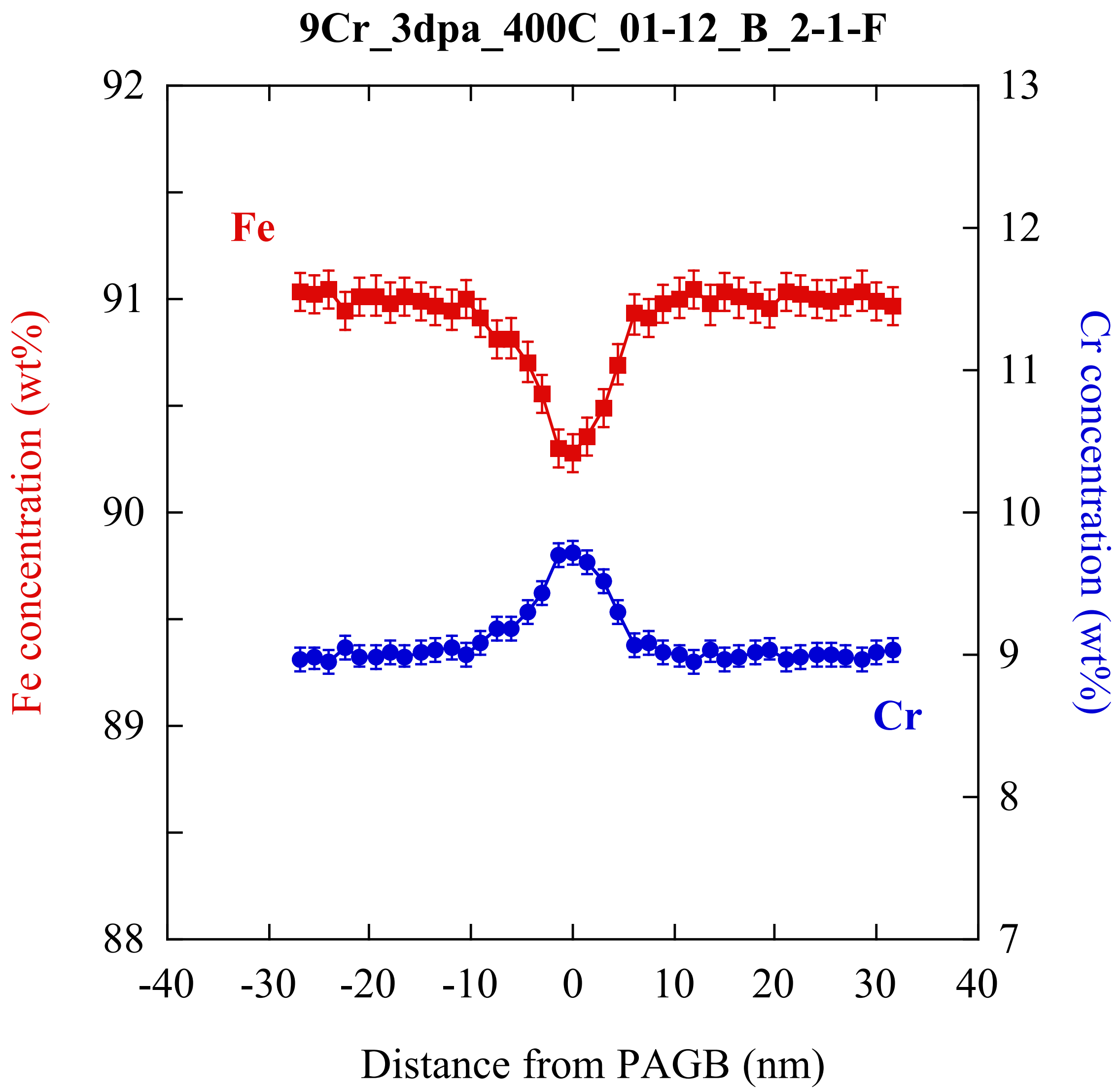

Figure 5.21. Representative concentration profile from 9Cr model alloy irradiated to 3 dpa at 400°C, 9Cr_3dpa_400C_01-12_B_2-1-F.

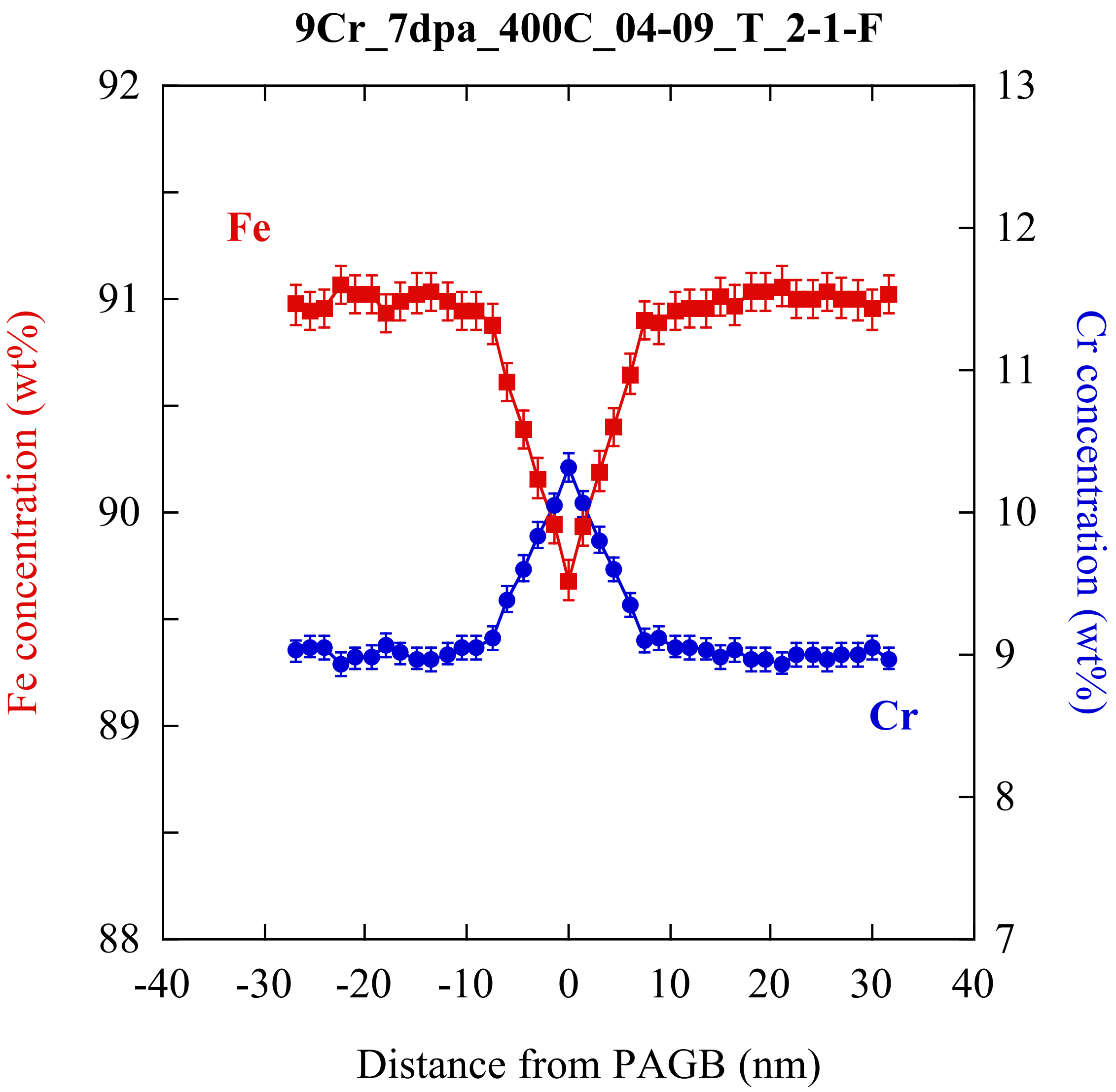

Figure 5.22. Representative concentration profile from 9Cr model alloy irradiated to 7 dpa at 400°C, 9Cr_7dpa_400C_04-09_T_2-1-F.

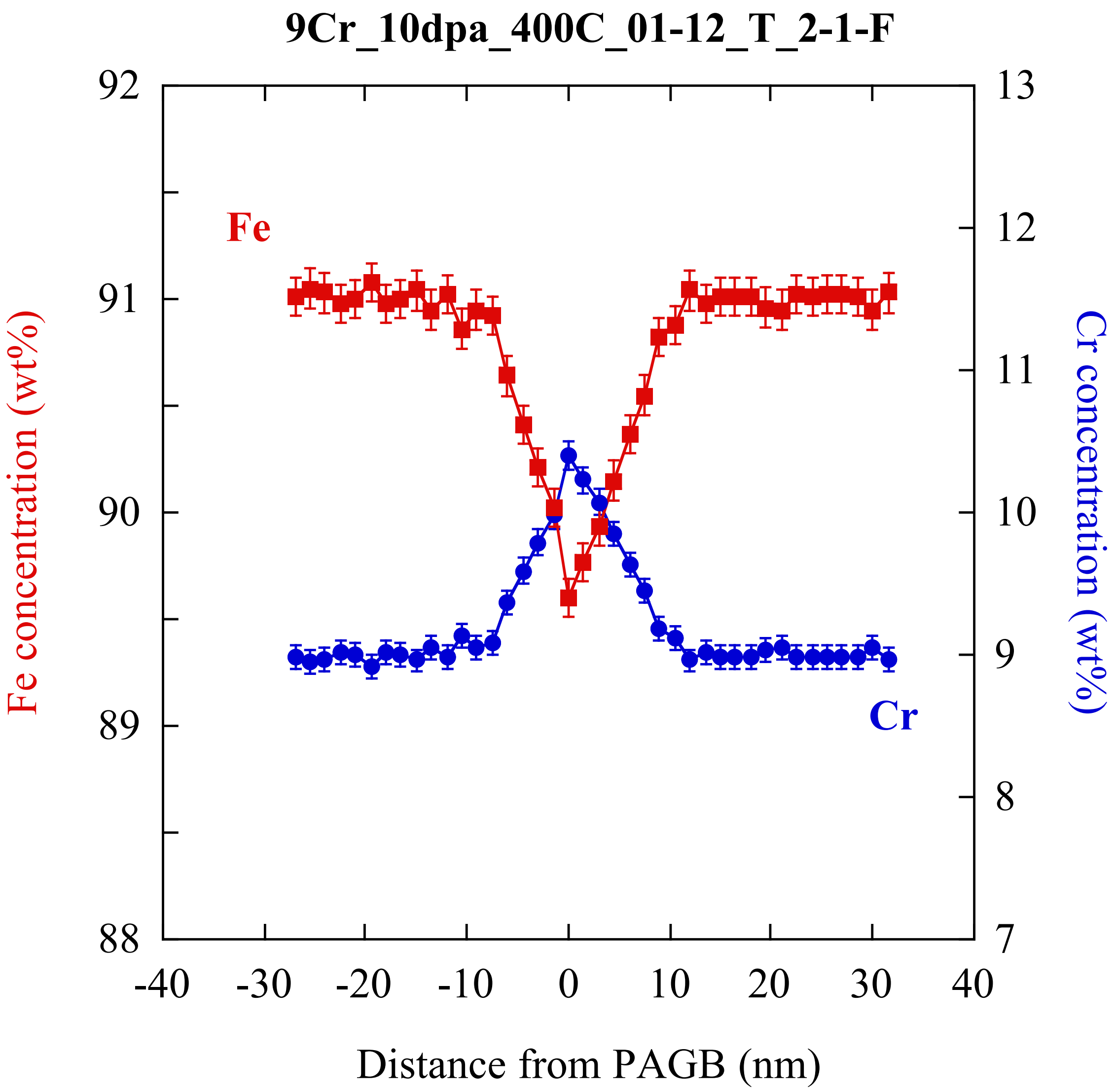

Figure 5.23. Representative concentration profile from 9Cr model alloy irradiated to 10 dpa at 400°C, 9Cr_10dpa_400C_01-12_T_2-1-F.

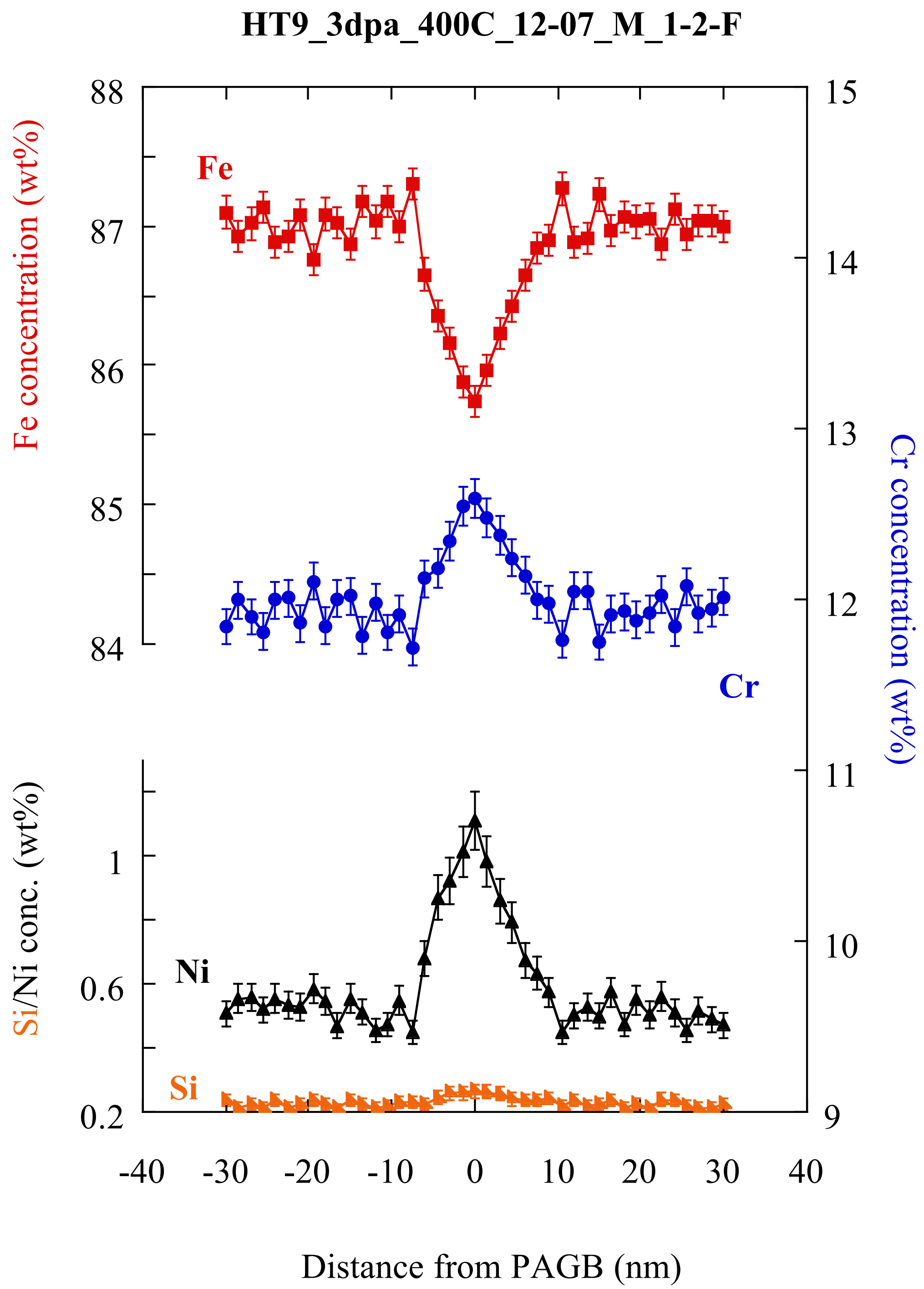

Figure 5.24. Representative concentration profile from HT9 irradiated to 3 dpa at 400°C, HT9_3dpa_400C_12-07_M_1-2-F.

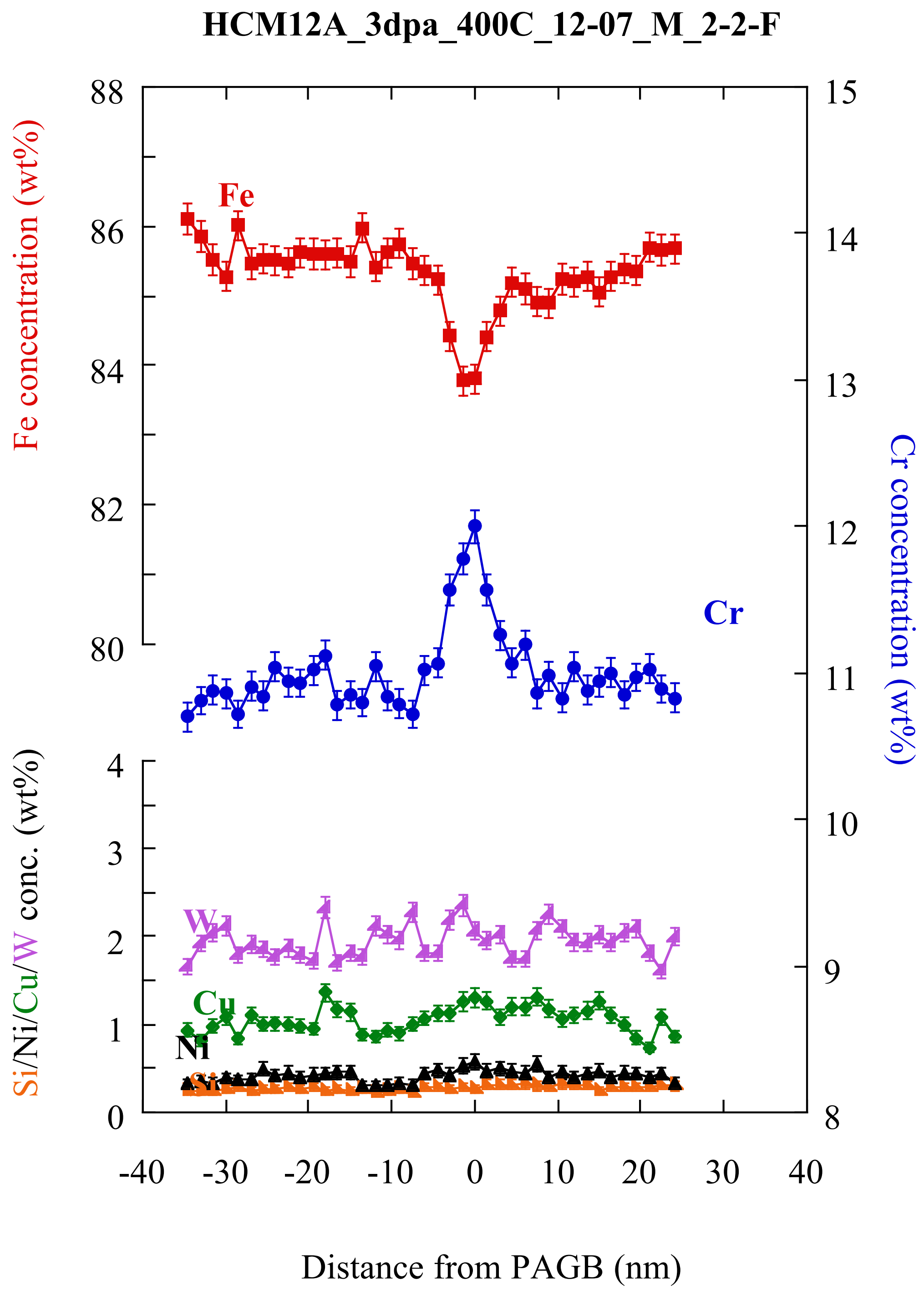

Figure 5.25. Representative concentration profile from HCM12A irradiated to 3 dpa at 400°C, HCM12A_3dpa_400C_12-07_M_2-2-F.

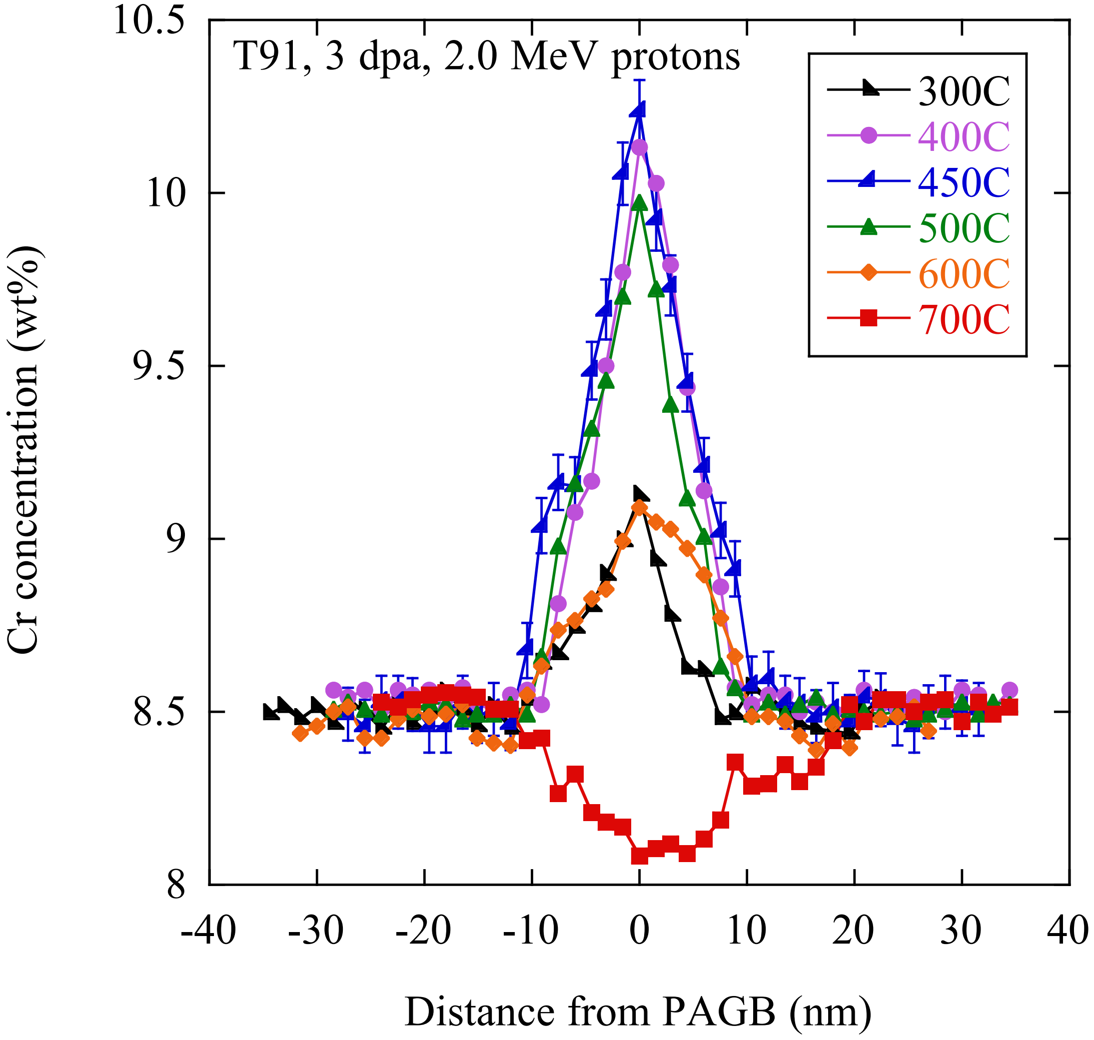

Figure 5.26. Representative Cr RIS profiles from T91 irradiated to 3 dpa over a range of temperatures.

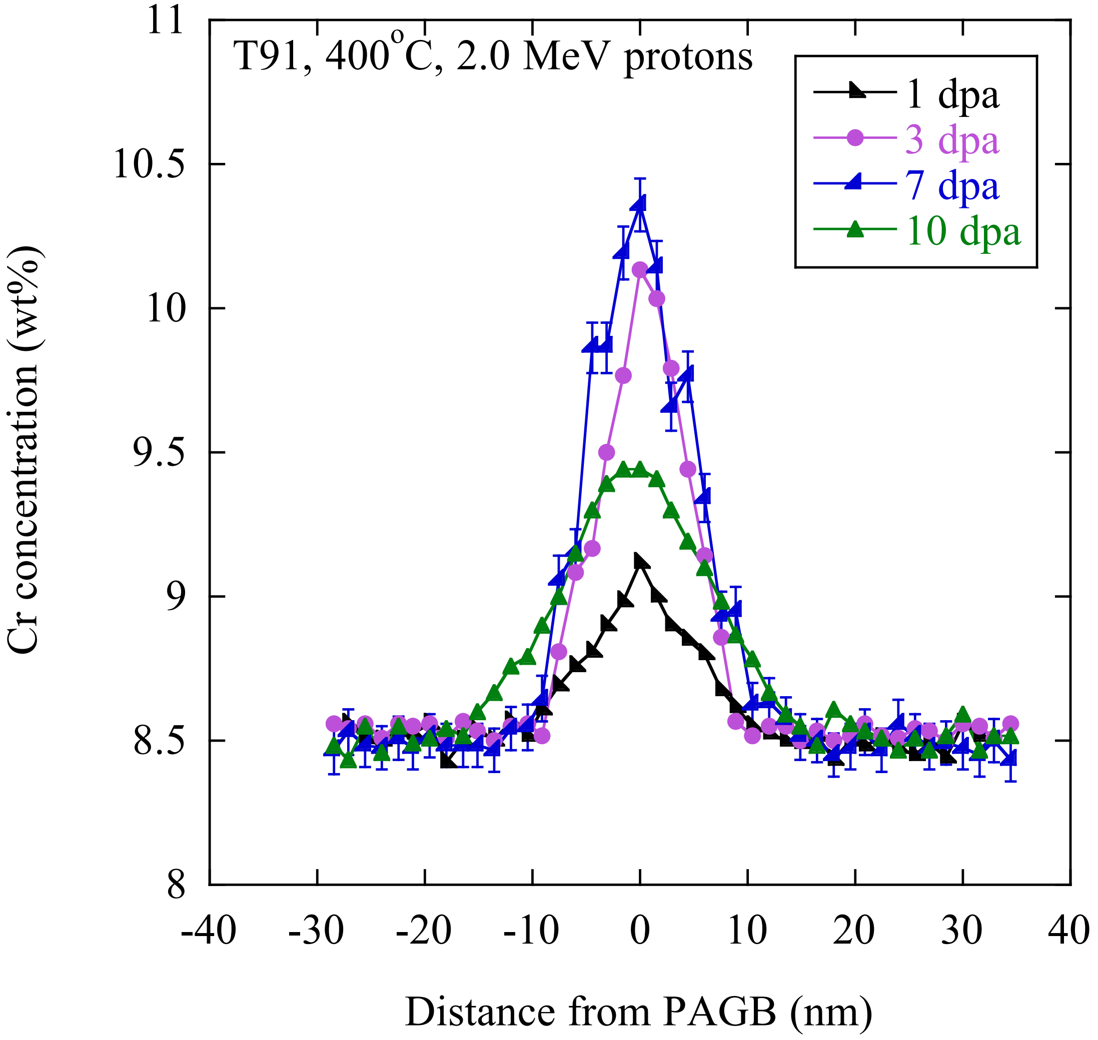

Figure 5.27. Representative Cr RIS profiles from T91 over a range of doses at 400°C.

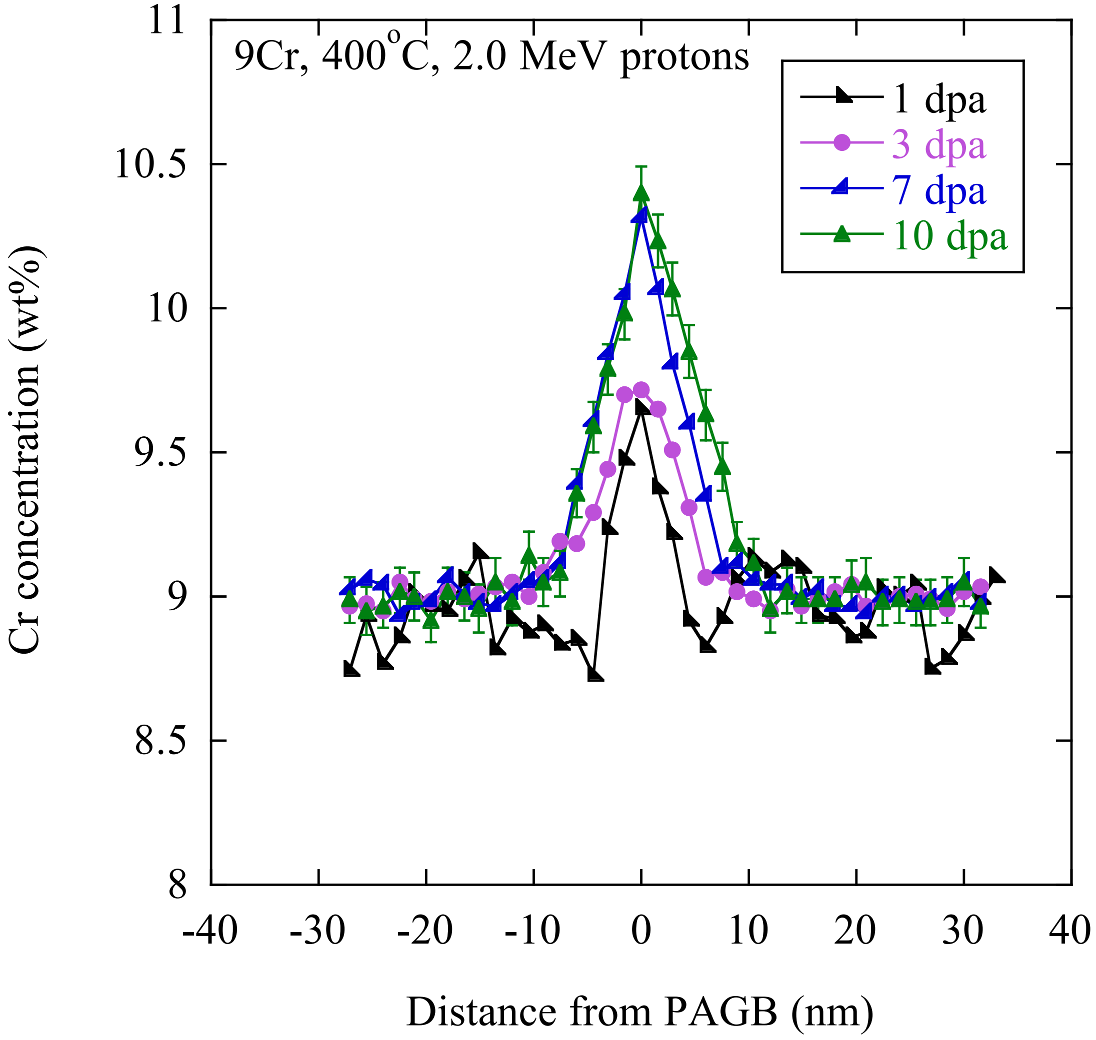

Figure 5.28. Representative Cr RIS profiles from 9Cr model alloy over a range of doses at 400°C.

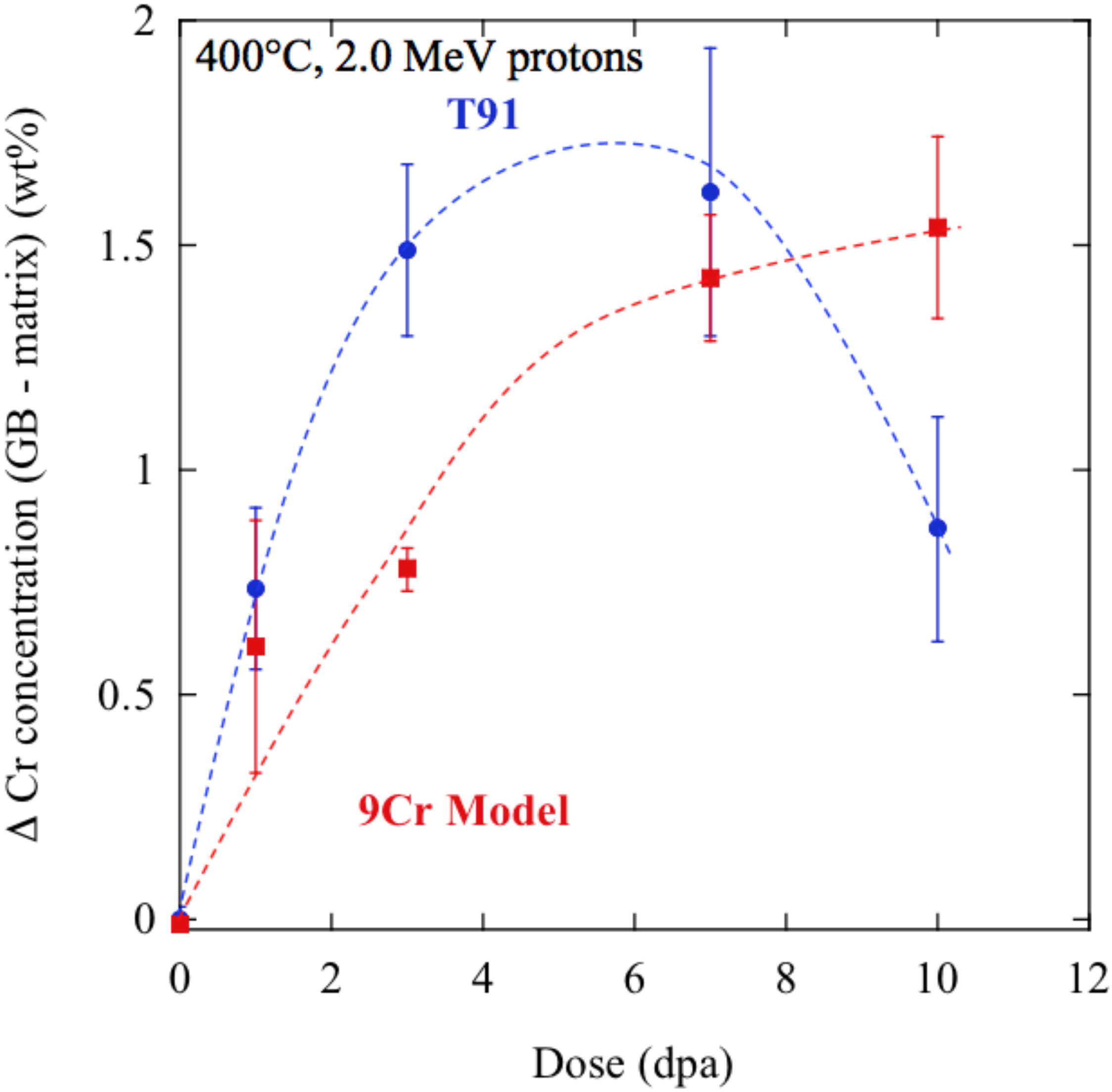

Figure 5.29. Average change in grain boundary Cr concentration for T91 and 9Cr model alloy, as a function of dose, when irradiated at 400°C with 2.0 MeV protons.

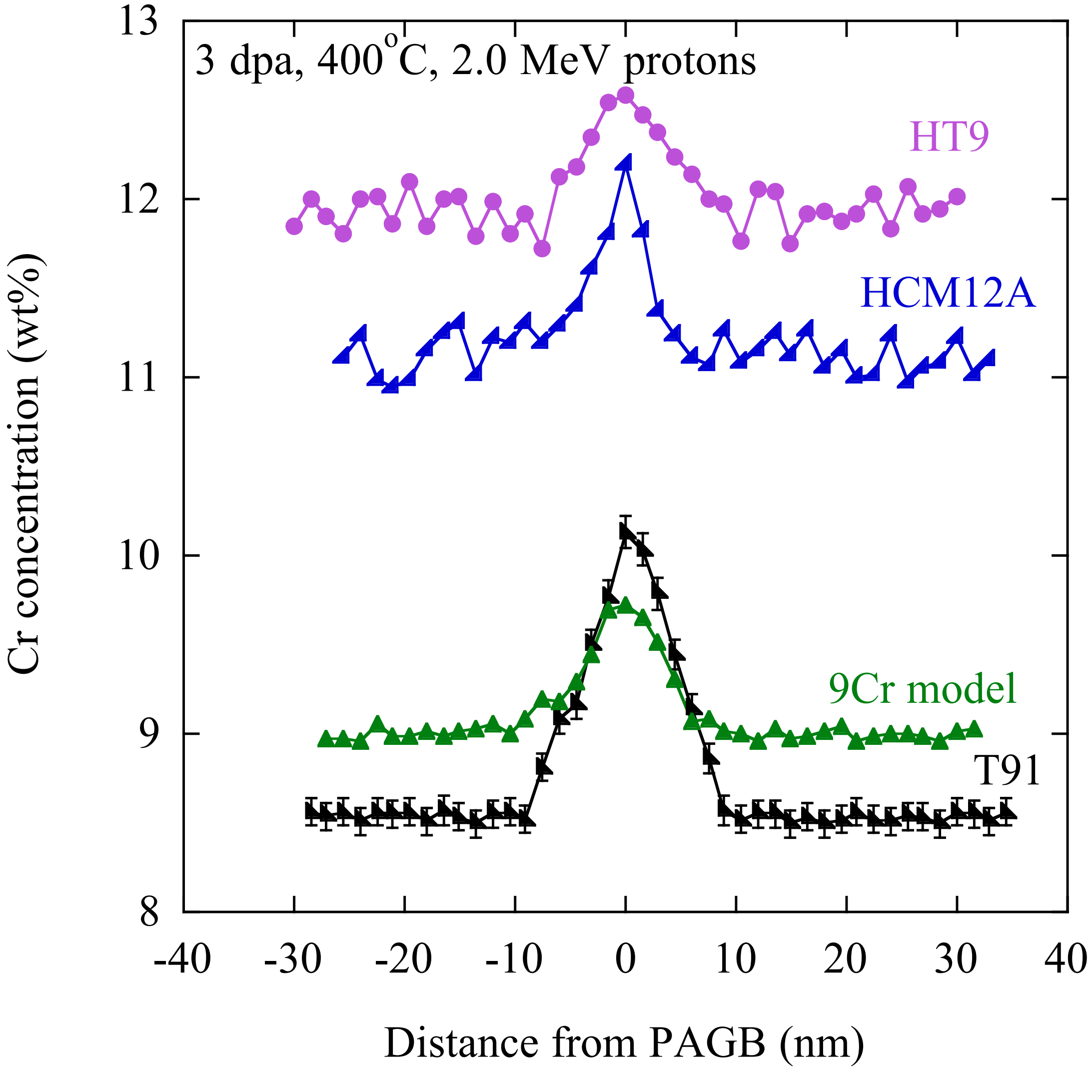

Figure 5.30. Representative Cr RIS profiles from four F-M alloys irradiated to 3 dpa at 400°C.

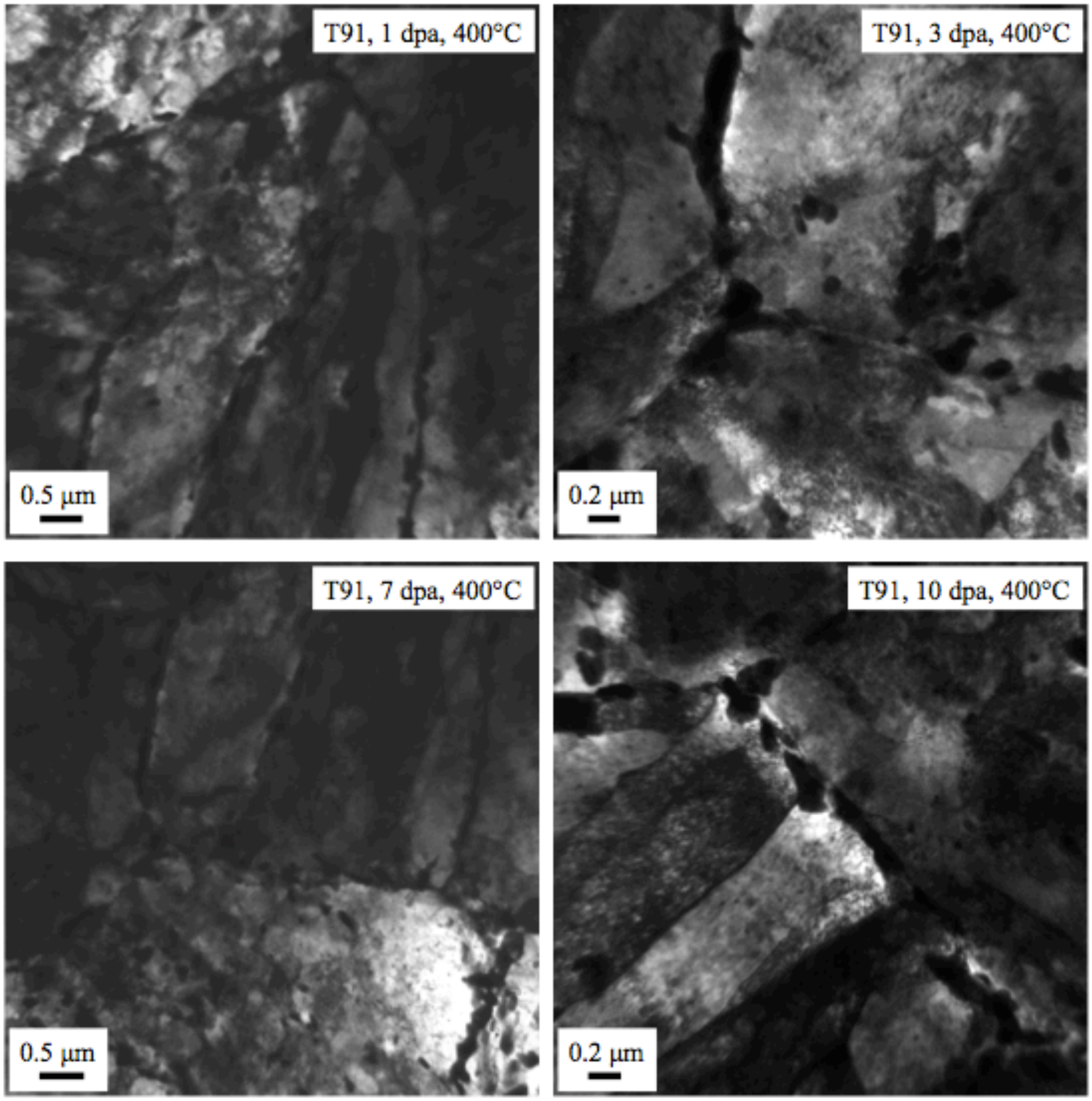

Figure 5.31. Bright field TEM images of the basic microstructure of T91 irradiated at 400°C to 1, 3, 7, and 10 dpa, showing lath structure, precipitates, dislocation loops and lines.

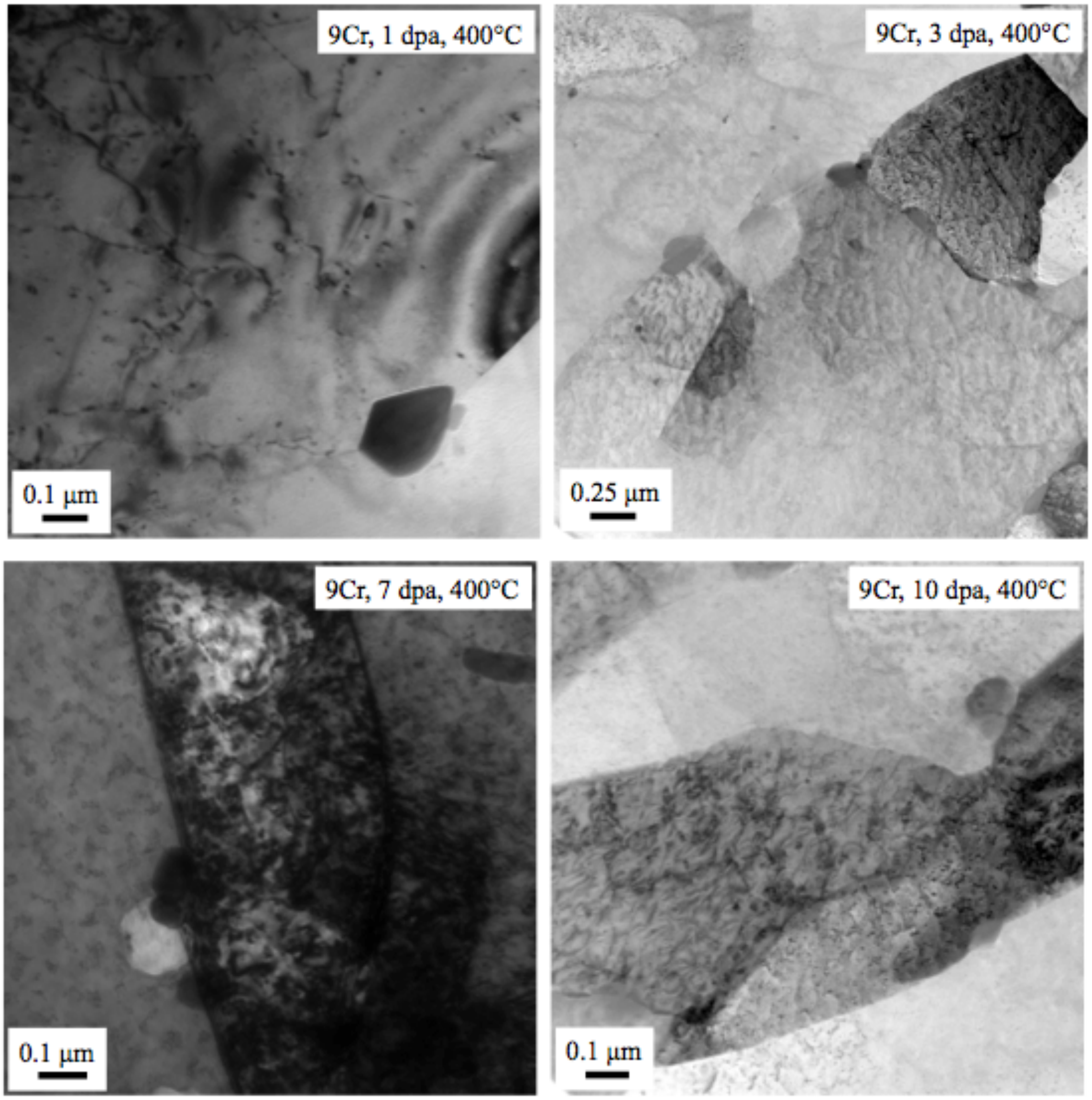

Figure 5.32. Bright field TEM images of the basic microstructure of 9Cr model alloy irradiated at 400°C to 1, 3, 7, and 10 dpa, showing lath structure, precipitates, dislocation loops and lines.

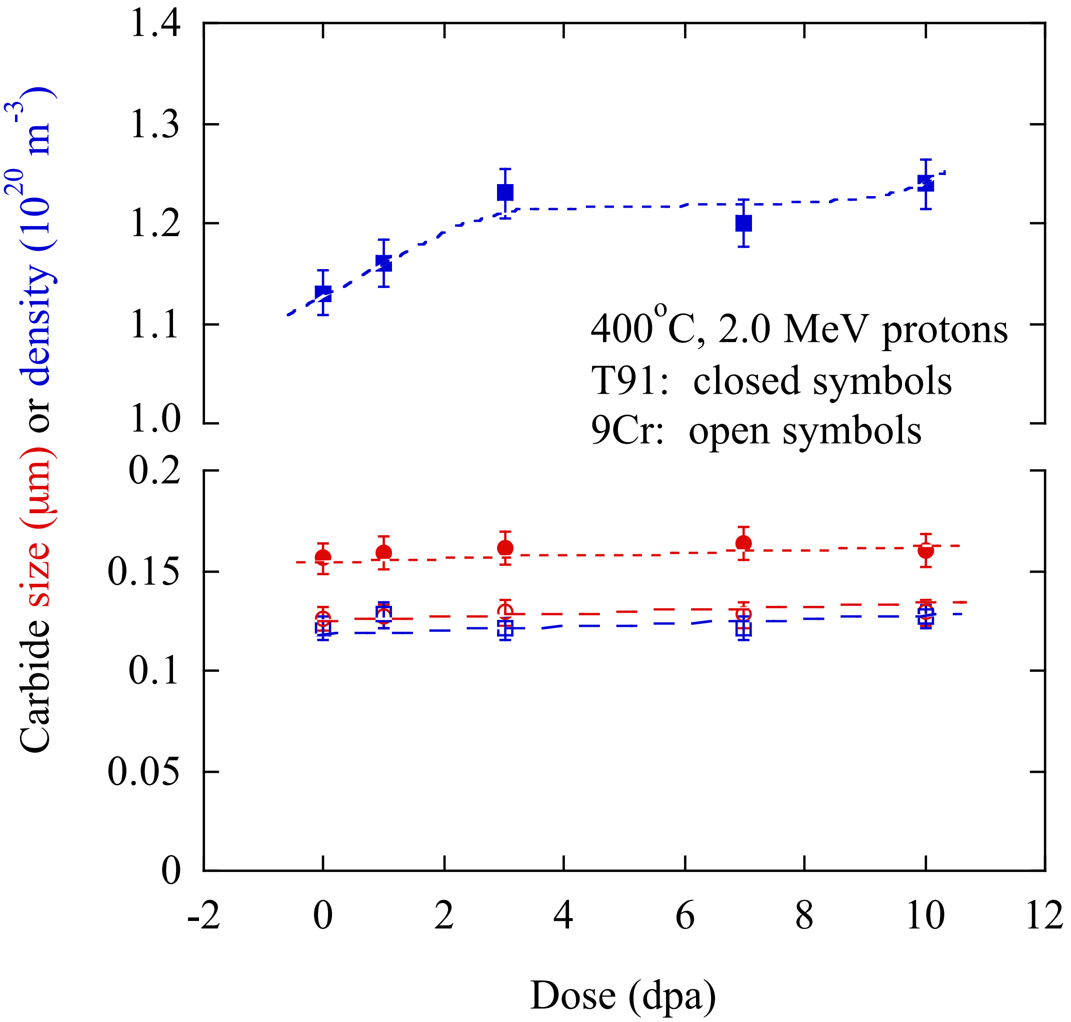

Figure 5.33. Precipitate size and density as a function of dose for T91 and 9Cr model alloy irradiated at 400°C with 2.0 MeV protons.

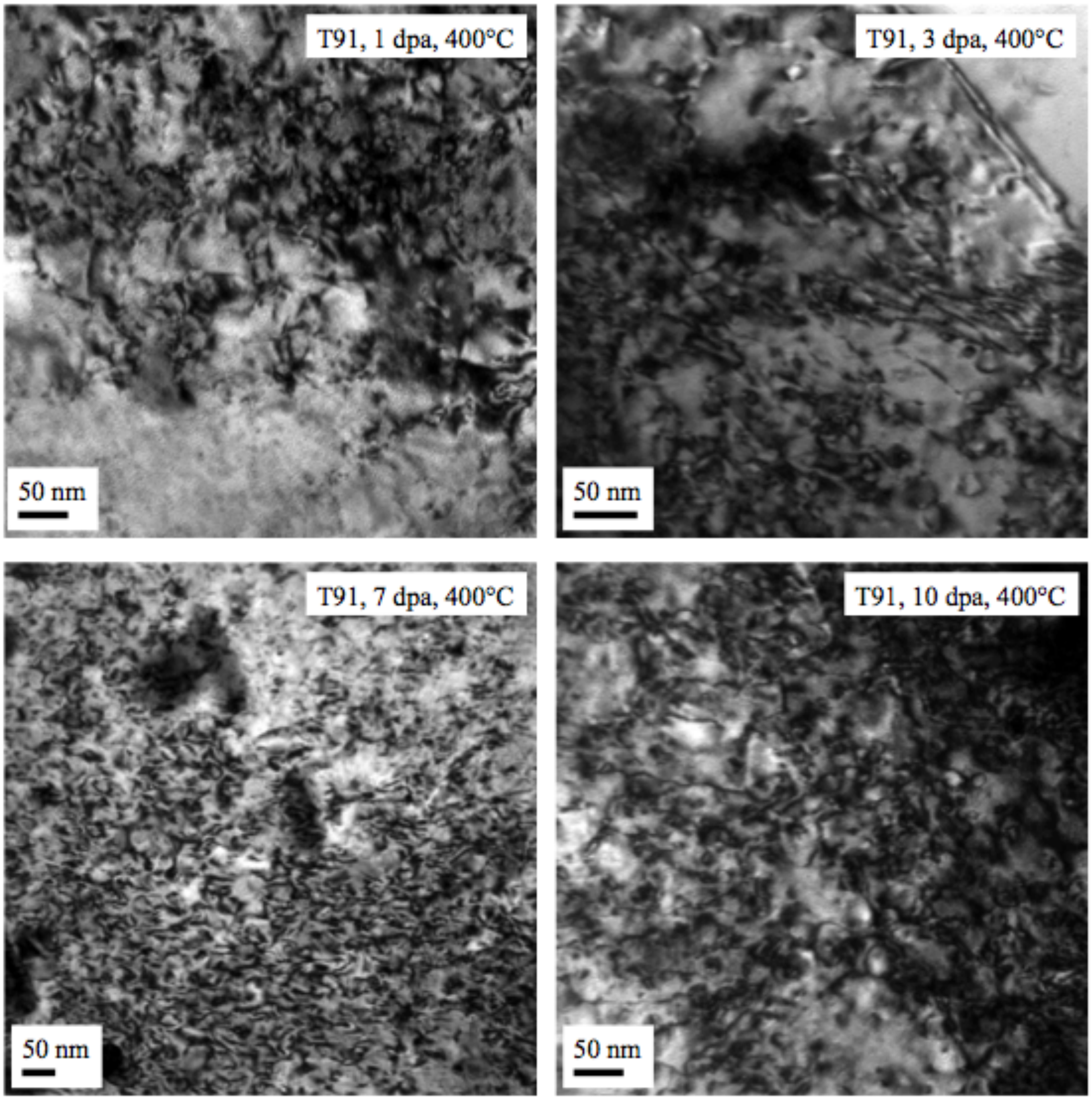

Figure 5.34. TEM images of dislocation loops in T91 irradiated at 400°C to 1, 3, 7, and 10 dpa.

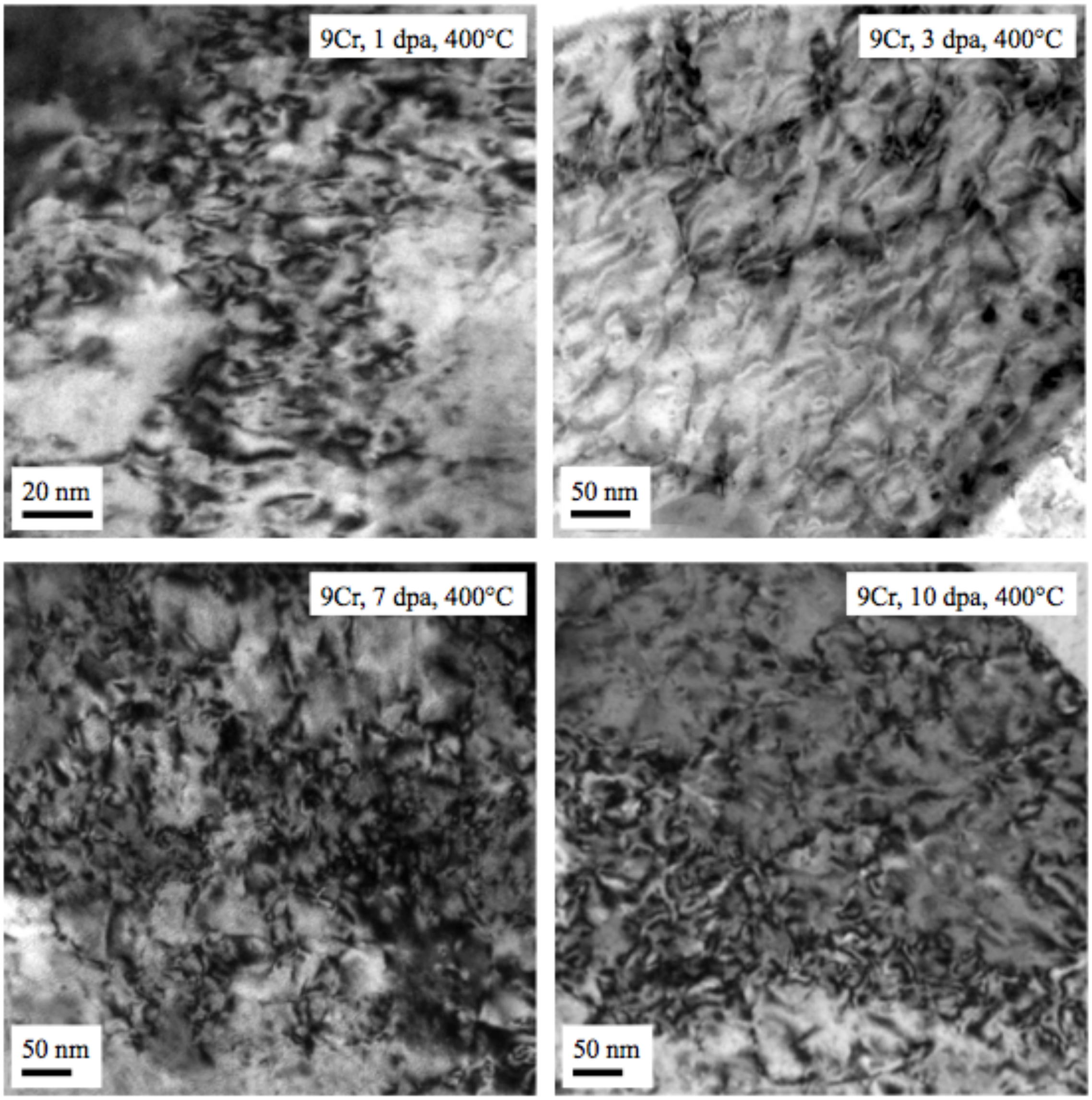

Figure 5.35. TEM images of dislocation loops in T91 irradiated at 400°C to 1, 3, 7, and 10 dpa.

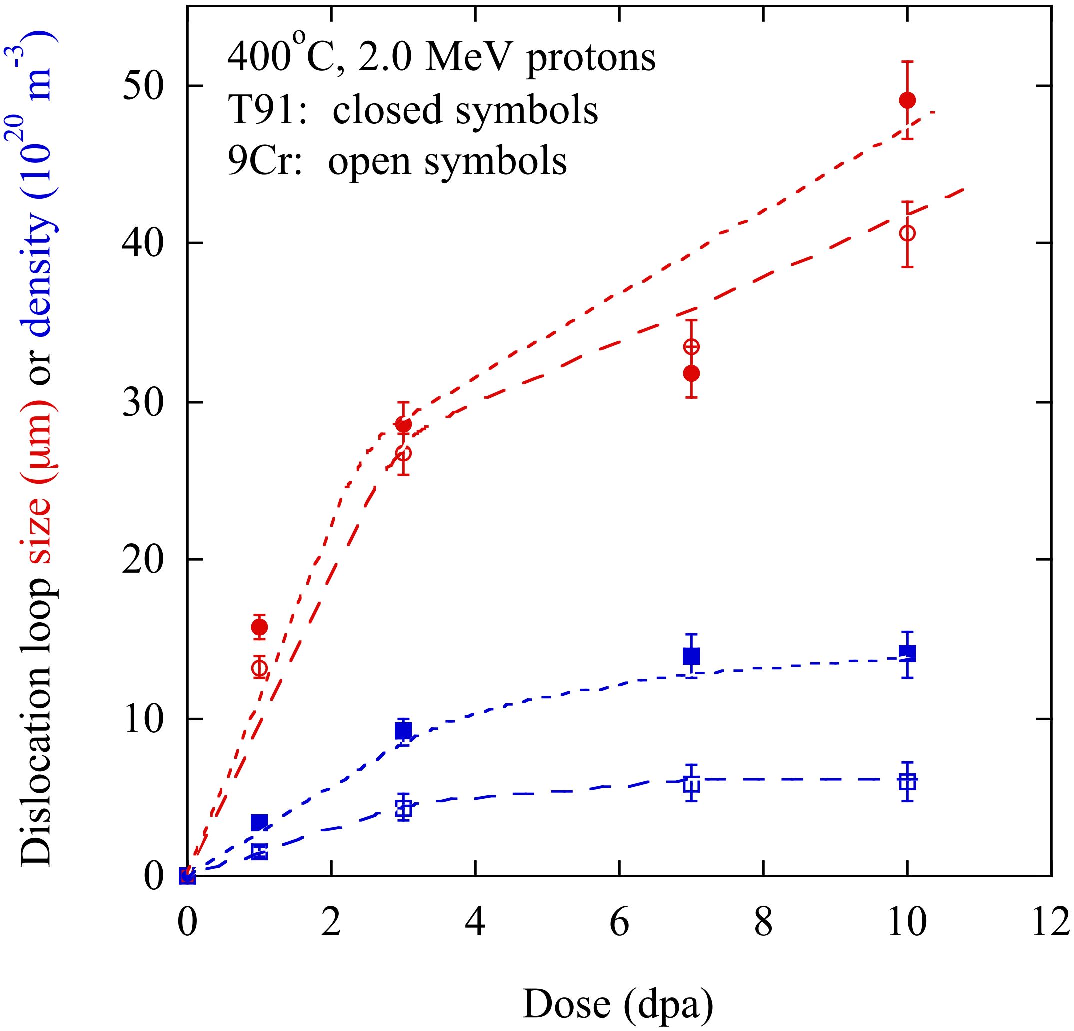

Figure 5.36. Dislocation loop size and density as a function of dose for T91 and 9Cr model alloy irradiated at 400°C with 2.0 MeV protons.

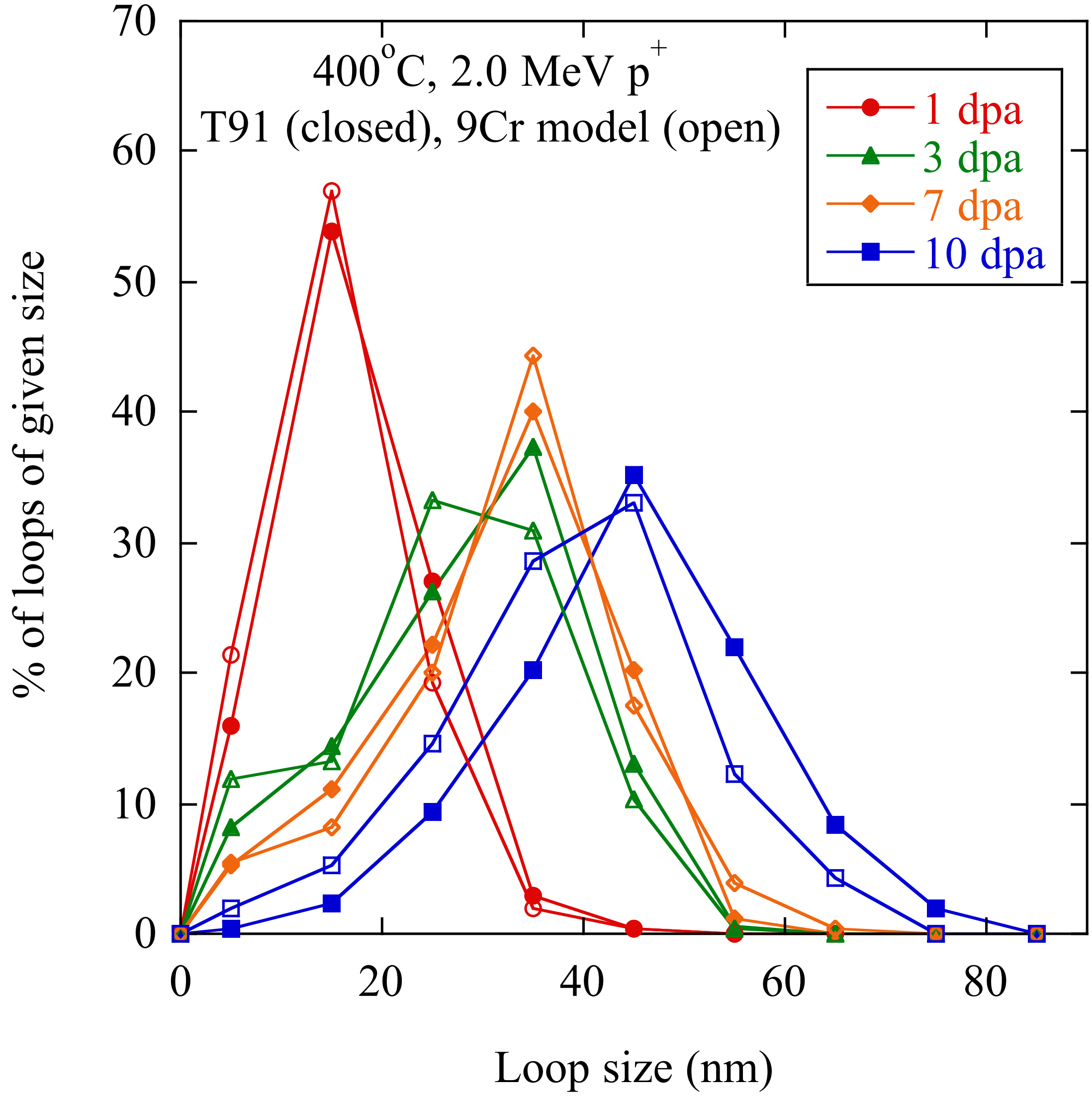

Figure 5.37. Dislocation loop size distribution for doses 1-10 dpa in T91 (closed symbols) and 9Cr model alloy (open symbols) irradiated at 400°C with 2.0 MeV protons.

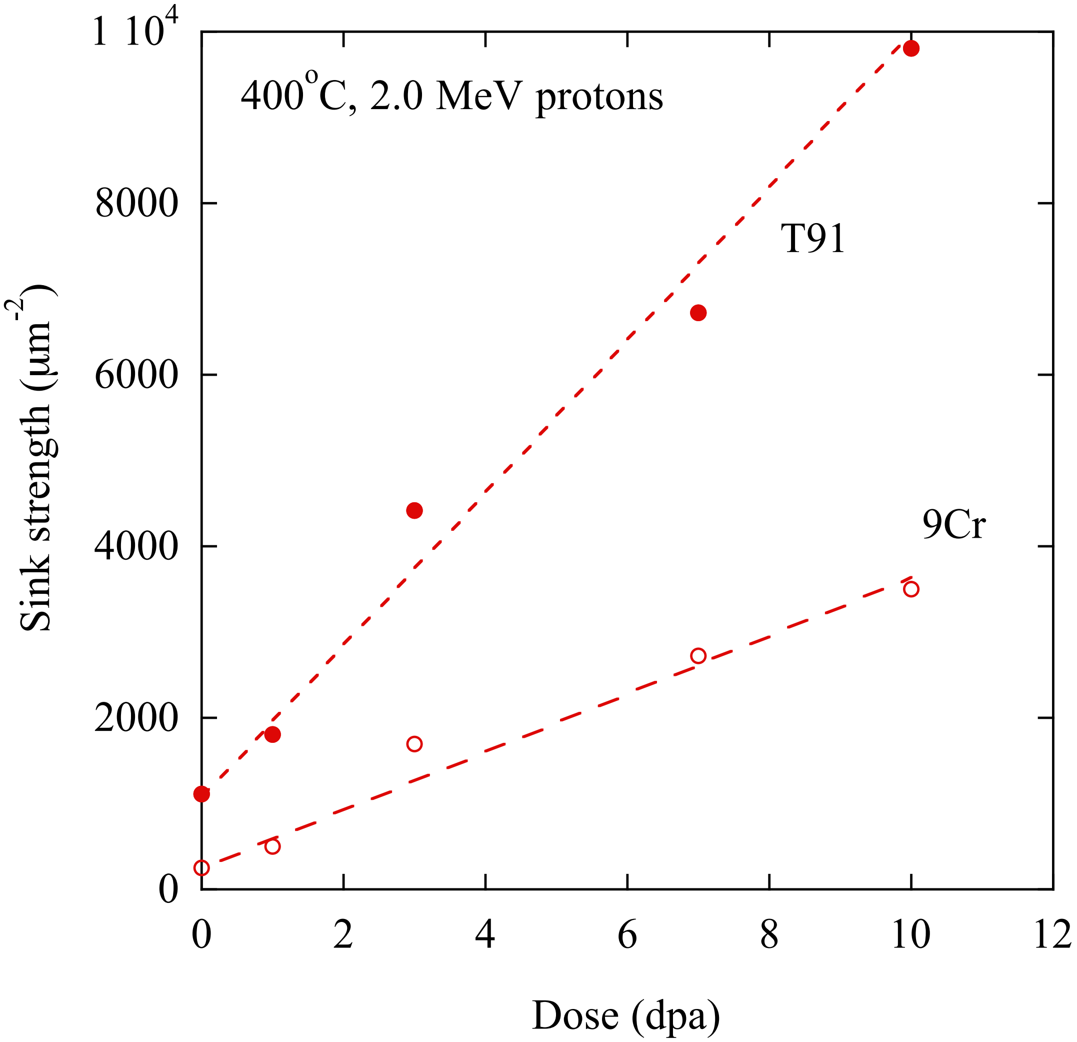

Figure 5.38. Sink strength as a function of dose for T91 and 9Cr model alloy irradiated at 400°C with 2.0 MeV protons.

CHAPTER 6   MODELING

This chapter covers the computational modeling effort, which, when coupled with the experimental measurements presented in the previous chapter, will provide the capability to test mechanisms of RIS. The modeling work accomplishes two primary objectives: (1) demonstrates the expected behavior of Cr and Fe RIS in F-M alloys according to the inverse Kirkendall mechanism, and (2) demonstrates how the expected behavior of RIS changes when the model accounts for a solute drag mechanism. As such, this chapter will present results from both of these aforementioned objectives, but first, the modeling methodology will be described and appropriate input parameters will be selected.

6.1 Modeling Methodology

The modeling effort in this thesis is built upon the inverse Kirkendall mechanism, into which the effects solute drag are later incorporated. This section first describes the inverse Kirkendall model, then demonstrates the sensitivity of the model to each of its input parameters. Lastly, input parameters appropriate to the F-M alloy system are selected. The purpose of this section is to provide a complete characterization of the modeling methodology, which will serve as background for the latter sections of this chapter, wherein model results will be presented.

6.1.1 The Inverse Kirkendall Model

The one-dimensional inverse Kirkendall model used in this thesis is based upon the Perks [17], [37] rate theory model, the equations for which have been presented in Section 2.1.3. The model is written to accommodate a ternary alloy, but in this work, is only executed for a binary (Fe-Cr) alloy by assigning the third alloy component a concentration of 0.0. The IK model used in this thesis was borrowed from the work of Allen and Was [18], in which the Perks model had been extended to include composition-dependent vacancy diffusivities for ternary Fe-Cr-Ni austenitic steels. The Allen and Was model can be utilized in this thesis, so long as the modifications accounting for the cohesive and ordering energies are removed, thus returning the model to its original Perks formulation.

The IK model is coded in Fortran and uses the GEAR software package, which is designed to solve initial value problems for a system of differential equations. The GEAR software solves a system of differential equations (in the IK model, this system of equations is the kinetic rate equations defined in Equations 2.32-2.36) with initial and boundary conditions, by using finite differences to solve spatial derivatives with a continuous time variable [99–101]. The model calls seven different subroutines according to the flowchart shown in Figure 6.1, in which subroutine names are shown in boldface. The role of each subroutine is described below:

INIT: The INIT subroutine reads in all input values, which are provided by the user in a text file format. INIT uses the input parameters to calculate and output diffusion coefficients and recombination coefficients. This subroutine is accessed only once per problem.

PREP: The PREP subroutine sets the control inputs and time steps to be used in the GEAR package. This subroutine is accessed only once per problem.

DRIVE: The subroutine DRIVE is the driver routine for the GEAR software package, and is called once for each value of T (i.e. each time step). This subroutine converts the system of ordinary differential equations (o.d.e.) into a matrix o.d.e. of the form Y(I,6). In the matrix, the variable I is an integer initialized to 1 that increments by 1 after every execution of the STIFF and DIFFUN subroutines, until it reaches a value N, equal to the number of first-order differential equations in the system. The other dimension in the Y matrix is a constant value of 6 as required by GEAR. The DRIVE subroutine makes repeated calls to the core integrator, STIFF.

STIFF: The STIFF subroutine is the core integrator routine of the GEAR package. It performs one step of the integration of an initial value problem for a system of o.d.e., and the associated error control. The DRIVE subroutine calls STIFF N times (N being the number of equations in the system) at each time step.

DIFFUN: The subroutine DIFFUN calculates the time rate of change of each component (atomic species, vacancies, and interstitials). DIFFUN is accessed by STIFF N times for each output time step.

INTERP: The INTERP subroutine interpolates from the last GEAR time step to the user-requested output step. This subroutine is accessed once per time step.

OUTPT: The OUTPT subroutine prepares the output text file, which prints atom fractions at the user-defined time steps. It is accessed only once per problem.

The IK model is compiled, debugged, and executed using SilverFrost Fortran 95 [102] for Microsoft® Windows™.

Being one-dimensional, the IK model solves the system of ordinary differential equations across a plane foil. One surface of the plane foil is fixed to simulate the grain boundary, as it is set to act as an unbiased point defect sink. Symmetry is assumed across the simulated grain boundary, as the plane foil represents the matrix on only one side of the grain boundary. The dimension of the foil is divided into a mesh, with origin at the fixed grain boundary surface. Solutions are calculated at each point along the mesh. The mesh is grouped into three sections, as illustrated in Figure 6.2. Each mesh group is defined by a user-specified distance and number, the quotient of which gives the spacing of the mesh within that group. The first mesh group ranges from the grain boundary (0 nm) to a few nanometers, specifically 4 nm, with spacing of 0.25 nm. Within this first mesh group, the solution changes rapidly, and thus many points spaced close together, provide the optimal solution. The second mesh group ranges from a few nanometers to 18 nm, with spacing of 1.0 nm; here, the solution does not change quite so rapidly that sub-nanometer intervals are required. The final mesh group ranges from 18 nm to a few micrometers, with spacing of a few hundred nanometers. In the final mesh group, the solution has begun to reach steady-state, as it approaches bulk concentration levels, and thus, small intervals are unnecessary. Given that the free surface of the plane foil is a few micrometers away from the grain boundary, and that the concentration profiles occur only within a few nanometers of the grain boundary, the foil can be approximated as being infinite.

The user is also called upon to define the timesteps at which the model is to calculate a solution. The timesteps are input in units of seconds, but can be converted to dose (dpa) when accounting for the user-input dose rate (dpa/sec). Similar to the mesh spacing, timesteps were selected to optimize the accuracy of the solution. Timesteps shorter than 1.0 second, for typical neutron, proton, or ion dose rates, often provide no information. The timesteps selected throughout this thesis, and the associated doses for a 10^{-5} dpa/sec dose rate, are shown in Table 6.1.

The model generates elemental and point defect concentrations at each mesh point, at every defined timestep. A number of inputs are required for model execution; these inputs can be classified as either input parameters or condition parameters. The condition parameters describe the experimental conditions which the model is attempting to simulate; a list of these is provided in Table 6.2. The input parameters, on the other hand, are generally fixed for the F-M alloy system and remain constant during all model executions. A complete list of the input parameters, with their definitions and units, is provided in Table 6.3. The selection of values for each of these input parameters will be addressed in Section 6.1.3, but it is first instructive to understand the sensitivity of the model to each of the parameters.

6.1.2 Sensitivity Analysis

The IK model requires the input of a large number of parameters, which collectively describe diffusivity in the alloy system being studied. Clearly, some of these input parameters will have a greater influence on the model output than other parameters. In this section, a sensitivity analysis is performed in order to identify the input parameters that have the greatest influence over the model output. The output parameter with respect to which sensitivity will be calculated is the grain boundary Cr concentration. Note that since the model considers a simple binary Fe-Cr alloy, the model sensitivity with respect to the grain boundary Cr concentration will be equal in magnitude but opposite in direction to the model sensitivity with respect to the grain boundary Fe concentration.

Model sensitivity was defined as the derivative of the grain boundary Cr concentration as a function of an input parameter, $\partial C / \partial P$. For calculational purposes, the sensitivity was approximated as the ratio of the change in grain boundary Cr concentration to the change in input parameter value, $\delta C / \delta P$. Each input parameter was varied by a factor of 10^{-4} about its reference value and the sensitivity was thus expressed as follows:

$$\frac{\partial C}{\partial P} \approx \frac{\delta C}{\delta P} = \frac{C' - C_{reference}}{P' - P_{reference}}, \qquad (6.1)$$

where $P_{reference}$ is the reference input parameter, $C_{reference}$ is the grain boundary Cr concentration calculated when $P_{reference}$ is used, P' is the varied input parameter, and C' is the grain boundary Cr concentration calculated when P' is used.

The sensitivity can more clearly be expressed as a significance, S_P^C, which is the fractional change in calculated grain boundary Cr concentration relative to the fractional change in input parameter. The significance is calculated as:

$$S_P^C = \frac{C' - C_{reference}}{P' - P_{reference}} \cdot \frac{P_{reference}}{C_{reference}}. \qquad (6.2)$$

It follows, then, that the variable of interest, grain boundary Cr concentration, is most sensitive to those parameters that have the largest significance values.

Significance was calculated at two different temperatures, 320°C and 500°C, for an Fe-9Cr alloy irradiated to a steady-state dose of 15 dpa at a dose rate of 10^{-5} dpa/sec. These two temperatures were selected because they are both below the crossover temperature, which eliminates the possibility of a change in Cr RIS direction (enrichment to depletion, or *vice versa*) from skewing the calculated significance values. Significance values for relevant input parameters are reported in Table 6.4, and are also shown graphically in Figure 6.3. Significance results at the two temperatures, 320°C and 500°C, are nearly identical, and thus, there is no evidence of a temperature dependence of the significance of each input parameter.

From Table 6.4, it is also clear that the grain boundary Cr concentration is highly sensitive to four parameters, each of which have absolute significance values around 50;

these parameters are the vacancy migration energies (EMA, EMB) and interstitial migration energies (EMIA, EMIB) of both A and B alloy components. The grain boundary Cr concentration is relatively insensitive to all other parameters studied, all of which have absolute significance values ≤ 5. These results are substantiated by the work of Allen and Was [18], which also demonstrated that even for austenitic alloys, the IK model is highly sensitive to point defect migration energies, but was insensitive to other parameters that do not affect the defect migration energies.

6.1.3 Input Parameter Selection

In the preceding section, it was shown that a small, incremental change in some parameters, namely the point defect migration energies, had a substantial influence on the grain boundary concentrations calculated by the IK model. It thus became evident that selecting appropriate values for these migration energies was critical to attaining useful, relevant results from the IK model. In this section, suitable values for the migration energies as well as all other input parameters are determined for modeling a binary b.c.c. Fe-Cr alloy.

Identifying appropriate values for the Fe and Cr vacancy and interstitial migration energies was not a straightforward task. Extremely limited experimental studies have examined point defect migration in bcc Fe-Cr alloys; these studies have exclusively utilized the resistivity recovery technique, which provides only qualitative results [103–106]. Quantitative experimental studies using positron annihilation or tracer diffusion techniques have been performed only on pure bcc α-Fe or pure bcc Cr, and can thus only provide a bounding limit of point defect migration energies [105], [107–110]. However, there have been a number of more recent studies using *ab initio* modeling [54], [55], [111–115] to calculate energies of vacancy and interstitial jumps, the orientations of which have been defined by LeClaire [116], [117]. In the following subsections, *ab initio* calculations will be used to determine the migration energies that will be input to the IK model; these *ab initio* results will then be compared to bounding and qualitative experimental results in order to confirm their validity.

6.1.3.1 Vacancy Migration Energies

Vacancy migration energies of both Fe and Cr, for use in the IK model, are determined from several *ab initio* calculations of bcc Fe containing dilute additions of Cr. Within such an alloy system, a number of vacancy-Fe or vacancy-Cr jump configurations can exist; these configurations are illustrated in Figure 6.4, which is borrowed from the work of Choudhury, *et al.* [55]. Each jump configuration is assigned an alphanumeric designation, such as w_3, based upon the earlier crystallography work of LeClaire [116], [117]; these designations will be carried throughout this section. The *ab initio* models calculate migration energies for each jump configuration, with some jumps being far more energetically-favorable than others. It is the purpose, then, of this subsection, to identify which of the jumps and their associated energies should be considered in the single value, which will be used in the IK model to represent vacancy migration energy in the F-M alloy system. Iron-vacancy jumps will be considered first; Cr-vacancy jumps second.

There are six Fe-vacancy nearest-neighbor jumps to consider: w_3, w_4, w_3', w_4', w_3'', and w_4'', as defined by LeClaire [116], [117], and illustrated in Figure 6.4. All six of these jumps are corner atom to center atom position jumps, but their energetics differ because of their differing proximity to the Cr solute atom. Choudhury, *et al.* [55] determine the energies of these six jumps to fall in the range from 0.62 eV to 0.69 eV, for a dilute Fe-Cr alloy, with solute mole fraction 0.01, corresponding to 8.5×10^{20} atoms/cm^3. The Choudhury work utilizes the Vienna *ab initio* Simulation Package (VASP) with the projector augmented wave (PAW) method with plane wave cutoff of 350 eV. Calculations had been performed for 54±1 atoms within a 3x3x3 supercell; the cell shape and volume had been fixed to that of pure bcc Fe, allowing for internal ionic relaxations. Another modeling work by Wong, *et al.* [54], uses a similar methodology as the work of Choudhury, *et al.* [55]. Wong calculates the Fe-vacancy jumps to range in energy from 0.57 eV to 0.66 eV, at the dilute limit of 2.3 atomic parts per million Cr in b.c.c. Fe.

A third modeling effort, performed by Nguyen-Manh, *et al.* [111], does not specifically set up the w_3 and w_4 jump configurations, but rather studies an Fe-vacancy jump in a similar environment in which the six nearest-neighbor sites are occupied by five Fe atoms and one Cr atom. No further details are provided to describe the atomic and jump configurations. The Nguyen-Manh work uses VASP with density functional theory (DFT) in a 4x4x4 supercell to calculate a migration energy of 0.627 eV for an Fe-vacancy jump in the aforementioned environment.

The Fe-vacancy migration energies calculated in dilute Fe-Cr alloys by *ab initio* methods, as described in this subsection, are organized in Table 6.5. Taking an average of these migration energies, one arrives at 0.63 eV, which is the Fe-vacancy migration energy that shall be used in this thesis. *Ab initio* calculations suggest that the addition of dilute amounts of Cr to bcc Fe causes the Fe-vacancy migration energy to decrease [54], [55]. Thus, one would expect the Fe-vacancy migration energy calculated here for dilute Fe-Cr systems, 0.63 eV on average, to be lower than the Fe-vacancy migration energy in pure bcc Fe. Indeed, this behavior is confirmed with Johnson's classical model [118] of 530 atoms surrounding a defect in pure bcc α-Fe, for which the Fe-vacancy migration energy is calculated to be 0.68 eV.

Turning attention now to the Cr-vacancy migration energy, there is only one possible Cr-vacancy jump in the dilute Fe-Cr b.c.c. system, defined as the w_2 LeClaire jump shown in Figure 6.4. The aforementioned studies of Choudhury, *et al.* [55], Wong, *et al.* [54], and Nguyen-Manh, *et al.* [111], using their methodologies previously described, calculate the w_2 migration energy to be 0.58 eV, 0.52 eV, and 0.571 eV, respectively. A fourth *ab initio* study performed by Olsson, *et al.* [112], uses the VASP package with DFT and PAW pseudopotential. The Olsson calculations maintain a constant volume based on the equilibrium bcc Fe lattice, while relaxing the atomic position. In both a 54-atom and 128-atom supercell, Olsson calculates the Cr-vacancy migration energy in a bcc Fe lattice to be 0.54 eV. The results of these four *ab initio* calculations are summarized in Table 6.6, and come to an average of 0.55 eV, which is the value that will be used for the Cr-vacancy migration energy in this study.

The Fe-vacancy and Cr-vacancy migration energy values determined here imply that Cr preferentially migrates via vacancies, a behavior which is confirmed by resistivity recovery experiments. Resistivity recovery experiments display a stage III peak at the energy at which vacancies become mobile; this peak occurs at a lower energy in binary Fe-Cr (205-201 K) [103], [104] than in pure bcc Fe (220 K) [105]. Thus, experiments

[103–105] and models [54], [55], [111], [112] show that Cr diffuses faster than does Fe by way of vacancies in F-M alloys; the same has been observed in austenitic steels.

6.1.3.2 Interstitial Migration Energies

Much like has been done for vacancy migration energies in Section 6.1.3.1, interstitial migration energies of Fe and Cr are determined from *ab initio* calculations of bcc Fe containing dilute Cr additions. As with vacancies, a number of interstitial jump configurations can exist for both Fe and Cr. However, models have suggested that it may be more energetically favorable for the interstitial in bcc Fe-Cr systems to diffuse as a dumbbell [54], [113], [114], rather than as a single interstitial. Note, also, that a dumbbell can be oriented in several different directions within the crystal lattice. Therefore, the size and orientation of the interstitial must be considered first; then, its possible jump configurations will follow.

In bcc α-Fe, interstitials can exist as a single interstitial in either the tetrahedral or octahedral position, or as an interstitial dumbbell along the <100>, <110>, or <111> direction. The work of Fu, *et al.* [113] has shown that in pure α-Fe, the <110> dumbbell formation energy is lower than the tetrahedral, <111> dumbbell, <100> dumbbell, and octahedral orientations by 0.50, 0.70, 1.00, and 1.18 eV, respectively, using DFT calculations in a 128-atom supercell. Other *ab initio* models corroborate that the <110> interstitial dumbbell is the most energetically favorable orientation in both dilute and concentrated Fe-Cr alloys [54], [114].

The work of Terentyev, *et al.* [114] further expounds upon the favorability of the <110> dumbbell, by demonstrating that this orientation accounts for the vast majority of interstitials in concentrated Fe-Cr alloys. Terentyev uses static molecular dynamics (MD) simulations with an empirical potential fitted to the mixing enthalpy obtained from PAW methods. Over a range of Cr concentrations up to 15 at%, the Terentyev model inserts a self-interstitial atom (SIA) into all possible interstitial sites in a simulation box of 32,000 Fe and Cr atoms, in which the Cr atoms are randomly distributed. To form SIAs, the atom occupying an SIA site is displaced 0.25 lattice units in the <110> direction, and then the second atom is added to form a <110> dumbbell. The system is then relaxed, unconstrained, while quenching to near 0 K, from which a formation energy probability distribution is determined. The frequency of each formation energy is used to determine the frequency of states of <110> Fe-Fe dumbbells, <110> Fe-Cr mixed dumbbells, <111> Fe-Fe dumbbells, and <111> Fe-Cr mixed dumbbells. As shown in Figure 6.5, the <110> Fe-Fe dumbbells account for ~90% of the SIAs, with <110> mixed Fe-Cr dumbbells accounting for ~10% of all SIAs. The frequency of <110> mixed dumbbells increases with Cr concentration. The <111> Fe-Fe and Fe-Cr dumbbells account for less than 1% of all SIAs. Thus, for the purpose of this thesis, it will be assumed that all interstitials are of the <110> dumbbell orientation. Interstitial migration energies for the IK model will hence be determined based on jumps of the <110> dumbbell.

The <110> interstitial dumbbell has a number of different jump configurations, as shown in Figure 6.6, each of which has an alphanumeric designation according to the work of LeClaire [116], [117]. Three of these jumps, w_0, w_4, and w_6, are Fe jumps, and can be studied to determine an appropriate Fe-interstitial migration energy for the IK model. Similarly, w_1 and w_2 are Cr jumps. The energies of each jump configuration will be discussed in the following paragraphs; Fe-interstitials will be discussed first, then Cr-interstitials second.

Ab initio calculations for the energies of the w_0, w_4, and w_6 jumps, which represent Fe-interstitial migration energies, are performed by Choudhury, *et al.* [55], Fu, *et al.* [113], and Olsson [115]. The methodologies of Choudhury and Fu have already been described in Section 6.1.3.1, so they will not be restated here. Choudhury finds the migration energies to range from 0.35 eV to 0.39 eV, while Fu finds the w_0 jump to have an energy of 0.34 eV. Olsson, using VASP calculations in the DFT framework with PAW approach and 300 eV plane wave cutoff energy, calculates migration energies of 0.34-0.35 eV within a 128-atom supercell. The results of these three *ab initio* calculations are summarized in Table 6.7, and come to an average of 0.35 eV, which shall be used for the Fe-interstitial migration energy in this thesis. The classical model from Johnson [118] in pure bcc α-Fe calculates a mono-interstitial migration energy of 0.33 eV, which is in good agreement with the value that shall be used in the IK model.

Ab initio calculations for the Cr-interstitial migration energies (the w_1 and w_2 jumps) range from 0.23 eV to 0.33 eV, as calculated by Choudhury, *et al*. [55] and Olsson [115]. The modeling methodologies of both of these works have been described previously, and shall not be repeated here. A summary of all *ab initio* Cr-interstitial calculations is provided in Table 6.8. Because the distribution of the calculated energies provided in Table 6.8 is double-humped rather than Gaussian, further discussion of these energies is warranted.

Both authors calculate the w_2 jump to be of consistently higher energy (0.33 eV, in both studies) than the w_1 jump (0.23 eV and 0.25 eV). The w_1 jump, as illustrated in Figure 6.6, is a jump from a mixed dumbbell configuration into another mixed dumbbell configuration, whereas the w_2 jump is a jump from a mixed dumbbell to an Fe-Fe dumbbell, with the Cr atom taking a lattice position. It is not known with what frequency w_1 jumps occur relative to w_2 jumps, so to assume they occur with equal frequency and take an arithmetic mean of their energies is a rather unbiased approach. Therefore, an average value of 0.26 eV will be used for the Cr-interstitial migration energy in this thesis.

Resistivity recovery experiments, while not quantitative, have shown that the addition of Cr (up to 0.095 at%) to α-Fe stabilizes mixed-dumbbell SIAs, confirming that Cr is a faster diffuser than Fe via interstitials [106]. Similarly, Terentyev, *et al*. [114] have shown via *ab initio* modeling that the migration energy of single SIAs—including multiple configurations of both pure Fe-Fe and mixed Fe-Cr dumbbells—decreases with increasing Cr concentration, from 0.31 eV in pure Fe, to 0.23 eV in Fe-15Cr. Thus, for alloys having higher Cr concentration, the Fe and Cr interstitial migration energies will follow the slope of Terentyev's results. Both experiments [106] and models [55], [113–115] show that Cr is a faster diffuser than Fe by way of interstitials.

6.1.3.3 Other Input Parameters

The grain boundary Cr concentration has been shown to exhibit very little sensitivity to any input parameters besides the vacancy and interstitial migration energies. However, it is nevertheless important to select appropriate values for the remaining input parameters. In this section, experimental and modeling results from literature will be used to arrive at suitable values for all remaining input parameters. A complete list of input parameters and their values is provided in Table 6.9; the following paragraphs will discuss how these values are determined.

ETAV, ETAI: The vacancy and interstitial production efficiency can be simulated by coupling molecular dynamics and kinetic Monte Carlo (KMC) techniques. Diaz de la Rubia, *et al*. [119] use MD simulations to describe the primary damage state and defect energetics and kinetics in a range of metals, including bcc α-Fe. These results are then implemented into a KMC simulation, from which the escape efficiency of defects from damage cascades and related damage accumulation parameters can be extracted. The results of the Diaz de la Rubia simulations state that for primary knock-on atoms having energy ≥ 5 keV in bcc α-Fe, the production efficiency for both vacancies and interstitials is 0.30.

FAV, FBV, FAI, FBI: The Fe vacancy correlation factor, 0.727, is determined from tracer self-diffusion experiments in bcc Fe in the temperature range 720-895°C [120–122], and is confirmed by a molecular dynamics study in pure b.c.c. Fe performed by Osetsky & Serra [123]. The Cr vacancy correlation factor, 0.777, is interpolated from a Monte Carlo simulation of dilute Cr in b.c.c. Fe, over a temperature range 450-813°C [124]. Iron and Cr interstitial correlation factors, both 0.727, are taken from a Monte Carlo simulation in pure b.c.c. Fe [125].

WAV, WBV, WAI, WBI: There have not been any experiments performed to determine the Fe and Cr vacancy and interstitial jump frequencies in bcc Fe-Cr alloys, so the values used for bcc austenitic alloys in the work of Allen and Was [18] are used here as an approximation. These Fe and Cr vacancy jump frequencies of 1.60×10^{13} s^{-1} and 2.40×10^{13} s^{-1}, respectively, are determined by radioactive tracer diffusion in various austenitic steels between 960°C and 1400°C [126]. The Fe interstitial jump frequency, 2.90×10^{12} s^{-1}, is from a molecular dynamics simulation in pure bcc Fe by Osetsky & Serra [123], performed over a wide range of temperatures. Finally, the Cr interstitial jump frequency, 1.50×10^{12} s^{-1}, is taken from the original Perks model [17], [37].

EFA, EFB, SV: The Fe vacancy formation energy is determined to be 1.6 eV by two positron annihilation studies in pure bcc Fe [107], [127]. The Cr vacancy formation energy is approximated to be 2.25 eV, which is the vacancy formation energy in pure bcc Cr, as determined by Campbell and Schulte [128] through a positron trapping and self-diffusion experiment. The vacancy formation enthalpy, 1.00 eV/m^3, is approximated from the work of Allen and Was [18] in fcc austenitic iron.

<u>EFGB</u>: Tschopp, *et al*. [129] performs a grain boundary statics simulation of b.c.c. Fe, in which vacancy formation energies are calculated over a number of grain boundaries, each of which has a different Σ value and tilt. The average vacancy formation energy, across all boundaries studied, is 0.87 eV.

<u>NAT, LAMBDA, Z</u>: The number density and jump distance are approximated to be that of the bcc Fe unit cell, 8.34 x 10^{28} atoms/m^3 and 2.48 x 10^{-10} m, respectively. The number of neighbors, 8, is a property of the bcc unit cell.

<u>H0, EPS, AL, NUOV, NUOI</u>: These parameters H0 and EPS are both initialized at 1 x 10^{-9}, as optimized for the GEAR subroutine. The thermodynamic factor of 1 is approximated from the austenitic stainless steel IK model of Allen and Was [18]. The Debye frequencies for vacancies and interstitials in Fe are also approximated from the austenitic stainless steel work of Allen and Was, as 1.50 x 10^{13} s^{-1} and 1.50 x 10^{12} s^{-1}, respectively.

<u>R1, R2, RF, N1, N2, N3</u>: These parameters set up the mesh groups and their intervals, the method for which has been discussed in Section 6.1.1. The three mesh groups extend 4.0 (R1), 18.0 (R2), and 2018.0 (RF) nm from the grain boundary, respectively. Given the N1, N2, and N3 values of 16, 14, and 20, the intervals at which the model is solved in each mesh group are 0.25, 1.0, and 100 nm, respectively.

6.1.4 Convolution of Model Results

The measured RIS profiles presented in Chapter 5 and Appendix B are convoluted by the STEM electron probe. Because STEM measurements of RIS rely on an electron beam of finite size, the measured concentration profiles are underestimated due to beam broadening and sample thickness effects. The actual grain boundary composition is thus averaged over an activation volume, which contains not just the grain boundary, but some volume of the matrix adjacent to the boundary. The IK model, on the other hand, does not account for the electron probe. But when comparing model calculations to convoluted experimental measurements, the model results should also be convoluted to ensure a fair comparison. The convolution process will be described in this section. The mathematical description of convolution, and the process for deconvoluting STEM composition profiles has been detailed by Carter, *et al.* [130]. Their procedure will be followed in this work.

The STEM-measured composition profile is the convolution of the actual composition profile with the x-ray generation function, which represents the broadening of the electron beam through the thickness of the specimen. Mathematically, this convolution is written as:

$$(g*h)(x) = \int_{-\infty}^{\infty} g(x')h(x-x')dx' \qquad (6.3)$$

where x is the distance from the grain boundary, $(g*h)(x)$ is the measured, convoluted composition profile, $g(x')$ is the x-ray generation function averaged over the two spatial dimensions of the grain boundary plane, and $h(x)$ is the actual composition profile. This convolution is illustrated schematically in Figure 6.7, which shows how a narrow and sharply-peaked concentration profile will broaden and decrease in magnitude when convoluted with the x-ray generation function. While the expression in Equation 6.3 can be difficult to calculate, the relationship is simplified by Fourier transform:

$$F(g*h) = F(g)\cdot F(h) \qquad (6.4)$$

where $F(g*h)$ is the Fourier transform of the convoluted profile, $F(g)$ is the Fourier transform of the x-ray generation function, and $F(h)$ is the Fourier transform of the actual composition profile. To convolute the calculated concentration profile, one can take the product of $F(g)$ and $F(h)$ to yield the Fourier transform of the convoluted profile.

In the work of Carter, *et al.* [130], the x-ray generation function was calculated using a Monte Carlo simulation for a 304L stainless steel specimen ~50 nm thick and an electron probe of ~2 nm at full width one-tenth maximum. For this work, it is assumed that the Carter, *et al.* [130] x-ray generation function, shown in Figure 6.8 (a), can be scaled for the smaller electron probe of ≤1.4 nm at full width one-tenth maximum used in this work. The resultant x-ray generation function for this work, then, is shown in Figure

6.8(b). The MATLAB program is utilized to compute the fast Fourier transform, using the built-in `fft` algorithm.

Both the deconvoluted and convoluted Cr concentration profile, as calculated for a reference case, will be presented in Section 6.2.1. After that, however, all calculated values of Cr RIS presented in this thesis will have already been convoluted. Both IK model and the solute drag model results will be passed through the convolution process.

6.2 Inverse Kirkendall Modeling

Now that the inverse Kirkendall model has been described, and the suitability of its input parameters established, the model can be executed and results presented. In this section, the IK model results will be presented, beginning with the results of an Fe-9Cr reference case. Then, the IK model will be executed at varying irradiation conditions, so as to determine the behavior of the model as a function of experimental parameters such as temperature, dose, alloy composition, and dose rate.

6.2.1 Reference Case

A reference case for the IK model is set up so as to best replicate the experimental conditions of the proton irradiations performed in this thesis, and thus provide a basis for comparison the model to experimental results. The reference case defines: (1) the alloy composition, (2) irradiation temperature, (3) irradiation dose rate, and (4) sink density input to the model. Later in this section, the dependence of RIS on temperature, composition, and sink density will be determined by altering the parameters of this reference case.

The reference case is for Fe-9Cr, irradiated at 400°C with dose rate 1×10^{-5} dpa/sec, having a sink density of 0 m^{-2}; these condition parameters are shown in Table 6.10. The reference case predicts Cr enrichment of 2.20 at% and Fe depletion of 2.20 at% at steady-state, but when convoluted, the amount of Cr enrichment drops to 1.96 at%

and Fe depletion of 1.96 at%. Convolution causes the grain boundary concentration to decrease, and the concentration profile to broaden, as shown in Figure 6.9. The change in grain boundary concentration prior to convolution is 12.2% larger than that following convolution. This difference can be confirmed by reversing the convolution process, starting with a measured concentration profile and performing a deconvolution. Deconvolution of the Cr profile from T91_7dpa_400C_07-08_B_1-1-F, shown in Figure 6.10, causes the change in grain boundary concentration to increase by 15.2%. In Carter's work [130], deconvolution is shown to increase the change in grain boundary concentration by 11-16%. Carter's deconvolutions are performed on Ni and Cr RIS profiles that have FWHM ~10-15 nm, which is consistent with the FWHM of profiles studied in this thesis, although the slopes of Carter's RIS profiles are larger in magnitude than those measured in this work. The electron probe used in Carter's work is the same shape, though broader, than that used in this thesis. These comparisons suggest consistency between the convolutions and deconvolutions performed in this thesis and by Carter, *et al.* [130].

Because RIS is a localized phenomenon, occurring only within a few-nanometer volume surrounding the grain boundary, it is relevant to understand the spatial behavior of point defects. The concentrations of point defects which experience one of three possible fates—recombination, annihilation at the grain boundary (i.e. contribute to RIS), or remaining in the matrix—are taken from the IK model at four different spatial distances away from the boundary. These concentrations are integrated over time (i.e. dose). The results are presented in Figure 6.11 for a dislocation line density of 0 m^{-2}, and in Figure 6.12 for 10^{15} m^{-2} dislocation line density. In both of these figures, the red region represents point defects which diffuse to the grain boundary and cause RIS, the green region represents those point defects remaining in the matrix, the blue region represents recombination, and in Figure 6.12 only, the yellow region represents point defects which annihilate at sinks in the matrix.

The simulations using 0 m^{-2} dislocation density (Figure 6.11) will be discussed first. At 0.25 nm, diffusion of some point defects to the grain boundary begins immediately, while the remaining point defects build up in the matrix. Recombination begins by 10^{-6} dpa, at which time the number of point defects remaining in the matrix decreases as they recombine. Ultimately, >99.9999 % of the point defects cause RIS at the grain boundary, while only ~0.01% recombine. Further away from the boundary at 7.75 nm, defects build up in the matrix until they begin to recombine and diffuse to the grain boundary; ~99.8% of the point defects reach the grain boundary, while the remaining ~0.2% recombine. Recombination becomes more dominant further from the grain boundary, while the boundary becomes less important as a sink. By 41.8 nm, ~99% of the point defects generated recombine, and only ~1% of the defects diffuse to the grain boundary. Even further into the matrix at 618 nm, >99% of the point defects recombine.

When a dislocation density of 10^{15} m^{-2} is added to the simulation (Figure 6.12), the number of point defects generating RIS decreases to 99.99% at 0.25 nm (as compared to 99.9999% when no sinks are included in the model) and 97% at 7.75 nm (as compared to 99.8% when no sinks are included in the model). A considerable amount of the recombination is replaced by annihilation of point defects at sinks. The presence of sinks decreases the number of defects available to diffuse to the grain boundary and cause RIS. By 41.8 nm away from the grain boundary, point defects are generally unable to escape recombination or annihilation at sinks, and are thus unable to diffuse to sinks to cause RIS. This analysis shows that RIS is largely caused by point defects generated within a few nm or few tens of nm around the grain boundary; of course, this dimension will be temperature-dependent.

6.2.2 Temperature Dependence

The temperature dependence of RIS in Fe-9Cr is predicted by the IK model, using the reference case condition parameters (10^{-5} dpa/sec, steady-state dose of 15 dpa) and altering the irradiation temperature in increments of ±50°C, as shown in Table 6.10. The resulting temperature dependence, as shown in Figure 6.13, exhibits Cr enrichment at lower temperatures and Cr depletion at elevated temperatures. Chromium enrichment behavior changes to depletion at what shall be called the "crossover temperature". Here, the crossover temperature occurs near 530°C, at which point there is no segregation. At the extremely low and extremely high temperature limits, ≤ 200°C and ≥ 800°C, RIS is suppressed, and little to no segregation is predicted. However, between the extreme limits and the crossover temperature, a double bell-shaped temperature dependence exists. Chromium enrichment is maximized near 400°C, while Cr depletion is maximized near 600°C.

The crossover behavior of Cr enrichment to Cr depletion is a significant and defining feature of the F-M IK model. The crossover can be explained by the Cr:Fe diffusion coefficient ratios for vacancies and interstitials. As shown in Figure 6.14, these ratios are both greater than unity, which means that Cr diffuses faster than Fe via both vacancies and interstitials. Therefore, at temperatures where vacancy diffusion dominates, Cr will deplete, and at temperatures where interstitial diffusion dominates, Cr will enrich. The Cr:Fe vacancy diffusion coefficient ratio crosses that of interstitials near 530°C, so for T<530°C, interstitial diffusion dominates and Cr enriches, whereas for T>530°C, vacancy diffusion dominates and Cr depletes.

The crossover between Cr enrichment and Cr depletion does not occur in austenitic steels, in which RIS is driven only by differences in the relative Ni and Cr association with the vacancy flux. Interstitials do not contribute significantly to RIS in austenitic steels, as all species are set to have equal interstitial diffusivities [15], [17], [18], [37]. As a result, the vacancy and interstitial diffusion coefficient ratios for austenitic steels do not cross one another in the temperatures range of interest, as shown in Figure 6.14. Unlike the F-M diffusion coefficient ratios, the austenitic ratios differ in slope and magnitude, specifically in the temperature range of interest.

Note also that when sinks are included in the IK simulations, the shape of the temperature dependence does not change, but its magnitude decreases. Results of temperature dependence with a sink density of 10^{17} m^{-2}, which represents the upper limit of sink density in a commercial F-M alloy, are shown in Figure 6.13.

6.2.3 Dose Dependence

Dose dependence is studied by considering the reference case condition parameters (Fe-9Cr, 400°C, 10^{-5} dpa/sec) over a range of irradiation doses, from 0.0001 dpa, up to 100 dpa, as shown in Table 6.10. As shown in Figure 6.15, the amount of RIS increases rather rapidly before 1 dpa. By just above 1 dpa, steady-state RIS behavior is achieved, and the amount of RIS plateaus through the maximum dose studied. This dose dependence is very similar to that obtained by the IK model for austenitic steels [15], [18]. Introducing a sink density of 10^{17} m^{-2} does not alter the dose dependence, nor the dose at which RIS steady-state is reached. The sink density simply decreases the amount of RIS present.

6.2.4 Composition Dependence

The composition dependence of the IK model is determined by executing the reference case condition parameters but varying the bulk Cr concentration between 7 at % and 15 at% in increments of 1 at%, as noted in Table 6.10. As shown in Figure 6.16, the IK model predicts an increasing amount of Cr RIS with increasing bulk Cr concentration for a range of Fe-Cr alloys irradiated at 400°C to a steady-state dose of 15 dpa at 10^{-5} dpa/sec. The amount of RIS can change by as much as 1.5 at% when the bulk Cr concentration is changed from 9 at% to 15 at%. The inclusion of sinks in the model decreases the magnitude of the slope of the RIS vs. Cr concentration line and decreases the predicted amount of RIS, but the sign of the slope (positive) remains the same.

6.2.5 Dose Rate Dependence

The dose rate dependence of the IK model is determined by altering the reference dose rate by factors of 10 such that the dose rate ranged from 10^{-7} dpa/sec to 0.1 dpa/sec. The condition parameters for the dose rate dependence are shown in Table 6.10. The IK model predicts a decreasing amount of Cr RIS with increasing dose rate, as shown in Figure 6.17. This negative slope makes sense as higher dose rates cause quicker accumulation of damage, without allowing sufficient time between damage events for point defects to diffuse to grain boundaries. However, the negative slope is very shallow, as the amount of Cr RIS is only predicted to change by ~0.75 at% over six orders of magnitude of dose rate. This behavior is markedly different than that of austenitic stainless steels, in which a considerable temperature shift is required to compensate for a two-orders-of-magnitude change in dose rate for comparable irradiated microchemistry [131], [132].

The very shallow slope along with experimental limitations make it unlikely that a dose rate dependence can be discerned experimentally. Even if it were possible to perform irradiation experiments at two dose rates six orders of magnitude apart, the predicted difference between the RIS results of these two points is too small to be distinguishable outside of experimental error. The slope of the RIS vs. dose rate line becomes even shallower when 10^{17} m^{-2} sinks are included in the IK model.

6.3 Modeling the Solute Drag Mechanisms

It is theorized that the solute drag mechanism can contribute to RIS, either in addition to, or instead of, the inverse Kirkendall mechanism. Since the modeling effort has thus far focused only on the inverse Kirkendall mechanism, an alternative mechanism of solute drag will now be addressed. First, the solute drag mechanism shall be implemented into the existing IK model framework. Next, appropriate input parameters for solute-defect binding will be selected. The, finally, results of the solute drag model will be presented.

6.3.1 Setup of the Solute Drag Model

Solute drag is suggested as a RIS mechanism because it considers the formation of tightly-bound solute-defect complexes, capable of diffusing a significant distance before breaking apart. This mechanism was devoloped and described by Faulkner, *et al.* [44] and it considers both solute-interstitial and solute-vacancy complexes. In the case of solute-interstitial complexes, the solute drag mechanism considers diffusion of di-interstitial dumbbells, as opposed to the mono-interstitials considered in the IK mechanism. For solute-vacancy complexes, atomic species strongly bound to vacancies will be carried, or “dragged”, along with the vacancy flux to grain boundaries. The solute-vacancy interaction will affect the ability of the solute to diffuse via the vacancy flux. Choudhury, *et al*. [55] find that in a dilute alloy, if the solute-vacancy interaction is negligible, the solute will diffuse though vacancy-solute exchange (the IK mechanism). But, if the solute-vacancy interaction is strongly attractive, the solute and the vacancy will migrate as a complex specie, in which the solute is dragged in the direction of vacancy defect flux. Clearly, solute drag is a very strong mechanism of RIS, potentially capable of generating considerable amounts of segregation at grain boundaries and other point defect sinks.

Johnson and Lam [31], [133] have developed a rate-theory RIS model for a ternary alloy that considers free self-interstitials, free mono-vacancies, free substitutional solute atoms, two types of solute-interstitial complexes, and solute-vacancy complexes. This model has been described in Section 2.1.2. The formulation of the Johnson and Lam model can be used to aid in implementing a solute drag model into the existing rate-theory IK model.

At present, the IK model considers alloying components, vacancies, and interstitials; kinetic rate equations are written for each of these species in Chapter 2, Equations 2.32-2.36. If the solute drag mechanism is to be represented by solute-vacancy and solute-interstitial complexes, kinetic rate equations for these complexes must be added to the IK set of kinetic rate equations. The equations for the solute-defect complexes can be adapted from the Johnson and Lam model as follows:

$$\frac{\partial C_{ib}}{\partial t} = D_{ib}\nabla^2 C_{ib} + K_{ib}C_iC_b - K_{ib}'C_{ib} - K_{vib}C_vC_{ib} \text{ , and} \qquad (6.5)$$

$$\frac{\partial C_{vb}}{\partial t} = D_{vb}\nabla^2 C_{vb} + K_{vb}C_vC_b - K_{vb}'C_{vb} - K_{ivb}C_iC_{vb} \text{ ,} \qquad (6.6)$$

where *D* are the diffusion coefficients, *C* are the concentrations, and *K* are the rate constants; the subscripts are *ib* for B-interstitial complexes, *vb* for B-vacancy complexes, *i* for interstitials, *b* for B atoms, *v* for vacancies, *vib* for the annihilation of B-interstitial complexes with a mono-vacancy, and *ivb* for the annihilation of a mono-interstitial with a B-vacancy complex. Note that Equations 6.5-6.6 imply that only atomic specie B forms solute-defect complexes. In an Fe-Cr binary alloy, Cr (specie B) is the solute, and is thus the specie that will participate in any solute-defect drag.

The diffusion coefficients from Equations 6.5-6.6 are given by:

$$D_{ib} = \frac{2}{21} a^2 v_i \exp\left(-E_{mib}/kT\right) \text{, and} \tag{6.7}$$

$$D_{vb} = \frac{1}{12} a^2 v_v \exp\left(-E_{mvb}/kT\right) , \tag{6.8}$$

where a is the lattice parameter, v_i and v_v are approximated as the Debye frequencies for interstitials and vacancies, E_{mib} is the migration energy of the B-interstitial complex, and E_{mvb} is the migration energy of the B-vacancy complex. The rate constants are:

$$K_{ib} = 168 v_i \exp\left(-E_{mi}/kT\right) , \tag{6.9}$$

$$K_{ib}' = 4 v_i \exp\left(-\left(E_{mi} + E_{ib}^b\right)/kT\right) , \tag{6.10}$$

$$K_{vib} = 126\left(v_v \exp\left(-E_{mv}/kT\right) + \frac{1}{7} v_i \exp\left(-E_{mib}/kT\right)\right), \tag{6.11}$$

$$K_{vb} = 84 v_v \exp\left(-E_{mv}/kT\right) , \tag{6.12}$$

$$K_{vb}' = 7 v_v \exp\left(-\left(E_{mv} + E_{vb}^b\right)/kT\right) \text{, and} \tag{6.13}$$

$$K_{ivb} = 168\left(v_i \exp\left(-E_{mi}/kT\right) + v_v \exp\left(-E_{mvb}/kT\right)\right) , \tag{6.14}$$

where E_{mi} and E_{mv} are the interstitial and vacancy migration energies, E_{ib}^b is the binding energy of the B-interstitial complex, and E_{vb}^b is the binding energy of the B-vacancy complex.

The equations presented in this subsection represent the solute drag mechanism in a rate-theory format. This set of Equations 6.5-6.14 is incorporated to the existing IK model, in order to understand how solute drag will alter the predicted amount of RIS. Clearly, there are a number of input parameters required by the solute drag formulation. Determining the appropriate values for these input parameters will be the focus of the upcoming subsection.

6.3.2 Input to the Solute Drag Model

The solute drag formulation presented above requires the input of six migration energies. Unfortunately, there are no empirical measurements of these energies. Instead, their values must be based upon molecular dynamics simulations, along with approximations from the mono-interstitial and mono-vacancy diffusion described in Section 6.1.3. The migration energies for which values are sought, and their values decided upon, are shown in Table 6.11. The reasoning and explanation behind the values of these energies is the focus of this section.

Solute-defect complex migration energies: The solute-defect complex migration energies, E_{mib} and E_{mvb}, will be discussed first. Keeping in mind that the solute being modeled is Cr, it is easier to think about these parameters as the migration energy of a bound Cr-interstitial complex and the migration energy of a bound Cr-vacancy complex. One will recall, from the discussion of Cr and Fe interstitial migration energies in Section 6.1.3.2, that it is most energetically favorable for interstitials in the bcc Fe-Cr system to form dumbbells and diffuse as dumbbells. Furthermore, the energies which were decided upon for single Cr interstitial migration and single Fe interstitial migration are, in actuality, based upon dumbbell diffusion (see Tables 6.7 and 6.8). Since, in the solute drag theory, a bound Cr-interstitial complex is essentially an interstitial dumbbell, it is a conservative approximation to use the Cr interstitial migration energy from the IK model, 0.26 eV, for the Cr-interstitial complex migration energy for the solute drag model. There have not been any studies performed on Cr-vacancy complexes, and thus no basis for knowing what an appropriate Cr-vacancy complex migration energy may be. A conservative estimate would be to use the Cr vacancy migration energy from the IK model, 0.55 eV, as an approximation to the Cr-vacancy complex migration energy.

Interstitial and vacancy migration energies: The interstitial and vacancy migration energies, E_{mi} and E_{mv}, will now be considered. As shown in Equations 6.9-6.14, these are mono-interstitial or mono-vacancy migration energies which are used to calculate rate constants for various reactions; expressions for these rate constants are written such that it does not matter whether the reacting mono-interstitial is Fe or Cr, nor whether the reacting mono-vacancy is in an Fe or Cr lattice position. In other words, these migration energies are blind to the alloying components. Thus, suitable values for these migration energies can be obtained by taking a composition-weighted average of the IK point defect migration energies. Therefore,

$$E_{mi} = \frac{(0.91Fe \times 0.35eV)(0.09Cr \times 0.26eV)}{1.00} = 0.34eV \text{ , and}$$

$$E_{mi} = \frac{(0.91Fe \times 0.63eV)(0.09Cr \times 0.55eV)}{1.00} = 0.62eV,$$

for an Fe-9Cr alloy.

Solute-defect complex binding energies: In this thesis, positive binding energy denotes attraction, while a negative binding energy denotes repulsion.

Solute-vacancy complex binding energies will be discussed first. Choudhury, *et al.* [55] used *ab initio* calculations to understand Cr-vacancy binding in bcc Fe as a function of nearest neighbor locations; their results are presented in Figure 6.18. Their results show that Cr-vacancy complexes have a weak attractive binding energy of around 0.01-0.05 eV. This suggests that Cr should enrich by Cr-vacancy solute drag.

Binding of a mixed <110> Fe-Cr dumbbell has been calculated by embedded atom method (EAM) potentials in a molecular dynamics simulation. Wallenius, *et al.* [134] calculated the binding energy to be 0.27 eV in Fe-5Cr, using an EAM potential constructed in that work; note the positive sign convention is adopted for attraction. Wallenius, however, also implemented the EAM potential constructed by Farkas, *et al.* [135], and found a weaker attractive binding energy of 0.05 eV. These results also suggest that Cr should enrich by Cr-interstitial solute drag.

6.3.3 Results of Solute Drag Mechanism

The IK model, with solute drag effects included, is executed using the IK reference case of Fe-9Cr irradiated at 400°C and dose rate 10^{-5} dpa/sec. Three code runs are conducted, each implementing just one of the solute-defect complex binding energies shown in Table 6.11. Because all of the binding energies suggest attraction between Cr atoms and defects, it is unsurprising that the solute drag model calculates Cr enrichment—notably, Cr enrichment greater than that calculated by the IK mechanism alone—in all three solute drag simulations. The results of these solute drag simulations will be discussed in greater detail here.

The reference IK model case, without the effects of solute drag, predicts Cr enrichment of 1.00 at%. When Cr-vacancy complexes with binding of 0.05 eV are included in the IK model, the Cr enrichment increases to 4.55 at%. Likewise, when Cr-interstitial complexes are considered in the IK model, Cr enrichment increases to 9.50 at% with 0.05 eV binding, or 43.6 at% with 0.27 eV binding. These results are evaluated at a steady-state dose of 15 dpa and shown graphically in Figure 6.19. It is obvious from these results that solute drag is a stronger mechanism than inverse Kirkendall; small solute-defect binding energies can lead to significant over-prediction of the amount of RIS.

Table 6.1. Timesteps used in inverse Kirkendall model.

Timestep (sec)	Dose (dpa) for 10^{-5} dpa/sec Dose Rate
1.00E-03	1.00E-08
1.00E-02	1.00E-07
1.00E-01	1.00E-06
1.00E+00	1.00E-05
1.00E+01	1.00E-04
5.00E+01	0.0005
2.50E+02	0.0025
1.30E+03	0.013
6.30E+03	0.063
1.60E+04	0.16
3.90E+04	0.39
9.80E+04	0.98
1.00E+05	1
2.40E+05	2.4
3.00E+05	3
6.10E+05	6.1
7.00E+05	7
1.00E+06	10
1.50E+06	15
3.00E+06	30
1.00E+07	100

Table 6.2. Definition of all condition parameters to inverse Kirkendall model.

Parameter	**Definition**	**Unit**
DISPRT	Peak displacement rate	dpa/sec
DOSE	Cutoff dose	dpa
TEMPC	Peak temperature	C
CONCB	Concentration of B	#/atom
CONCC	Concentration of C	#/atom
DISL	Peak dislocation density	$\#/m^2$

Table 6.3. Definition of all input parameters to inverse Kirkendall model.

Parameter	**Definition**	**Unit**
R1	Distance to end of 1st mesh group	nm
R2	Distance to end of 2nd mesh group	nm
RF	Distance to end of 3rd mesh group	nm
N1	Number of points in 1st mesh group	unitless
N2	Number of points in 2nd mesh group	unitless
N3	Number of points in 3rd mesh group	unitless
H0	Input timestep to GEAR package	s
EPS	Error control parameter	unitless
ETAV	Vacancy production efficiency	unitless
ETAI	Interstitial production efficiency	unitless
NAT	Number density	at/m^3
LAMBDA	Jump distance	m
FAV	Vacancy jump correlation factor, element A	unitless
FBV	Vacancy jump correlation factor, element B	unitless
FCV	Vacancy jump correlation factor, element C	unitless
FAI	Interstitial jump correlation factor, element A	unitless
FBI	Interstitial jump correlation factor, element B	unitless
FCI	Interstitial jump correlation factor, element C	unitless
WAV	Vacancy jump frequency, element A	s^{-1}
WBV	Vacancy jump frequency, element B	s^{-1}
WCV	Vacancy jump frequency, element C	s^{-1}
WAI	Interstitial jump frequency, element A	s^{-1}
WBI	Interstitial jump frequency, element B	s^{-1}
WCI	Interstitial jump frequency, element C	s^{-1}
EMIA	Interstitial migration energy, element A	eV
EMIB	Interstitial migration energy, element B	eV
EMIC	Interstitial migration energy, element C	eV
SV	Vacancy formation enthalpy	eV/m^3
EMA	Vacancy migration energy, element A	eV
EMB	Vacancy migration energy, element B	eV
EMC	Vacancy migration energy, element C	eV
EFA	Vacancy formation energy, element A	eV
EFB	Vacancy formation energy, element B	eV
EFC	Formation energy, element C	eV
EFGB	GB formation energy	eV
NUOV	Debye frequency, vacancy	s^{-1}
NUOI	Debye frequency, interstitial	s^{-1}
AL	Thermodynamic factor	unitless
Z	Number of neighbor atoms	unitless
BIASV	Dislocation bias for vacancies	unitless
BIASI	Dislocation bias for interstitials	unitless

Table 6.4. Results of sensitivity analysis of inverse Kirkendall model.

Parameter	**Significance at 320°C**	**Significance at 500°C**
FAV	-0.10	-0.30
FBV	-0.10	-0.30
FAI	-0.10	-0.30
FBI	-0.10	-0.30
WAV	1.52	1.86
WBV	-0.71	-1.23
WAI	-0.20	-0.51
WBI	0.75	1.33
EMIA	-52.15	-50.52
EMIB	52.15	50.52
SV	0.002	0.01
EMA	-52.41	-51.03
EMB	52.41	51.03
EFA	-5.10	-4.50
EFB	4.70	4.20
EFGB	0.17	0.15
AL	0.86	1.46

Table 6.5. Iron-vacancy migration energies determined from *ab initio* models.

Jump Configuration	**Migration Energy (eV)**	**Reference**
w_3	0.69	[55]
w_4	0.65	[55]
w_3’	0.67	[55]
w_4’	0.63	[55]
w_3’’	0.64	[55]
w_4’’	0.62	[55]
w_3	0.66	[54]
w_4	0.62	[54]
w_3’	0.65	[54]
w_4’	0.59	[54]
w_3’’	0.60	[54]
w_4’’	0.57	[54]
5Fe + 1Cr lattice	0.627	[111]
Average	0.63	n/a

Table 6.6. Chromium-vacancy migration energies determined from *ab initio* models.

Jump Configuration	**Migration Energy (eV)**	**Reference**
w_2	0.58	[55]
w_2	0.52	[54]
w_2	0.571	[111]
w_2	0.54	[112]
Average	0.55	n/a

Table 6.7. Iron-interstitial migration energies determined from *ab initio* models.

Jump Configuration	**Migration Energy (eV)**	**Reference**
w_0	0.35	[55]
w_4	0.39	[55]
w_6	0.36	[55]
w_0	0.34	[115]
w_4	0.35	[115]
w_0	0.34	[113]
Average	0.35	n/a

Table 6.8. Chromium-interstitial migration energies determined from *ab initio* models.

Jump Configuration	**Migration Energy (eV)**	**Reference**
w_1	0.25	[55]
w_2	0.33	[55]
w_1	0.23	[115]
w_2	0.33	[115]
Average	0.26	n/a

Table 6.9. List of values for input parameters to IK model.

Parameter	Definition	Unit	Value
R1	Distance to end of 1st mesh group	nm	4.0
R2	Distance to end of 2nd mesh group	nm	18.0
RF	Distance to end of 3rd mesh group	nm	2018.0
N1	Number of points in 1st mesh group	unitless	16
N2	Number of points in 2nd mesh group	unitless	14
N3	Number of points in 3rd mesh group	unitless	20
H0	Input timestep to GEAR package	s	1×10^{-9}
EPS	Error control parameter	unitless	1×10^{-9}
ETAV	Vacancy production efficiency	unitless	0.3
ETAI	Interstitial production efficiency	unitless	0.3
NAT	Number density	at/m^3	8.34×10^{28}
LAMBDA	Jump distance	m	2.48×10^{-10}
FAV	Vacancy jump correlation factor, Fe	unitless	0.727
FBV	Vacancy jump correlation factor, Cr	unitless	0.777
FAI	Interstitial jump correlation factor, Fe	unitless	0.727
FBI	Interstitial jump correlation factor, Cr	unitless	0.727
WAV	Vacancy jump frequency, Fe	s^{-1}	1.60×10^{13}
WBV	Vacancy jump frequency, Cr	s^{-1}	2.40×10^{13}
WAI	Interstitial jump frequency, Fe	s^{-1}	2.90×10^{12}
WBI	Interstitial jump frequency, Cr	s^{-1}	1.50×10^{12}
EMIA	Interstitial migration energy, Fe	eV	0.35
EMIB	Interstitial migration energy, Cr	eV	0.26
SV	Vacancy formation enthalpy	eV/m^3	1.00
EMA	Vacancy migration energy, Fe	eV	0.63
EMB	Vacancy migration energy, Cr	eV	0.55
EFA	Vacancy formation energy, Fe	eV	1.6
EFB	Vacancy formation energy, Cr	eV	2.25
EFGB	GB formation energy	eV	0.87
NUOV	Debye frequency, vacancy	s^{-1}	1.50×10^{13}
NUOI	Debye frequency, interstitial	s^{-1}	1.50×10^{12}
AL	Thermodynamic factor	unitless	1
Z	Number of neighbor atoms	unitless	8
BIASV	Dislocation bias for vacancies	unitless	1
BIASI	Dislocation bias for interstitials	unitless	1

Table 6.10. List of values for condition parameters to IK model.

Parameter	**Value of Parameter Used in:**				
	Reference Case	**Temperature Dependence**	**Dose Dependence**	**Composition Dependence**	**Dose Rate Dependence**
DISPRT (dpa/sec)	10^{-5}	10^{-5}	10^{-5}	10^{-5}	10^{-7}-0.1 dpa/sec in increments of an order of magnitude
DOSE (dpa)	15 (steady-state)	15 (steady-state)	10^{-5}-100 dpa every decade, plus 0.25, 0.5, 0.75, 2.5, 5, 7.5	15 (steady-state)	15 (steady-state)
TEMPC (°C)	400	100-900°C in increments of 50°C	400	400	400
CONCB (at%)	9	9	9	7-15 at% in increments of 1 at%	9
DISL (#/m^2)	0	0	0	0	0

Table 6.11. List of input parameters and their values for the solute drag mechanism.

Parameter	**Definition**	**Unit**	**Value**
E_{mib}	B-interstitial complex migration energy	eV	0.26
E_{mvb}	B-vacancy complex migration energy	eV	0.55
E_{mi}	Interstitial migration energy	eV	0.34
E_{mv}	Vacancy migration energy	eV	0.62
E_{ib}^{b}	B-interstitial complex binding energy	eV	0.05-0.27 (attractive)
E_{vb}^{b}	B-vacancy complex binding energy	eV	<0.05 (attractive)

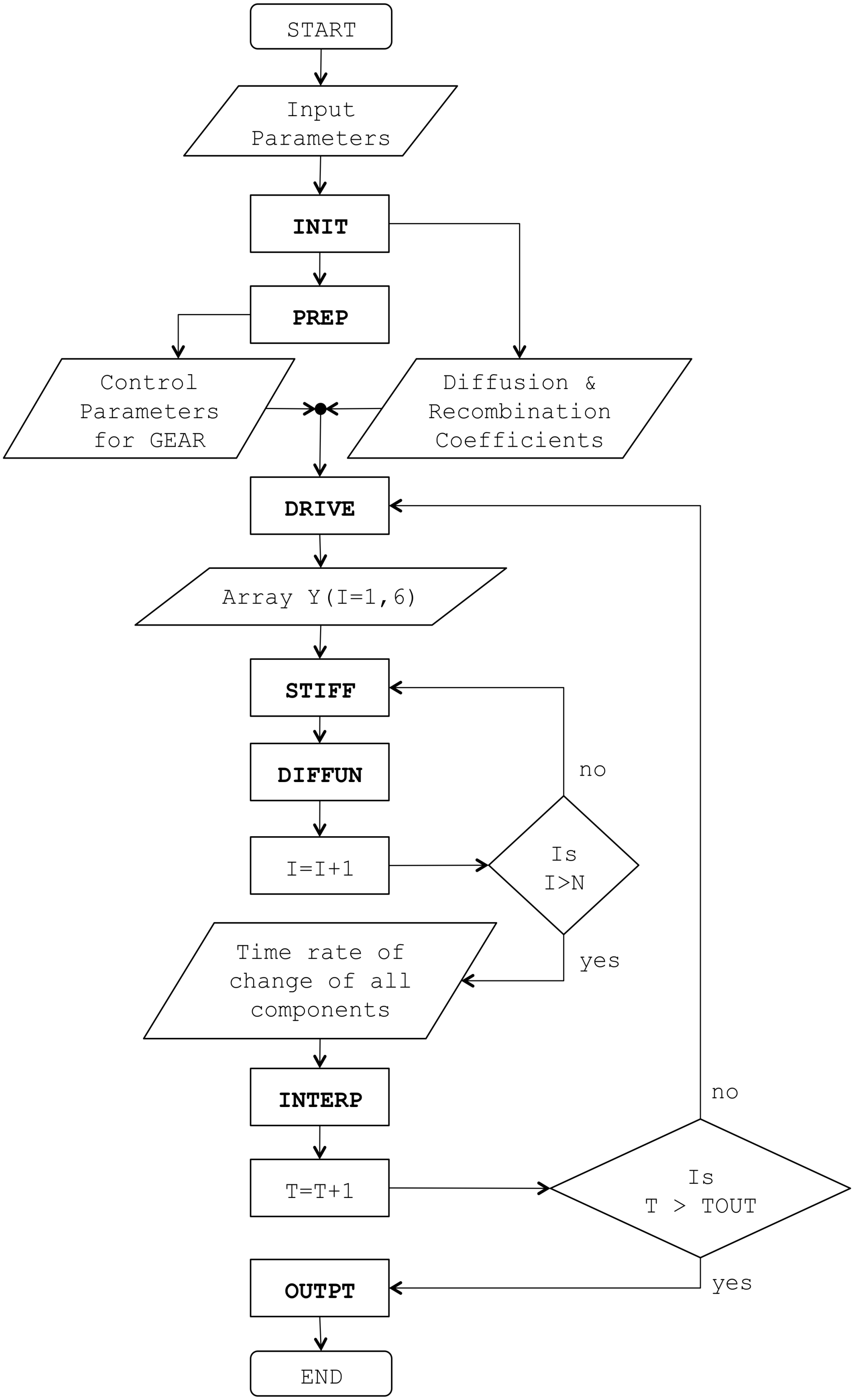

Figure 6.1. Flowchart of IK code.

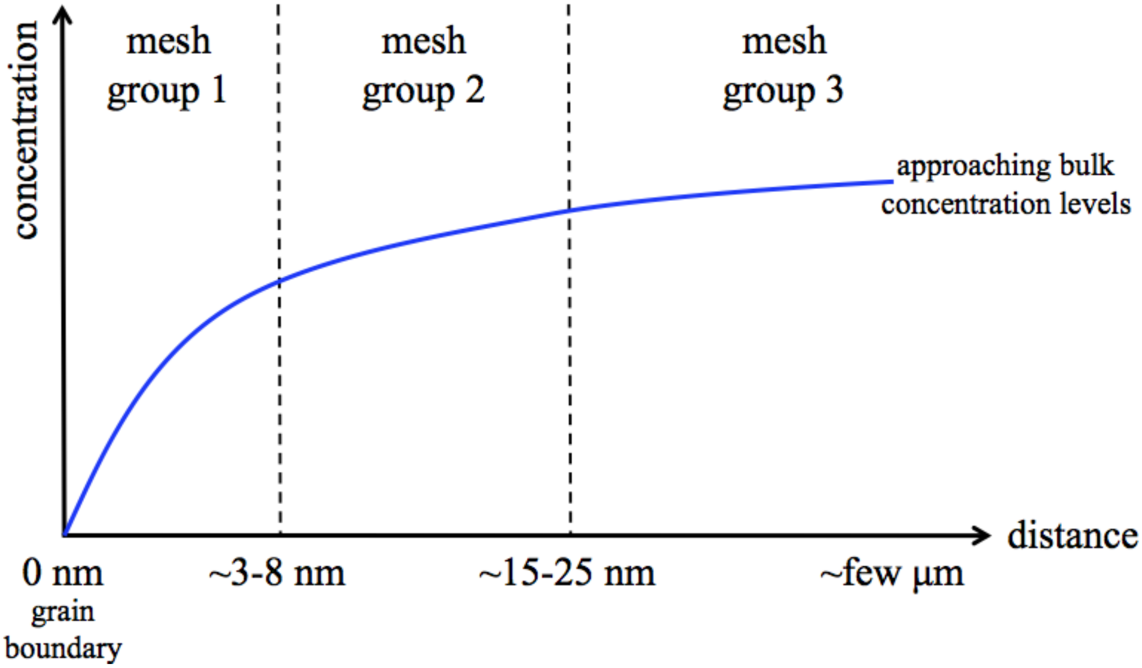

Figure 6.2. Schematic of one-dimensional positional mesh in IK model.

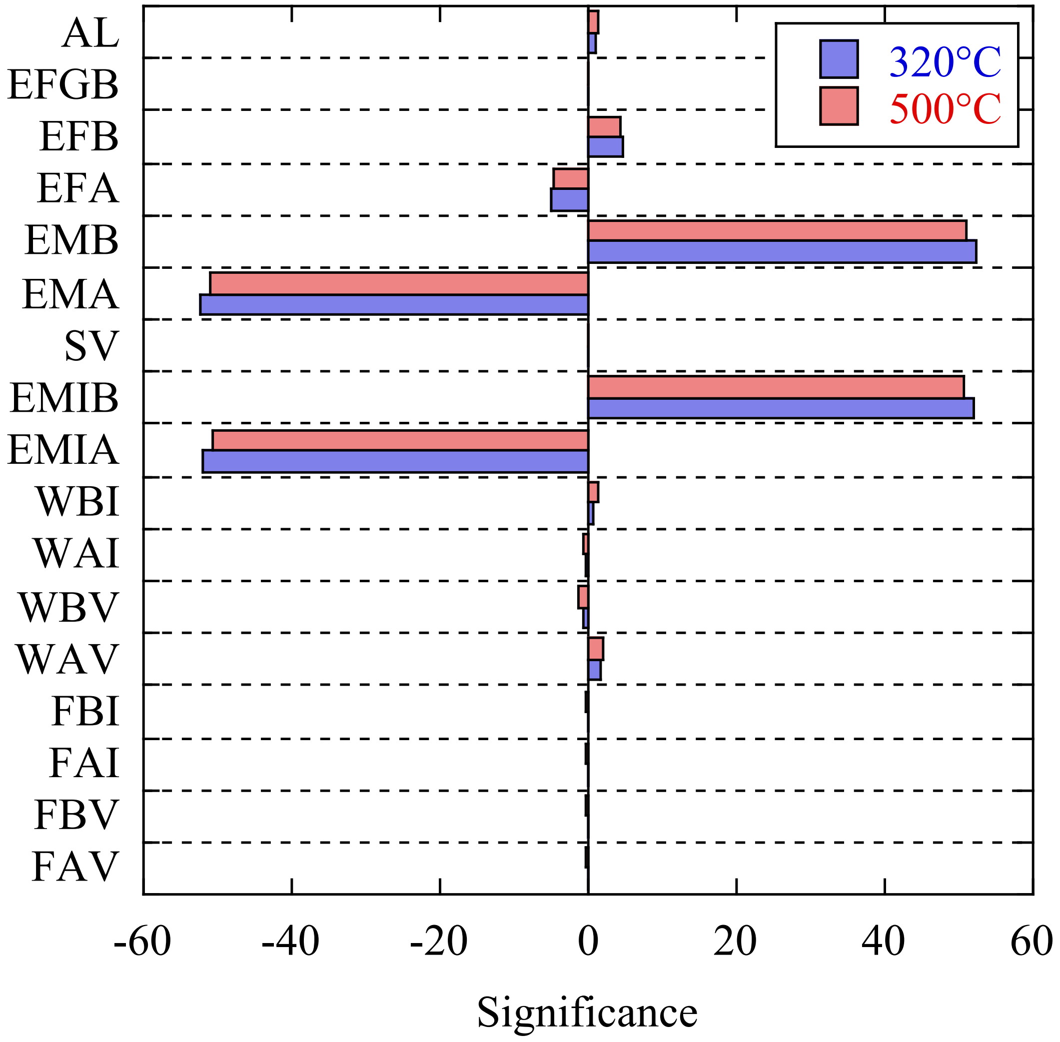

Figure 6.3. Results of sensitivity analysis of inverse Kirkendall model.

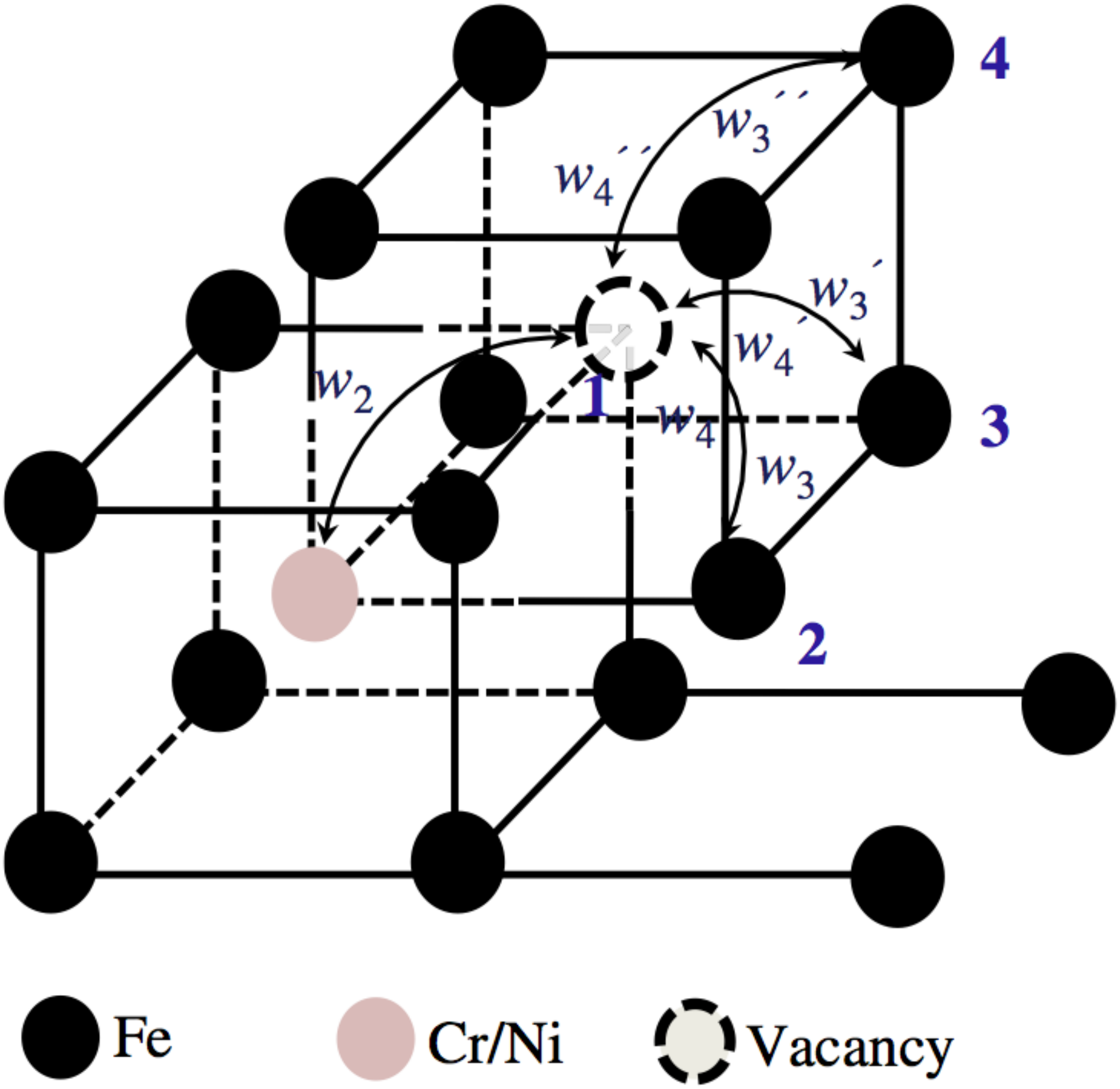

Figure 6.4. Configurations of Fe and Cr vacancy jumps, used for *ab initio* migration energy calculations, taken from [55].

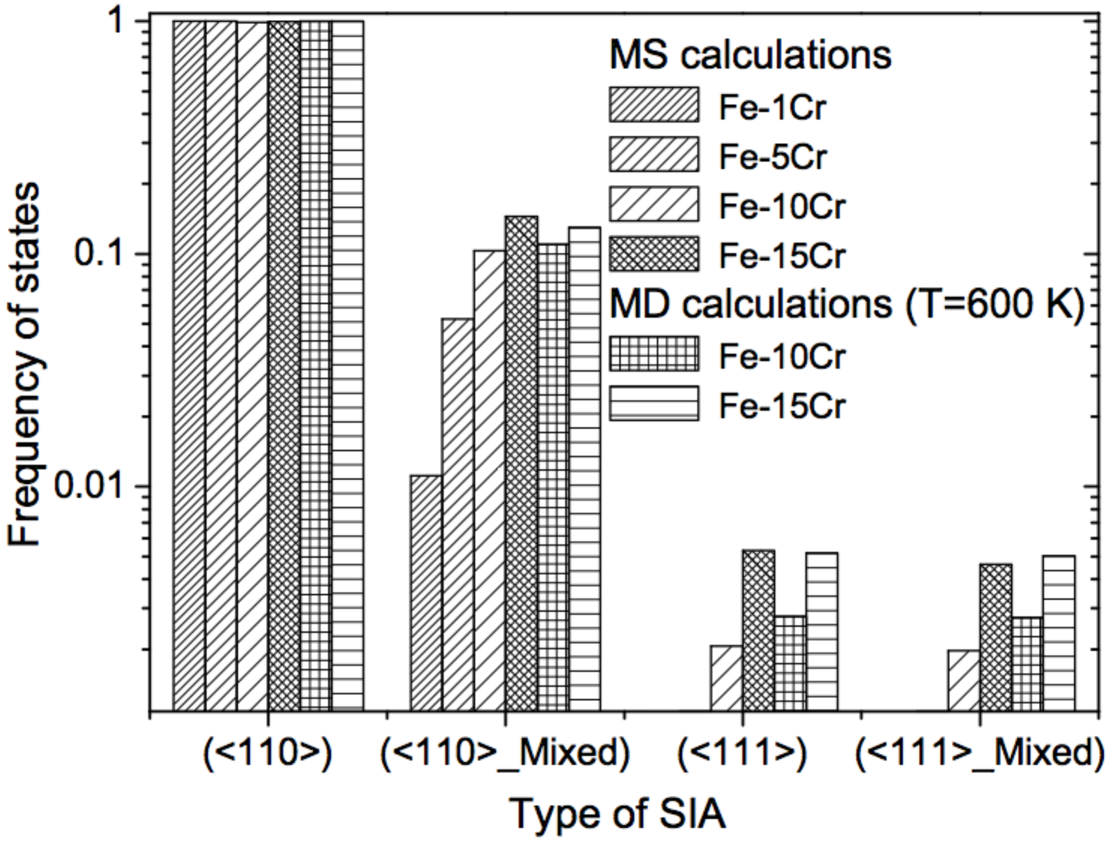

Figure 6.5. Results of molecular dynamics simulations in concentrated b.c.c. Fe-Cr systems, showing that <110> Fe-Fe and mixed dumbbells account for nearly 100% of all interstitials in the system; taken from [114].

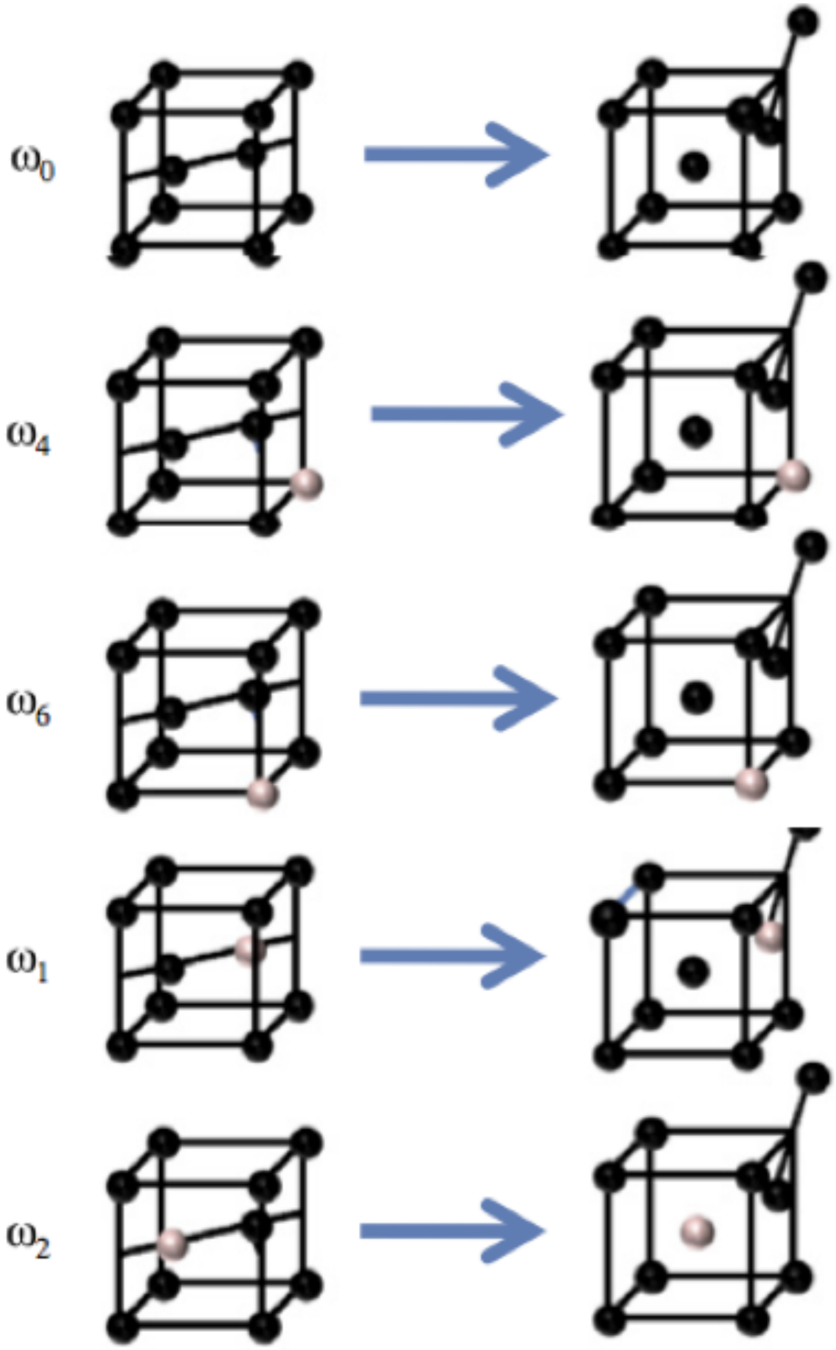

Figure 6.6. Configurations of Fe and Cr interstitial jumps, used for *ab initio* migration energy calculations, taken from [115].

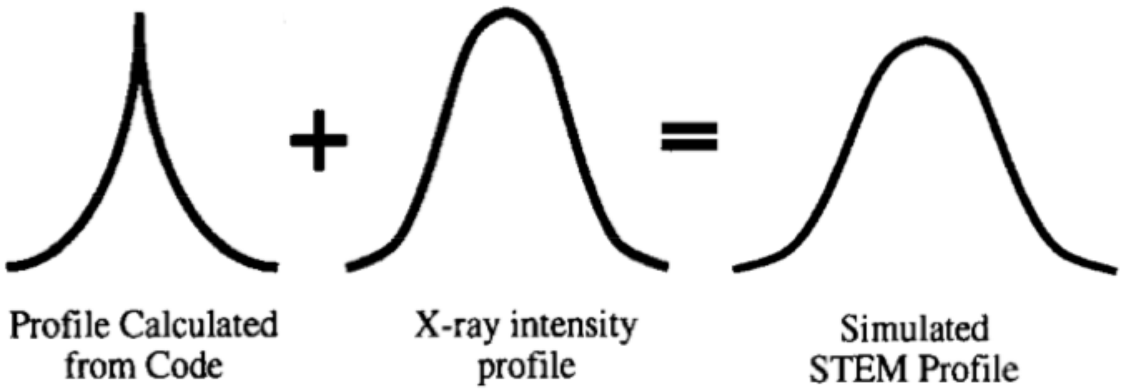

Figure 6.7. Schematic illustrating the effect of convolution on a RIS profile calculated by the model, after Carter, *et al*. [130].

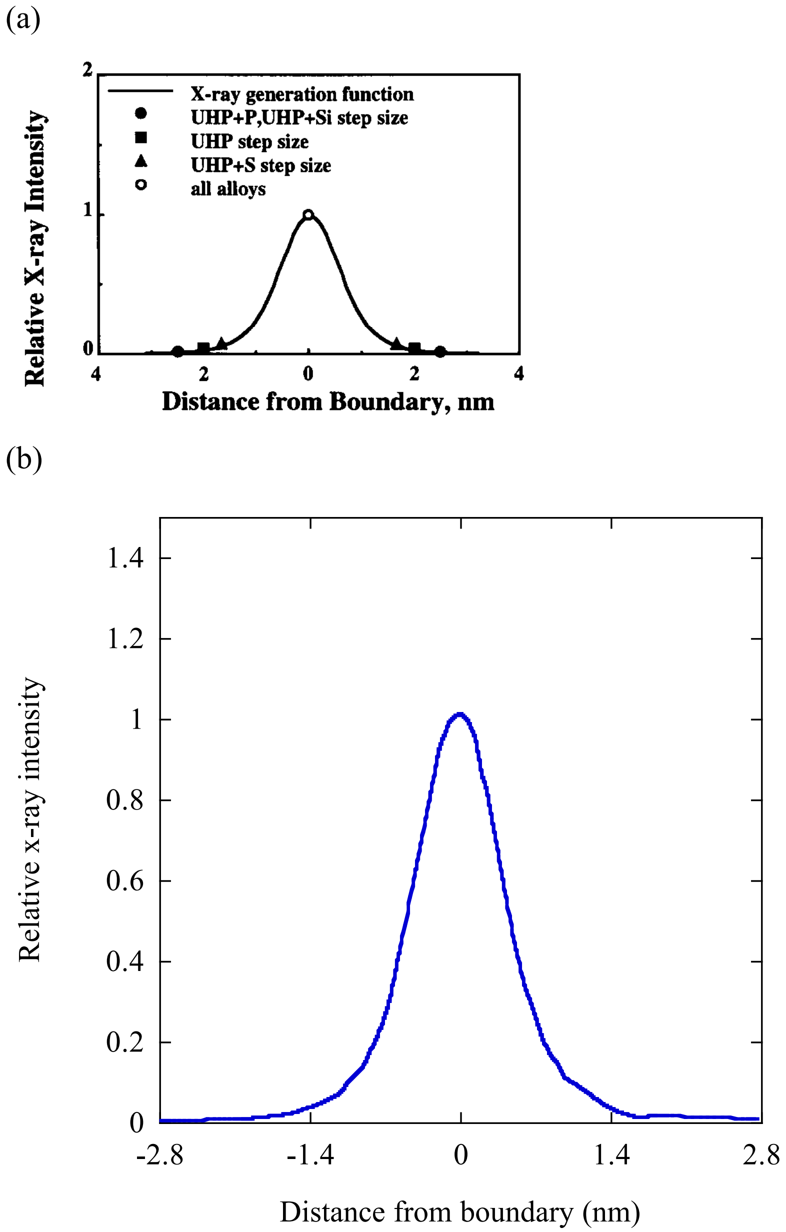

Figure 6.8. X-ray generation functions (a) as calculated by Monte Carlo methods in a 304L stainless steel specimen ~50 nm thick for a STEM electron probe ~2 nm at full width one-tenth maximum, taken from Carter, *et al*. [130] and (b) as scaled for a STEM electron probe ≤1.4 nm at full width one-tenth maximum, used in this work.

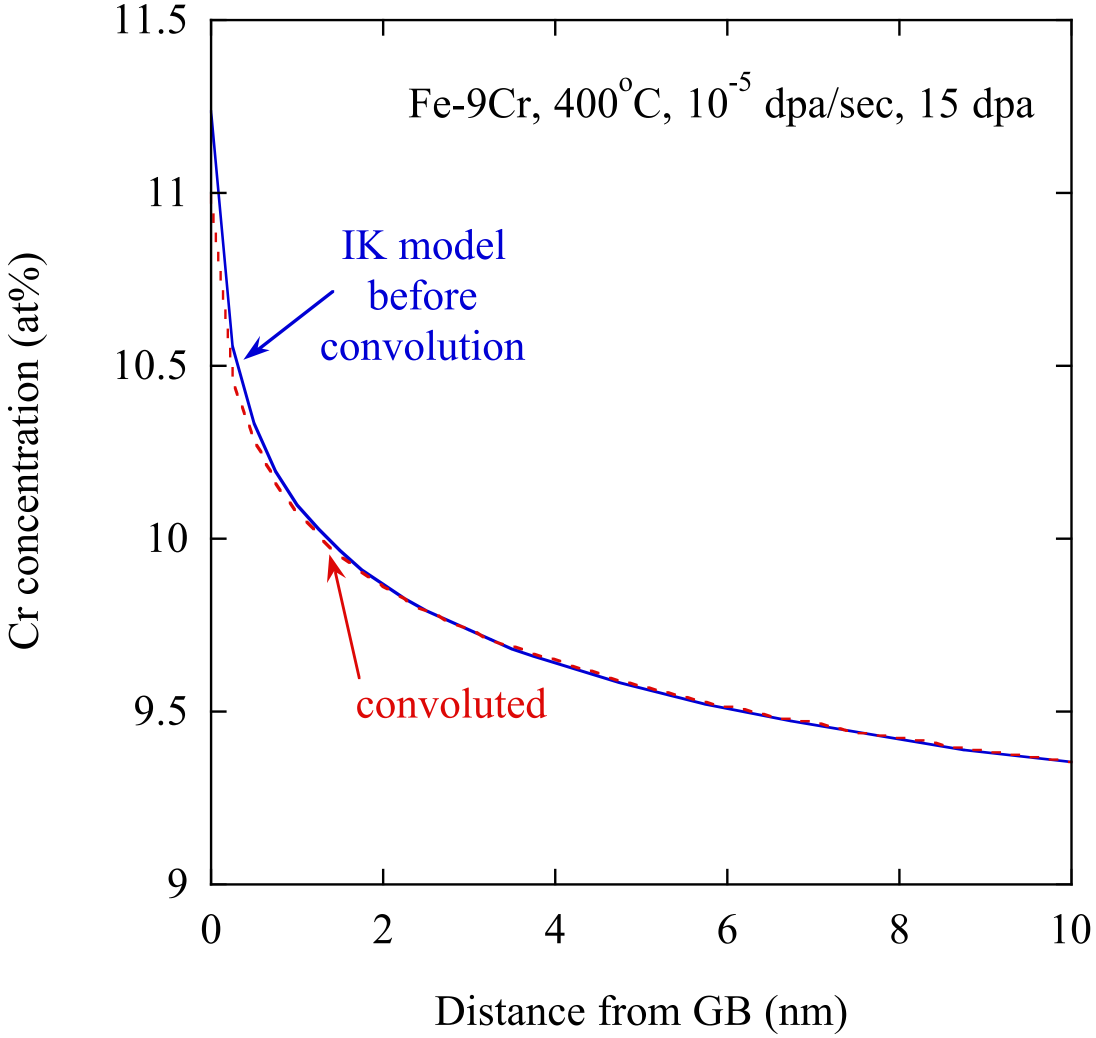

Figure 6.9. Chromium concentration profile at the grain boundary, from the IK model reference case of Fe-9Cr irradiated at 400°C to steady-state dose of 15 dpa, at a dose rate of 10^{-5} dpa/sec. Model result prior to convolution is shown as a solid line; convoluted model result is shown as dashed line.

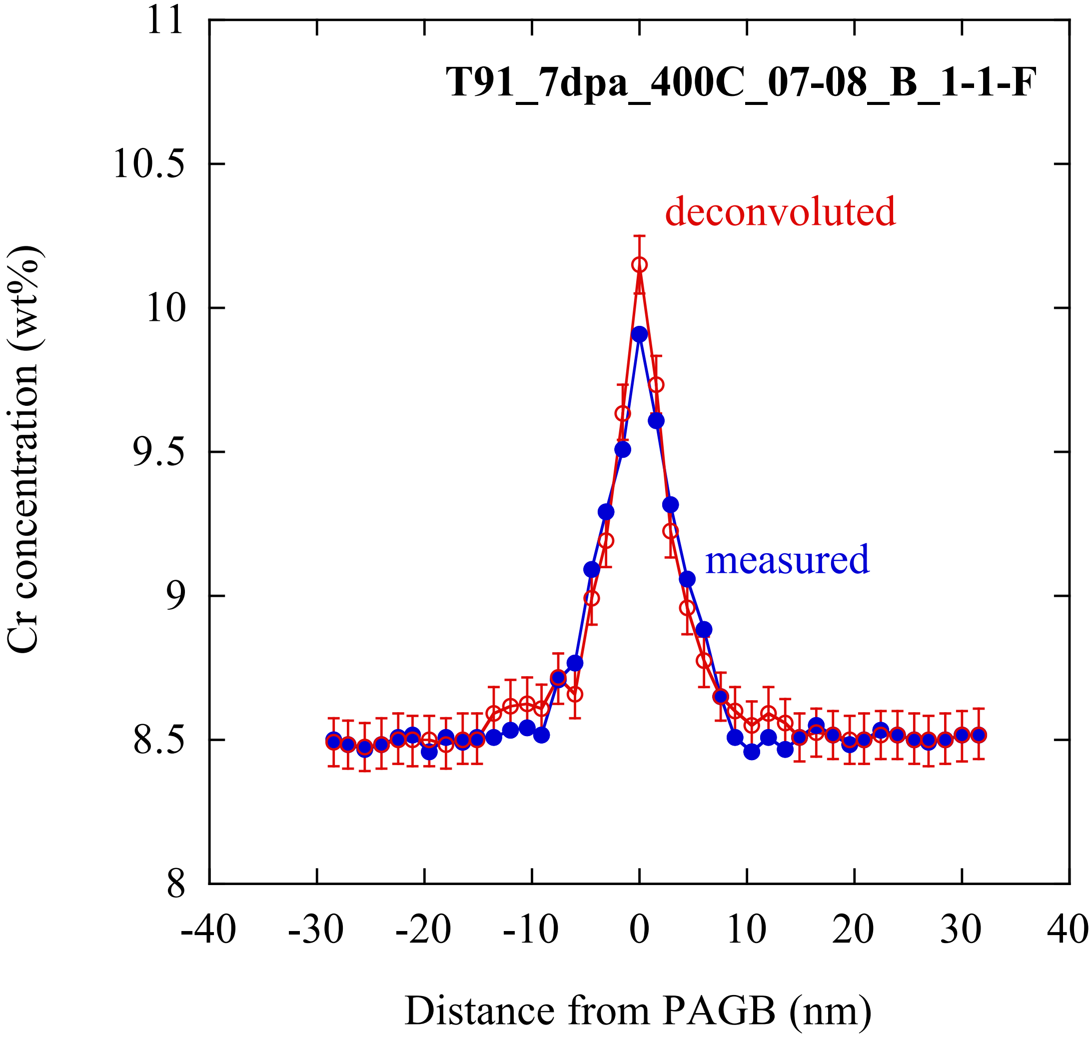

Figure 6.10. Example of a measured and deconvoluted Cr concentration profile from line scan T91_7dpa_400C_07-08_B_1-1-F.

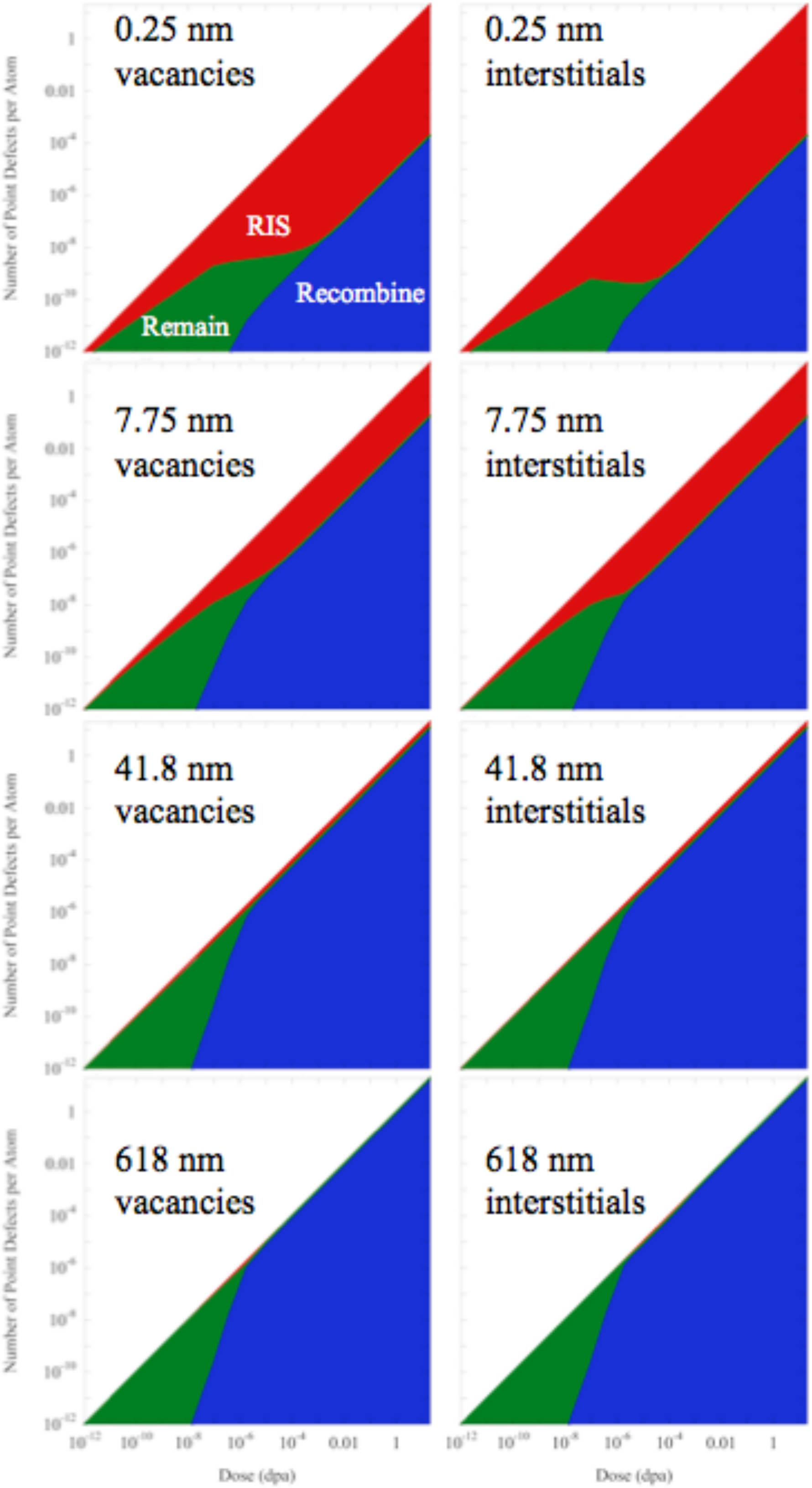

Figure 6.11. Point defect fates calculated by IK model for Fe-9Cr, 400°C, ρ_d=0 m^{-2}.

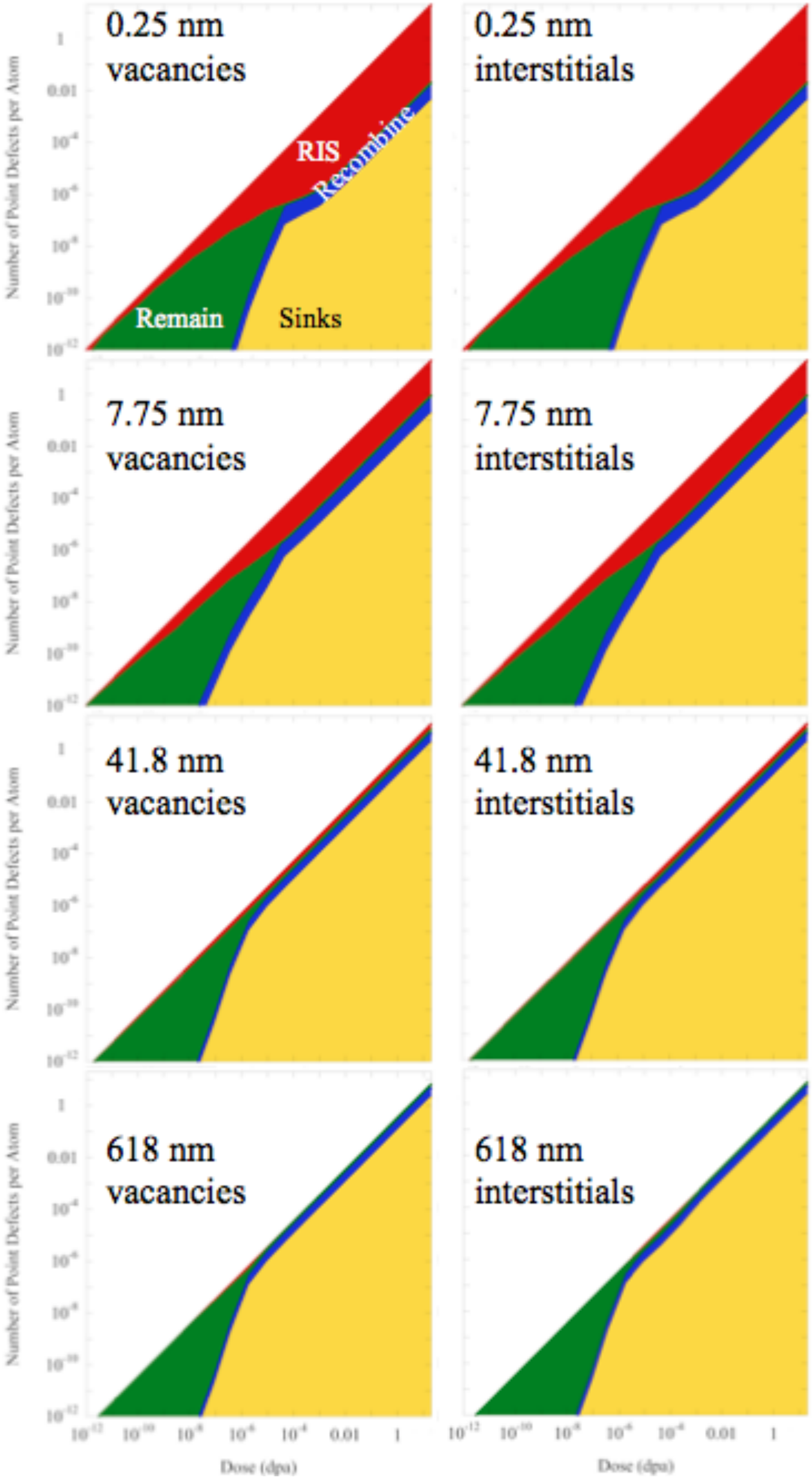

Figure 6.12. Point defect fates calculated by IK model for Fe-9Cr, 400°C, ρ_d=10^{15} m^{-2}.

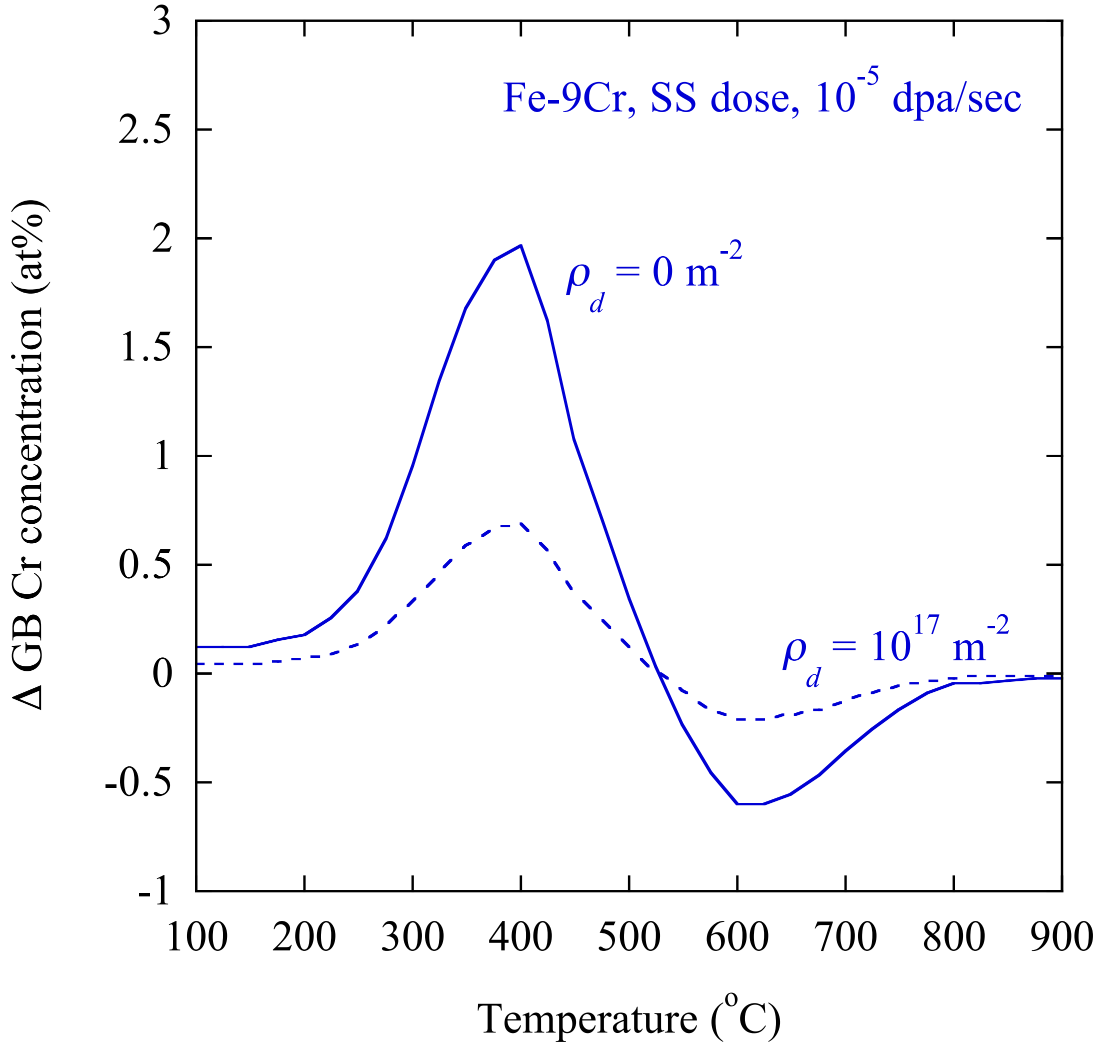

Figure 6.13. Chromium RIS predicted by IK model, as a function of irradiation temperature for Fe-9Cr irradiated to a steady-state dose of 15 dpa at 10^{-5} dpa/sec.

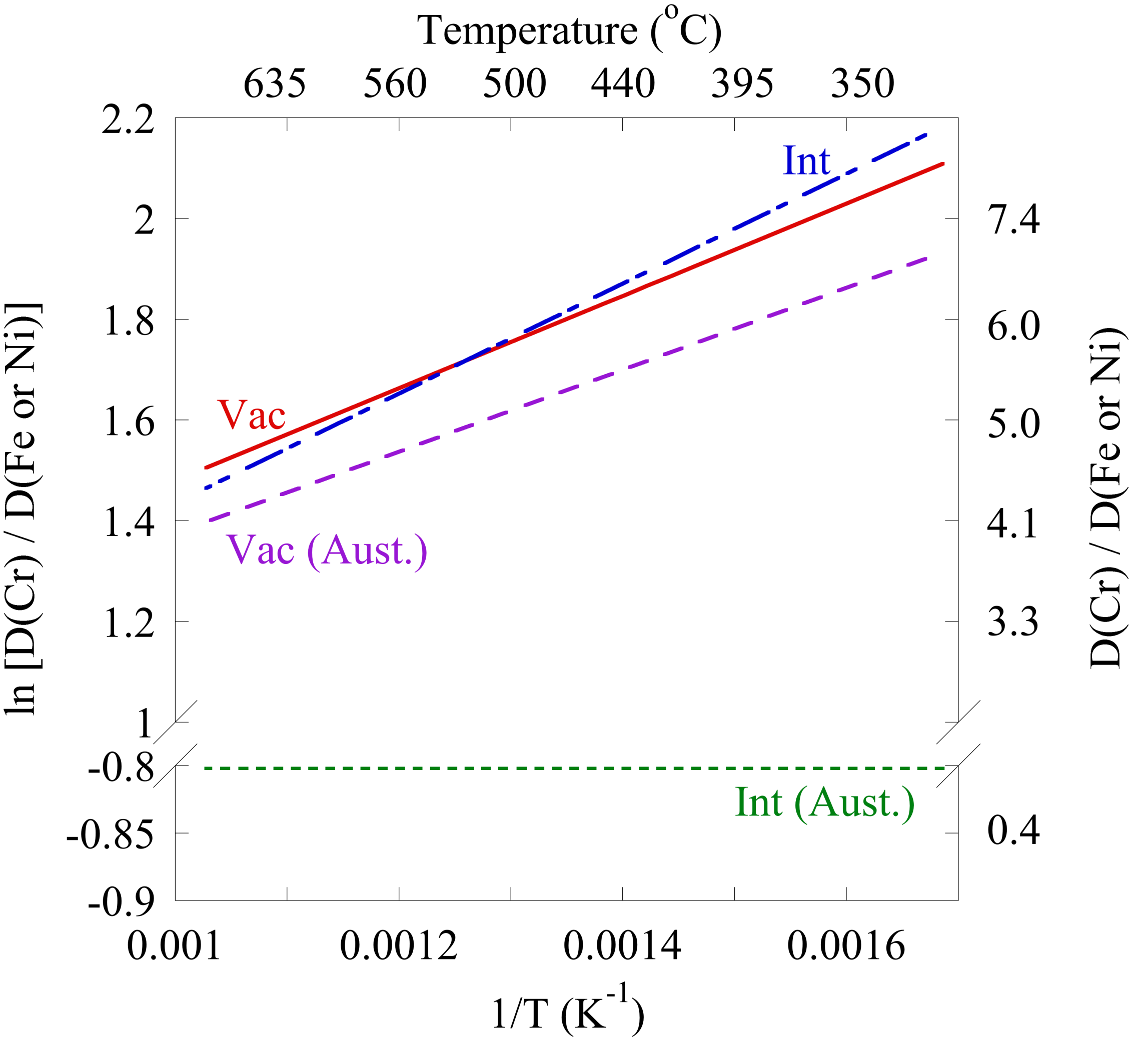

Figure 6.14. Cr:Fe vacancy and interstitial diffusion coefficient ratios for F-M alloys, with Cr:Ni vacancy and interstitial diffusion coefficient ratios for austenitic alloys.

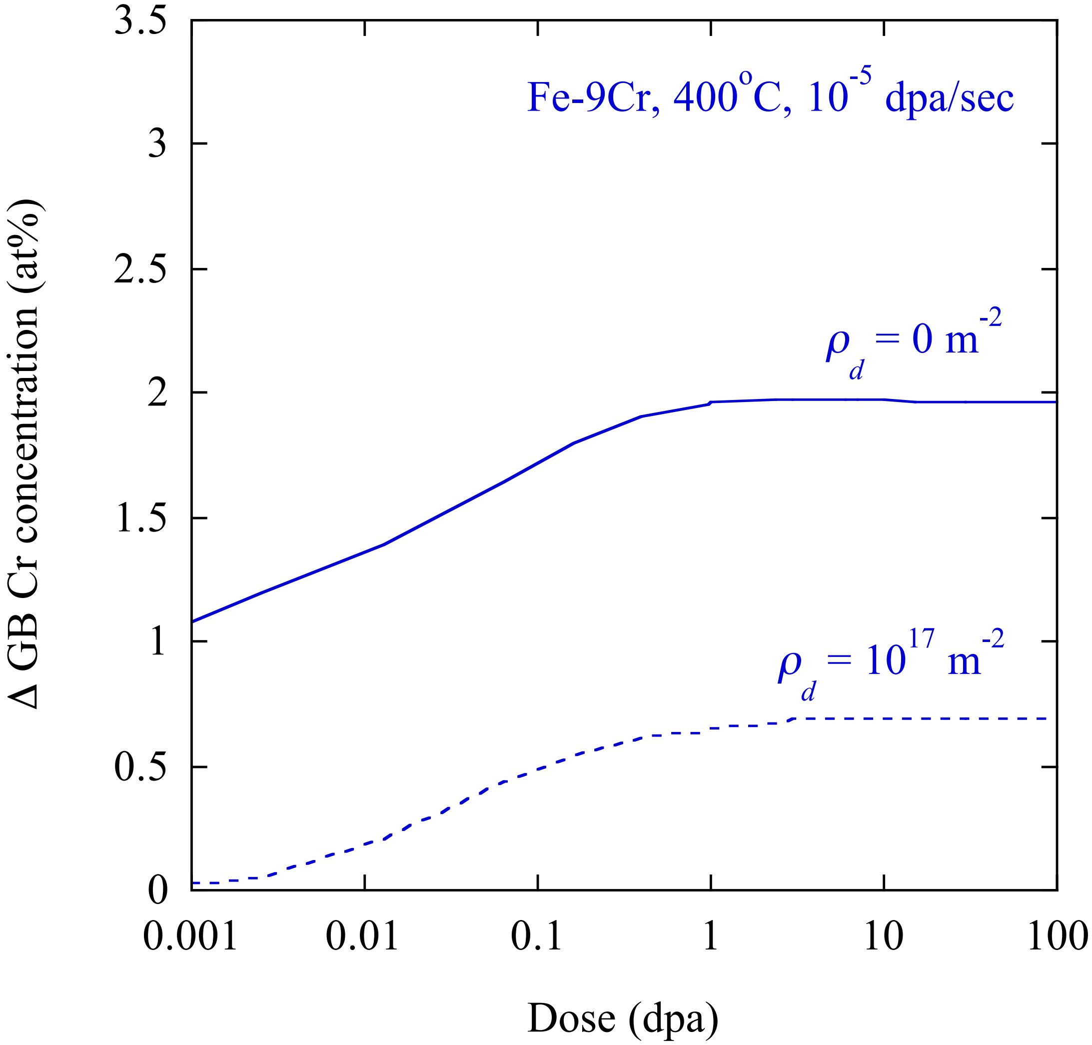

Figure 6.15. Chromium RIS predicted by IK model, as a function of dose for Fe-9Cr irradiated at 400°C, 10^{-5} dpa/sec.

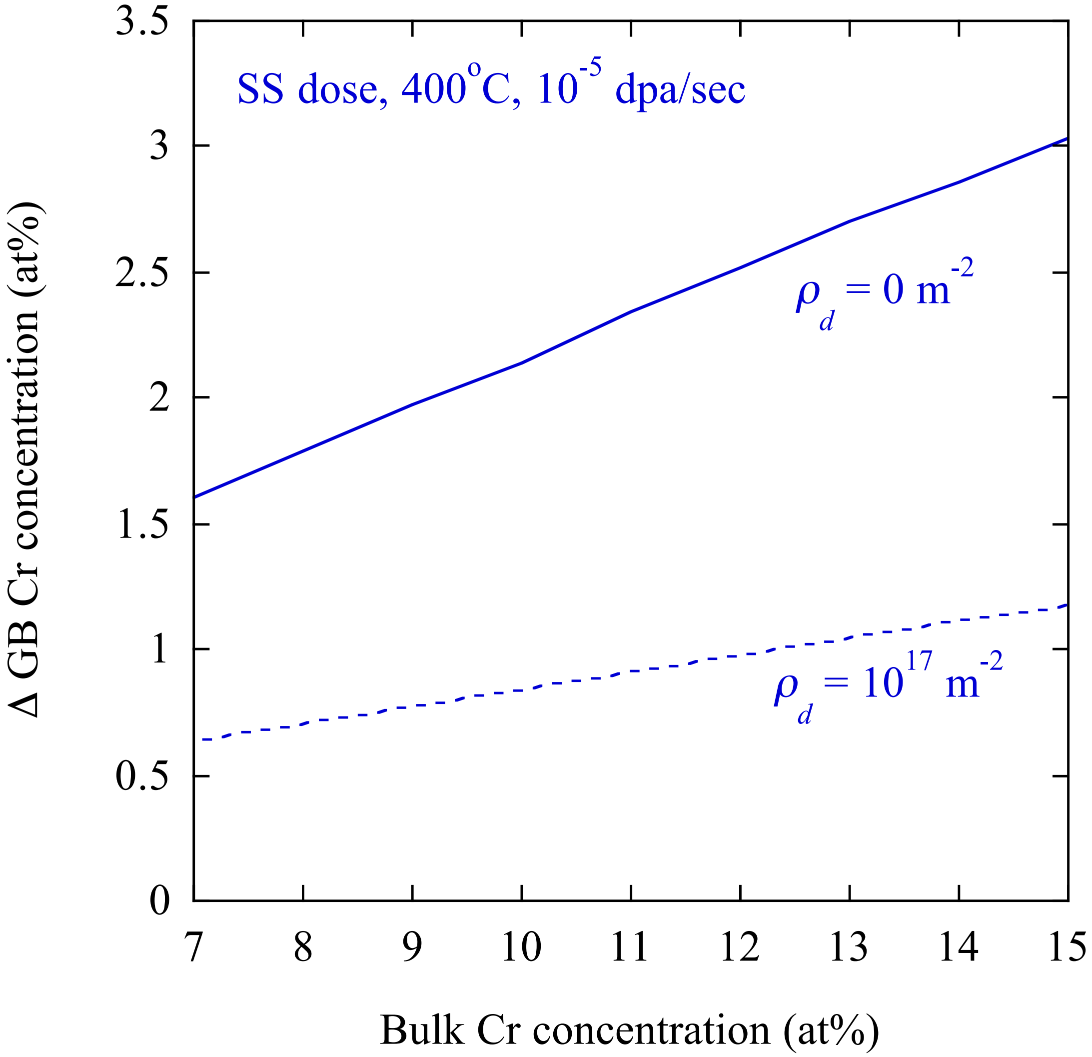

Figure 6.16. Chromium RIS predicted by IK model, as a function of bulk Cr concentration for a range of Fe-Cr binary alloys irradiated at 400°C to a steady-state dose of 15 dpa at 10^{-5} dpa/sec.

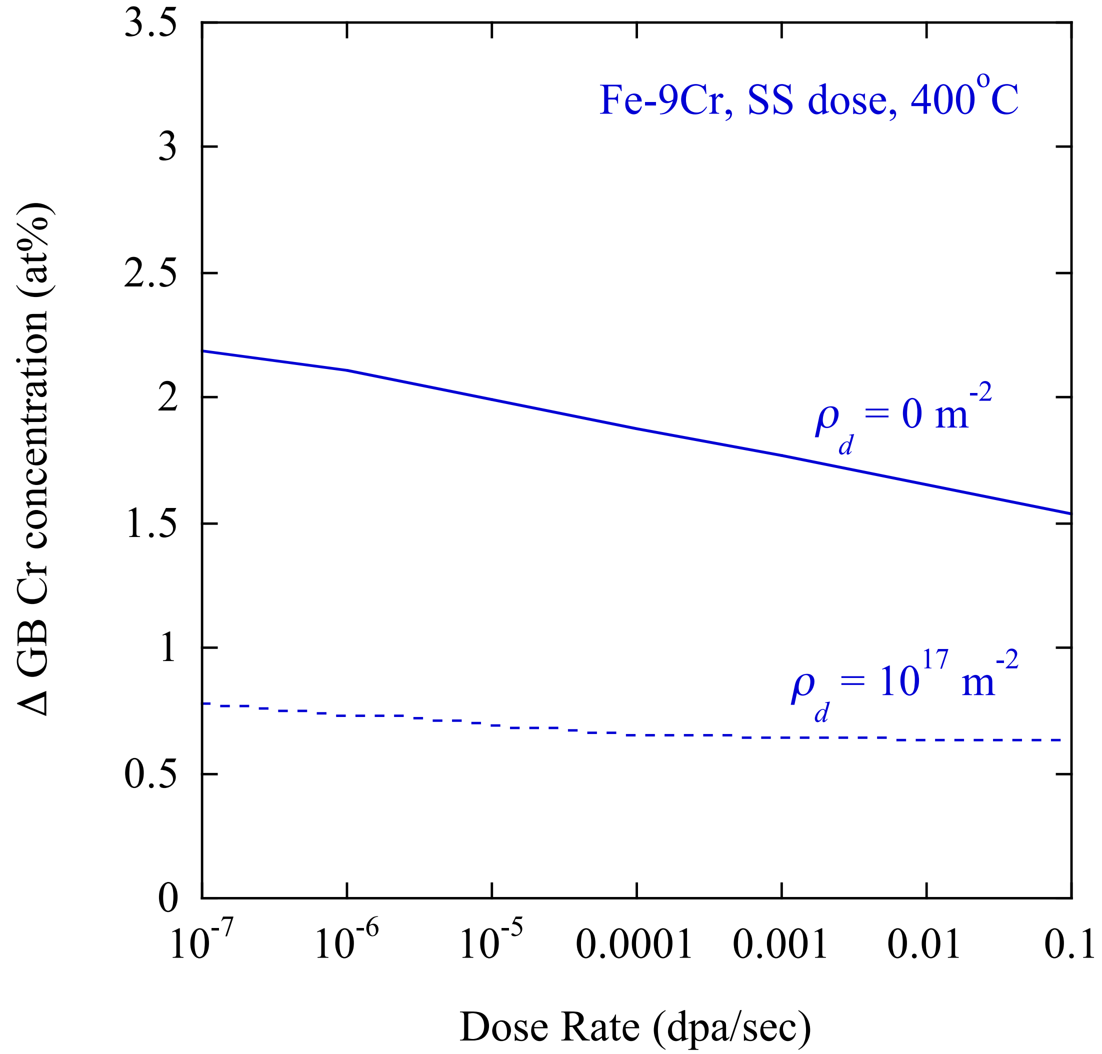

Figure 6.17. Chromium RIS predicted by IK model, as a function of irradiation dose rate.

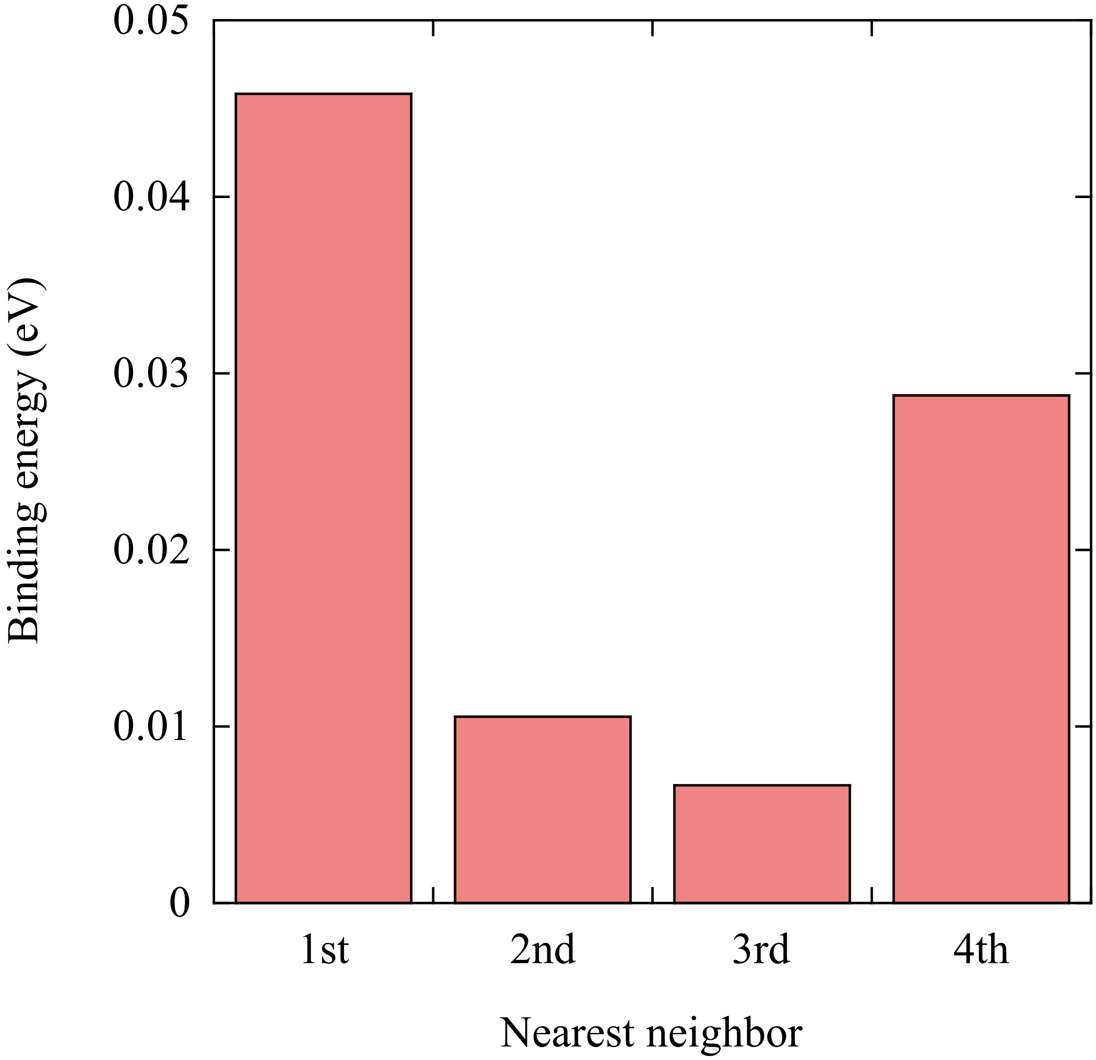

Figure 6.18. *Ab initio* calculations of Cr-vacancy binding as a function of nearest neighbor position in bcc Fe, taken from [55].

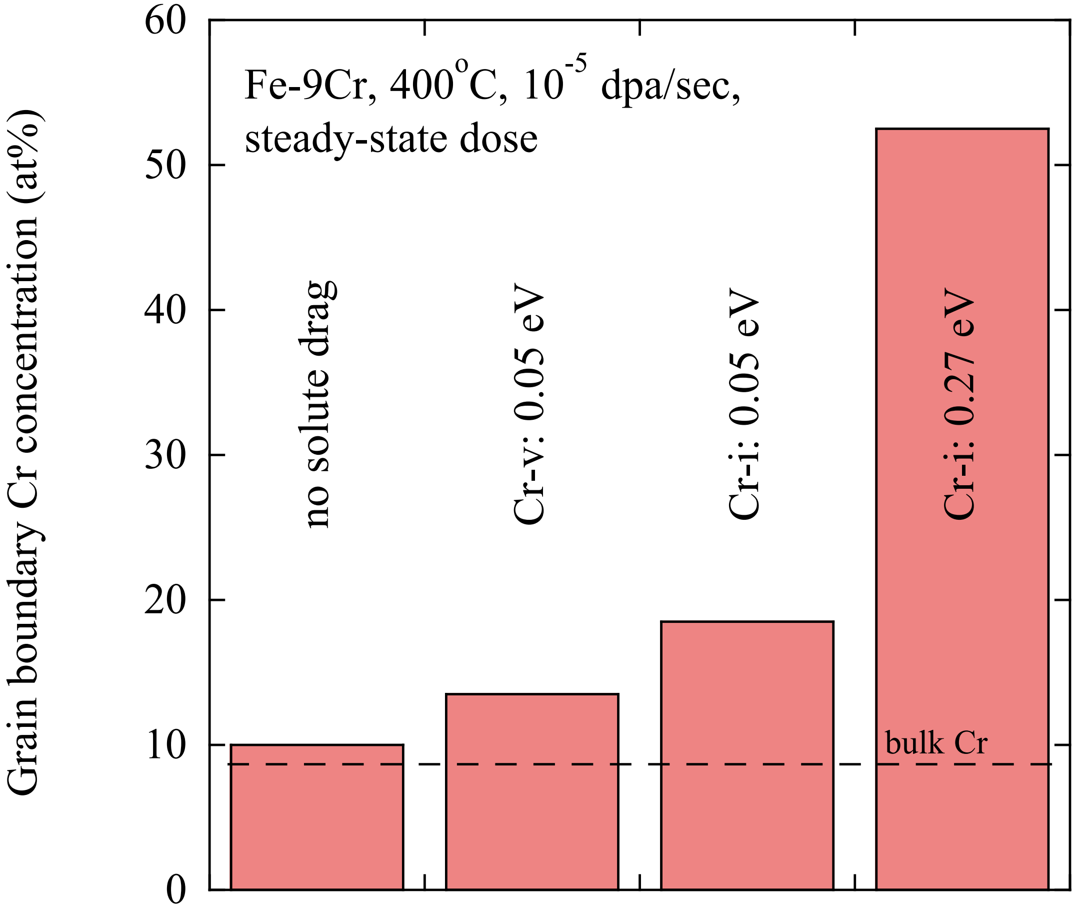

Figure 6.19. Results of solute drag model, a compared to reference IK model case, for Fe-9Cr irradiated at 400°C and dose rate 10^{-5} dpa/sec, evaluated at a steady-state dose of 15 dpa.

CHAPTER 7 DISCUSSION

The previous chapters have presented experimental measurements of radiation-induced segregation, collected from several alloys over a range of experimental conditions, as well as predicted values of RIS calculated by models of two proposed RIS mechanisms. In this chapter, the measured and predicted results will be brought together in an effort to deduce the mechanism driving RIS in F-M alloys. It is hypothesized that this mechanism is inverse Kirkendall, so the primary purpose of this chapter is to determine whether experimental measurements are consistent with the behaviors predicted by the IK mechanism. Consistency between experimental and IK model results, however, does not wholly confirm the hypothesis. Thus, it must also be shown that experimental results are inconsistent with alternative mechanisms, such as solute drag. This chapter will be organized as follows. Section 7.1 will present the limitations of the experimental measurements and the model results, respectively. Then, Section 7.2 will compare experimental results to the IK model. Finally, Section 7.3 will compare experimental results to the solute drag model.

7.1 Analysis and Limitations of Experimental Measurements

Prior to comparing experimental measurements to model calcualtions, the limitations of both of these sets of results must be examined. In this section, the limitations and simplifying assumptions will be described, and their effect on the results will be noted.

7.1.1 Shape of RIS Profiles

The RIS profiles presented in Chapter 5 reveal that in some cases, the RIS profiles are not symmetric about the grain boundary. Conversely, the modeling work presented in Chapter 6 assumes symmetry about the boundary, and simulates composition gradients on only one side of the modeled boundary. In this section, the asymmetry in some of the measured boundaries will be described, and possible explanations for this behavior will be presented.

Asymmetry exists in many of the RIS profiles presented in Chapter 5, for example, in the Fe and Cr RIS profiles in Figure 5.11, from T91 irradiated to 3 dpa at 300°C. In this figure, the concentration gradient on the right side of the PAGB is steeper than the concentration gradient on the left side of the PAGB. Similar asymmetry can be observed in most of the RIS profiles shown in Chapter 5. This asymmetry may suggest grain boundary migration. The phenomenon of grain boundary migration has been observed in other F-M alloys, notably in a 500°C Fe^+ ion irradiated model Fe-12Cr ODS steel [13]. In that work, as well as in earlier studies in electron irradiated austenitic alloys [38], the direction of grain boundary migration was noted to be toward the steeper side of the asymmetric concentration profile.

Some of the RIS profiles also contain some kinks, such as the representative profiles from T91 irradiated to 3 dpa at 450°C, shown in Figure 5.16. In this figure, the Fe and Cr concentration profiles each contain a kink on the concentration gradient, approximately 6-9 nm to the left of the PAGB. The kink is in the direction of Cr enrichment and Fe depletion, consistent with grain boundary RIS directions. Kinks along the slope of the concentration profile may be attributed two possibilities. First, they could be due to counting error. But in cases in which multiple scans along the same boundary all exhibit a kink in approximately the same position, these kinks are likely due to the line scans traversing a dislocation line, where some segregation may have occurred. Since in Figure 5.16, the direction of RIS in the kink is the same as the direction of RIS at the grain boundary, this observation is consistent with the hypothesis of traversing a dislocation.

Another feature of note is that in some cases, the shape of the Cr enrichment peak is sharper, while the minor element peaks are more rounded. An example of this behavior can be seen in the representative profiles from T91 irradiated to 3 dpa at 450°C, Figure 5.16. The cause of this behavior is unknown. One can speculate that it may be attributed to counting statistics or to precipitate nucleation, but there is no basis for further speculation. Rounded profiles have not been mentioned in other literature on RIS in F-M alloys.

7.1.2 Which Measurements should be used in Comparison to Model

It is important to note here that there are many ways to quantify RIS at a grain boundary. Some studies measure only the grain boundary concentration of an element. Other studies measure the change in grain boundary concentration, or the difference between the grain boundary concentration and the matrix concentration of a given element. Yet other studies measure the area under an enrichment peak. In this work, the experiment-model comparison will be performed using the change in grain boundary concentration.

The change in grain boundary concentration (grain boundary concentration minus matrix concentration) shall be used in this work because it relies only on obtaining an accurate measurement of the grain boundary concentration and the matrix concentration. This is also a better measure than only the grain boundary concentration itself, because the *change* accounts for a decrease in the matrix concentration of an element enriched at the grain boundary. Furthermore, if a fair experiment-model comparison is to be made using the area under an enrichment peak, the experimental and modeled results would need to be measured or calculated at identical intervals. Due to the electron probe dimensions, the experimentally-measured intervals are limited to 1.5 nm. As mentioned in Section 6.1.1, the modeled RIS is maximized when a 0.25 nm interval is implemented. Thus, different intervals are used to maximize the amount of RIS measured experimentally and calculated by the model, and thus, the area under the enrichment peaks will not be used for experiment-model comparison.

7.1.3 Sink density

Although the initial IK model executed in Chapter 6 ignored sinks, the dislocation density will be used later in this chapter to aid in the comparison between the measurements and the IK calculation. Although point defect sinks are discrete features, the IK model treats the input sink density as a dislocation line density homogenized across the entire modeled volume. Thus, it is relevant here to identify the limitations of the dislocation density as it is utilized within the IK model. It is also critical to describe how these limitations affect the experiment-model comparison.

Sink density is temperature dependent. Specimens irradiated at lower temperatures exhibit nucleation and growth of dislocation loops, an example of which is given for T91 irradiated to 3 dpa at 400°C in Figure 7.1(a). But dislocation loops are not found at higher irradiation temperatures, an example of which is given for T91 irradiated to 3 dpa at 700°C in Figure 7.1(b). Other microstructural studies [11], [61], [136–138] have confirmed that in F-M alloys, the size and number density of loops increase with temperature up to ~450-500°C, above which the number density decreases until no dislocation loops can be seen at temperatures >~600°C. So with increasing temperature, the sink density will decrease, making more point defects available to diffuse to grain boundaries and generate RIS; this would in turn cause the IK model to increasingly under-predict the extent of segregation with increasing temperature.

To minimize the effects of the temperature dependence of the sink density, the as-received sink density is used in IK simulations. The as-received sink density does not account for loops, but only for boundaries, precipitates, and dislocation lines. It must be noted, however, that thermal annealing may occur [139] as the specimens are heated to their irradiation temperatures (particularly 700°C), and could cause sinks to anneal out of the specimens. If so, the IK model could over-predict RIS at higher temperatures.

Using the as-received sink density in IK calculations is a valid assumption at low irradiation doses. But as loops and irradiation-induced phases nucleate and grow with increasing dose, the as-received sink density will cause the IK model to increasingly over-predict the extent of RIS. This effect is lessened since experiments are performed to only 3 dpa, except for those conditions investigated for dose dependence. This issue will be addressed in greater detail in the forthcoming Section 7.2.4.

It must also be determined whether it is reasonable to account for each sink type in the IK model. Since point defect sinks are discrete features in the alloys, not all point defects may "see" these sinks while they diffuse to a grain boundary. Furthermore, in Section 6.2.1 and Figure 6.11-6.12, it was shown that only the point defects created within ~10 nm of the grain boundary actually diffuse to that boundary and generate RIS. Thus, it is reasonable for the as-received sink density to account for only the sinks found within ~10 nm to a few tens of nm of the PAGB. The average positions of sinks relative to the PAGB are noted in Table 7.1 and will be discussed here.

- *Grain boundaries*: Laths are ~400 nm wide, so the nearest lath boundaries will not affect RIS occurring within ~10 nm of a PAGB. Some lath boundaries may intersect PAGBs near the analysis region. But overall, other boundaries will have very little, if any, effect on RIS at a PAGB.
- *Precipitates*: All RIS line scans are taken ≥20 nm away from precipitates located on PAGBs. Since most point defects that generate RIS are created within ~10 nm of the region being analyzed, precipitates will have a small effect, if any, on RIS.
- *Dislocation lines*: Dislocation lines are distributed uniformly throughout the alloy, even within tens of nm of the PAGB. On average, dislocation lines are spaced 40 nm apart, as back-calculated from their density provided in Tables 5.30-5.31. Thus, dislocation lines can affect RIS, and it is reasonable to account for them in the as-received sink density and also to homogenize them across the modeled volume.

Since the as-received sink density considers grain boundaries and precipitates in addition to dislocation lines, the model calculations should under-predict the extent of RIS. However, irradiation-induced sinks such as black dots and dislocation loops, nucleate as early as 1 dpa (see Tables 5.30-5.31 for dislocation loop dose evolution), and reduce the amount by which the model will under-predict RIS. Both black dots and loops are uniformly distributed throughout the specimen, so homogenization of these sinks is reasonable. Furthermore, there is no denuded zone of dislocation loops, as shown in

Figure 7.2, for T91 irradiated to 3 dpa at 400°C. In this figure, dislocation loops are observed at the PAGB, which could explain scan-to-scan variations along a given PAGB. Ultimately, model calculations offer a reasonable match to the experimental measurements because the under-prediction of RIS using the as-received sink density is reconciled by a reduction in RIS due to nucleation of irradiation-induced features.

This section has shown that although sink density is temperature-dependent, use of the as-received sink density in the IK model calculations can minimize temperature dependence effects. Use of the as-received sink density has been justified. The effects of these assumptions on the experiment-model comparison have been noted. In the forthcoming Section 7.2.1, the IK model temperature dependence will be calculated over a range of sink densities, 0-10^{17} m^{-2}, which will further illustrate the significance of the temperature dependence and uniformity of the sink density.

7.2 Comparison of Experimental Results to Inverse Kirkendall Predictions

In this section, experimental measurements will be compared against inverse Kirkendall model predictions, to determine whether the IK mechanism is consistent with the experimental results. For this comparison to be of value it is critical to first establish which features or behaviors are important and relevant to the comparison. In Chapter 6, a number of IK model dependencies were presented, specifically the dependence of Cr RIS on irradiation temperature, dose, alloy composition, and dose rate. From these dependencies, one can glean five distinct features, which collectively characterize the IK mechanism in F-M alloys: (1) a bell-shaped temperature dependence, (2) a temperature at which a “crossover” between Cr enrichment and Cr depletion occurs, (3) increasing amount of RIS with bulk Cr concentration, (4) saturation of RIS with dose, and (5) minimal dependence of RIS on dose rate. Each of these features shall constitute the focus of one of the following subsections. All subsections will first compare experimental measurements to the model prediction. Differences between model and experiment will be noted, and if necessary and possible, justifiable adjustments will be made to the IK model to bring calculations into better agreement with experimental results. Then, it will be deduced whether RIS in F-M alloys is consistent with the IK mechanism. Finally, since the IK model considers only a binary Fe-Cr alloy, this section will conclude with a discussion on minor and impurity element segregation.

7.2.1 Bell-Shaped Temperature Dependence

In Chapter 6, it was shown that the IK mechanism exhibits a Cr RIS behavior that follows a bell-shaped temperature dependence, in which the amount of RIS is maximized at some moderate temperature, while being suppressed at low (≤ 200°C) and high (≥ 800°C) temperatures. Similarly, experimental measurements of Cr RIS in alloy T91 were shown in Chapter 5 to also follow a bell-shaped temperature dependence below the crossover temperature. But, a bell-shaped temperature dependence is not unique to the IK mechanism; most RIS mechanisms will exhibit a peak amount of segregation at some intermediate temperature. Thus, in order for the experimentally observed bell-shaped temperature dependence to be attributed to the IK mechanism, extremely good agreement between model and experiment must be demonstrated. In this section, then, it will be shown that varying IK model input parameters within their measured or calculated ranges, brings the IK model temperature dependence into very good agreement with the experimental results. This section will also discuss factors that cause the bell-shaped temperature dependence.

The bell-shaped temperature dependence was initially observed in the IK model results when the model was executed using the set of input parameters from Table 6.8 (henceforth referred to as “version 0” of the IK input parameters) and condition parameters from Table 6.10. These results simulated a binary Fe-9Cr alloy system under 10^{-5} dpa/sec irradiation, over a temperature range 100-900°C in 25°C intervals, assuming no sinks (0 m^{-2} dislocation density). The calculated Cr RIS values were taken at a steady-state dose of 15 dpa, noting that the onset of RIS steady-state occurs by ~1 dpa. Experimental results were taken from alloy T91, irradiated with 2.0 MeV protons to 3 dpa at a dose rate of ~10^{-5} dpa/sec, over a temperature range of 300-700ºC. The IK model experiment parameters quite accurately described the experimental conditions. Although these model and experimental results had been presented individually in

Chapters 5 and 6, they are now directly compared to each other in Figure 7.3, which shows that the experimental results exhibit a bell-shaped temperature dependence similar to the IK model results. However, the model calculation is offset from the measurements by ~50°C; in other words, the IK model under-predicts the temperature of maximum segregation by ~50ºC. In order to achieve consistency between the experimental measurements and the inverse Kirkendall mechanism, adjustments shall be made to the IK model input data so as to produce IK model output which falls more closely in line with the experimental data points.

The IK model was shown to be most sensitive to the four solute-defect migration energies (see Section 6.1.2), so adjustments to the IK model input values shall begin with these parameters. In Section 6.1.3, values of 0.63, 0.55, 0.35, and 0.26 eV were selected for the Fe vacancy, Cr vacancy, Fe interstitial, and Cr interstitial migration energies, respectively. These values were the average of several *ab initio*-based calculations for the energies of various jump configurations, as described in Sections 6.1.3.1-6.1.3.2. The range over which the *ab initio* results fall can be assumed to be the range over which the given solute-defect migration energy can be expected to fall. This assumption will be justified by considering the possible jump configurations for each solute-defect jump. Consider, for example, the Fe vacancy migration energy. The *ab initio* works of Choudhury, *et al*. [55], Wong, *et al*. [54], and Nguyen-Manh, *et al*. [111], calculated the energies of a number of possible Fe-vacancy jump configurations, as shown in Table 6.4. The configurations differed in the proximity of the jumping atom to a vacancy or impurity atom. In actuality, the relative frequency with which each jump configuration occurs is not well-understood; the fraction of all Fe-vacancy jumps which are, say, of the w_4 configuration, is unknown. Thus, all configurations must be considered to be possible, and the jump energies of all configurations must also be considered possible. Consequently, the jump energies calculated by *ab initio* methods, as listed in Table 6.4, establish the range over which the Fe vacancy migration energy falls: a minimum of 0.57 eV, and a maximum of 0.69 eV. The same argument can be made for the Cr vacancy, Fe interstitial, and Cr interstitial migration energies (Tables 6.5-6.7, respectively).

The resultant migration energy ranges, based on the *ab initio* solute-defect jump energies, are shown in Table 7.2. If any one, or more, of the input migration energies is varied within the range given in Table 7.2, the results of the IK model prediction will also change. It follows, then, that any one (or more) of the migration energies can be adjusted such that the IK-predicted temperature dependence curve of Cr RIS will fall into better alignment with the experimental measurements. This can most clearly be illustrated by calculating the possible variability of the Cr:Fe vacancy and interstitial diffusion coefficient ratios, given the migration energy ranges of Table 7.2. The result is an uncertainty band over which the diffusion coefficient ratios would occur, as shown in Figure 7.4. The wide uncertainty bands about each diffusion coefficient ratio clearly demonstrates how much the temperature dependence of the calculated RIS might vary, based only on very small changes to the migration energies.

Since the Fe vacancy migration energy had the largest range of the four migration energies, as shown in Table 7.2, this parameter was selected for adjustment. Decreasing the Fe vacancy migration energy shifted the Cr depletion via vacancies to higher temperatures. This change is illustrated with the Fe:Cr vacancy and interstitial diffusion coefficient ratios, as shown in Figure 7.5. In this figure, a decrease in the Fe vacancy migration energy by just 0.03 eV (from 0.63 to 0.60 eV) shifted the Cr:Fe vacancy diffusion coefficient ratio in the negative direction and made a very small change to its slope. These effects manifest by an increase in the crossover temperature from ~550°C to ~660°C, and an overall shift in the entire temperature dependence curve of Cr RIS. A 0.03 eV change in the Fe vacancy migration energy, Figure 7.6, results in a shift of the temperature of maximum segregation by ~+50°C in a Fe-9Cr alloy at steady-state dose, dose rate 10^{-5} dpa/sec, using a dislocation density of 0 m^{-2}. Clearly, decreasing the Fe vacancy migration energy input to the IK model aligned the calculated bell-shaped temperature dependence with the experimental results. This modification to the IK input parameters is highlighted in Table 7.3, and clearly falls within the range established in Table 7.2. This modified set of input parameters shall henceforth be referred to as version 1 of the input parameters, abbreviated as “version 1”.

At this juncture, it is now important to address the issue of dislocations and point defect sinks, and how to account for them in the IK model. Although Figure 7.6 shows that the IK model accurately predicted the experimentally observed bell-shaped temperature dependence and the temperature of maximum segregation, it is clear that the

IK model, in the absence of sinks, over-predicted the magnitude of Cr RIS. The treatment of sinks in the IK model is to consider a single, user-input dislocation density, ρ_d, in units of m^{-2}, which the model assumes are distributed homogeneously throughout the volume being considered. The IK calculated magnitude of Cr RIS decreases as a function of dislocation density, which is shown in Figure 7.7 for Fe-9Cr irradiated at 400°C, 10^{-5} dpa/sec, steady state dose. Interestingly, this dependence is non-linear, and requires ~10^{14} m^{-2} before the dislocation density begins to affect the IK model calculation; above this density, however, the calculated segregation decreases very rapidly with increasing dislocation density.

The sink strength of alloy T91 is calculated in Chapter 5 based upon microstructural analysis. Here, the sink strength shall be converted into an equivalent dislocation line density, as needed for the IK model input. The conversion shall be performed by equating the absorption of all sinks present with the absorption of the equivalent dislocation line density. The absorption of each type of point defect for a given sink is calculated by multiplying the sink strength by the point defect concentration and diffusion coefficient,

$$A_{is} = k_s^2 D_i C_i \text{, and} \qquad (7.1)$$

$$A_{vs} = k_s^2 D_v C_v , \qquad (7.2)$$

where A_{is} and A_{vs} are the absorption by sink s of either interstitials or vacancies, respectively, k_s^2 is the sink strength, D_i and D_v are the diffusion coefficients of interstitials and vancies, and C_i and C_v are the concentrations of interstitials and vacancies. The sum of the absorptions over all sinks can then be equated to the absorption of the equivalent dislocation line density:

$$A_{i,eqdisl} = \sum_s A_{is} \text{, and} \qquad (7.3)$$

$$A_{v,eqdisl} = \sum_s A_{vs} , \qquad (7.4)$$

where $A_{i,eqdisl}$ and $A_{v,eqdisl}$ are the absorption of the equivalent dislocation line density of interstitials and vacancies, respectively. Following the form of Equations 7.3-7.4, the absorption of the equivalent dislocation line density can also be written as

$$A_{i,eqdisl} = k_{eqdisl}^2 D_i C_i \text{, and} \qquad (7.5)$$

$$A_{v,eqdisl} = k_{eqdisl}^2 D_v C_v \,, \tag{7.6}$$

Combining Equations 7.3-7.8, it is obvious that the quantities D_iC_i and D_vC_v will cancel out, leaving

$$k_{eqdisl}^2 = \sum_s k_s^2 \,. \tag{7.7}$$

In Equation 7.9, the summed quantity on the right-hand-side is simply the total sink strength calculated in Section 5.3. The sink strengths on both sides of Equation 7.9 are calculated in units of m^{-2}; because of the two-dimensional nature of dislocation lines, a dislocation line density is also written in units of m^{-2}. Therefore, the equivalent dislocation line density, ρ_d, which will be input into the IK model, is:

$$\rho_d = k_{eqdisl}^2 \,. \tag{7.8}$$

As calculated in Chapter 5, the sink strength of T91 is 10^{15} m^{-2}. Thus, the equivalent dislocation line density, which shall be used in the IK model, is also 10^{15} m^{-2}.

The IK model is reevaluated using a dislocation density of 10^{15} m^{-2} as well as an upper bound of 10^{17} m^{-2}; these results are shown in Figure 7.8. This figure demonstrates that the absence of sinks (0 m^{-2}) led to the over-prediction of the amount of Cr RIS, while an extremely high dislocation density (10^{17} m^{-2}) led to under-prediction of the amount of RIS. Clearly, when sinks were considered in a more realistic manner, such as a dislocation density of 10^{15} m^{-2}, the IK model calculated a RIS magnitude that matched the experimentally measured values very well. The IK model input parameters in version 1 were updated to include a dislocation density of 10^{15} m^{-2}; as given in Table 7.3, resulting in version 2 (version 2). Numerical results from all of the aforementioned IK simulations and experimental measurements are summarized in Table 7.4.

The bell-shaped temperature dependence of the change in grain boundary Cr concentration arises because of point defect mobilities. At very low temperatures, defects are immobile and cannot diffuse to sinks, thus severely limiting the amount of segregation. At the opposite extreme, elevated temperatures allow for significant diffusion of highly-mobile point defects, but any segregation that may arise at a sink is quickly neutralized by back-diffusion of the very mobile defects. Hence, the most segregation will occur at moderate temperatures. This effect is clearly demonstrated by the IK model, as shown in Figure 7.6: when migration energies were adjusted, the bell-shaped temperature dependence persisted on both sides of the crossover temperature, but RIS was consistently suppressed at extremely low (≤ 200°C) and extremely high (≥ 800°C) temperatures.

It is also useful to examine the temperature dependence of the area under the Cr enrichment peak and the FWHM of the peak. Experimental measurements of both of these parameters are shown in Figure 7.9 as a function of temperature. Not surprisingly, the area under the Cr enrichment peak also exhibited a bell-shaped temperature dependence, much like the amount of Cr RIS (Δ grain boundary Cr concentration). The FWHM of the Cr peak, however, was considerably larger at 600°C than at lower temperatures, likely due to a small amount of back-diffusion at such a high irradiation temperature. There was very little variation in FWHM between 400°C and 500°C. At 300°C, the FWHM initially appeared to be larger than at 400-500°C, but when scan T91_3dpa_300C_01-12_T_2-1-F is ignored, the FWHM at 300°C is slightly lower than at 400-500°C. This particular scan was collected on a part of the grain boundary which may not have been in perfect edge-on alignment, and as seen in Table 5.11, is considerably different than the other scans collected on the same boundary. The result of decreasing FWHM with decreasing temperature is reasonable, since limited back-diffusion at lower temperatures should produce narrower RIS profiles.

7.2.2 Crossover Temperature

The existence of a crossover temperature is a unique feature of the IK mechanism in the F-M alloy system. In this section, it will be shown that both the IK model and experimental measurements of alloy T91 exhibit the crossover behavior. Causes of the crossover behavior will also be discussed in the context of implications on the RIS mechanism.

The IK model version 2 was developed in the preceding section, and it was there noted that the model predicted the crossover temperature to be approximately 660°C for a modeled Fe-9Cr alloy irradiated at 10^{-5} dpa/sec over a temperature range 100-900°C, with 10^{15} m^{-2} dislocation density. The calculated crossover behavior is illustrated in Figure 7.8 (and corresponding Table 7.4), which predicts that Cr will enrich at temperatures ≤660°C and that Cr will deplete at temperatures ≥660°C. Experimental observations presented in Chapter 5 showed that alloy T91 irradiated with 2.0 MeV protons to 3 dpa exhibited Cr enrichment at 600°C and Cr depletion at 700°C. It can be deduced, then, from these experimental measurements, that the crossover temperature falls somewhere between the binding experimental temperatures of 600°C and 700°C. Thus, the IK model predicted crossover temperature falls within the temperature range deduced from experiments.

The crossover behavior calculated by the IK model is a direct result of differences in the solute-defect diffusion rates. As described in Section 6.2.2, the IK modeled crossover behavior arose because the ratio of the vacancy diffusion coefficient in Cr to that in Fe crosses the ratio for interstitials in the temperature range over which RIS occurs. The natural logarithm of the ratio of the diffusion coefficient in Cr to that in Fe is greater than unity for both interstitial and vacancy diffusion (see Figure 7.5), indicating that Cr is a faster diffuser than Fe by both types of point defects. When the interstitial and vacancy diffusion coefficient ratios are equal (i.e. at the crossover temperature), the contribution of Cr enrichment by interstitials is cancelled out by the contribution of Cr depletion by vacancies. But when the interstitial diffusion coefficient ratio is greater than that for vacancies (i.e. at temperatures below the crossover temperature), Cr enrichment by interstitials dominates Cr depletion by vacancies, resulting in a net Cr enrichment. Conversely, at temperatures above the crossover, the IK mechanism predicts Cr depletion by vacancies will dominate Cr enrichment by interstitials, resulting in a net Cr depletion.

A Cr enrichment-depletion crossover has never been observed in austenitic steels, and as shown in Figure 7.10, the austenitic vacancy and interstitial diffusion coefficient ratios do not intersect in the RIS temperature range. The diffusion coefficients used in Figure 7.10 were calculated using the IK input parameters for austenitic steels, taken from the work of Allen and Was [18]. For the austenitic steels, the natural logarithm of the vacancy diffusion coefficient ratio of Cr to Ni is positive, while that for interstitials is negative. This demonstrates that RIS in the austenitic alloy should be dominated by Cr depletion and Ni enrichment, which is indeed consistent with the many experimental observations of RIS in a number of austenitic alloys.

Figure 7.10 also illustrates why the amount of RIS in F-M alloys is so low (never exceeding ~2.5 wt% enrichment of Cr) as compared to that in austenitic alloys, in which up to 20 wt% Cr depletion has been measured. In the austenitic alloys, the natural logarithm of the vacancy diffusion coefficient ratio of Cr to Ni is greater than unity, while that of the interstitial coefficient ratio is negative. At any fixed temperature, the difference between the vacancy and interstitial diffusion coefficient ratios is large. But in F-M alloys, on the other hand, the vacancy and interstitial diffusion coefficient ratios lie nearly right on top of one another, so their difference at a fixed temperature is very small, especially as compared to that of austenitic alloys. Smaller differences between the vacancy and interstitial diffusion coefficient ratios gives rise to smaller amounts of RIS, which can explain why such small amounts of Cr RIS are observed in F-M alloys as compared to austenitic alloys.

Since the values of the diffusion coefficient ratios of Cr to Fe are essential to the conclusions drawn here, it is valuable to confirm the consistency of these diffusion coefficient ratios with other calculations. Wong, *et al*. [54] generated vacancy diffusion coefficient ratios from a multi-frequency *ab initio* model for both Fe with Cr at the dilute limit and for a concentrated Fe-10Cr alloy, as shown in Figure 7.11. But since the IK model deals with concentrated Fe-9Cr (or higher Cr) alloys, it is most relevant to compare the IK vacancy diffusion coefficient ratios to Wong's Fe-10Cr vacancy diffusion coefficient ratio.

The Wong model considers nine vacancy diffusion frequencies which have been defined in the LeClaire models [116], [117], including the diffusion of bound vacancy-solute complexes (i.e. of the solute drag mechanism) up to the second-nearest-neighbor. Wong assumes that the frequencies of each vacancy exchange with Fe atoms near a Cr atom follow a standard Arrenhius expression. In the dilute limit of Cr in bcc Fe, Wong uses these expressions from all frequencies to obtain the diffusion coefficients of Cr and of Fe. Thus, the Wong model accounts for mono-vacancy diffusion, such as in the IK mechanism, as well as solute drag effects.

However, LeClaire's models indicate that the presence of solutes which bind vacancies (Cr binds vacancies, as was noted in Section 6.3.2), the vacancy concentration will increase. Since the diffusion coefficient of Fe is proportional to the vacancy concentration [54], it will subsequently increase as well. Thus, when the Wong model is extended to a concentrated Fe-10Cr bcc system, this enhancement of Fe self-diffusion reduces the diffusion coefficient ratio of Cr to Fe, thus providing the curvature for the Fe-10Cr line in Figure 7.11.

The IK model relies on the intersection of the vacancy and interstitial diffusion coefficient ratios to produce Cr enrichment at $T<T_{crossover}$ and Cr depletion at $T>T_{crossover}$. And while the Wong Fe-10Cr vacancy diffusion coefficient ratio never intersects, and is always less than, the IK interstitial diffusion coefficient ratio, Wong's *ab initio* approach has yet to be extended to interstitial diffusion, so it cannot yet be determined whether Wong's model will also predict Cr depletion at higher temperatures. However, the high-temperature region is the one in which the Wong Fe-10Cr and the IK vacancy diffusion coefficient ratios are closest in both magnitude and slope.

The IK mechanism is a rate theory mechanism, in which RIS occurs because of differences in the solute-defect diffusion rates. Studying the diffusion coefficient ratios, as has been done in the preceding paragraph, demonstrates that a crossover behavior is the direct result of differences in solute-defect diffusion. The consistency, then, between experimental and calculated crossover behaviors, makes a compelling argument that the mechanism of Cr RIS in F-M alloys is inverse Kirkendall.

7.2.3 Composition Dependence

In Chapter 6, the IK model showed that the amount of Cr RIS increased linearly as a function of bulk Cr concentration. In this section, it shall be shown that the actual behavior of Cr RIS, as measured experimentally in four F-M alloys, has the opposite slope of that predicted by the IK model. It will then be shown that the reason for this difference is that the interstitial migration energies are composition-dependent.

The initial comparison of composition dependence between model and experiment was completed using version 2 of the IK model, since, in the preceding sections, it yielded results very comparable to the measured data. Version 2 of the IK model was used to determine how increasing alloy bulk Cr concentration would affect Cr RIS using alloys Fe-7Cr through Fe-15Cr, at 1 at% Cr increments, 400°C, steady-state dose, 10^{-5} dpa/sec, 10^{15} m^{-2} dislocation density. These results were compared to experimental measurements from T91, HT9, HCM12A, and 9Cr model alloy, irradiated with 2.0 MeV protons at 400°C to 3 dpa. The comparison is shown graphically in Figure 7.12 (orange line represents IK version 2 and red dots represent experimental measurements). Clearly, the IK model predicted that the amount of Cr RIS would increase with increasing bulk Cr concentration, whereas experimental results showed that Cr RIS would decrease as a function of increasing bulk Cr concentration.

The IK simulation used fixed interstitial migration energies for all bulk Cr concentrations. But, both modeling and experimental studies [106], [114] have suggested that this parameter is highly dependent upon the alloy composition. Especially at the temperature of interest in these simulations, 400°C (i.e. below the crossover temperature), IK-predicted RIS is dominated by interstitial diffusion. Therefore, the value used for the Cr interstitial migration energy is critical for producing a relevant, realistic IK simulation.

The studies which have shown composition-dependence of the interstitial migration energy will be considered here, and used to arrive at a more appropriate set of interstitial migration energies to input into the IK model. The resistivity recovery experiments performed by Abe and Kuramoto [106], while not quantitative, showed that increasing additions of Cr (of 0, 0.019, 0.047, and 0.095 at%) to α-Fe stabilized mixed-dumbbell SIAs, as evidenced by the shift of the I_E peak (which indicates the temperature at which some resistivity is recovered from the onset of interstitial migration) to lower temperatures with increasing Cr concentration. This observation confirmed that Cr is a faster diffuser than Fe via interstitials [106]. Similarly, Terentyev, *et al*. [114] showed via *ab initio* modeling that the migration energy of single SIAs (including multiple configurations of both pure Fe-Fe and mixed Fe-Cr dumbbells) decreased with increasing Cr concentration: from 0.31 eV in pure Fe, to 0.23 eV in Fe-15Cr, as shown in Table 7.6. Composition-dependent Fe and Cr interstitial migration energies were calculated by interpolating the results of Terentyev. Since the results from the preceding sections showed good agreement between IK modeled Fe-9Cr and alloy T91, the interstitial migration energies were fixed at Fe-9Cr composition; the interpolated composition-dependent interstitial migration energies were used only for compositions other than 9 at% Cr. All other input parameters remained unchanged from IK model inputs version 2.

The new set of input parameters, using the composition-dependent interstitial migration energies, shall henceforth be referred to as IK model inputs version 3. When concentration-dependent interstitial migration energies from Table 7.5 were used in the RIS calculation, the IK model predicted the same trend as the experiment—decreasing Cr enrichment with increasing Cr concentration, Figure 7.12 (purple line). Numerical values of Cr RIS as a function of composition, are provided in Table 7.6.

The decreasing amount of Cr enrichment as a function of increasing bulk Cr concentration can be explained by differences in solute-defect diffusion rates. The composition-dependent interstitial migration energies used for IK model inputs version 3, cause the interstitial diffusion coefficient ratio of Cr to Fe, to change. This change is illustrated in Figure 7.13 for the 11-12 wt% Cr interstitial migration energies (solid line) compared to the original or 9 wt% Cr interstitial migration energies (dashed line). Obviously, the vacancy diffusion coefficient ratio of Cr to Fe does not change when only the interstitial migration energies are made composition-dependent. But as can be seen in Figure 7.13, the shift in the interstitial diffusion coefficient ratio causes two significant effects: (1) a decrease in the crossover temperature to ~550°C, and (2) the difference between the vacancy and interstitial diffusion coefficient ratios at 400°C to decrease. The latter of these effects explains the observed decrease in Cr enrichment as a function of increasing bulk Cr concentration, which was measured in specimens irradiated with protons at 400°C.

Bulk Cr concentration is most certainly not the only difference between the alloys T91, HT9, HCM12A, and 9Cr model alloy. Differences in the minor and impurity elements amongst the alloys can affect Cr RIS. Considerable enrichment or depletion of minor or impurity elements—particularly those which have a high degree of size misfit with the bcc Fe-Cr system—can cause localized lattice parameter changes at the PAGB, which could then alter the migration energy and diffusivity of Cr within that localized region. This idea has been modeled by Liu and Huang [140], who have shown that the presence of both substitutional and interstitial impurities can expand the $LiFePO_4$ lattice parameter, and thereby increase the energy for Li diffusion in the crystal. In addition, both undersized and oversized substitutional impurities, as well as interstitial impurities, have been measured to alter the lattice parameter as well as the point defect diffusivity in metals AlRu and AlCo [141], [142]. Microstructural differences could also play a role in the variation of the Cr RIS behaviors observed amongst the alloys. However, in a simplified model such as the IK model used in this thesis, in which only bulk Cr concentration differences could be captured, there was good agreement between measured and predicted Cr RIS as a function of bulk Cr concentration, as long as composition-dependent migration energies were utilized.

7.2.4 Irradiation Dose

The IK simulations in Chapter 6 showed that the amount of RIS increased quickly with dose, then eventually reached a steady-state plateau, at which point the amount of RIS remained constant. At an irradiation dose rate of 10^{-5} dpa/sec, the IK model predicted that steady-state occurred by ~1 dpa. It is critical, here, to emphasize that steady-state or plateau-type behavior does not mean that RIS ceases after the steady-state dose is reached. Rather, RIS continues to occur, but does not increase because back-diffusion counteracts the concentration gradient, resulting in a condition of steady-state. In this section, the dose dependence of the IK model results will be compared to the measured amounts of segregation. It will be shown that experimental measurements from the 9Cr model alloy exhibit steady-state behavior, whereas T91 does not reach a steady-state. Then, it will be determined whether the experimental measurements are consistent with the IK mechanism.

IK model version 3 was used to study the Cr RIS dose dependence in Fe-9Cr irradiated at 400°C, 10^{-5} dpa/sec, with $\rho_d = 10^{15}$ m^{-2}. These results are shown in Figure 7.14, in which they are compared to experimental measurements of Cr RIS from T91 and 9Cr model alloy, irradiated with 2.0 MeV protons at 400°C to doses ranging from 1 dpa to 10 dpa. Numerical values are provided in Table 7.7.

Upon initial inspection, there was very little similarity between the experiment and model results shown in Figure 7.14. Most notably, kinetics appeared to be enhanced in the IK model version 3 as compared to experimental measurements: the IK version 3 results indicated that the onset of RIS should occur at a very early dose, with enrichment of ~0.5 at% Cr by only 0.0001 dpa, whereas experimental data showed this amount of Cr enrichment at 1 dpa. Furthermore, IK version 3 calculated steady-state RIS would occur by approximately 1 dpa, whereas in experiments on T91 and the 9Cr model alloy, the onset of what may be a steady-state regime, does not occur until 3 and 7 dpa, respectively. The comparison shown in Figure 7.14 suggests that the IK model begins to develop RIS earlier than in the experimental data and that RIS calculated by the model builds up at a much slower rate than it does in reality.

Another unusual behavior is the difference in dose dependence between the T91 and 9Cr model alloy. The 9Cr model alloy exhibited an increase in Cr enrichment, discernible outside of the error bars, from 1 dpa to 7 dpa. But between 7 dpa and 10 dpa, the rate of increase in Cr enrichment slowed considerably, and there was significant overlap in the error bars of these two data points, which suggests that the 9Cr model alloy was beginning to reach a steady-state amount of Cr RIS at 7-10 dpa. Conversely, T91 never achieved steady-state RIS, and instead the amount of Cr RIS increased from 1 dpa to 3 dpa, leveled off between 3 dpa and 7 dpa, then between 7 dpa and 10 dpa, there was a statistically-significant decrease in the amount of Cr enrichment. While the data point for T91 at 10 dpa may appear to be an outlier, this result was the average of fifteen different line scans, from which three scans were taken across each of five different grain boundaries. The five grain boundaries were found over two different TEM specimens. All scans were collected with good counting statistics, and the standard deviation of the mean of the overall average amount of Cr RIS is only 0.25 wt%.

Thus, there appear to be two major issues with the dose dependence. First, there is a discrepancy in the measured dose dependence, particularly at 10 dpa, between the two alloys, T91 and 9Cr model. Second, there is what appears to be a kinetics-based difference in the onset and development of Cr RIS between the model and experiment. Each of these issues will now be addressed.

Differences in composition and microstructure between T91 and 9Cr model alloy may explain the difference in the dose dependence of Cr RIS in these two alloys. Both alloys have a similar bulk Cr concentration, and a similar grain structure. The most notable differences between them are: (1) microstructural, with the 9Cr model alloy being relatively free of carbides and precipitates as compared to T91, and (2) the absence of minor elements and impurities (e.g. Si, Ni, Cu) in the 9Cr model alloy. Each of these differences will be discussed here.

First, microstructural and precipitation differences will be studied. In Tables 5.30-5.31, it was shown that the dislocation loop microstructure and sink strength changes as a function of dose in both T91 and the 9Cr model alloy irradiated at 400°C. These dose-dependent sink strengths were implemented into the IK model version 3. Increasing sink strength as a function of dose caused the calculated change in grain boundary Cr concentration to decrease, as shown in Figure 7.15, for both the T91 and 9Cr model alloy dislocation densities. The model calculates that the amount of Cr enrichment will begin to decrease as soon as the sink density begins to increase at 1 dpa. But this is not the case in experimental measurements, in which Cr enrichment increases between 0 and 7 dpa (in T91) or 10 dpa (in the 9Cr model alloy). Clearly, a dose-dependent dislocation density, alone, cannot explain either the decrease in Cr RIS in T91 from 7 to 10 dpa, or the difference in Cr RIS at 10 dpa between T91 and the 9Cr model alloy.

However, a related study [143] showed that in T91 irradiated at 400°C, chromium carbides located on PAGBs followed the same dose dependence as Cr RIS. These results are shown in Figure 7.16. Between 0 and 3 dpa, the precipitates grow, covering a higher fraction of the PAGB length, while the linear density of the precipitates decreases. Then, between 3 and 10 dpa, the precipitates shrink and cover a smaller fraction of the PAGB length, while the linear density of the precipitates increases back to nearly its as-received value. That the precipitate dose dependence is identical to that of Cr RIS, suggests the precipitates act as point defect sinks in a similar manner as do the PAGBs. This result also suggests that when the precipitates shrink, the released atoms return to the matrix rather than diffusing along the grain boundary; if they were to do so, the measured Cr RIS would increase—not decrease—between 3 and 10 dpa.

The absence of minor elements in the 9Cr model alloy may be able to explain the difference in RIS behavior between T91 and the 9Cr model alloy. In Chapter 5, the RIS behavior of minor elements Si, Ni, and Cu, in alloy T91 was described. These minor elements always enrich in proton-irradiated T91, over all doses and temperatures studied. As shown in Table 7.8, Si [144], Ni [145], and Cu [146] all have atomic radii smaller than that of Cr [147] and Fe [148]. Since grain boundaries enrich significantly in Si, Ni, and Cu, the increased concentration of these elements at the grain boundary could be causing the lattice parameter to decrease in the immediate vicinity of the grain boundary. If so, Cr atoms that have caused Cr enrichment at the grain boundary could begin to become slightly oversized, changing the migration energy of Cr. As a result, it could be more energetically favorable for Cr atoms to begin to diffuse away from the grain boundary, therefore causing the amount of Cr enrichment to decrease. Because the IK model considers only Fe and Cr alloy components, the effect of minor elements on RIS cannot yet be determined by the IK model.

Another possible cause of Cr diffusion away from the boundary, following minor element RIS-induced lattice parameter changes, is that the Cr concentration profile at the grain boundary should begin to broaden, which is exactly what was observed in experiments. Figure 7.17 shows that the FWHM of the Cr enrichment peak increased with dose, especially between 7 dpa and 10 dpa. Furthermore, the area under the Cr enrichment peak—or, the total amount of Cr segregated to the grain boundary—remained constant between 7 dpa and 10 dpa. Together, these measurements show that the *amount* of Cr segregated at the boundary reached a steady-state, and that segregated Cr was simply redistributing itself when it became energetically-favorable to do so due to sufficient minor element enrichment.

There remains the issue of the earlier onset of RIS and steady-state RIS in the IK version 3 model result as compared to that in experiment. This inconsistency could be attributed to the actual microstructural evolution in the alloys. It was shown in the sink strength analysis in Section 5.3 that the dislocation loops are very strong sinks, having a total strength about an order of magnitude larger than that of any other feature (grain boundaries, carbides, dislocation lines). As such, nucleation and growth of dislocation loops may be such a strong point defect sink, that point defects take a longer time (i.e. require a higher irradiation dose) to arrive at grain boundary sinks. This would result in a delayed onset of RIS, relative to that predicted by the IK model, which does not consider sink types individually, but rather distributes an "effective" dislocation density homogenously throughout the material..

There remain unresolved issues between the measured and calculated Cr RIS dose dependence, which prevent this work from determining whether the observed dose dependence is consistent with the IK mechanism. However, both experiment and model have appeared to exhibit some type of steady-state behavior. The differences can be rationalized by microstructural evolution, kinetics, and the presence of significant grain boundary enrichment of smaller elements such as Si, Ni, and Cu.

7.2.5 RIS of Other Elements

The IK model, thus far, has only been developed so as to model a binary Fe-Cr alloy. Additional elements, particularly those whose segregation has been observed, such as Si, Ni, and Cu, are not considered in the IK simulations. There is, however, strong evidence, shown in Tables 5.11-5.28 and Figures 5.11-5.24, that these elements enriched under irradiation, over a range of doses, temperatures, and alloys studied. It is therefore relevant to this work to understand the RIS behaviors of these minor elements, which is the aim of this section.

In alloy T91, the temperature dependence of Si, Ni, and Cu enrichment was markedly different than that of Cr enrichment. The amount of Cr enrichment followed a bell-shaped temperature dependence as shown in Figure 7.18; there was some Cr enrichment at 300°C and 600°C, although a greater amount of Cr enrichment existed in the temperature range 400-500°C. Similarly, the enrichment of Si, Ni, and Cu also followed a bell-shaped temperature dependence, peaking between 400°C and 500°C. However, Si, Ni, and Cu enrichment was almost entirely suppressed at 300°C and 600°C, where there was still some Cr enrichment. Clearly, these differences at the extreme temperatures suggest that Cr enrichment does not occur together with Si, Ni, and Cu enrichment. Thus, the mechanism by which Si, Ni, and Cu enrich is different than that by which Cr enriches. Unfortunately, it is outside of the scope of this thesis to expand the IK model to include Si, Ni, and Cu.

7.3 Comparison of Experimental Results to Solute Drag Predictions

In the preceding section, experimental measurements of Cr RIS were shown to be consistent with the inverse Kirkendall mechanism. Demonstrating consistency, however, does not irrefutably confirm that RIS in F-M alloys is driven by the IK mechanism. Rather, alternative mechanisms for RIS must also be examined to determine whether they could also contribute to RIS, or whether they can be ruled out from consideration. One such mechanism is the solute drag mechanism, the initial results from which were presented in Chapter 6. There, both Cr-interstitial complexes and Cr-vacancy complexes were included in the IK model. Accounting for these solute-defect complexes yields Cr RIS predictions that are significantly different than experimental measurements. In this section, it will be determined whether the migration parameters of the solute-defect complexes can be adjusted, within reasonable limits, such that the resulting Cr RIS predictions are sufficiently close to experimental measurements. This section will be organized into two parts: First, the Cr-interstitial complexes will be studied, and second, Cr-vacancy complexes will be treated.

7.3.1 Cr-Interstitial Complexes

It is the task of this section to determine whether Cr-interstitial binding can be accounted for in the IK model, while still producing reasonable RIS predictions that compare well to measured values. This will be accomplished by first understanding the range over which Cr-interstitial binding energies fall. The effect of this binding on the Cr RIS predictions will be addressed. And finally, it will be determined whether Cr-interstitial binding can lead to the amounts of RIS observed experimentally.

In the initial solute drag modeling work done in Chapter 6, binding energies of the Cr-interstitial complexes were determined to range from 0.05 eV to 0.27 eV, and predicted considerable amounts of Cr enrichment. The solute drag model is re-evaluated here using the IK version 3 input parameters and letting the Cr-interstitial binding energy vary. For a simulated Fe-9Cr alloy at 400°C, 10^{-5} dpa/sec, steady-state dose, and a dislocation density of 10^{15} m^{-2}, the amount of predicted Cr RIS increased as a function of increasing Cr-interstitial binding energy, as shown in Figure 7.19 and Table 7.9. In this figure, the known range of Cr-interstitial binding energy values is shaded yellow. A maximum of ~35 at% Cr enrichment is calculated wtih 0.27 eV Cr-interstitial binding energy.

The comparable experimental condition is alloy T91 irradiated with 2.0 MeV protons to 3 dpa at 400°C. There, the amount of Cr RIS measured was only 1.49 at%. In order for the solute drag model to calculate Cr RIS of such low magnitudes, the Cr-interstitial binding energy must be nearly 0. But, setting the solute-defect binding energy to 0 eliminates solute drag effects, which suggests that the solute-interstitial solute drag mechanism may not be able to accurately calculate Cr RIS comparable to that measured experimentally.

The temperature dependence of RIS calculated by the solute drag model can also be compared to that of the IK model and the experimental measurements, as shown in Figure 7.20. Here, the solute drag model is calculated for an Fe-9Cr alloy irradiated at 10^{-5} dpa/sec to a steady-state dose, over a range of temperatures from 100°C to 900°C. Three different interstitial binding energies are used in the simulations, showing that the calculated amount of Cr RIS decreases with decreasing Cr-interstitial binding energy. But over the entire known Cr-interstitial binding energy range, and at all temperatures, the solute drag model with interstitial binding severely over-predicts the amount of Cr RIS, as compared to the IK model and the experimental measurements. The Cr-interstitial binding energy would need to be reduced below 0.05 eV (i.e. outside of the minimum of its known range) in order for the solute drag mechanism to produce Cr RIS comparable to that measured experimentally; such a reduction in the Cr-interstitial binding energy would essentially eliminate the effects of solute drag.

It may, however, be possible to achieve better agreement between the solute drag model and experimental measurements, if adjustments are made to the solute-defect migration energies, much like was done in Section 7.2.1. Keeping in mind that the solute drag model is set up so as to incorporate solute drag effects into the IK model, the calculated RIS can be thought of as the result of an IK contribution and a solute drag contribution. Since the solute drag model over-predicts Cr enrichment but the IK model alone does not, one may be able to bring the solute drag model into better agreement with experimental data by forcing Cr depletion in the IK contribution. Adjusting the solute-defect migration energies within their known ranges (ranges provided in Table 7.2) can change the amount of Cr RIS. In order to induce the most Cr depletion possible in the IK contribution, all four IK solute-defect migration energies are adjusted to the limits of their range: Fe-vacancy migration energy increased to 0.69 eV, Cr-vacancy energy decreased to 0.52 eV, Fe-interstitial energy decreased to 0.33 eV, and Cr-interstitial energy increased to 0.33 eV. Yet still, the over-prediction of Cr enrichment by the solute drag mechanism persists, as can be seen in Figure 7.21.

Furthermore, even when the migration and binding energies are varied to the limits of their known range, the solute drag mechanism remains unable to calculate a crossover between Cr enrichment and Cr depletion. This behavior can be seen in Figure 7.22, which is a zoomed-in view of the 600-800°C region from the preceding plot, Figure 7.21. While both experimental data and the IK model exhibit a crossover between 600°C and 700°C, the solute drag mechanism exhibits Cr enrichment at all temperatures, which asympototically approaches 0 (no segregation) above 750°C. The inability of the solute drag model to calculate this key inflection point in the data presents an additional reason why the solute-interstitial drag mechanism cannot explain the observed Cr RIS.

7.3.2 Cr-Vacancy Complexes

Cr-vacancy complexes, much like the Cr-interstitial complexes analyzed in the preceding section, have an attractive binding energy, and will always cause RIS in the direction of Cr enrichment. The Cr-interstitial complex behaviors presented in this section will be similar to those presented in the preceding section. Here, it shall be determined whether the solute drag model of Cr-vacancy binding can produce reasonable RIS predictions that compare favorably to measured values. Input parameters will be varied within their known ranges in an attempt to achieve consistency between model and experiment. Finally, it will be determined whether the Cr-vacancy solute drag mechanism can predict the RIS behaviors observed experimentally.

In the initial solute drag modeling work done in Chapter 6, binding energies of the Cr-vacancy complexes were found to range over ~0.01-0.05 eV and produce Cr enrichment. The solute drag model is re-evaluated here, as a function of Cr-vacancy binding energy, for Fe-9Cr at 400°C, 10^{-5} dpa/sec, at a steady-state dose of 15 dpa, using the IK input parameters version 3. A maximum of ~4.4 at% Cr enrichment is predicted, as shown in Figure 7.23 and Table 7.10. In this figure, the shaded region indicates the known range of the Cr-vacancy binding energies. The experimental condition comparable to the simulation presented in Figure 7.23 is alloy T91 irradiated with 2.0 MeV protons to 3 dpa at 400°C, for which 1.49 at% Cr enrichment was observed. Again, the solute drag model over-predicts Cr RIS.

The temperature dependence of the solute-vacancy drag mechanism is shown in Figure 7.24, for an Fe-9Cr alloy irradiated at 10^{-5} dpa/sec to a steady-state dose, over a range of temperatures from 100°C to 900°C. Three different vacancy binding energies are used in the simulations, again showing a decrease in the extent of Cr RIS with decreasing binding energy. But, even at the minimum of the known range for Cr-vacancy binding energy, the solute drag model continues to over-predict Cr RIS.

It is possible, though, to achieve better agreement between the solute drag model and experimental measurements, if solute-defect migration energies are adjusted, as was discussed in Section 7.2.1. Increasing the Fe vacancy migration energy, for example, from 0.60 eV to 0.67 eV—well within its range provided in Table 7.1—brings the solute drag model into good agreement with the measured Cr RIS magnitudes at ≤450°C, as shown in Figure 7.25. Nevertheless, the Cr-vacancy solute drag model remains unable to predict the crossover from Cr enrichment to Cr depletion, which raises doubt as to its validity as a viable mechanism to explain RIS in F-M alloys. The asymptotic approach from Cr enrichment to 0 in the Cr-vacancy solute drag model is shown in closer detail in Figure 7.26, which is a zoomed-in view of the 600-800°C region from the preceding plot, Figure 7.25.

In this and the preceding section, it has been shown that there are three ways in which the solute drag model—for both Cr-interstitial and Cr-vacancy complexes—fails to reproduce experimental measurements. First, within the known ranges of the complex binding energies and solute-defect migration energies, the solute drag mechanism consistently over-predicts the measured amount of Cr RIS. Second, it is only possible to achieve agreement between the solute drag mechanism and measurements if binding energies are reduced so significantly (and outside of their known range) that binding effects are essentially being ignored. Finally, the solute drag mechanism does not predict a crossover from Cr enrichment to Cr depletion; this is a key inflection point in the measured data, which the IK mechanism, unlike the solute drag mechanism, is capable of explaining.

7.4 Understanding RIS Measurements in Literature

This chapter has demonstrated that the RIS measurements collected in this thesis are both self-consistent and consistent with the IK mechanism. A more rigorous test, however, is to determine whether RIS measurements from literature—a seemingly contradictory and inconsistent collection of data—can be explained by the IK mechanism. In this section, RIS data from literature will be compared against the IK mechanism, and possible explanations for inconsistencies between the model and experiments will be presented.

As has been demonstrated in Figures 7.5, the IK model predicts that Cr will enrich at low temperatures, but deplete at high temperatures, due to the intersection of the diffusion coefficient ratios of vacancies and of interstitials. The temperature at which this intersection occurs decreases with increasing bulk Cr concentration. Thus, an effective way to compare the IK mechanism to literature measurements is to plot the crossover temperature as a function of composition, then overlay the experimental data onto this plot, as in Figure 7.27. Experiments in which Cr enrichment was observed (green circle symbols) should fall below the crossover temperature line, while Cr depletion points (red triangle symbols) should fall above the crossover.

The Cr enrichment measured by Gupta, *et al*. [11], Little, *et al*. [7], Kato, *et al*. [4], and Clausing, *et al*. [6], fall below the crossover temperature line at their respective bulk Cr compositions, demonstrating consistency with the IK mechanism. These four experiments were performed on both commercial and model alloys, with bulk Cr compositions ranging from ~8Cr to nearly 13Cr. The four experiments were performed at temperatures ranging from 410-465°C, and with a variety of irradiating particles and dose rates: Kato irradiated with 1 MV electrons at a dose rate of 1.9 x 10^{-3} dpa/sec, Gupta with 2 MeV protons at 2 x 10^{-5} dpa/sec, and both Little and Clausing worked with fast neutrons. The variety of alloys, irradiating particles, and dose rates of these experiments demonstrates the versatility and robustness of the IK mechanism for a wide range of experimental conditions.

The Cr depletion measured by Hamaguchi, *et al*. [8] and Neklyudov and Voyevodin [9] fall above the crossover temperature line at their respective bulk Cr compositions. Hamaguchi studied SUS410L (12.34 wt% Cr in bulk) irradiated with 11 MeV protons over a range of temperatures as high as 647°C. Neklyudov and Voyevodin irradiated 13Cr alloys with 1 MeV Cr^{3+} ions over a range of temperatures as high as 800°C. These experiments are consistent with the IK mechanism.

Four experiments [3], [10], [12] measured Cr depletion at irradiation temperatures below the crossover; these measurements are inconsistent with the IK mechanism. However, experimental techniques or methods may be able to explain the inconsistency. The Lu, *et al*. [12] experiment, for example, used 250 keV Ni^+ ions (which have a range of <100 nm) to irradiate pre-perforated TEM discs of E911. Given this experimental setup, surface effects would be significant; the surface could be a much stronger sink than any grain boundary, and could thus explain the observed Cr depletion at boundaries. Schäublin, *et al*. [10] found both Cr and Fe depleted at boundaries in F82H irradiated at 250°C. It is impossible for both Cr and Fe to deplete without other elements enriching, which calls into question these results. In addition, very little—if any—RIS is predicted to occur at an irradiation temperature as low as 250°C, so without the authors noting the amount of Cr and Fe depletion they observed, the measured depletion could simply be an artifact of counting statistics. Finally, Takahashi, *et al*. [3] observed Cr depletion in Fe-5Cr and Fe-13Cr irradiated at 400°C. However, the Cr depletion profiles were measured to have FWHM ~200 nm. This suggests that in order to cause such a broad composition gradient, atoms would have to diffuse over 200 nm—much larger than the diffusion length in a 400°C irradiation (see Section 7.1.3).

Three experiments measured both Cr enrichment and Cr depletion. Two of these were done by Marquis, *et al*. [13], [14], using 0.5 MeV and 2 MeV Fe^+ ions to generate a double-humped damage profile. In one of their studies on Fe-14.25Cr [14], Cr was enriched in the as-received material, and remained enriched following irradiation, although the amount of enrichment was less than in the as-received condition. Two measurements were taken in the irradiated condition, each at a different depth into the damage profile—one measurement was taken at 300 nm, the implantation peak of the 0.5 MeV ions, and the second measurement was taken at 800 nm, the 2 MeV implantation peak. The implanted ions are very likely affecting the observed RIS. The other Marquis [13] study on Fe-12Cr ODS, exhibits similar behaviors in which the surface and the ion implantation peaks are likely affecting the RIS measurements. Finally, Ohnuki, *et al.* [5] irradiated an Fe-13Cr alloy with additions of Si and Ti, using 200 keV C^+ ions. However, their TEM specimen preparation method is such that the analyzed region is the surface on which ions are incident, which is a considerably stronger sink than a grain boundary deeper along the damage profile. In addition, the as-received grain boundary concentrations are not identified, and these specimens are irradiated to high doses (57 dpa), and the dose evolution of RIS in F-M alloys remains unclear.

Table 7.1. Diffusion length in irradiation conditions studied.

Defect	Does as-received sink density consider this sink?	Distribution (nm)	Will point defects created within ~10 nm of PAGB "see" this sink?
Grain boundaries	Yes	~400 nm from PAGB being studied	No
Precipitates	Yes	≥ 20 nm from PAGB region being studied	Very little effect, if any
Dislocation lines	Yes	Uniform distribution, ~40 nm spacing	Yes
Dislocation loops	No	Uniform distribution, no denuded zone	Yes
Black dots and other defect clusters	No	Uniform distribution, spacing not measured	Yes

Table 7.2. Ranges of migration energies input to IK model, as calculated by *ab inito* model (all energies given in units of eV).

Migration energy	**Value used in v.0 of IK input parameters**	**Range given by *ab initio* calculations**
Fe interstitial	0.35	0.34 – 0.39 [55], [113], [115]
Cr interstitial	0.26	0.23 – 0.33 [55], [115]
Fe vacancy	0.63	0.57 – 0.69 [54], [55], [111]
Cr vacancy	0.55	0.52 – 0.58 [54], [55], [111], [112]

Table 7.3. Versions of the IK input parameters, differences highlighted.

Parameter	**version 0**	**version 1**	**version 2**	**version 3**
R1	4.0	4.0	4.0	4.0
R2	18.0	18.0	18.0	18.0
RF	2018.0	2018.0	2018.0	2018.0
N1	16	16	16	16
N2	14	14	14	14
N3	20	20	20	20
H0	1×10^{-9}	1×10^{-9}	1×10^{-9}	1×10^{-9}
EPS	1×10^{-9}	1×10^{-9}	1×10^{-9}	1×10^{-9}
ETAV	0.3	0.3	0.3	0.3
ETAI	0.3	0.3	0.3	0.3
NAT	8.34×10^{28}	8.34×10^{28}	8.34×10^{28}	8.34×10^{28}
LAMBDA	2.48×10^{-10}	2.48×10^{-10}	2.48×10^{-10}	2.48×10^{-10}
FAV	0.727	0.727	0.727	0.727
FBV	0.777	0.777	0.777	0.777
FAI	0.727	0.727	0.727	0.727
FBI	0.727	0.727	0.727	0.727
WAV	1.60×10^{13}	1.60×10^{13}	1.60×10^{13}	1.60×10^{13}
WBV	2.40×10^{13}	2.40×10^{13}	2.40×10^{13}	2.40×10^{13}
WAI	2.90×10^{12}	2.90×10^{12}	2.90×10^{12}	2.90×10^{12}
WBI	1.50×10^{12}	1.50×10^{12}	1.50×10^{12}	1.50×10^{12}
EMIA	0.35	0.35	0.35	c.d.
EMIB	0.26	0.26	0.26	c.d.
SV	1.00	1.00	1.00	1.00
EMA	0.63	0.60	0.60	0.60
EMB	0.55	0.55	0.55	0.55
EFA	1.6	1.6	1.6	1.6
EFB	2.25	2.25	2.25	2.25
EFGB	0.87	0.87	0.87	0.87
NUOV	1.50×10^{13}	1.50×10^{13}	1.50×10^{13}	1.50×10^{13}
NUOI	1.50×10^{12}	1.50×10^{12}	1.50×10^{12}	1.50×10^{12}
AL	1	1	1	1
Z	8	8	8	8
BIASV	1	1	1	1
BIASI	1	1	1	1
DISL	0	0	10^{15}	10^{15}

c.d. = composition-dependent (see Table 7.5 for exact values)

Table 7.4. Comparison of temperature dependence of Cr RIS between IK model calculations v.0, v.1, v.2, and experimental measurements.

Temperature (°C)	IK v. 0		IK v.1		IK v.2	T91 Experiment
	0 sinks/m^2	10^{17} sinks/m^2	0 sinks/m^2	10^{17} sinks/m^2	10^{15} sinks/m^2	
300	0.96	0.36	0.38	0.13	0.31	0.62
400	1.97	0.69	1.55	0.54	1.24	1.49
450	1.07	0.38	2.07	0.73	1.66	1.72
500	0.35	0.12	1.64	0.57	1.31	1.35
600	-0.60	-0.21	0.50	0.18	0.41	0.64
700	-0.36	-0.13	-0.20	-0.07	-0.16	-0.43

Table 7.5. Composition dependence of Cr interstitial migration energy, as calculated by Terentyev, *et al.* [114], which is used as the basis for interpolation of the Fe-interstitial and Cr-interstitial migration energies for the IK model v.3 containing composition-dependent interstitial migration energies.

Alloy	Terentyev, *et al.* [114] calculated migration energy of single SIA in Fe-Cr alloys (eV)	Migration energy interpolated based on slope of Terentyev data (eV)	
		Fe-interstitial	Cr-interstitial
Fe	0.31	n/a	n/a
Fe-0.2Cr	0.29	n/a	n/a
Fe-5Cr	0.28	n/a	n/a
Fe-7Cr	n/a	0.36	0.27
Fe-7.5Cr	0.26	n/a	n/a
Fe-8Cr	n/a	0.36	0.27
Fe-9Cr	n/a	0.35 *	0.26 *
Fe-10Cr	0.25	0.35	0.26
Fe-11Cr	n/a	0.34	0.25
Fe-12Cr	n/a	0.34	0.25
Fe-13Cr	n/a	0.33	0.24
Fe-14Cr	n/a	0.33	0.24
Fe-15Cr	0.23	0.32	0.23

* = Fe-9Cr interstitial migration energy is fixed at value determined in Chapter 5; non-asterisked migration energies are interpolated based upon the slope of the Terentyev data

Table 7.6. Comparison of composition dependence of Cr RIS between IK model calculation v.1 and experimental measurements.

Bulk Cr Concentration (at%)	IK v.0	IK v.1			Experiment
	f.i.m.e. 0 sinks/m^2	f.i.m.e. 0 sinks/m^2	c.d.i.m.e. 0 sinks/m^2	c.d.i.m.e. 10^{15} sinks/m^2	
7	1.60	1.26	2.18	1.74	n/a
8	1.79	1.41	1.85	1.48	n/a
8.37 (T91)	n/a	n/a	n/a	n/a	1.49
9 (9Cr model)	1.97	1.55	1.55	1.24	0.78
10	2.14	1.69	1.27	1.02	n/a
10.83 (HCM12A)	n/a	n/a	n/a	n/a	0.86
11	2.34	1.85	1.01	0.81	n/a
11.63 (HT9)	n/a	n/a	n/a	n/a	0.69
12	2.52	1.99	0.79	0.63	n/a
13	2.70	2.13	0.59	0.47	n/a
14	2.86	2.26	0.43	0.34	n/a
15	3.03	2.39	0.27	0.22	n/a

c.d.i.m.e. = composition-dependent interstitial migration energies
f.i.m.e. = fixed interstitial migration energies

Table 7.7. Comparison of dose dependence of Cr RIS between IK model calculation v.1, and experimental measurements.

Dose (dpa)	IK v.0	IK v.1			T91 Experiment	9Cr Experiment
	0 sinks/m^2	0 sinks/m^2	10^{15} sinks/m^2	10^{17} sinks/m^2		
1	1.96	1.55	1.24	0.54	0.74	0.61
3	1.97	1.55	1.24	0.54	1.49	0.78
7	1.97	1.55	1.24	0.54	1.62	1.43
10	1.97	1.55	1.24	0.54	0.87	1.54

Table 7.8. Atomic radii of component elements in alloy T91.

Element	**Calculated atomic radius (pm)**	**Empirical atomic radius (pm)**
Fe	156 [148]	140 [148]
Cr	166 [147]	140 [147]
Si	111 [144]	110 [144]
Ni	149 [145]	135 [145]
Cu	145 [146]	135 [146]

Table 7.9. Cr enrichment calculated by the solute drag mechanism over a range of Cr-interstitial binding energies.

Cr-interstitial binding energy (eV)	Δ GB Cr concentration (at%) IK v.1 + solute drag	
	0 sinks/m^2	10^{15} sinks/m^2
0.00	1.94	1.55
0.05	10.46	8.37
0.10	20.63	16.50
0.15	30.67	24.54
0.20	40.61	32.48
0.25	43.95	35.16
0.30	44.52	35.62

Table 7.10. Cr enrichment calculated by the solute drag mechanism over a range of Cr-vacancy binding energies.

Cr-vacancy binding energy (eV)	Δ GB Cr concentration (at%) IK v.1 + solute drag	
	0 sinks/m^2	10^{15} sinks/m^2
0	1.94	1.55
0.005	2.21	1.77
0.01	2.50	2.00
0.015	2.97	2.37
0.02	3.39	2.72
0.025	3.89	3.11
0.03	4.40	3.52
0.035	4.92	3.94
0.04	5.21	4.17
0.045	5.44	4.35
0.05	5.52	4.41

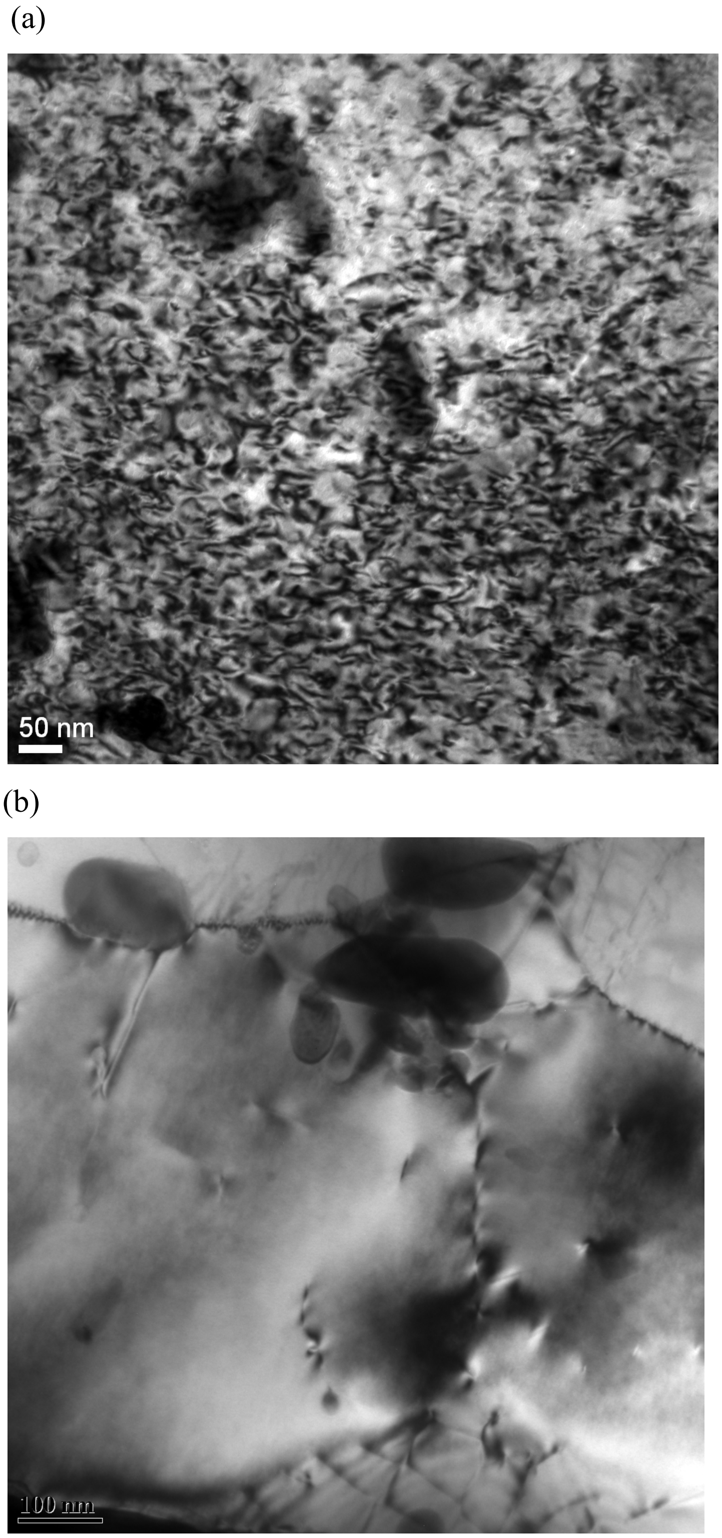

Figure 7.1. Bright field TEM images of T91 irradiated to 3 dpa at (a) 400°C and (b) 700°C, illustrating the high density of dislocation loops in the lower-temperature specimen and an absence of loops in the higher-temperature specimen.

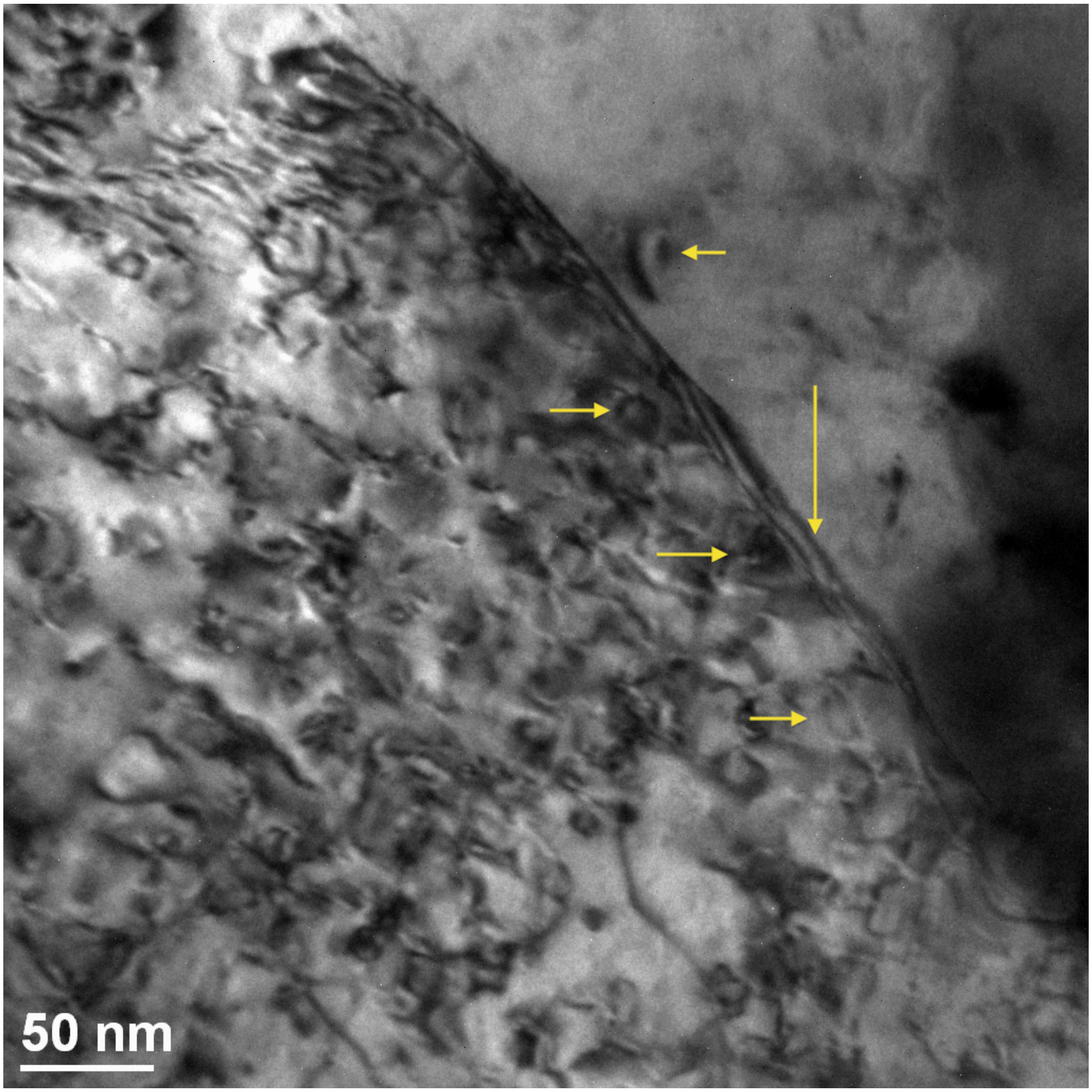

Figure 7.2. Dark field HAADF STEM image of T91 specimen irradiated to 3 dpa at 400°C, identifying a PAGB (vertical arrow) and dislocation loops near the PAGB (horizontal arrows), suggesting that there is no denuded zone.

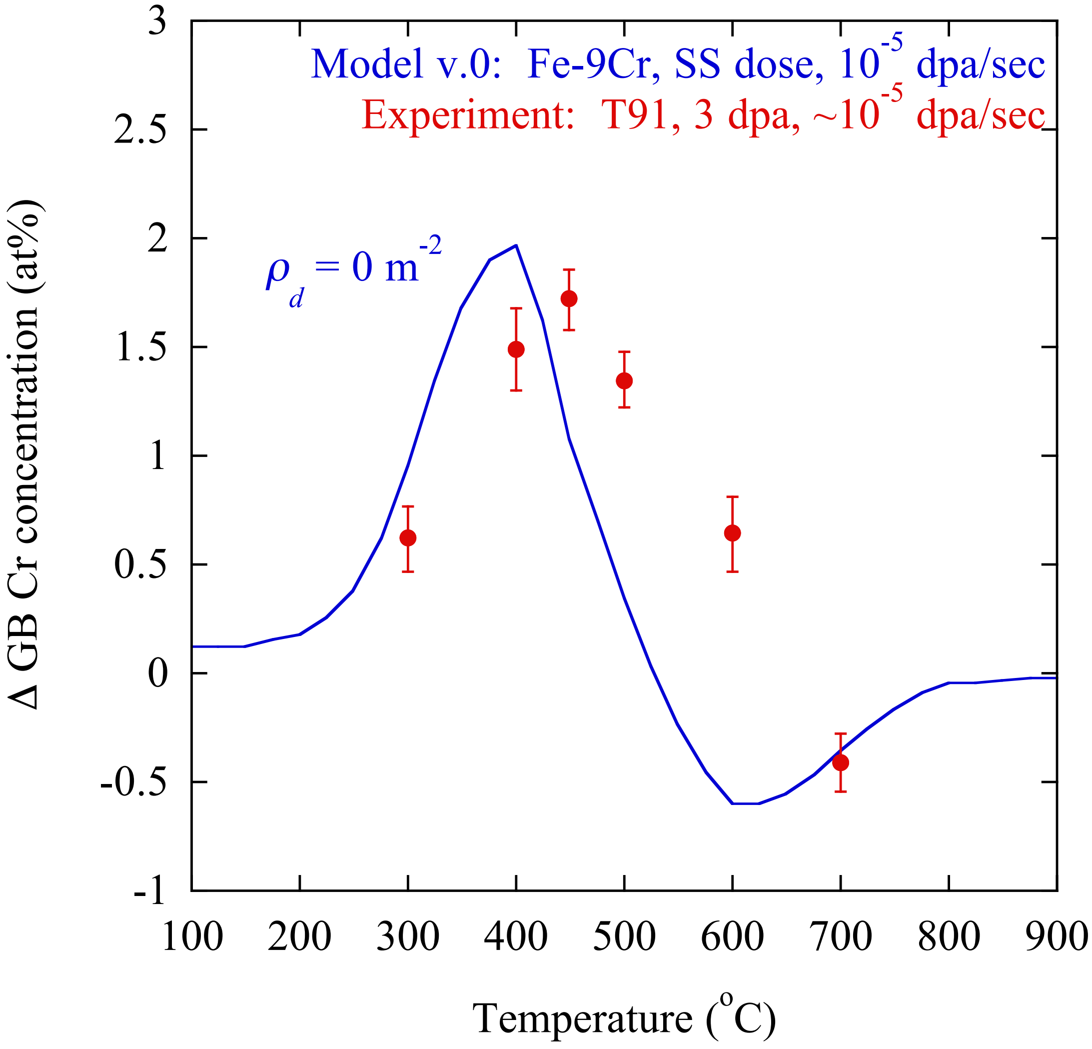

Figure 7.3. Comparison of temperature dependence of Cr RIS between IK model calculation v.0 (Fe-9Cr, steady-state dose of 15 dpa, 10^{-5} dpa/sec, 0 m^{-2} dislocation density) and experimental measurements (T91, 3 dpa, ~10^{-5} dpa/sec).

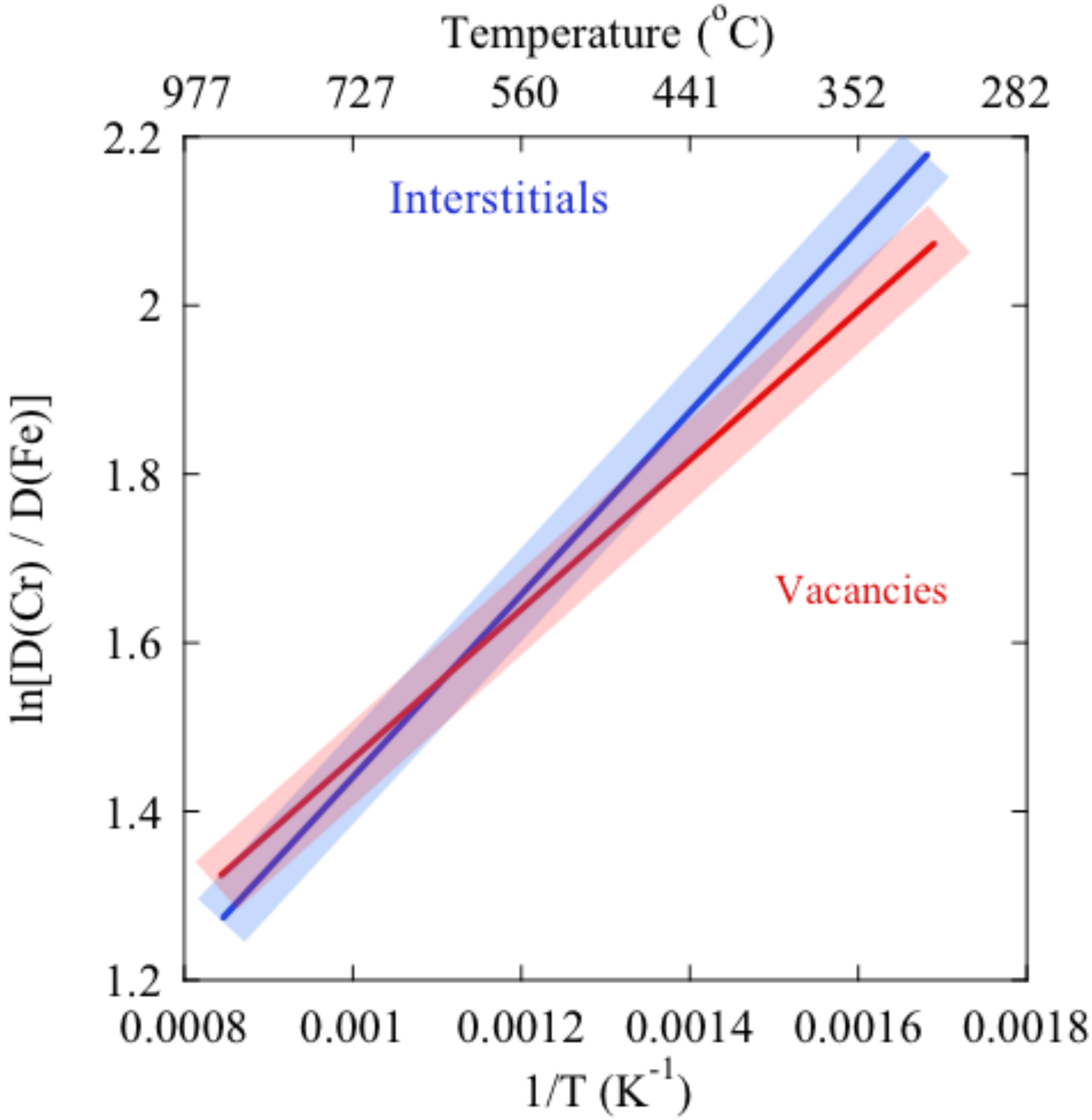

Figure 7.4. Uncertainty bands about diffusion coefficient ratios.

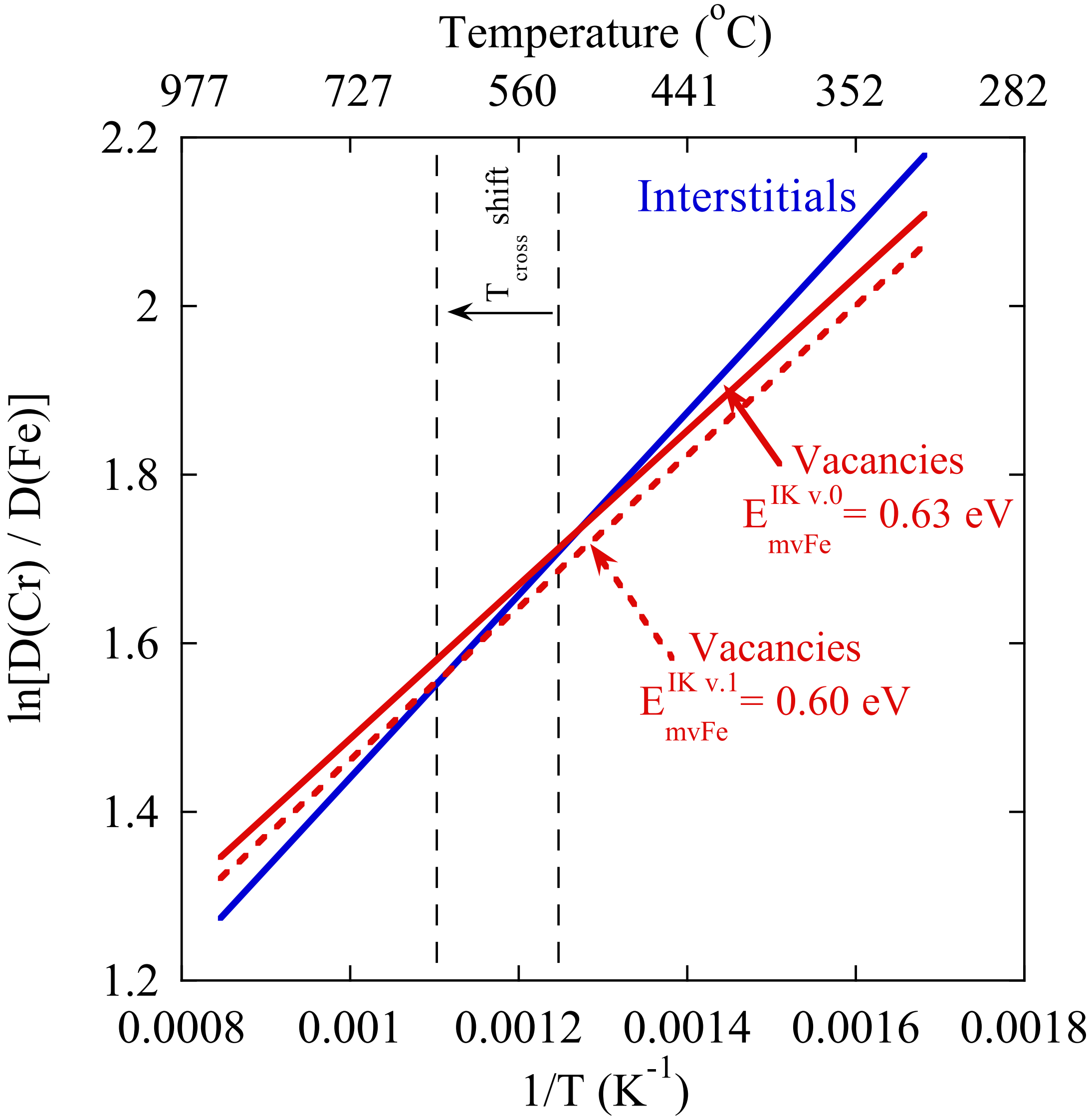

Figure 7.5. Effect of migration energy variations on the Fe:Cr vacancy and interstitial diffusion coefficient ratios for F-M alloys.

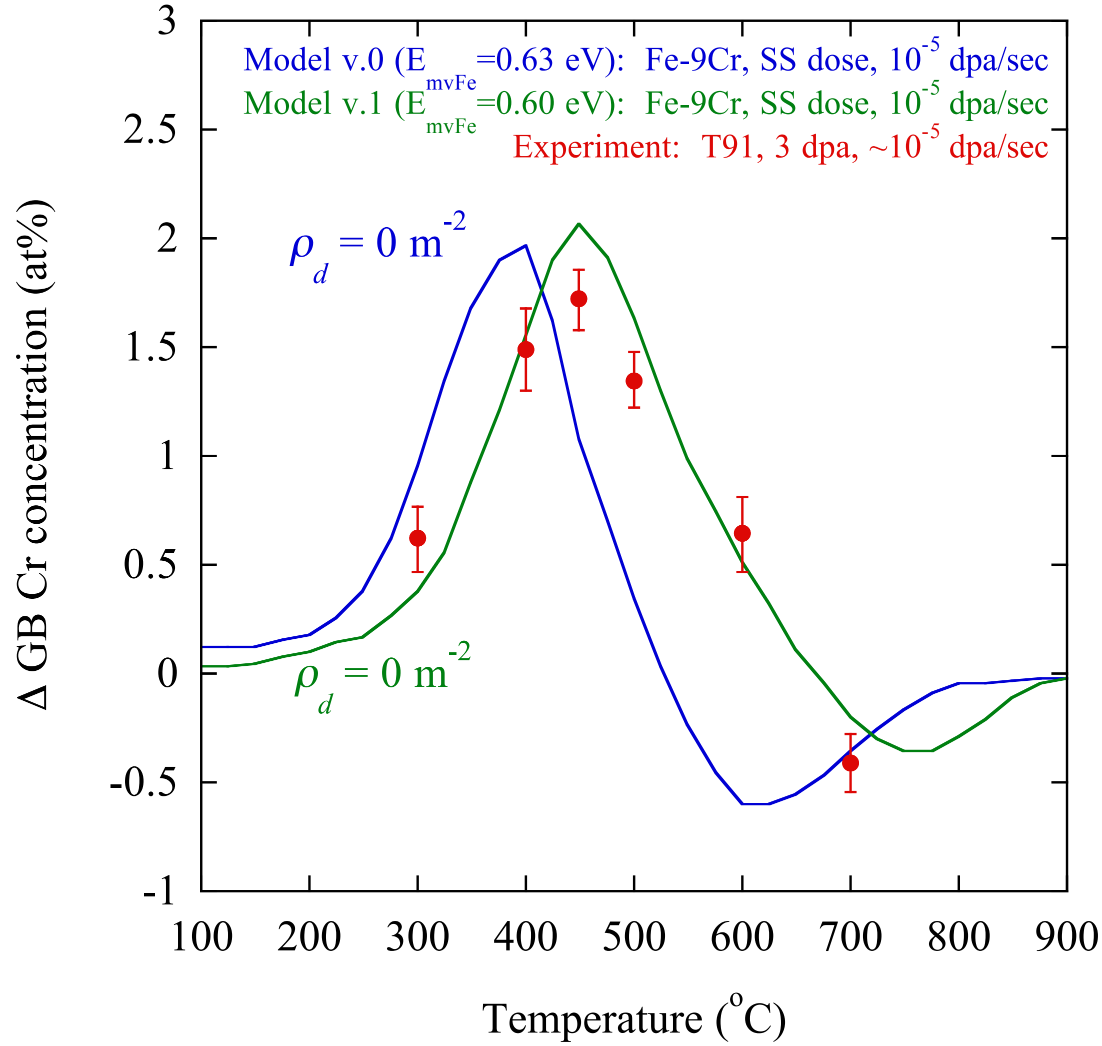

Figure 7.6. Comparison of temperature dependence of Cr RIS between IK model calculation v.0 and v.1 (Fe-9Cr, steady-state dose of 15 dpa, 10^{-5} dpa/sec, 0 m^{-2} dislocation density) and experimental measurements (T91, 3 dpa, ~10^{-5} dpa/sec). Difference between IK v.0 and v.1 is that Fe vacancy migration energy value is changed from 0.63 eV to 0.60 eV, respectively.

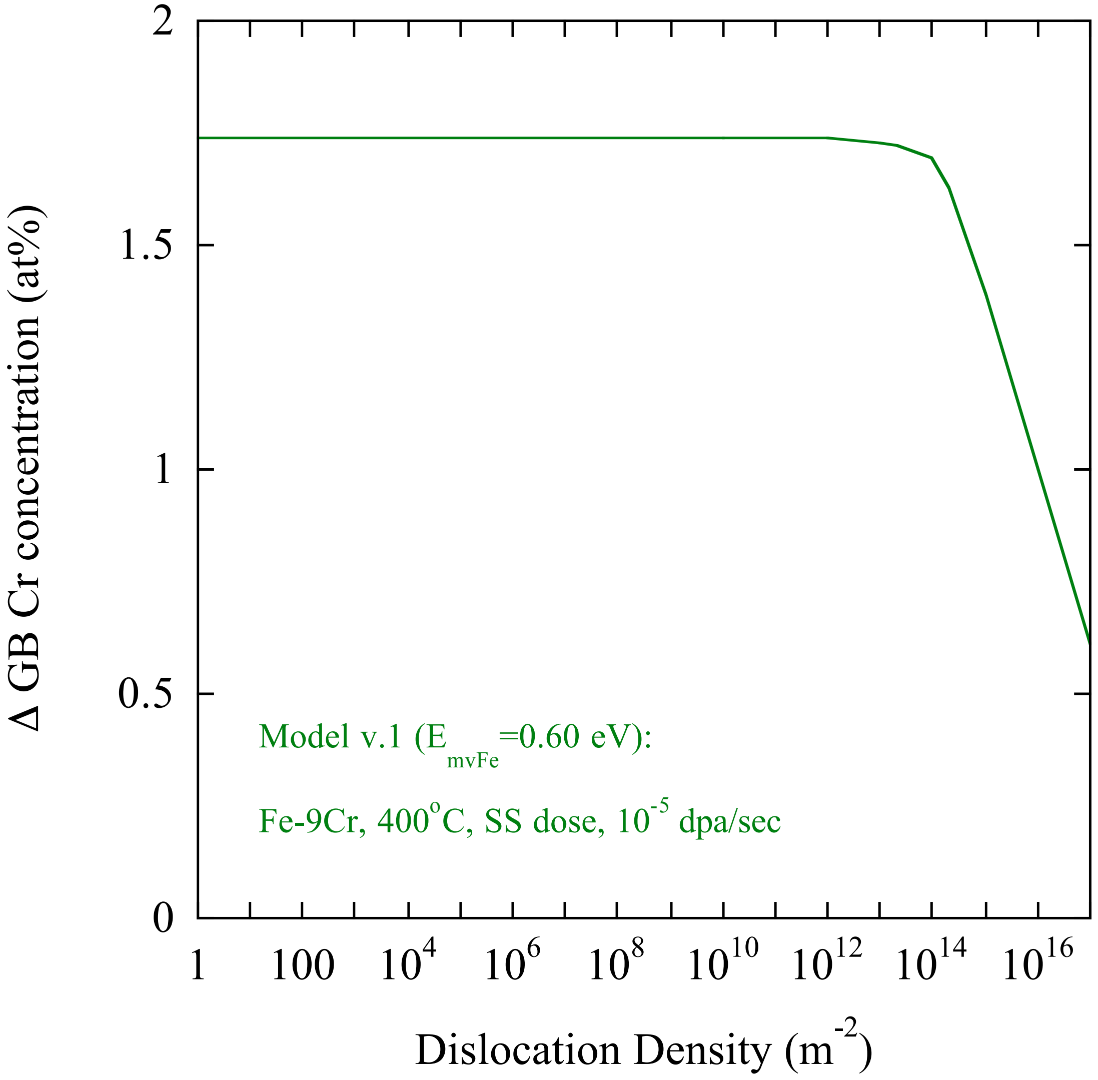

Figure 7.7. Effect of sink density on Cr RIS calculated by IK model v.1 (Fe-9Cr, 400°C, steady-state dose of 15 dpa, 10^{-5} dpa/sec, 0 m^{-2} dislocation density).

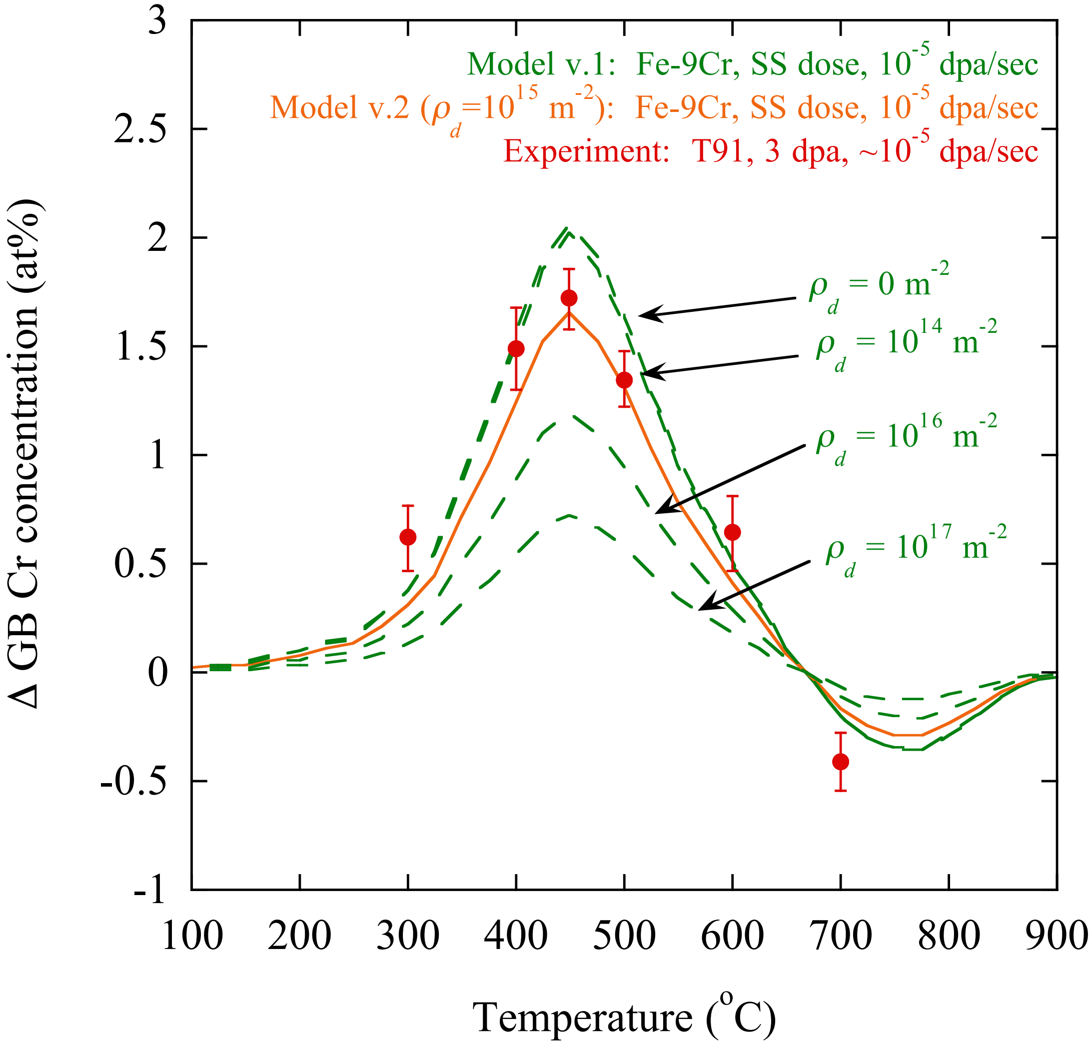

Figure 7.8. Effect of sink density on temperature dependence of Cr RIS, comparison between IK model prediction v.1 and v.2 (Fe-9Cr, steady-state dose of 15 dpa, 10^{-5} dpa/sec) and experimental measurements (T91, 3 dpa, ~10^{-5} dpa/sec). Difference between IK model v.1 and v.2 is dislocation density.

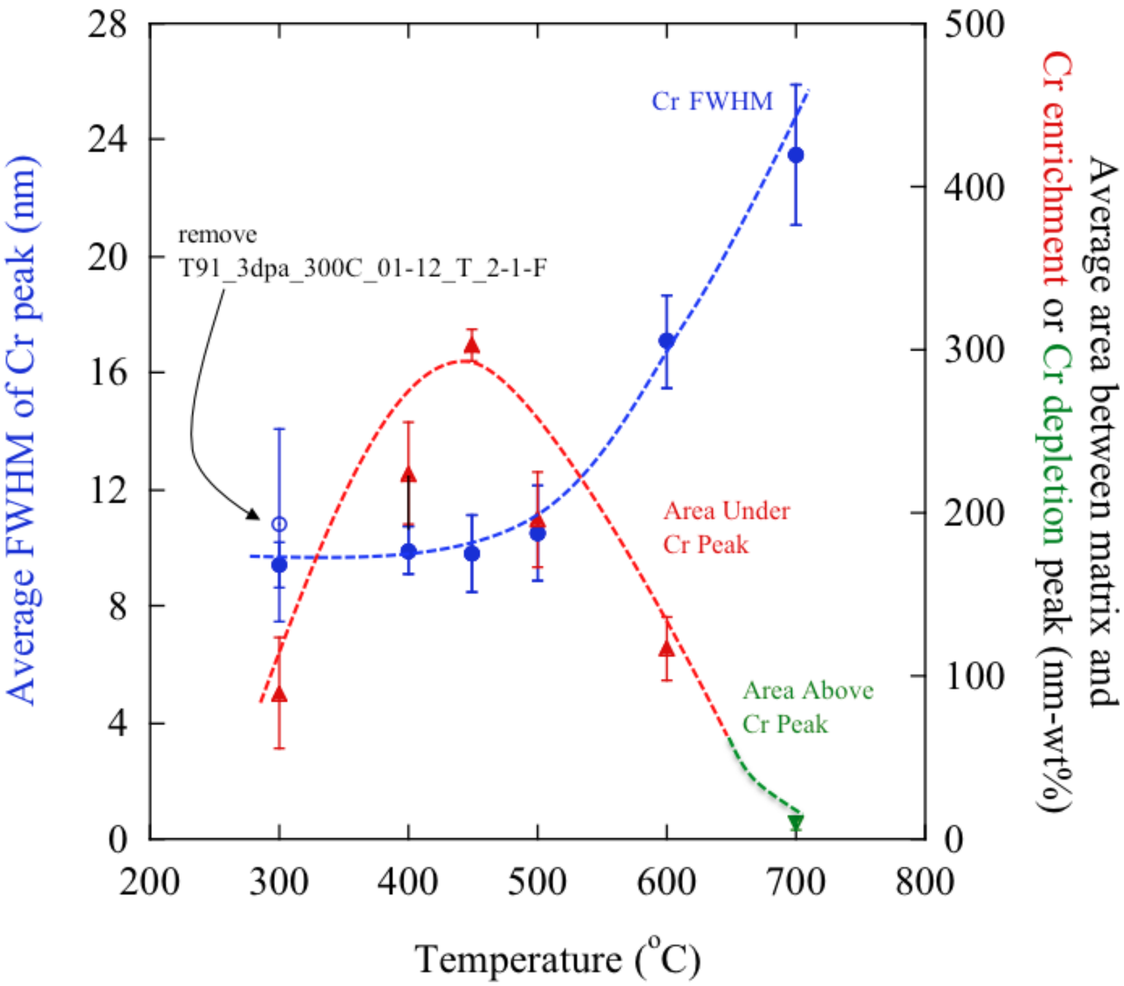

Figure 7.9. Temperature dependence of area under Cr enrichment peak and FWHM of Cr peak.

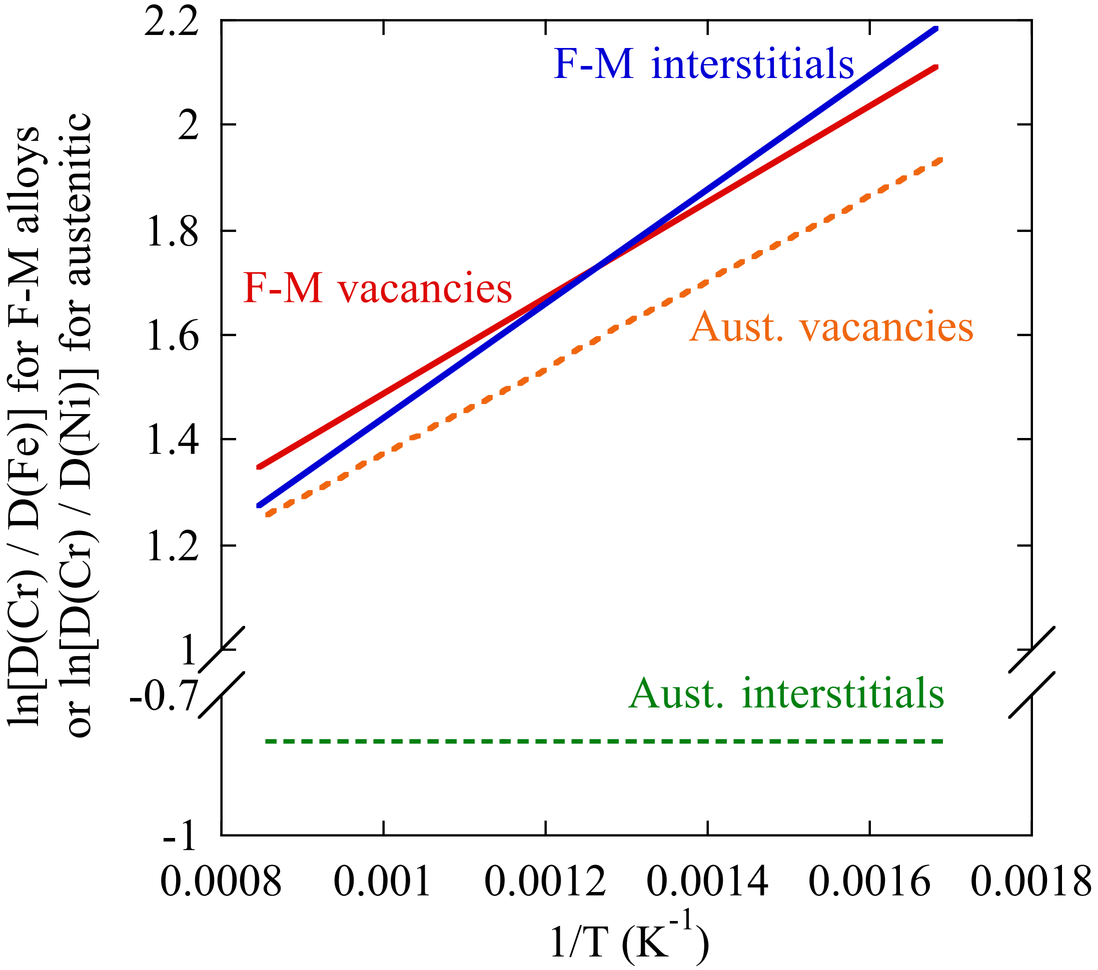

Figure 7.10. Vacancy and interstitial diffusion coefficient ratios for F-M alloys (Cr to Fe ratio) as compared to that for austenitic alloys (Cr to Ni ratio).

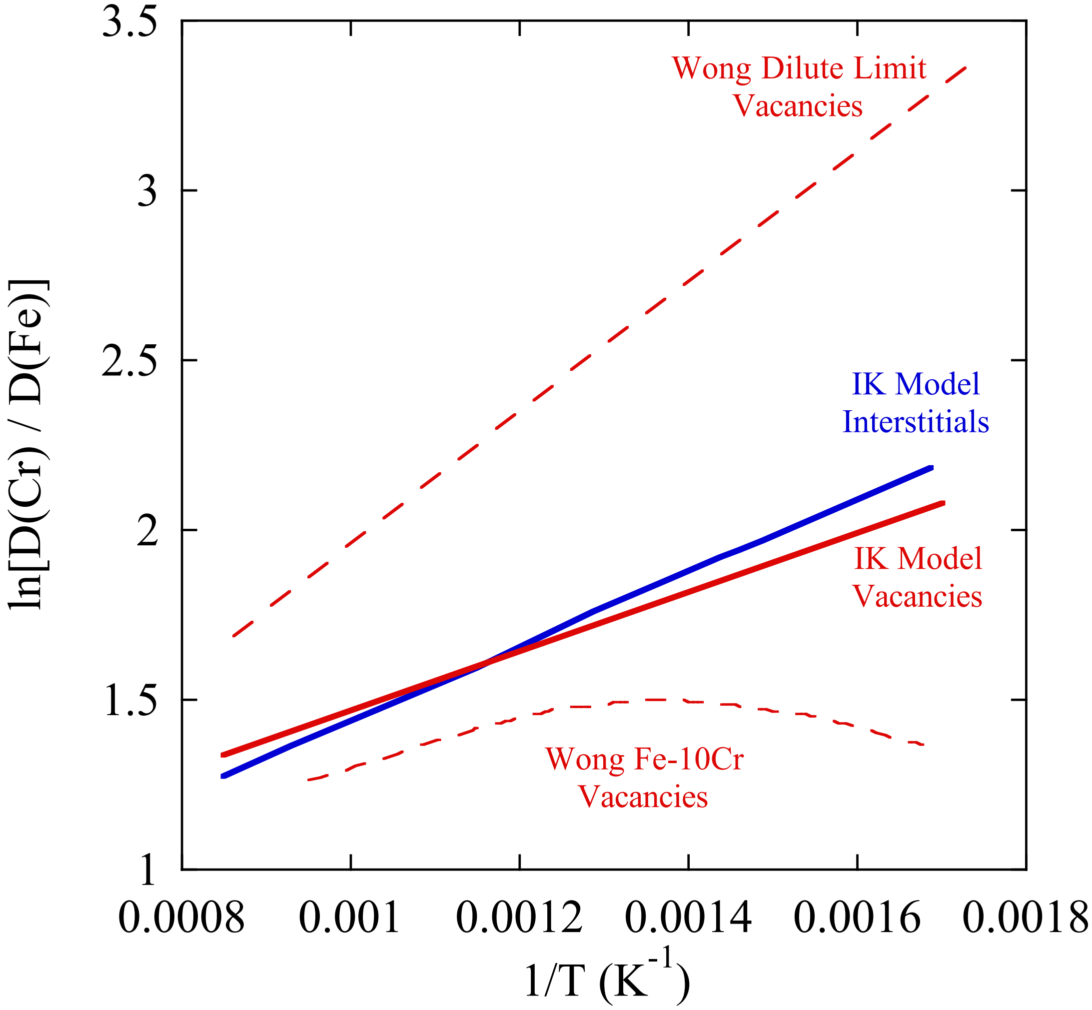

Figure 7.11. Diffusion coefficient ratio of Cr to Fe for vacancies, used in the IK model, compared to those calculated by Wong, *et al*. [54] for dilute Fe-Cr and Fe-10Cr.

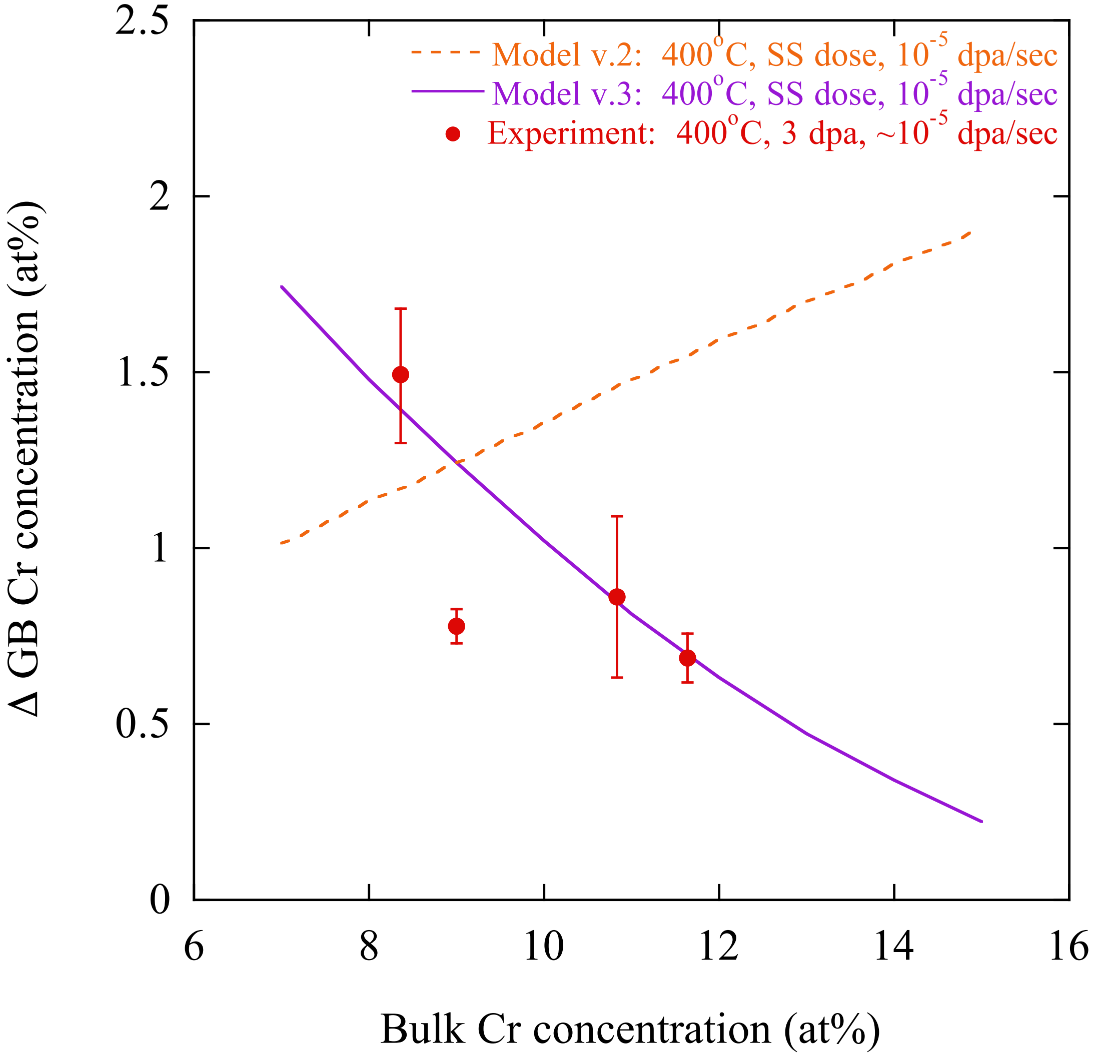

Figure 7.12. Comparison of composition dependence of Cr RIS between IK model v.2 and v.3 (range of alloys from Fe-7Cr through Fe-15Cr, 400°C, steady-state dose, 10^{-5} dpa/sec) and experimental measurements. Difference between v.2 and v.3 is the inclusion of composition-dependent interstitial migration energies in the latter.

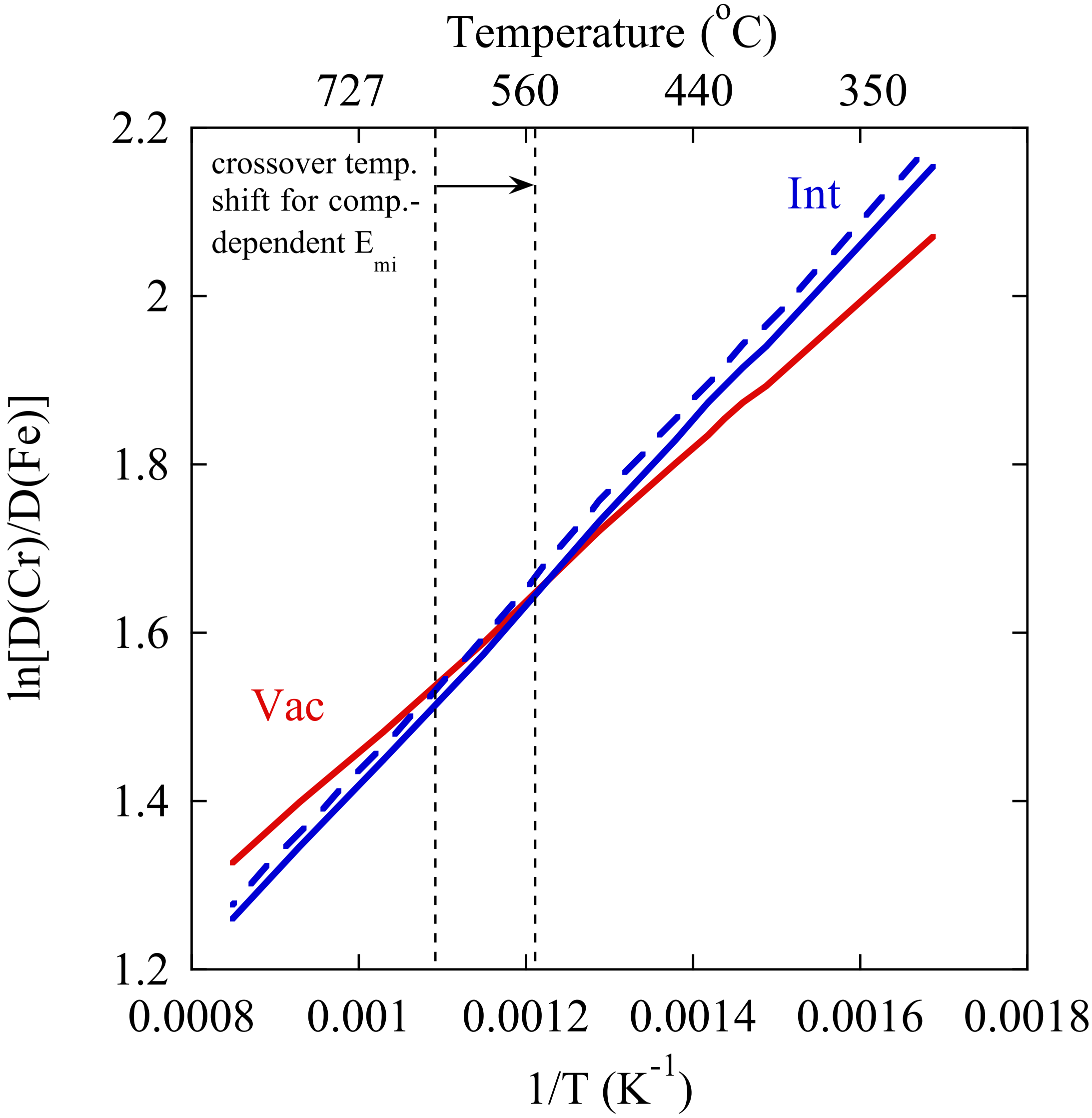

Figure 7.13. The effect of composition-dependent interstitial migration energies on the Cr to Fe interstitial diffusion coefficient ratio for 11-12 wt% Cr F-M (solid lines) compared to that for 9 wt% Cr (dashed line); vacancy diffusion coefficient ratio is not affected by composition-dependent interstitial migration energies.

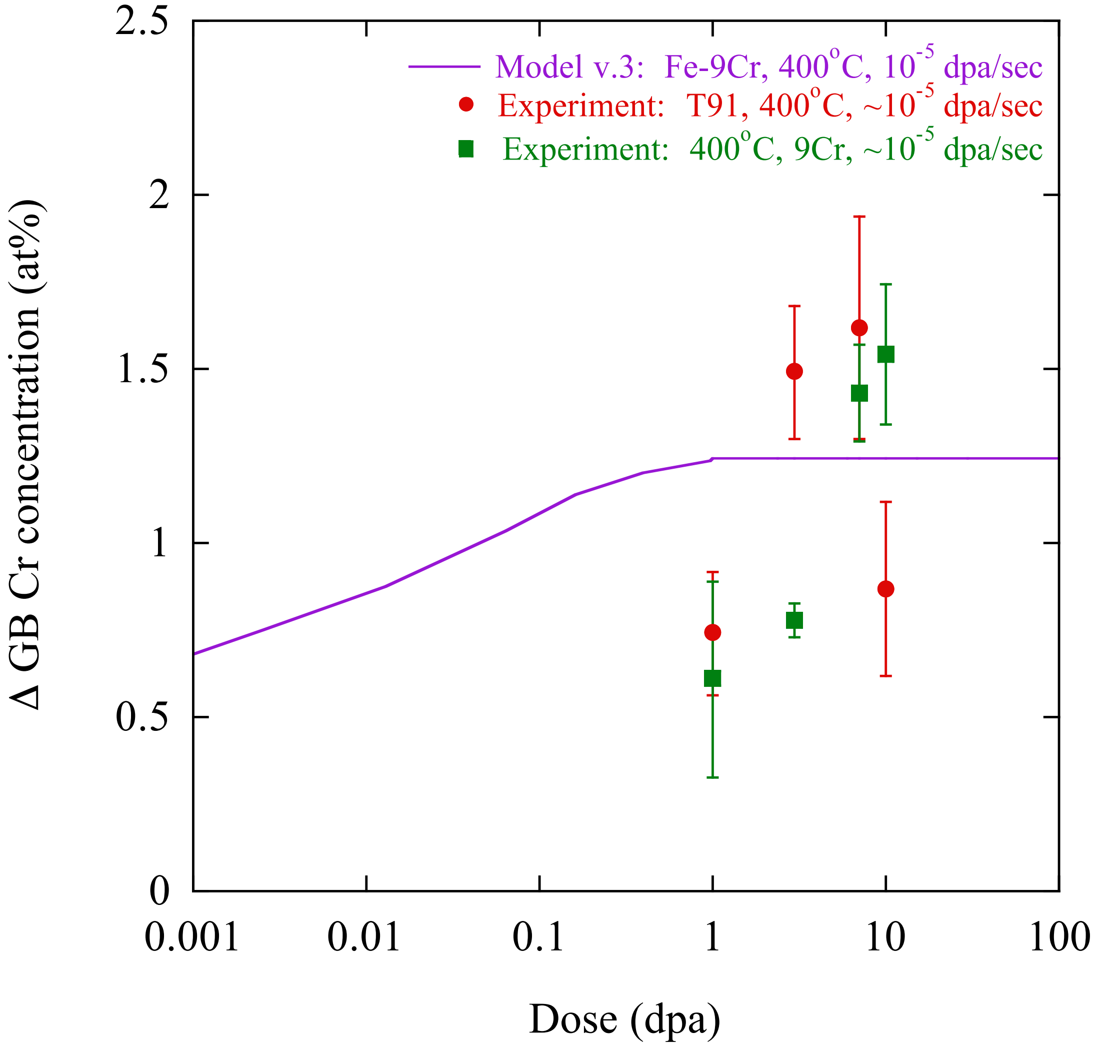

Figure 7.14. Comparison of dose dependence of Cr RIS between IK model v.3 (Fe-9Cr, 400°C, 10^{-5} dpa/sec) and experimental measurements (T91 and 9Cr model alloy, 400°C, ~10^{-5} dpa/sec).

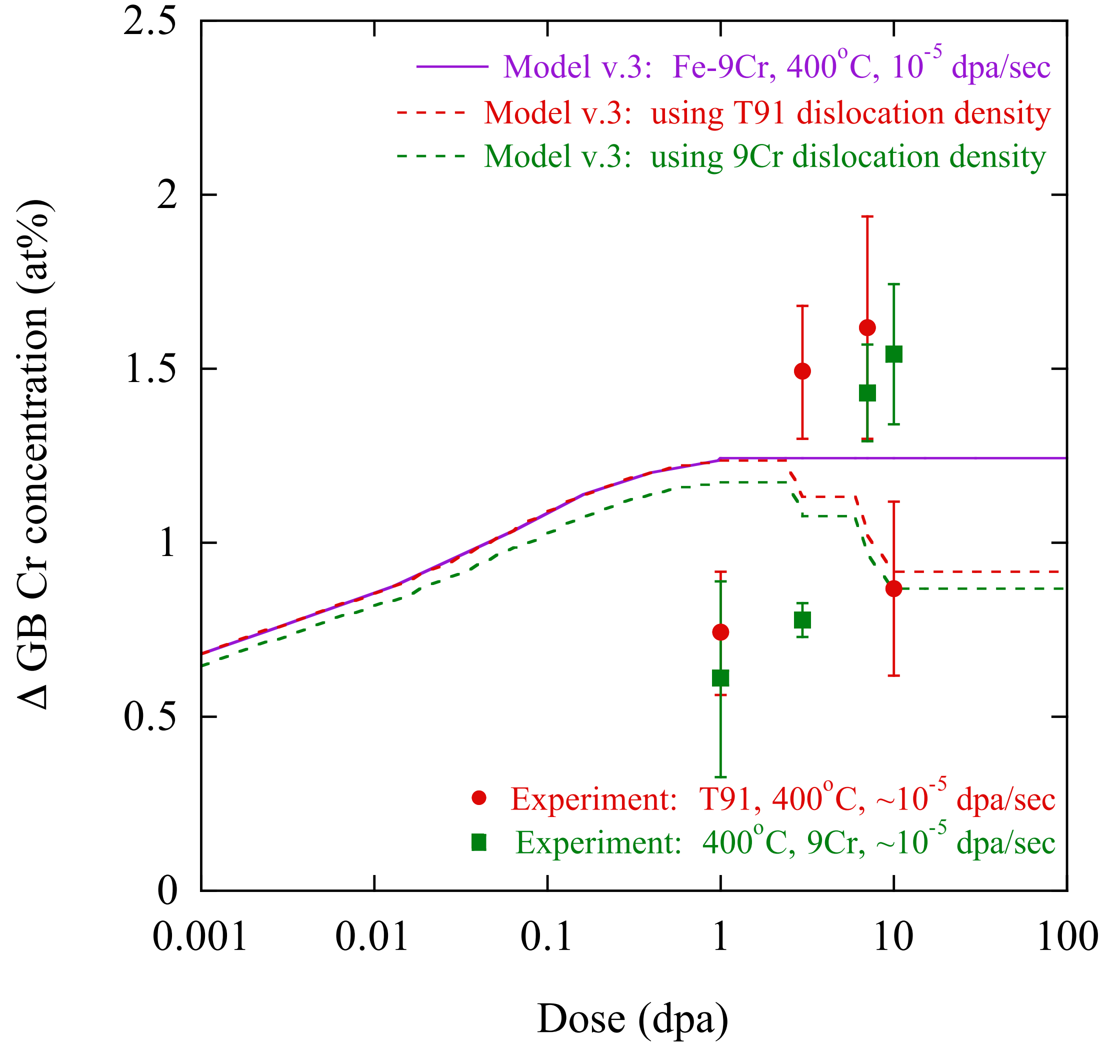

Figure 7.15. Comparison of dose dependence of Cr RIS between IK model v.3 and experimental measurements, when dose-dependent dislocation densities from Tables 5.30-5.31 are used in the IK model.

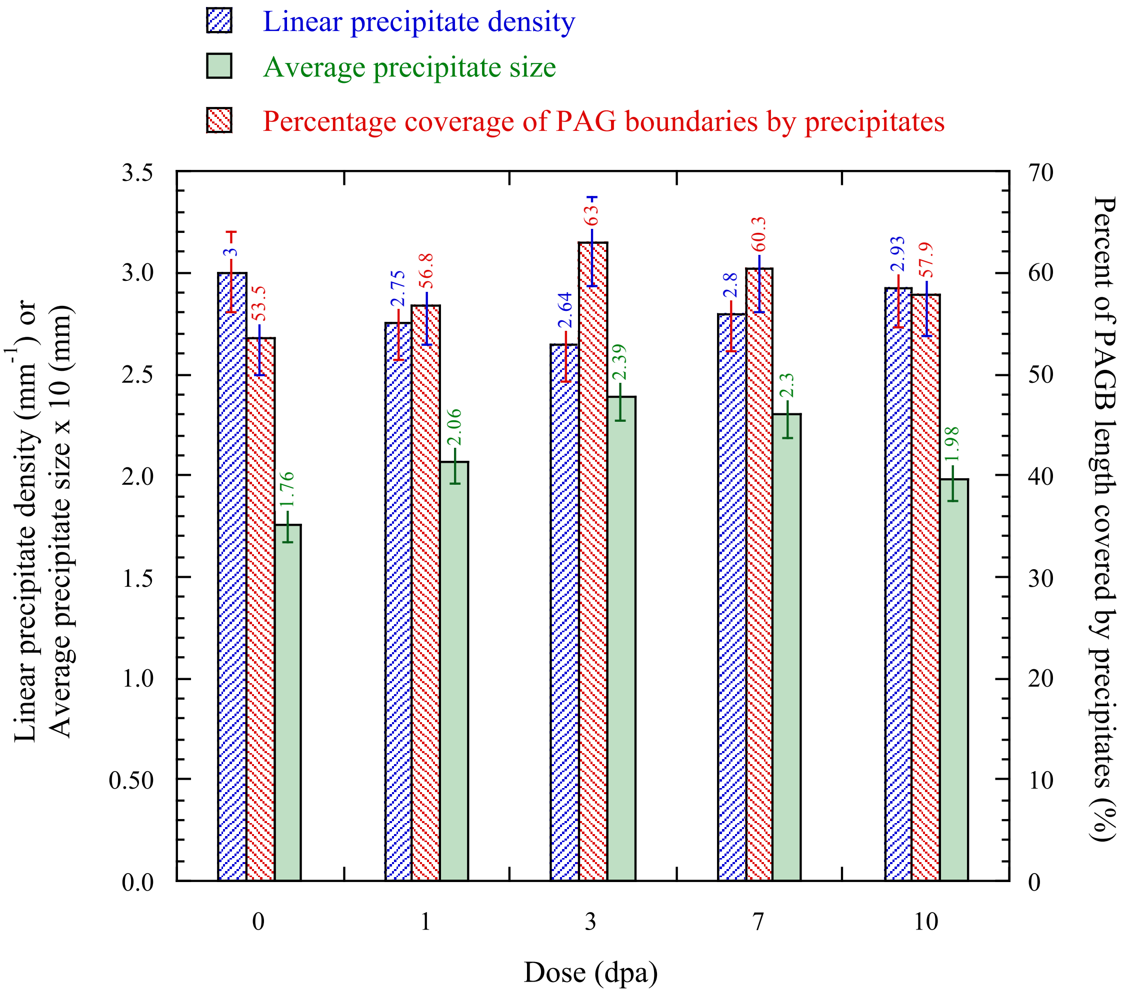

Figure 7.16. Dose dependence of linear density, average size, and percent coverage of precipitates located on PAGBs in T91 irradiated at 400°C, from [143].

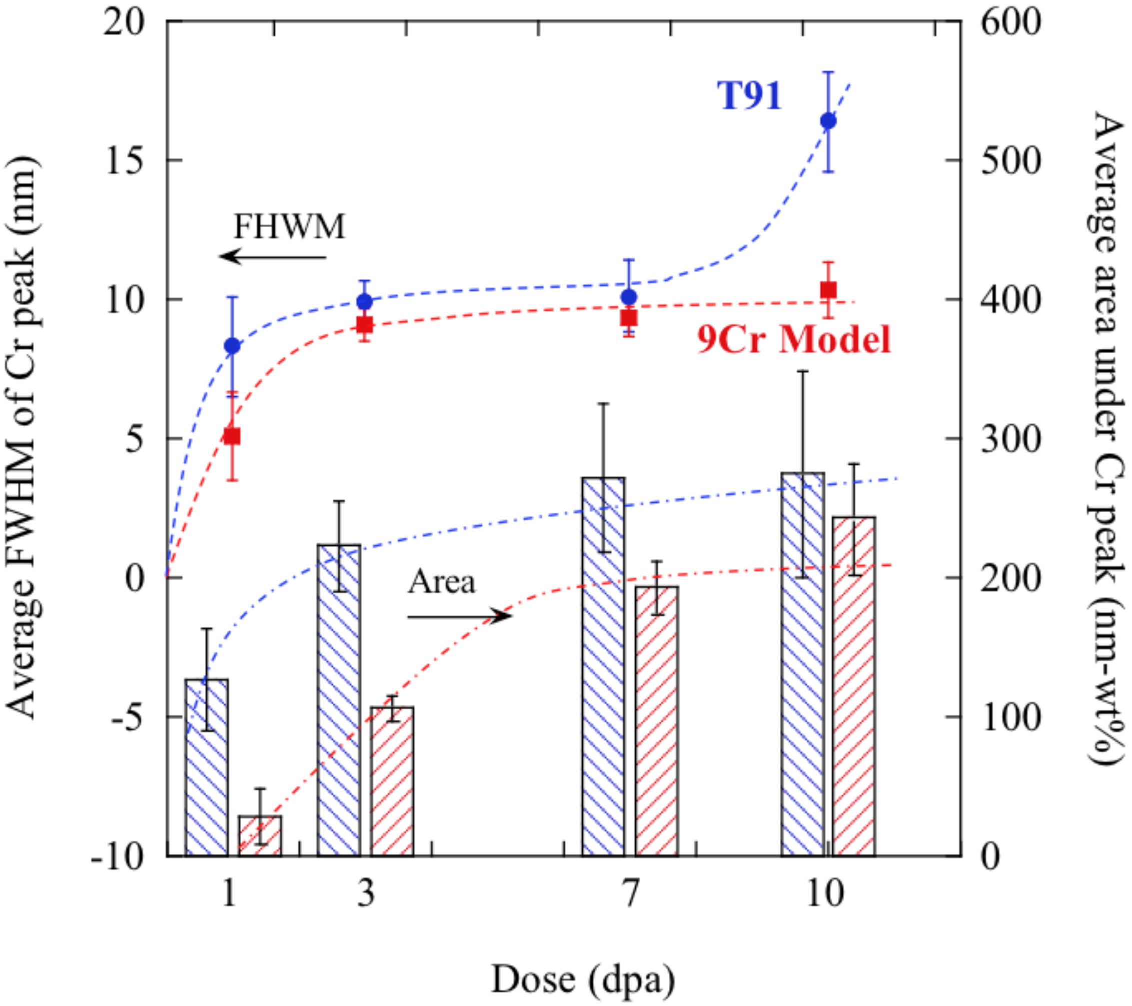

Figure 7.17. Dose dependence of area under Cr enrichment peak and FWHM of Cr peak.

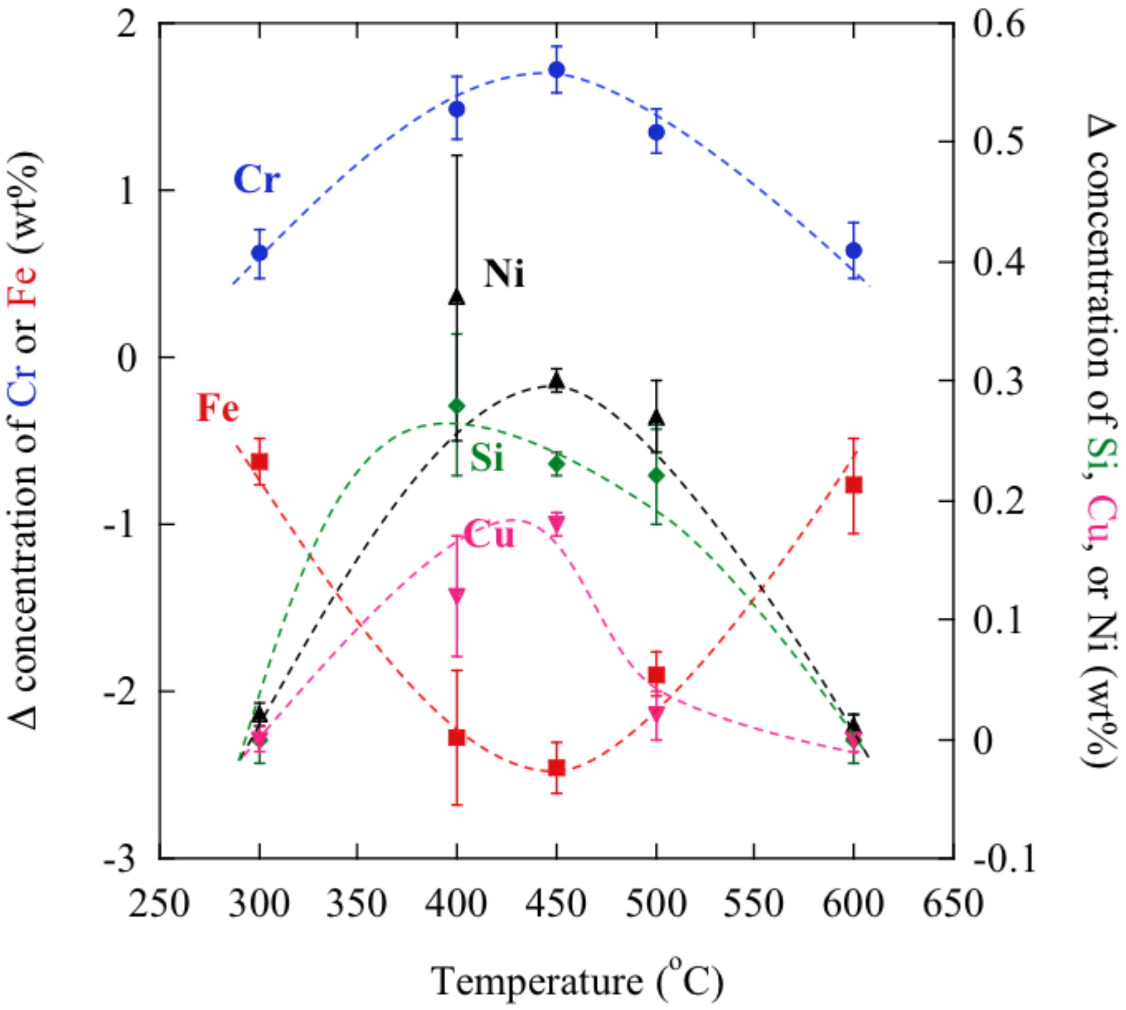

Figure 7.18. Temperature dependence of Cr, Fe, Si, Ni, and Cu RIS in T91 irradiated to 3 dpa with 2.0 MeV protons at ~10^{-5} dpa/sec.

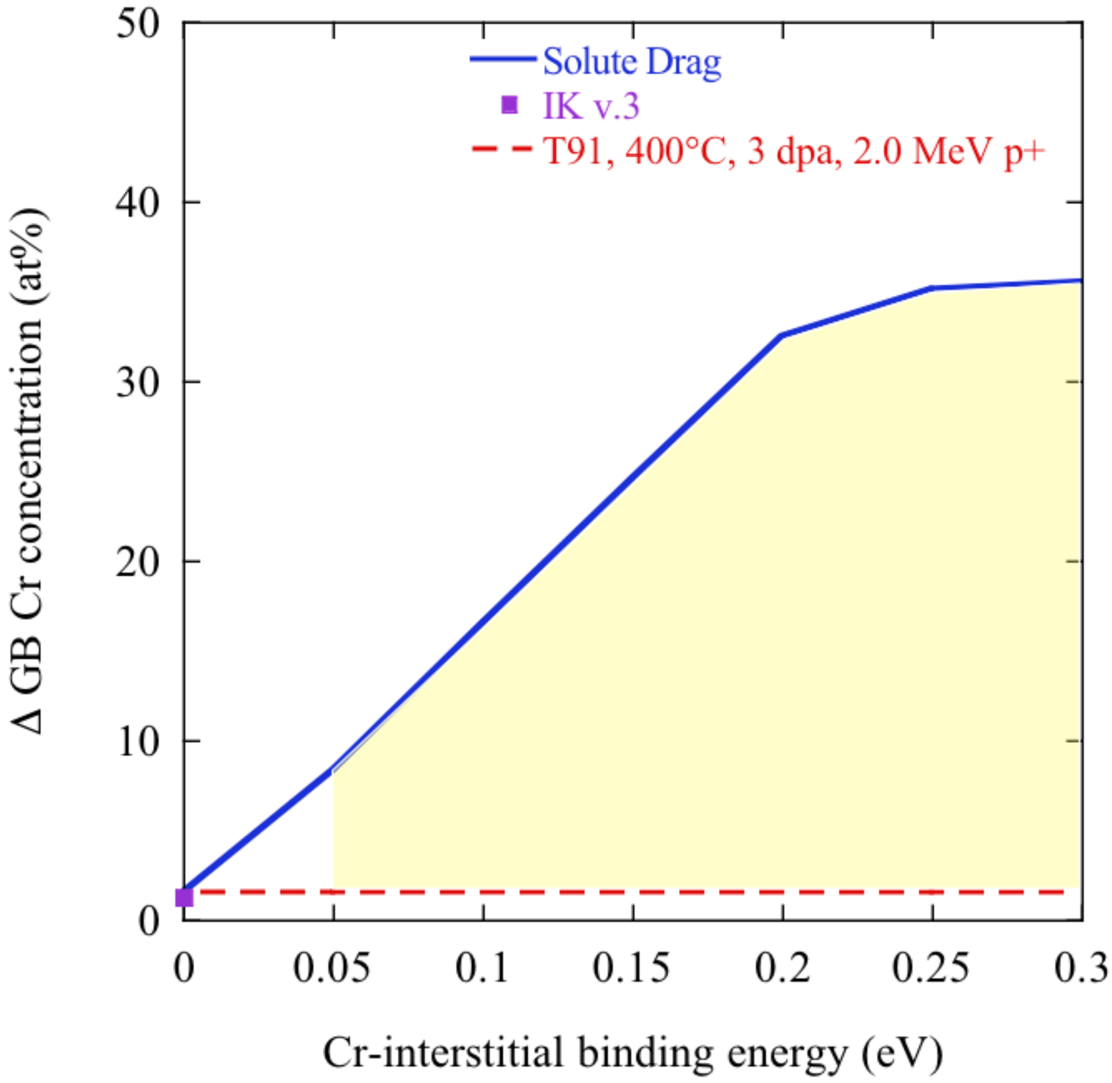

Figure 7.19. Solute drag predictions for Cr RIS as a function of Cr-interstitial binding energy, shaded region indicates known range of Cr-interstitial binding energy values.

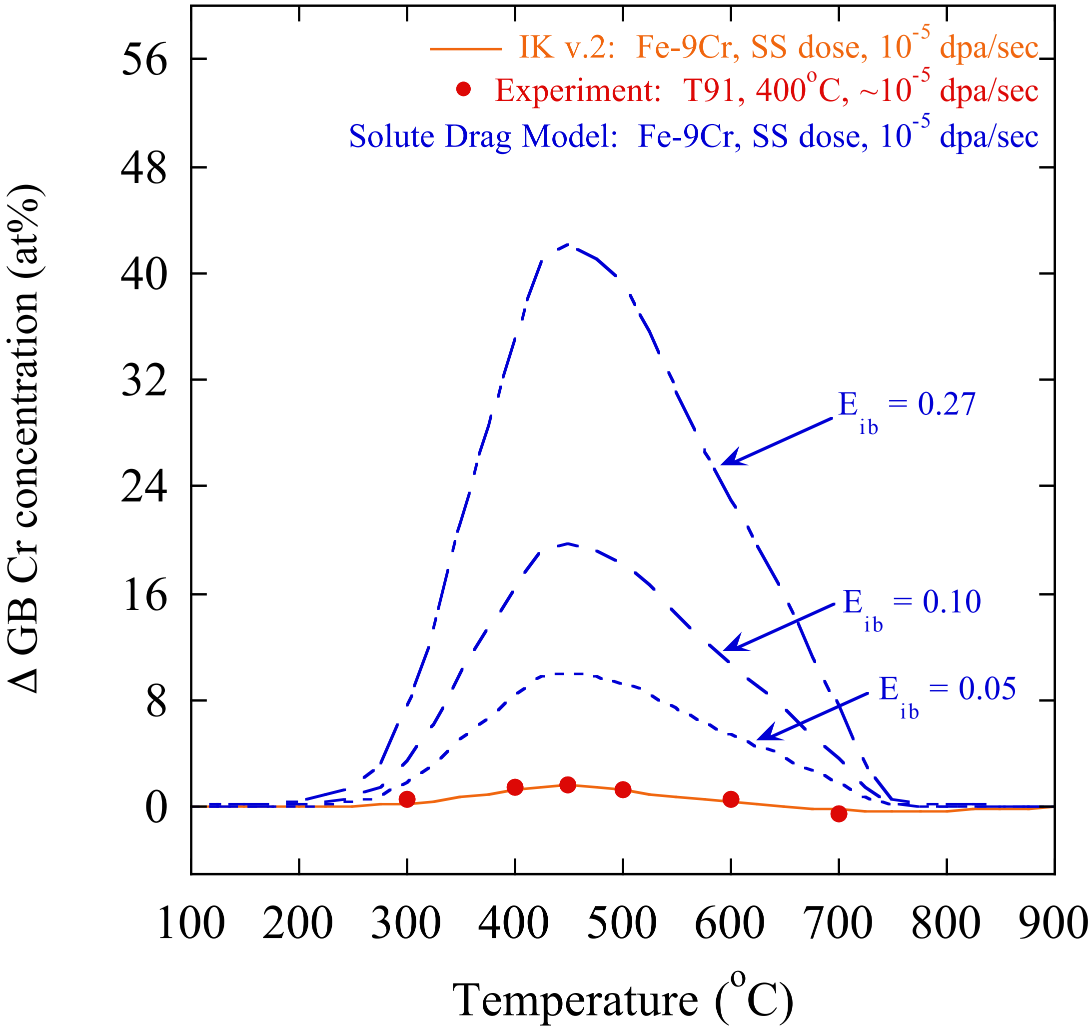

Figure 7.20. Temperature dependence of Cr RIS calculated by solute drag model, for three different interstitial binding energies, as compared to experimental measurements and IK model calculations.

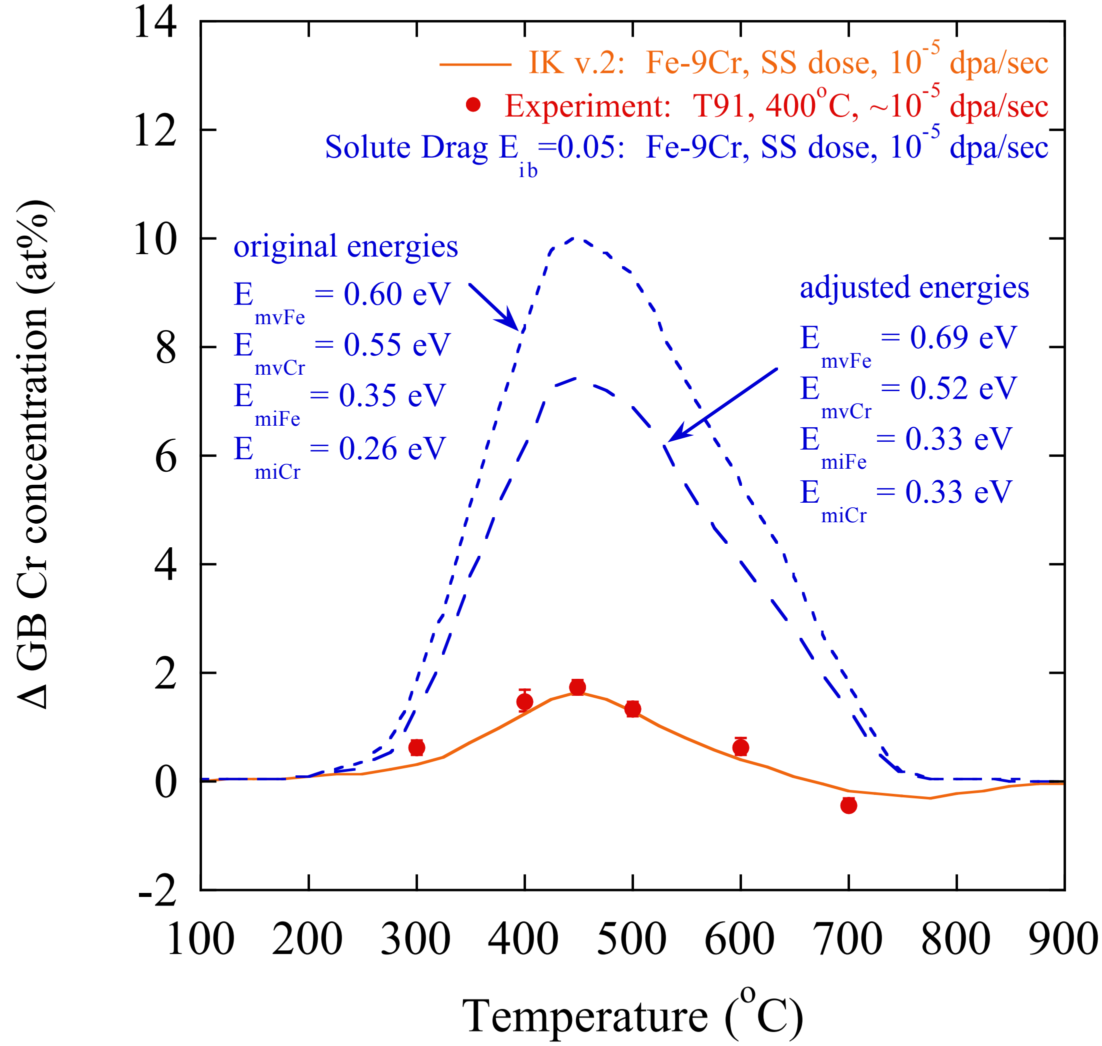

Figure 7.21. Effect of adjusting solute-defect migration energies on the temperature dependence of Cr RIS calculated by the solute drag model with interstitial binding energy 0.05 eV.

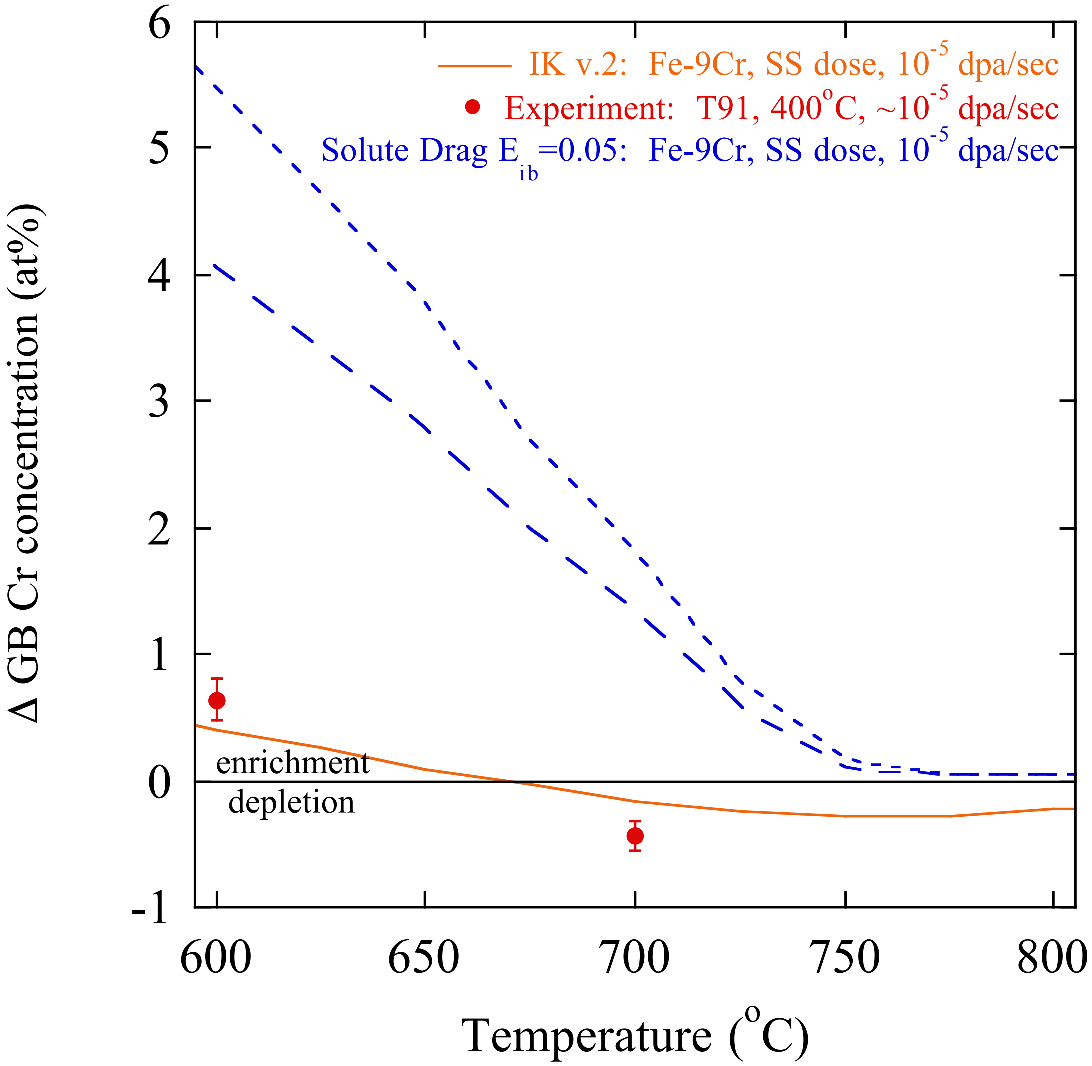

Figure 7.22. Zoomed in view of >600°C region of previous figure (Figure 7.21), illustrating that the solute-interstitial drag mechanism cannot calculate a crossover from Cr enrichment to Cr depletion.

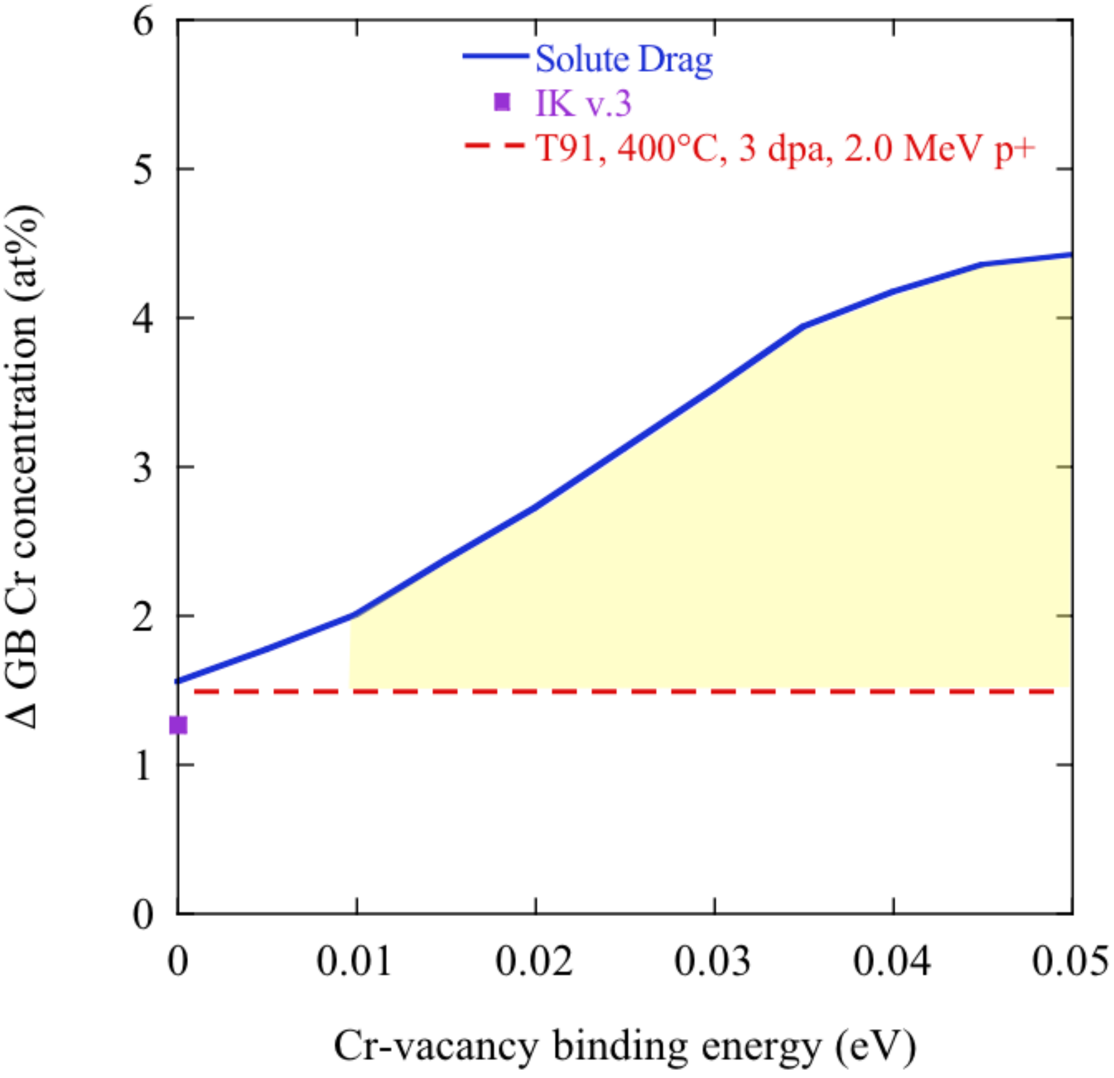

Figure 7.23. Solute drag predictions for Cr RIS as a function of Cr-vacancy binding energy.

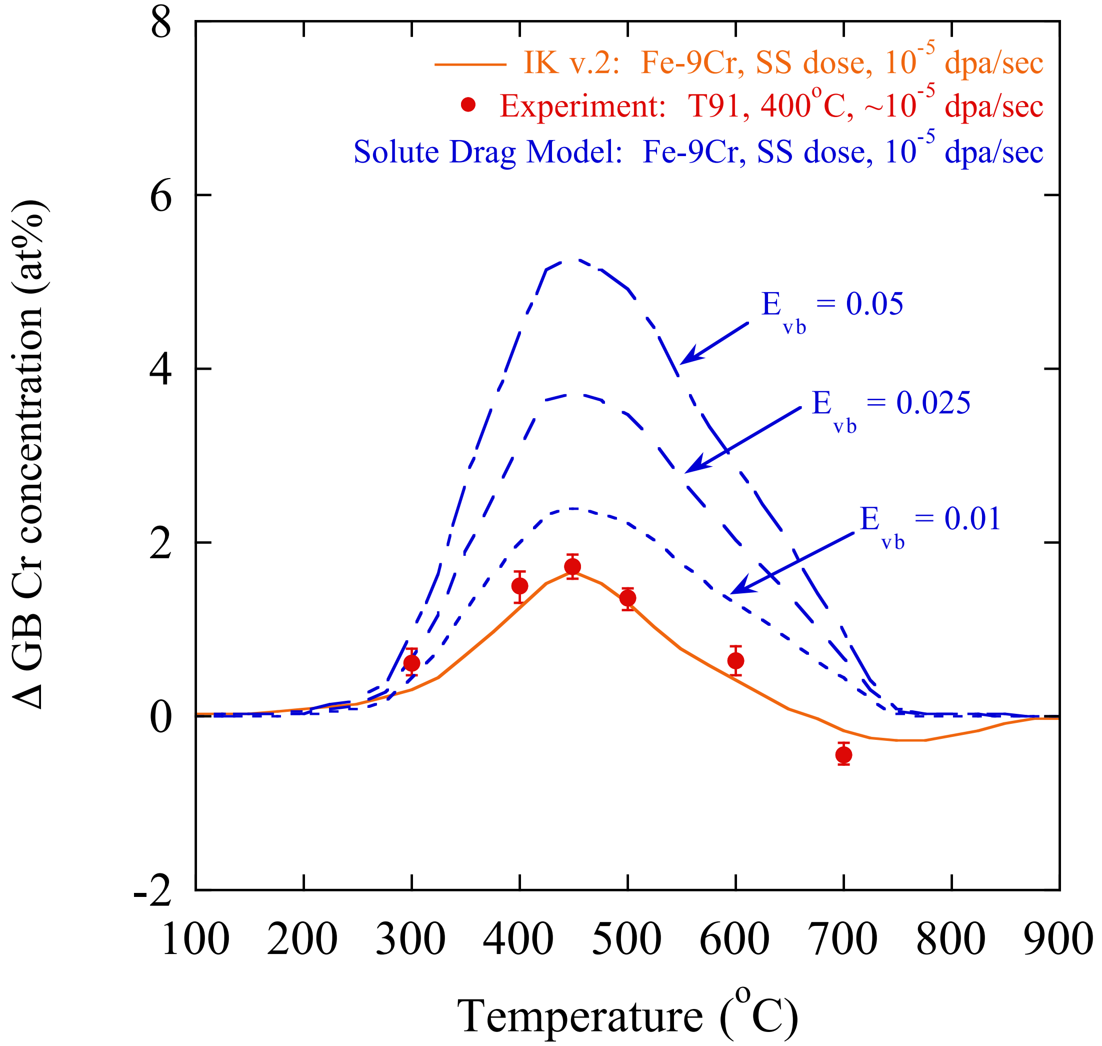

Figure 7.24. Temperature dependence of Cr RIS calculated by solute drag model, for three different vacnacy binding energies, as compared to experimental measurements and IK model calculations.

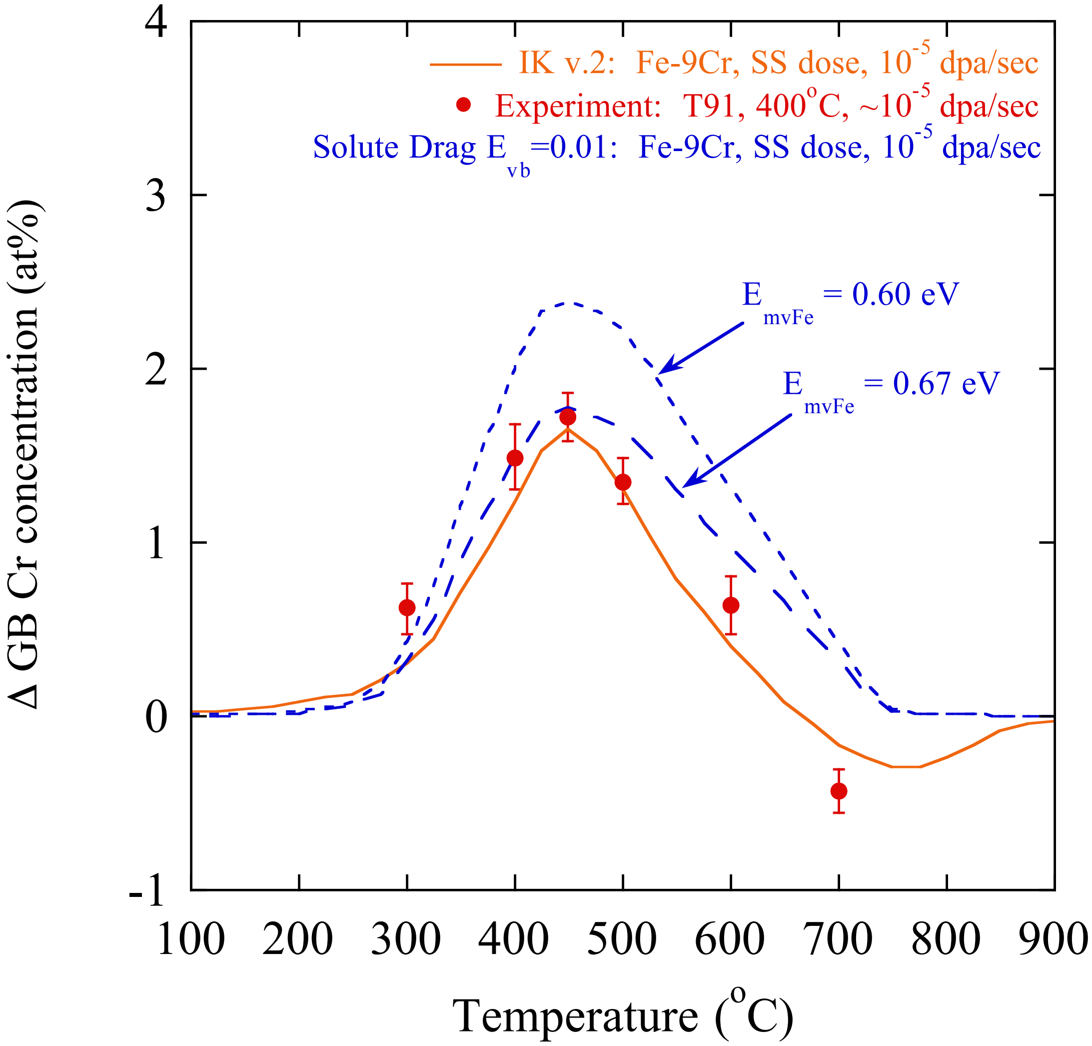

Figure 7.25. Effect of adjusting Fe vacancy migration energy on the temperature dependence of Cr RIS calculated by the solute drag model with vacancy binding energy of -0.002 eV.

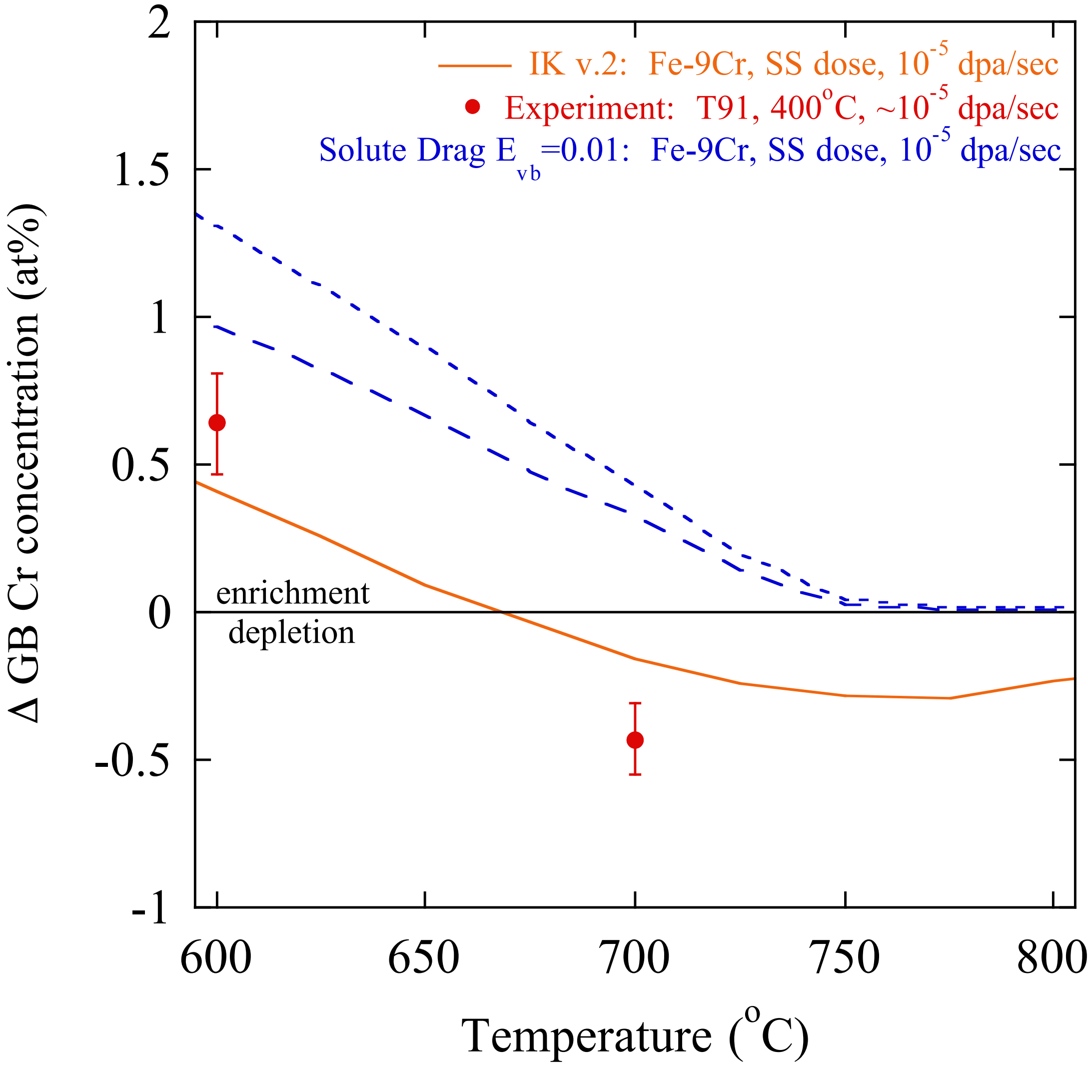

Figure 7.26. Zoomed in view of >600°C region of previous figure (Figure 7.25), illustrating that the solute-vacancy drag mechanism cannot calculate a crossover from Cr enrichment to Cr depletion

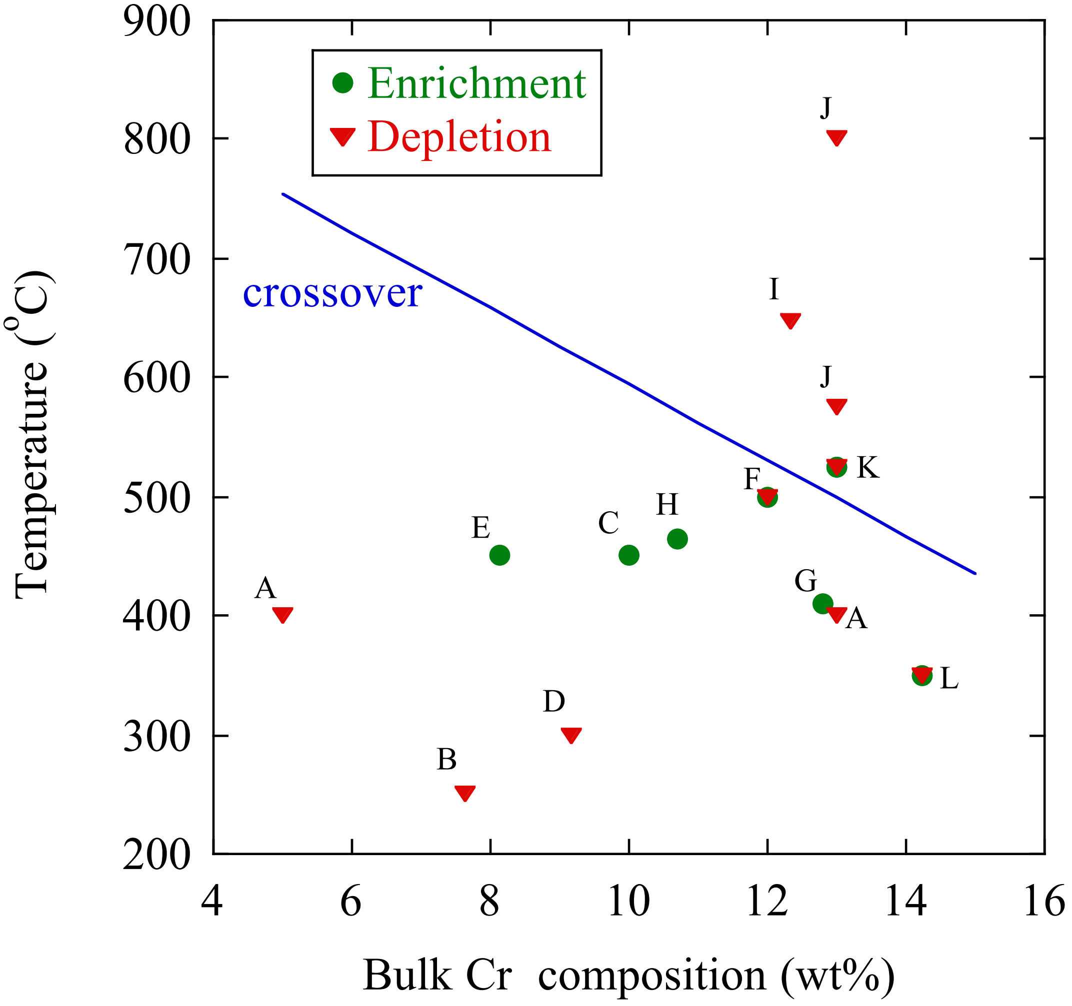

A) Takahashi, *et al.*, JNM 103 (1981) 1415.
B) Schaeublin, *et al.*, JNM 351 (1998) 1350.
C) Kato, *et al.*, JNM 179 (1991) 623.
D) Lu, *et al.*, JNM 351 (2006) 155.
E) Gupta, *et al.*, JNM 351 (2006) 162.
F) Marquis, *et al.*, JNM 417 (2011) 257.
G) Clausing, *et al.*, JNM 141 (1986) 978.
H) Little, *et al.*, Mat Sci Forum 97 (1992) 323.
I) Hamaguchi, *et al.*, JNM 133 (1985) 636.
J) Neklyudov & Voyevodin, JNM 212 (1994) 39.
K) Ohnuki, *et al.*, JNM 103 (1981) 1121.
L) Marquis, *et al.*, JNM 413 (2011) 1.

Figure 7.27. Experimental measurements of the directions of Cr RIS in F-M alloys published in the literature, as compared to the crossover temperature calculated in this thesis.

CHAPTER 8 CONCLUSIONS & FUTURE WORK

This thesis has reached the following conclusions:

1) *Under most irradiation conditions, chromium enriches at grain boundaries in F-M alloys, and this observation can be explained by differences in solute-defect diffusion rates*. Consistent Cr enrichment has been observed in all four alloys studied in this work--T91, HCM12A, HT9, and a 9Cr model alloy—over a wide temperature range of 300-600°C, at doses of up to 10 dpa. Only one instance of Cr depletion has been observed, in T91 irradiated to 3 dpa at 700°C. Chromium RIS in F-M alloys occurs in small amounts; no more than 2.5 wt% Cr enrichment was ever recorded. These behaviors are in quite stark contrast to Cr RIS tendencies in austenitic steels, in which Cr depletion of up to 20 wt% has been routinely measured.

The inverse Kirkendall mechanism can explain the observed differences in Cr RIS between F-M and austenitic alloys. In austenitic alloys, the diffusion coefficient ratio of Cr to Ni for vacancies is greater than unity, while that for interstitials is less than unity, particularly in the temperature range of interest. The relative magnitude of these ratios mean that RIS in austenitic steels should be dominated by Cr transport via vacancies, resulting in Cr depletion. In addition, because the difference between the vacancy and interstitial diffusion coefficients is rather large, the expected amount of RIS will also be large.

However, in F-M alloys, the diffusion coefficient ratios of Cr to Fe for vacancies and for interstitials are both greater than unity and are of almost identical magnitudes. This means that both vacancies and interstitials are causing Cr RIS, the vacancies causing depletion and the interstitials, enrichment. At any particular temperature, whichever diffusion coefficient ratio—that for vacancies, or that for interstitials—is greater will decide the direction of RIS. In most of the conditions studied in this thesis, the interstitial diffusion coefficient was greater than that for vacancies, causing the observed Cr enrichment. And since the vacancy and interstitial diffusion coefficients are similar in magnitude, the difference between them is small, so the expected amount of RIS will also be small.

2) *A "crossover" from Cr enrichment to Cr depletion occurs between 600°C and 700°C in alloy T91, and this provides further confirmation for the inverse Kirkendall mechanism of Cr RIS in F-M alloys*. In alloy T91 irradiated to 3 dpa, Cr enrichment is observed at 600°C, and Cr depletion at 700°C. The temperature interval in which the crossover occurs is consistent with the crossover predicted by the diffusion coefficient ratios of Cr to Fe for vacancies and for interstitials. As mentioned in the preceding paragraph, the diffusion coefficient ratios in F-M alloys are similar in magnitude. But small differences in their slopes cause the vacancy and interstitial diffusion coefficient ratios to cross one another near ~660°C. At temperatures below the crossover temperature, the diffusion coefficient ratio for interstitials exceeds that for vacancies, which can explain the observed Cr enrichment in T91 irradiated between 300°C and 600°C. But above the crossover temperature, the diffusion coefficient ratio for vacancies becomes greater than that for interstitials, which explains the observed Cr depletion in T91 at 700°C. The existence of a crossover behavior is particular to the F-M alloy system. The existence of a crossover between Cr enrichment and Cr depletion in F-M alloys provides support for the inverse Kirkenall mechanism.

3) *The amount of Cr enrichment decreases with increasing bulk Cr concentration, and this behavior can also be attributed to differences in diffusion rates between atomic species*. Chromium enrichment is measured in T91, HCM12A, HT9, and the 9Cr model alloy following 3 dpa irradiation at 400°C. The amount of Cr enrichment is observed to decrease as a function of increasing bulk Cr concentration. The inverse Kirkendall model calculates a consistent behavior, as long as Cr-composition-dependent interstitial migration energies for both Fe and Cr are input into the model. Composition-dependent interstitial migration energies are calculated for bulk Cr concentrations less than or greater than 9 wt% Cr; the migration energies for 9 wt% Cr are fixed at their original values.

The decreasing amount of Cr with increasing bulk Cr concentration, as measured in the 400°C experiment, can be explained by differences in atomic diffusion rates. When composition-dependent interstitial migration energies are used for alloys with bulk Cr concentration > 9 wt%, the diffusion coefficient ratio of Cr to Fe for interstitials decreases slightly in magnitude, causing two major effects. First, the predicted crossover temperature decreases, although Cr is still calculated to enrich at the experiment temperature of 400°C. Second, the Cr-to-Fe interstitial diffusion coefficient ratio moves closer to that of vacancies at 400°C. The difference between the two diffusion coefficient ratio lines becomes even smaller, and thus, the expected amount of Cr RIS should be even smaller than at lower bulk Cr concentrations.

4) *The experimentally observed Cr RIS behaviors cannot be attributed to the solute drag mechanism*. When the solute drag mechanism is incorporated into the IK model using a positive Cr-interstitial binding energy, unreasonably large amounts of Cr enrichment are calculated. Conversely, when the solute drag mechanism implements a positive Cr-vacancy binding energy, unreasonable quantities of Cr depletion are calculated. Clearly, the solute drag mechanism results in Cr RIS that is entirely inconsistent with experimental measurements

6) *The behavior of Cr RIS—and thus, of Fe RIS, as well—in F-M alloys is largely consistent with the inverse Kirkendall mechanism and not consistent with the solute drag mechanism, supporting IK as the mechanism controlling Cr RIS in commercial F-M alloys.*

7) *Minor elements such as Si, Ni, and Cu, segregate by a different, yet undetermined mechanism, than that by which Cr and Fe segregate*. RIS of minor elements exhibit a different temperature dependence than does RIS of Cr and Fe. The temperature range over which the minor elements segregate is more limited (400-500°C) than that over which Cr and Fe segregate (at least 300-700°C). However, the driving mechanism of minor element RIS has not been determined.

While some notable conclusions have been reached in this work, there remain some unanswered questions that deserve future attention:

1) *There remain unresolved issues with the dose dependence of Cr RIS, especially with respect to the interrelationship of RIS and microstructure*. There are

significant differences in the kinetics of RIS between the IK model and experiment, particularly regarding the onset of RIS and the onset of steady-state RIS. It is theorized that the model-experiment difference in the onset dose may be due to a microstructurally-related incubation period in the experimental steels. It is also theorized that the model-experiment difference in the steady-state RIS behavior is due to microstructural evolution. Future work could more closely study the microstructural issues and kinetics of RIS in the IK mechanism. In addition, studying RIS at the boundaries of microstructural features such as dislocation loops and precipitates, may offer further insight into the RIS-microstructure relationship.

2) *The RIS mechanism of minor elements in F-M alloys has yet to be determined.* Work in this thesis, particularly in the modeling effort, has focused largely on Cr and Fe RIS. However, it has been concluded that minor elements Si, Ni, and Cu segregate by a different mechanism than that by which Cr and Fe segregate. This conclusion necessitates further study into the mechanism driving RIS of the minor elements. Furthermore, only a limited number of minor elements have been studied in this thesis, due to detectability issues with the STEM technique. Future work should use a technique capable of detecting a greater number of the constituent elements, in order to determine whether additional elements are segregating.

APPENDIX A: Temperature Histograms

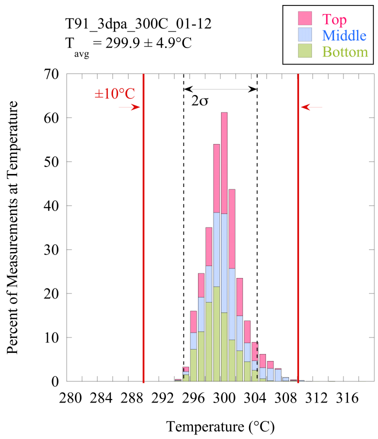
T91_3dpa_300C_01-12
T avg = 299.9 ± 4.9°C
Top
Middle
Bottom
±10°C
2σ
Percent of Measurements at Temperature
0
10
20
30
40
50
60
70
280 284 288 292 296 300 304 308 312 316
Temperature (°C)

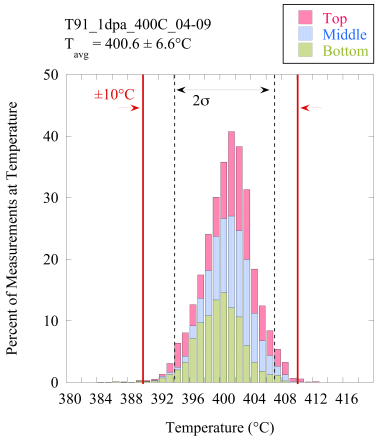
T91_1dpa_400C_04-09
T avg = 400.6 ± 6.6°C
Top
Middle
Bottom
±10°C
2σ
Percent of Measurements at Temperature
0
10
20
30
40
50
380 384 388 392 396 400 404 408 412 416
Temperature (°C)

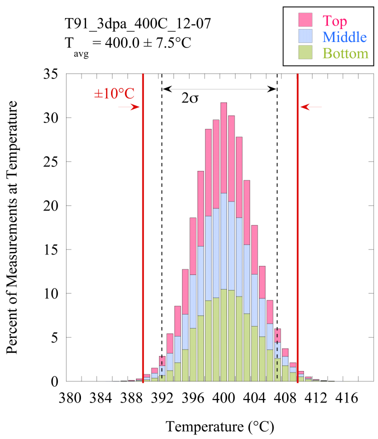
T91_3dpa_400C_12-07
T avg = 400.0 ± 7.5°C
Top
Middle
Bottom
±10°C
2σ
Percent of Measurements at Temperature
0
5
10
15
20
25
30
35
380 384 388 392 396 400 404 408 412 416
Temperature (°C)

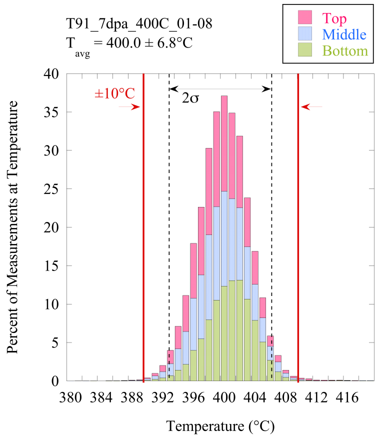
T91_7dpa_400C_01-08
T avg = 400.0 ± 6.8°C
Top
Middle
Bottom
±10°C
2σ
Percent of Measurements at Temperature
0
5
10
15
20
25
30
35
40
380 384 388 392 396 400 404 408 412 416
Temperature (°C)

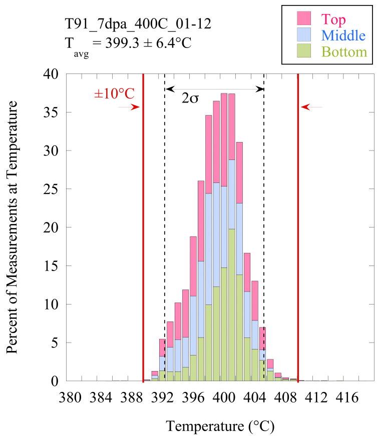
T91_7dpa_400C_01-12
T avg = 399.3 ± 6.4°C
Top
Middle
Bottom
±10°C
2σ
Percent of Measurements at Temperature
0
5
10
15
20
25
30
35
40
380 384 388 392 396 400 404 408 412 416
Temperature (°C)

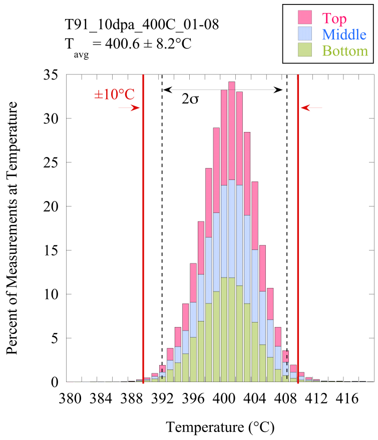
T91_10dpa_400C_01-08
T avg = 400.6 ± 8.2°C
Top
Middle
Bottom
±10°C
2σ
Percent of Measurements at Temperature
0
5
10
15
20
25
30
35
380 384 388 392 396 400 404 408 412 416
Temperature (°C)

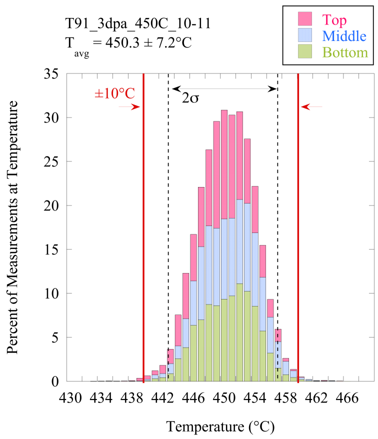
T91_3dpa_450C_10-11
T avg = 450.3 ± 7.2°C
Top
Middle
Bottom
±10°C
2σ
Percent of Measurements at Temperature
0
5
10
15
20
25
30
35
430 434 438 442 446 450 454 458 462 466
Temperature (°C)

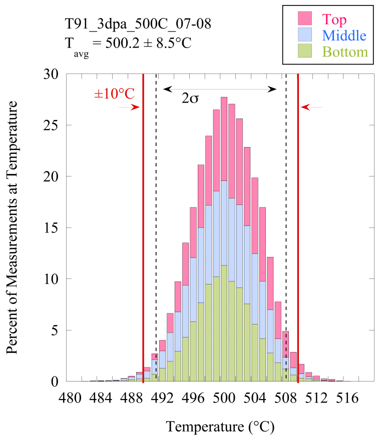
T91_3dpa_500C_07-08
T avg = 500.2 ± 8.5°C
Top
Middle
Bottom
±10°C
2σ
Percent of Measurements at Temperature
0
5
10
15
20
25
30
480 484 488 492 496 500 504 508 512 516
Temperature (°C)

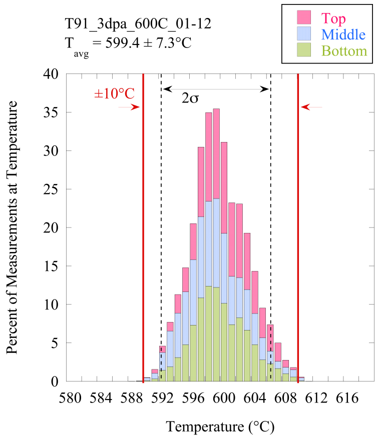
T91_3dpa_600C_01-12
T avg = 599.4 ± 7.3°C
Top
Middle
Bottom
±10°C
2σ
Percent of Measurements at Temperature
0
5
10
15
20
25
30
35
40
580 584 588 592 596 600 604 608 612 616
Temperature (°C)

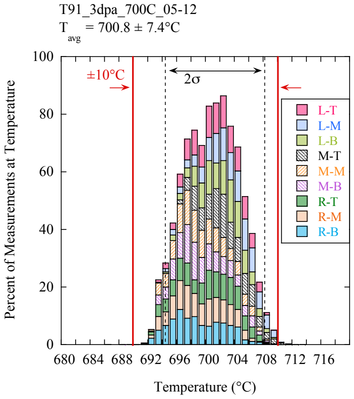
T91_3dpa_700C_05-12
T_{avg} = 700.8 ± 7.4°C
±10°C
2σ
L-T
L-M
L-B
M-T
M-M
M-B
R-T
R-M
R-B
Percent of Measurements at Temperature
0
20
40
60
80
100
680 684 688 692 696 700 704 708 712 716
Temperature (°C)

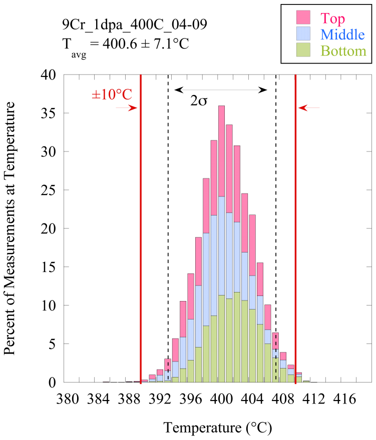
9Cr_1dpa_400C_04-09
T_{avg} = 400.6 ± 7.1°C
Top
Middle
Bottom
±10°C
2σ
Percent of Measurements at Temperature
0
5
10
15
20
25
30
35
40
380 384 388 392 396 400 404 408 412 416
Temperature (°C)

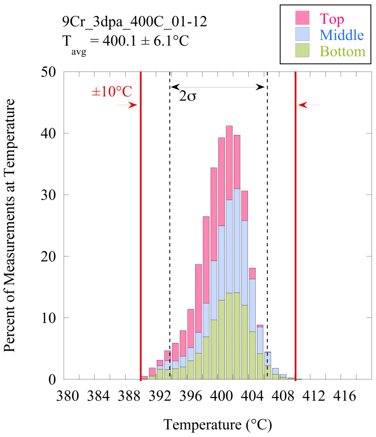
9Cr_3dpa_400C_01-12
T_{avg} = 400.1 ± 6.1°C
Top
Middle
Bottom
±10°C
2σ
Percent of Measurements at Temperature
0
10
20
30
40
50
380 384 388 392 396 400 404 408 412 416
Temperature (°C)

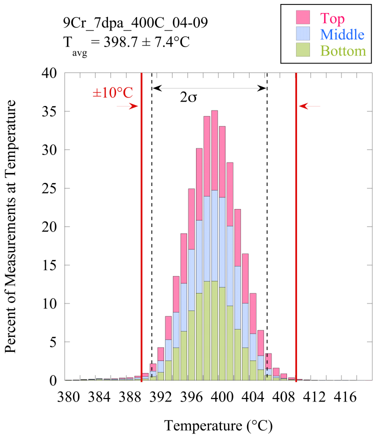
9Cr_7dpa_400C_04-09
T_{avg} = 398.7 ± 7.4°C
Top
Middle
Bottom
±10°C
2σ
Percent of Measurements at Temperature
0
5
10
15
20
25
30
35
40
380 384 388 392 396 400 404 408 412 416
Temperature (°C)

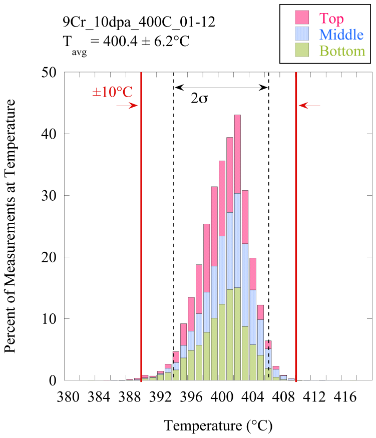
9Cr_10dpa_400C_01-12
T_{avg} = 400.4 ± 6.2°C
Top
Middle
Bottom
±10°C
2σ
Percent of Measurements at Temperature
0
10
20
30
40
50
380 384 388 392 396 400 404 408 412 416
Temperature (°C)

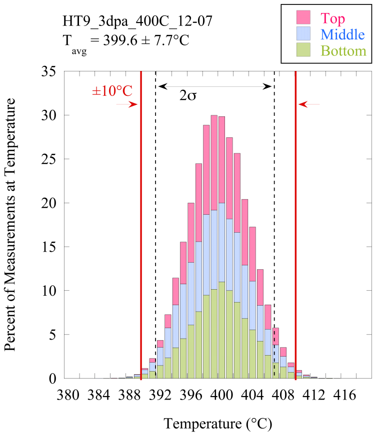
HT9_3dpa_400C_12-07
T_{avg} = 399.6 ± 7.7°C
Top
Middle
Bottom
±10°C
2σ
Percent of Measurements at Temperature
0
5
10
15
20
25
30
35
380 384 388 392 396 400 404 408 412 416
Temperature (°C)

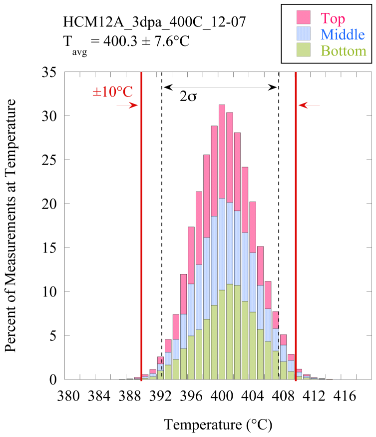
HCM12A_3dpa_400C_12-07
T_{avg} = 400.3 ± 7.6°C
Top
Middle
Bottom
±10°C
2σ
Percent of Measurements at Temperature
0
5
10
15
20
25
30
35
380 384 388 392 396 400 404 408 412 416
Temperature (°C)

APPENDIX B: Composition Profiles

T91_UI

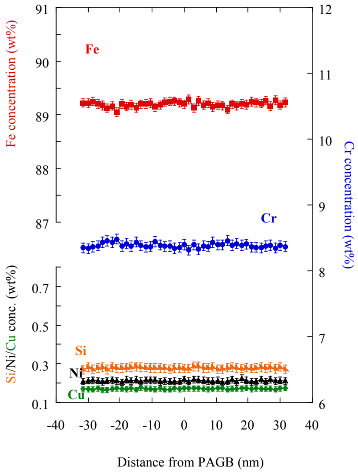
T91_UI_1-1-F

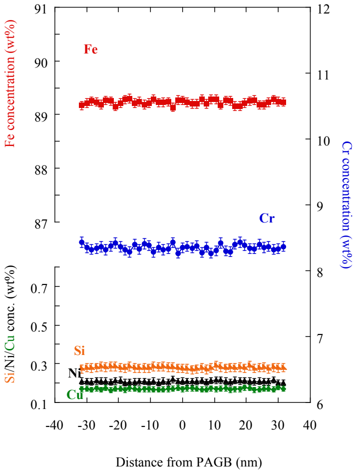
T91_UI_1-2-F

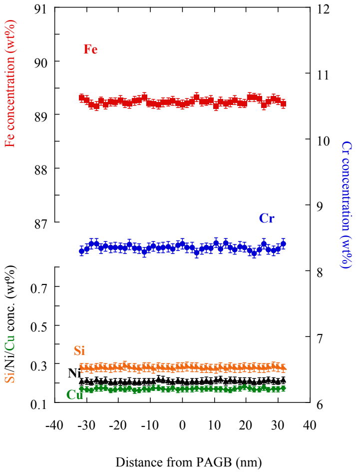
T91_UI_1-3-F

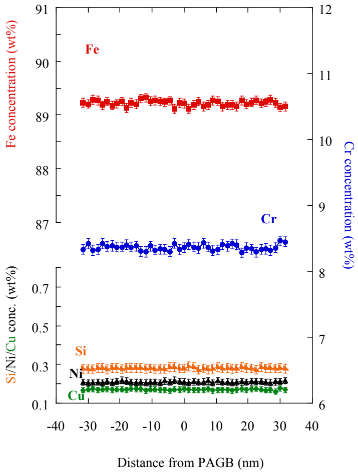
T91_UI_2-1-F

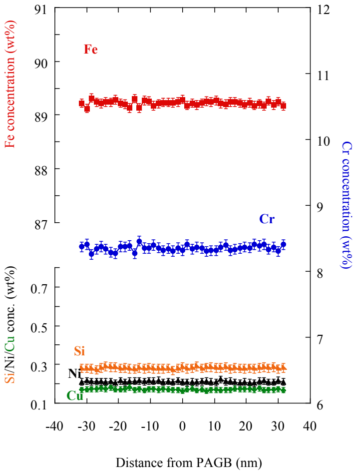
T91_UI_2-2-F

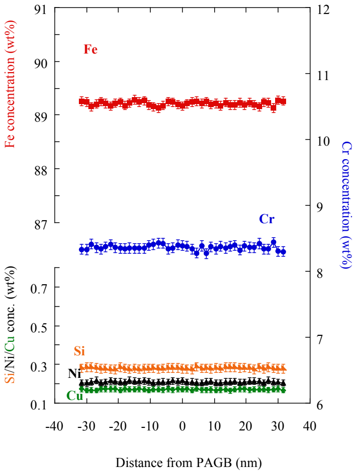
T91_UI_2-3-F

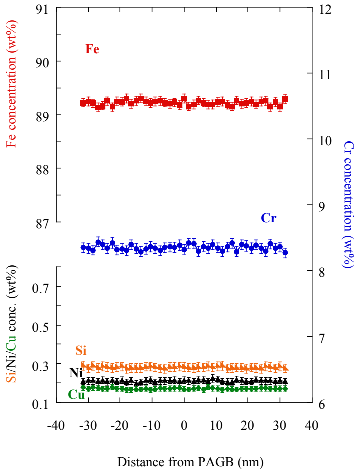
T91_UI_3-1-F

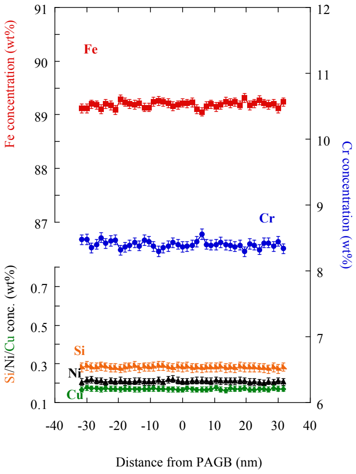
T91_UI_3-2-F

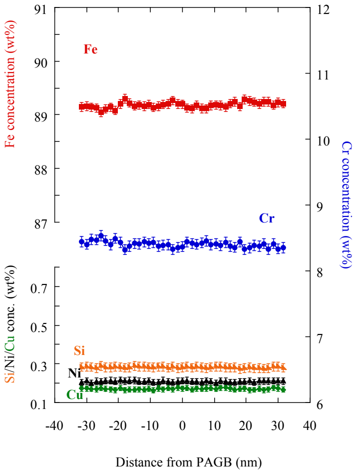
T91_UI_3-3-F

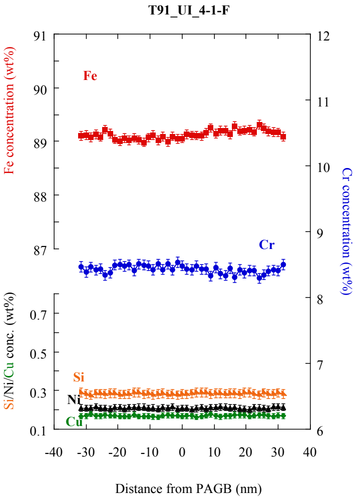
T91_UI_4-1-F
Fe
Cr
Si
Ni
Cu
Fe concentration (wt%)
Si/Ni/Cu conc. (wt%)
Cr concentration (wt%)
Distance from PAGB (nm)
91
90
89
88
87
0.7
0.5
0.3
0.1
12
11
10
9
8
7
6
-40
-30
-20
-10
0
10
20
30
40

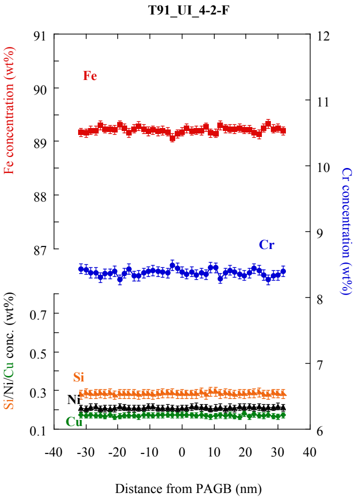
T91_UI_4-2-F
Fe
Cr
Si
Ni
Cu
Fe concentration (wt%)
Si/Ni/Cu conc. (wt%)
Cr concentration (wt%)
Distance from PAGB (nm)
91
90
89
88
87
0.7
0.5
0.3
0.1
12
11
10
9
8
7
6
-40
-30
-20
-10
0
10
20
30
40

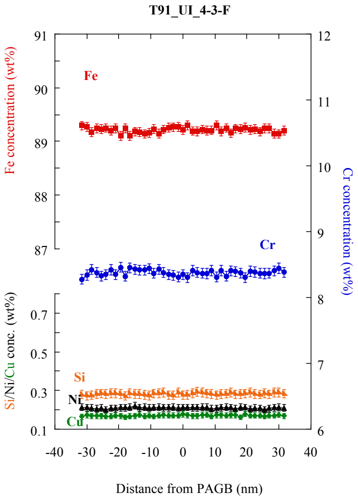
T91_UI_4-3-F
Fe
Cr
Si
Ni
Cu
Fe concentration (wt%)
Si/Ni/Cu conc. (wt%)
Cr concentration (wt%)
Distance from PAGB (nm)
91
90
89
88
87
0.7
0.5
0.3
0.1
12
11
10
9
8
7
6
-40
-30
-20
-10
0
10
20
30
40

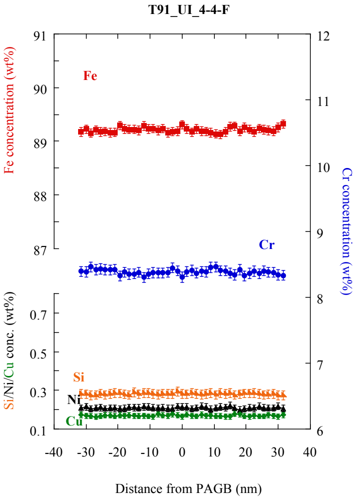
T91_UI_4-4-F
Fe
Cr
Si
Ni
Cu
Fe concentration (wt%)
Si/Ni/Cu conc. (wt%)
Cr concentration (wt%)
Distance from PAGB (nm)
91
90
89
88
87
0.7
0.5
0.3
0.1
12
11
10
9
8
7
6
-40
-30
-20
-10
0
10
20
30
40

9Cr_UI

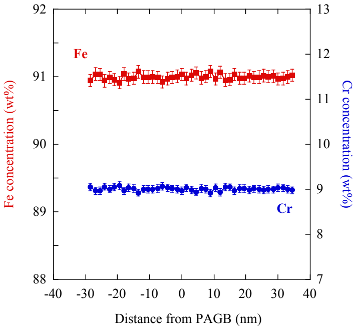
9Cr_UI_1-1-F

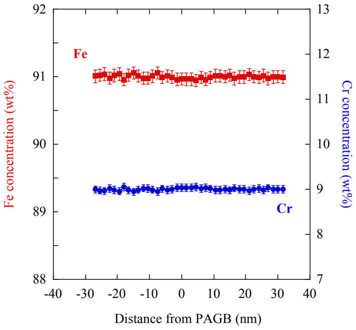
9Cr_UI_1-2-F

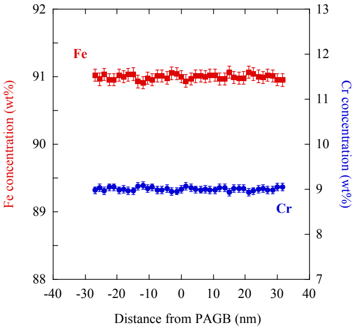
9Cr_UI_1-3-F

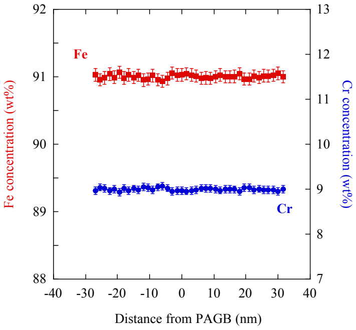
9Cr_UI_2-1-F

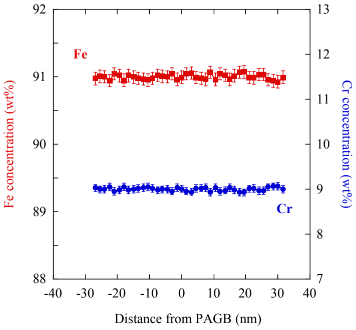
9Cr_UI_2-2-F

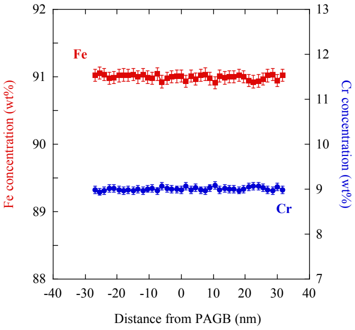
9Cr_UI_2-3-F

HT9_UI

HT9_UI_1-1-F

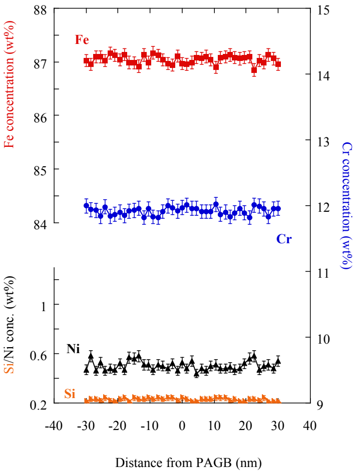

HT9_UI_1-2-F

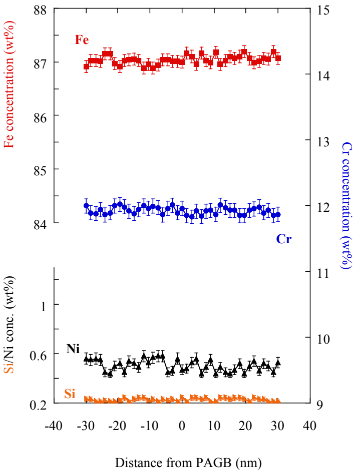

HT9_UI_1-3-F

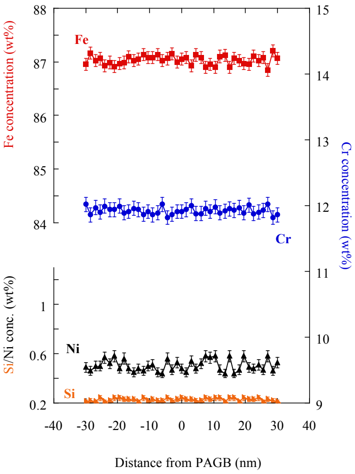

HT9_UI_2-1-F

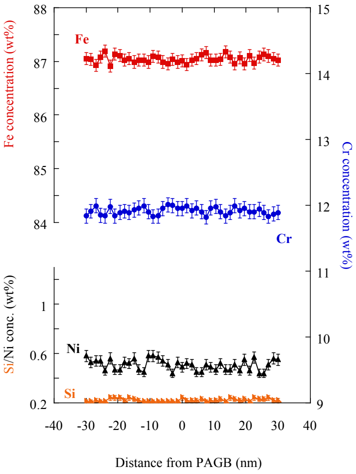

HT9_UI_2-2-F

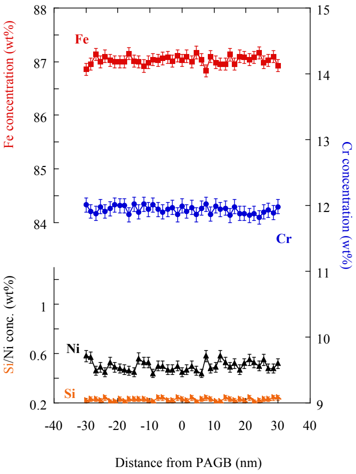

HCM12A_UI

HCM12A_UI_1-1-F

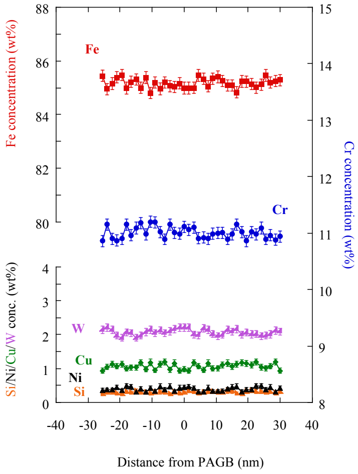

HCM12A_UI_1-2-F

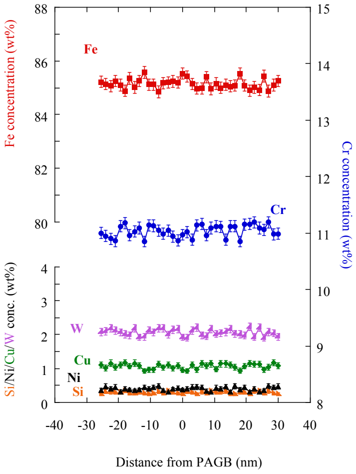

HCM12A_UI_1-3-F

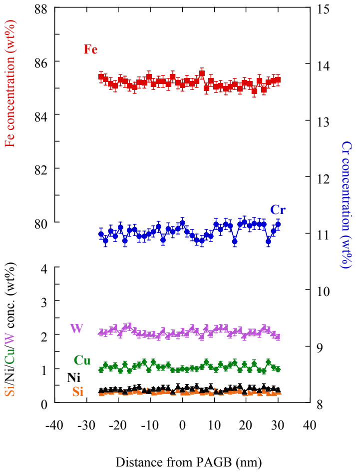

HCM12A_UI_2-1-F

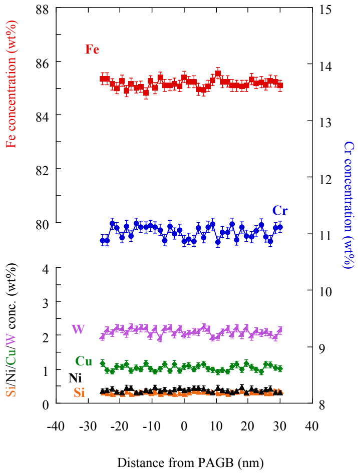

HCM12A_UI_2-2-F

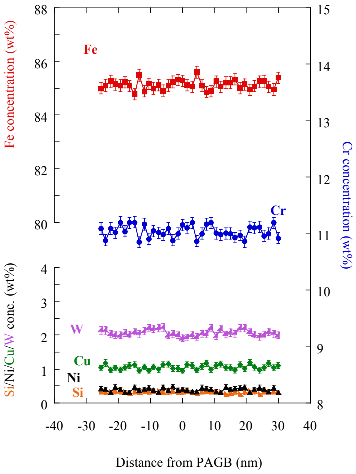

HCM12A_UI_2-3-F

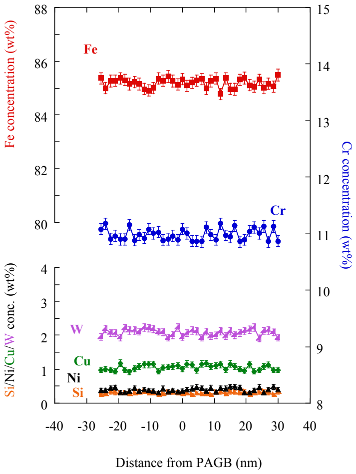

HCM12A_UI_3-1-F

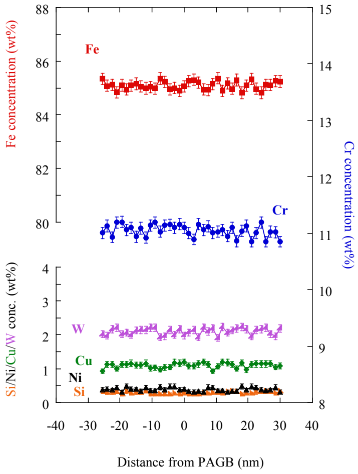

HCM12A_UI_3-2-F

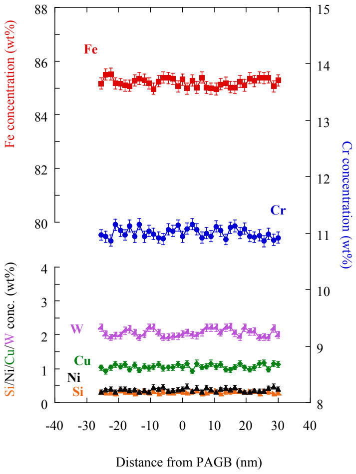

HCM12A_UI_3-3-F

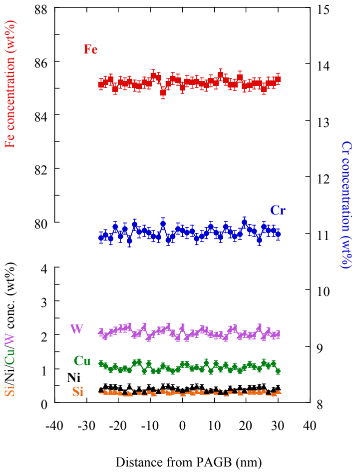

T91_3dpa_300C_01-12

T91_3dpa_300C_01-12_T_1-1-F

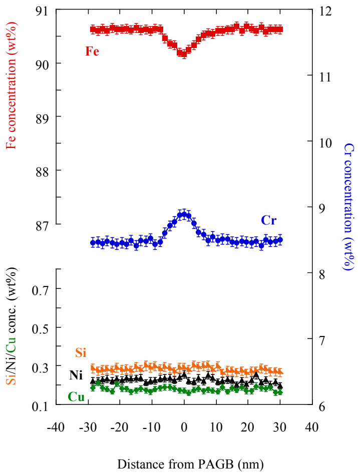

T91_3dpa_300C_01-12_T_1-2-F

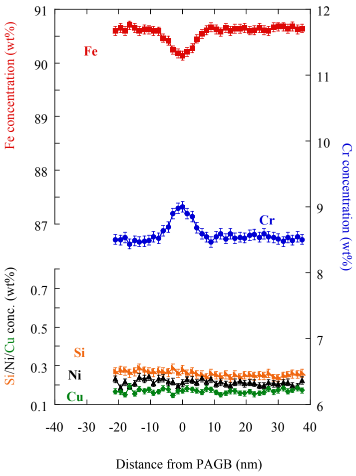

T91_3dpa_300C_01-12_T_1-3-S

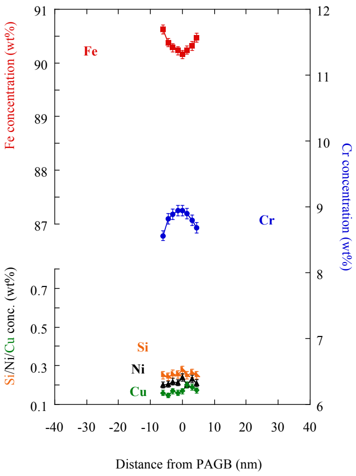

T91_3dpa_300C_01-12_T_1-4-S

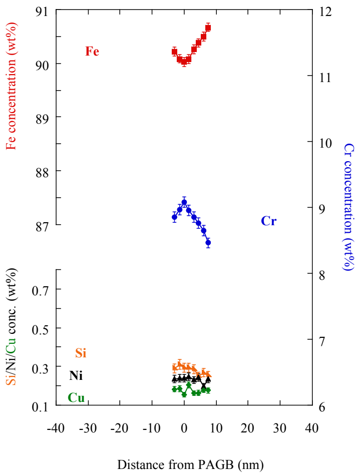

T91_3dpa_300C_01-12_T_2-1-F

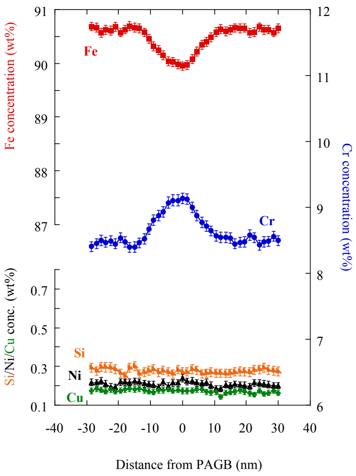

T91_3dpa_300C_01-12_T_2-2-F

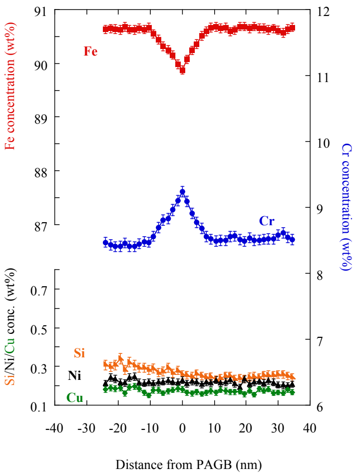

T91_3dpa_300C_01-12_T_2-3-F

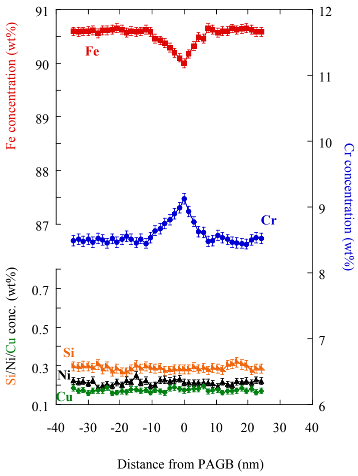

T91_3dpa_300C_01-12_T_2-4-S

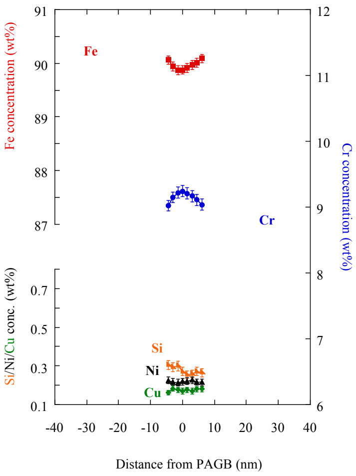

T91_3dpa_300C_01-12_T_2-5-S

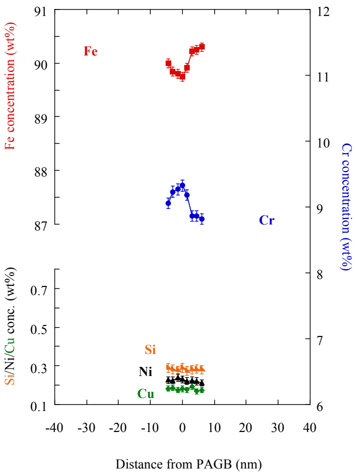

T91_1dpa_400C_04-09

T91_1dpa_400C_04-09_B_1-1-F

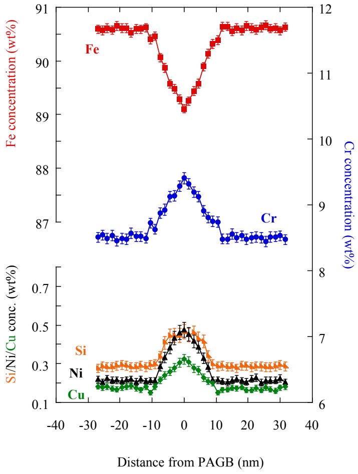

T91_1dpa_400C_04-09_B_1-2-F

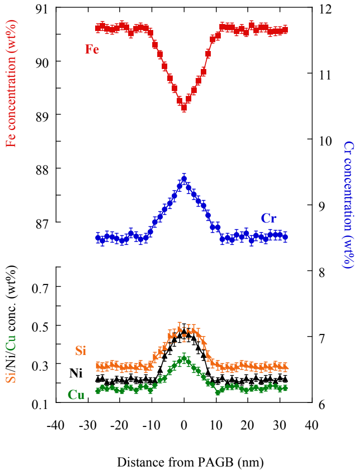

T91_1dpa_400C_04-09_B_1-3-F

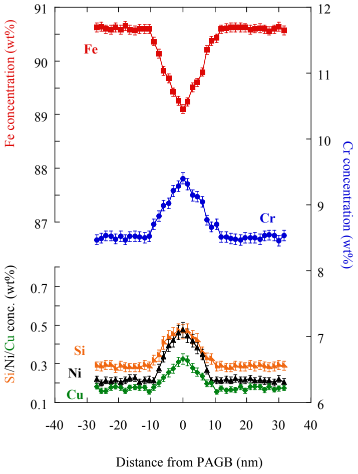

T91_1dpa_400C_04-09_B_1-4-S

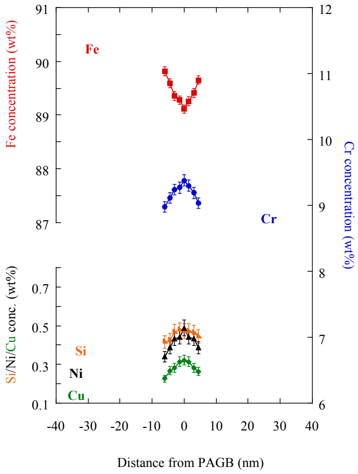

T91_1dpa_400C_04-09_B_1-5-S

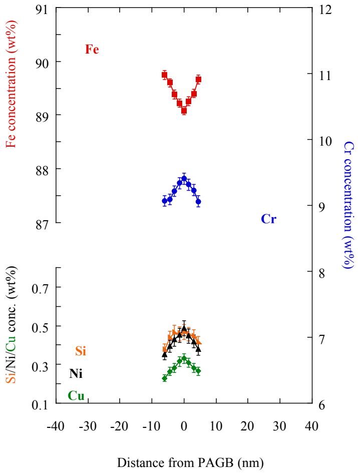

T91_1dpa_400C_04-09_B_1-6-S

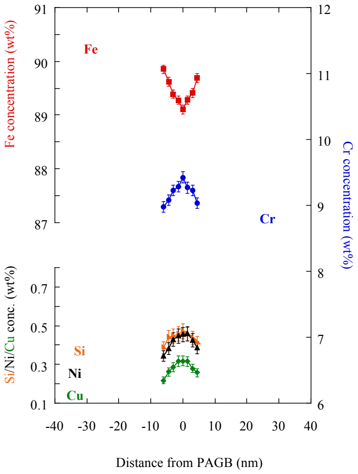

T91_1dpa_400C_04-09_B_1-7-S

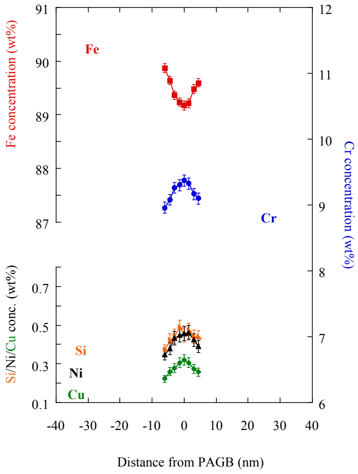

T91_1dpa_400C_04-09_B_1-8-S

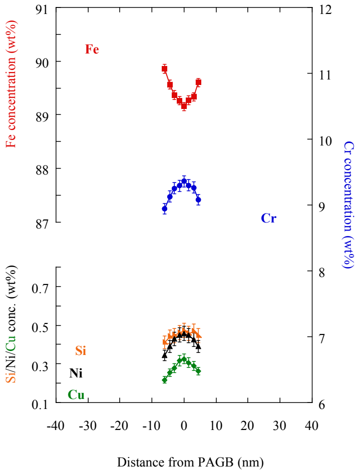

T91_1dpa_400C_04-09_B_2-1-F

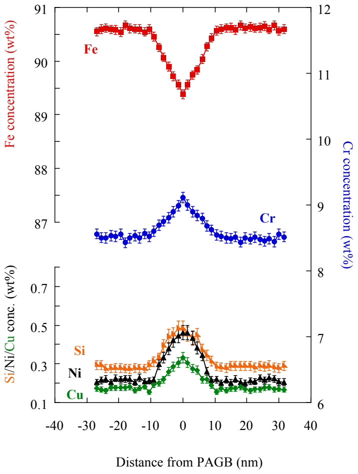

T91_1dpa_400C_04-09_B_2-2-F

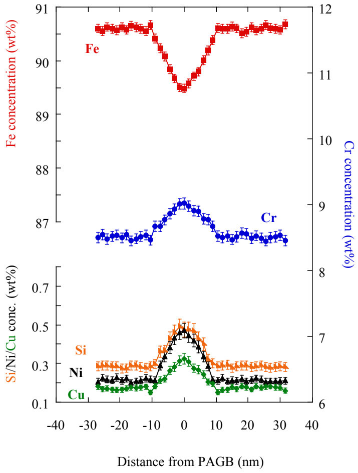

T91_1dpa_400C_04-09_B_2-3-S

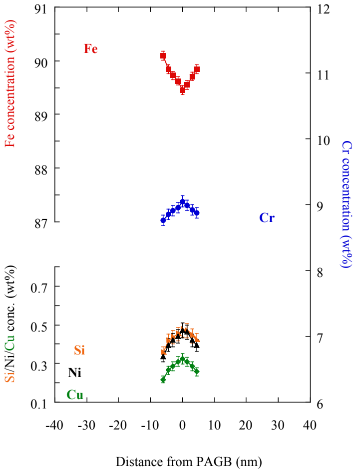

T91_1dpa_400C_04-09_B_2-4-S

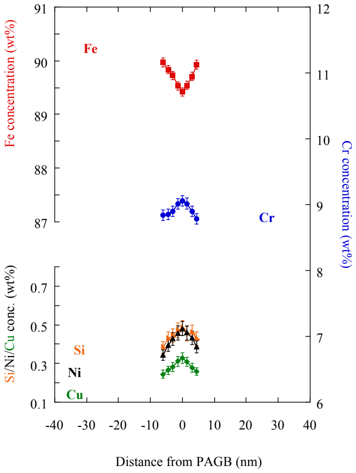

T91_1dpa_400C_04-09_B_2-5-S

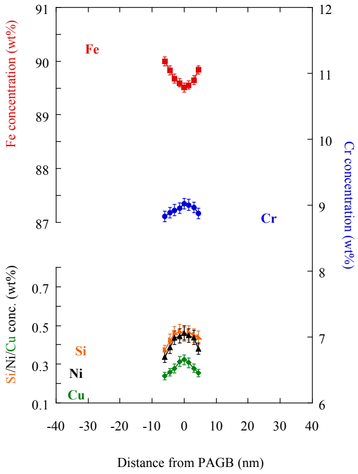

T91_1dpa_400C_04-09_B_2-6-S

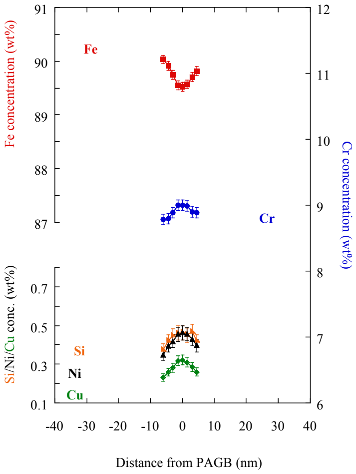

T91_3dpa_400C_12-07

T91_3dpa_400C_12-07_M_1-1-F

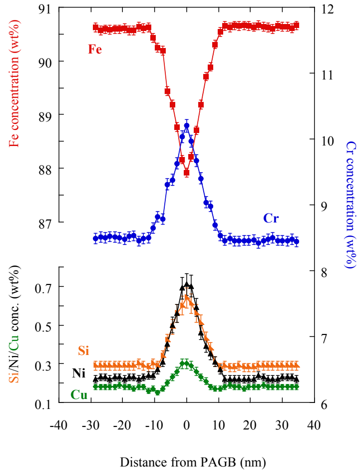

T91_3dpa_400C_12-07_M_1-2-F

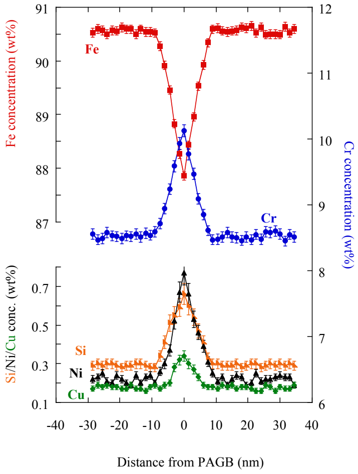

T91_3dpa_400C_12-07_M_2-1-F

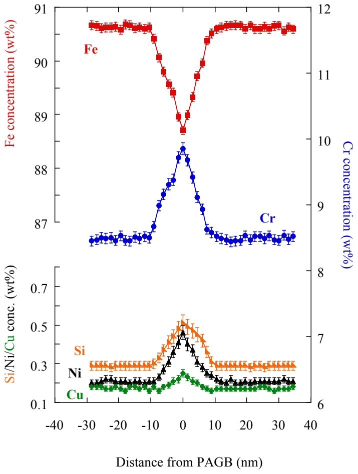

T91_3dpa_400C_12-07_M_2-2-F

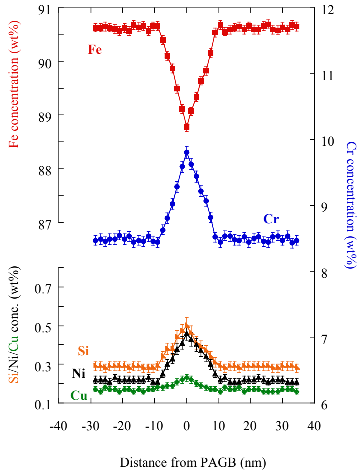

T91_3dpa_400C_12-07_M_2-3-F

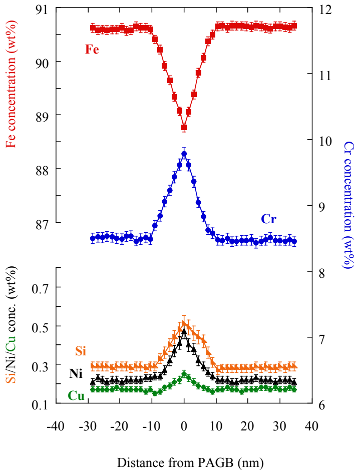

T91_3dpa_400C_12-07_M_3-1-F

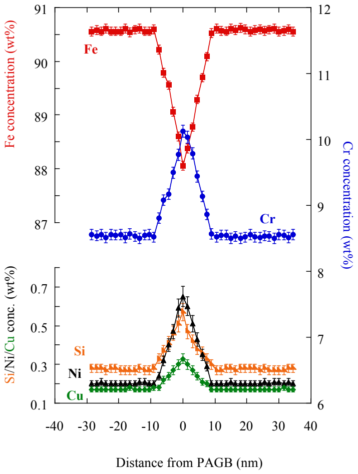

T91_3dpa_400C_12-07_M_3-2-F

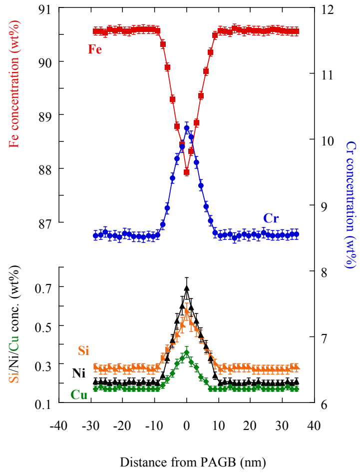

T91_7dpa_400C_01-08

T91_7dpa_400C_01-08_B_1-1-F

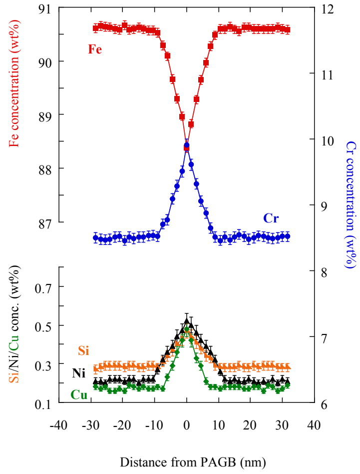

T91_7dpa_400C_01-08_B_1-2-F

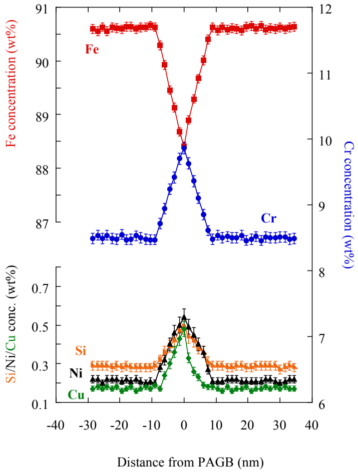

T91_7dpa_400C_01-08_B_2-1-F

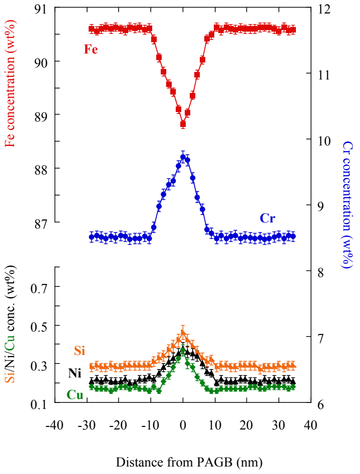

T91_7dpa_400C_01-08_B_2-2-F

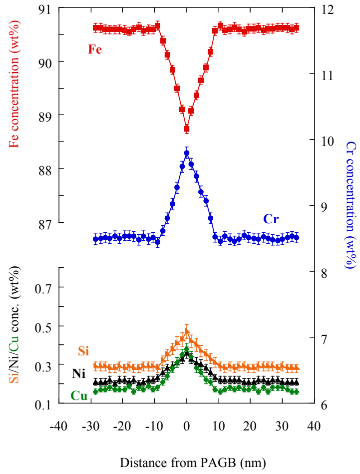

T91_7dpa_400C_01-08_B_3-1-F

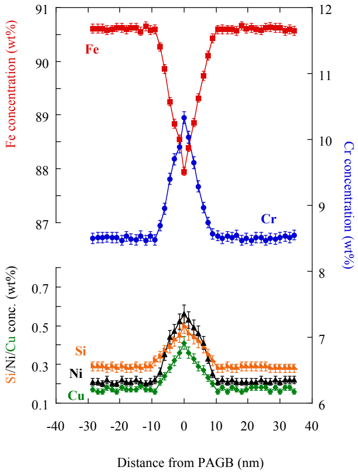

T91_7dpa_400C_01-08_B_3-2-F

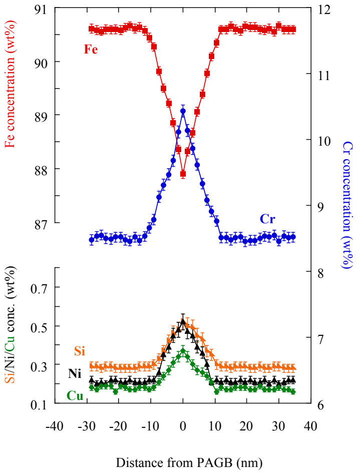

T91_7dpa_400C_01-12

T91_7dpa_400C_01-12_M_1-1-F

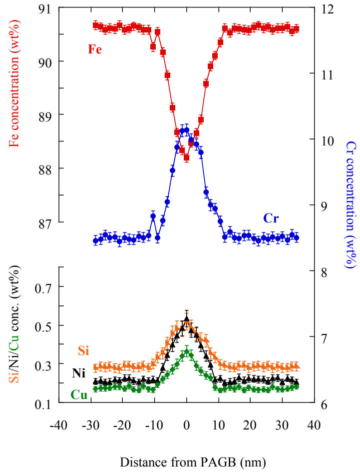

T91_7dpa_400C_01-12_M_1-2-F

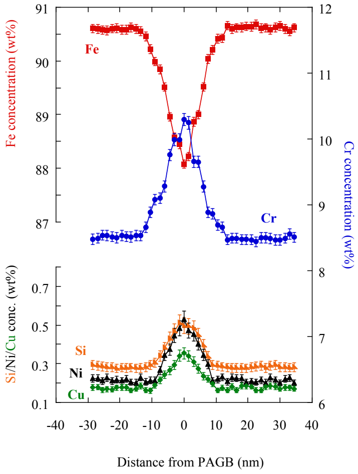

T91_7dpa_400C_01-12_M_1-3-F

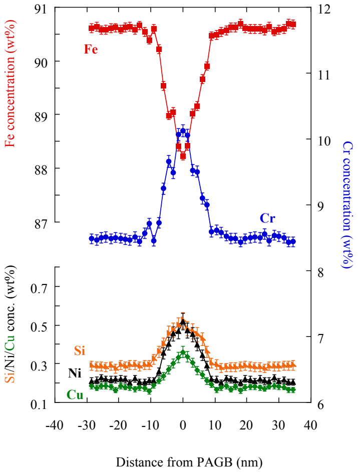

T91_7dpa_400C_01-12_M_1-4-F

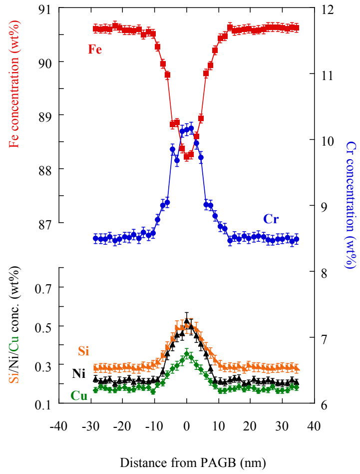

T91_7dpa_400C_01-12_M_1-5-F

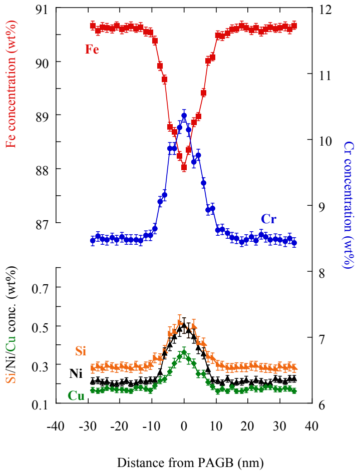

T91_7dpa_400C_01-12_M_1-6-F

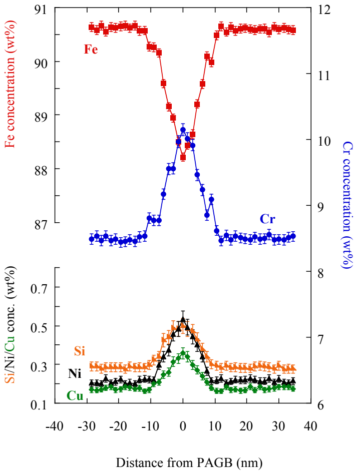

T91_7dpa_400C_01-12_M_2-1-F

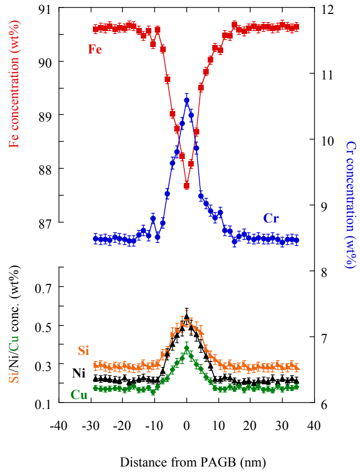

T91_7dpa_400C_01-12_M_2-2-F

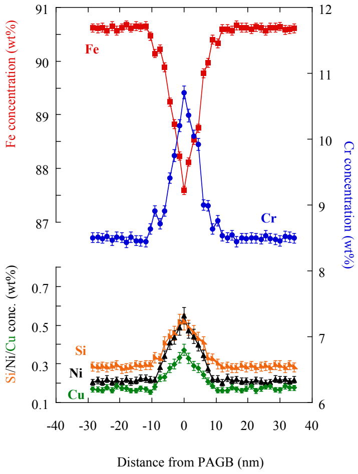

T91_7dpa_400C_01-12_M_2-3-F

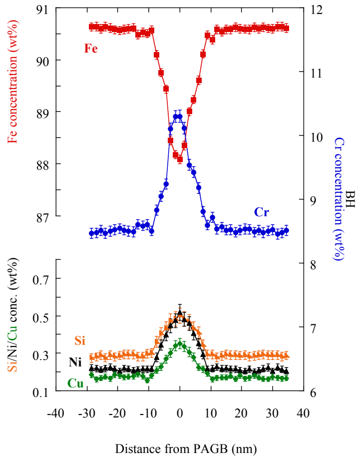

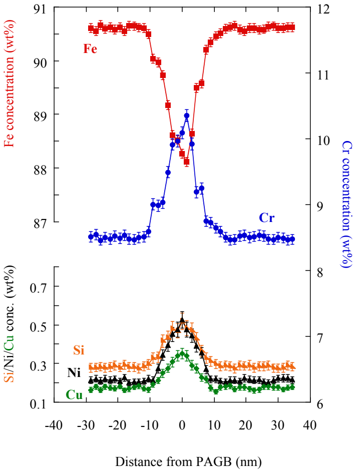
T91_7dpa_400C_01-12_M_3-1-F

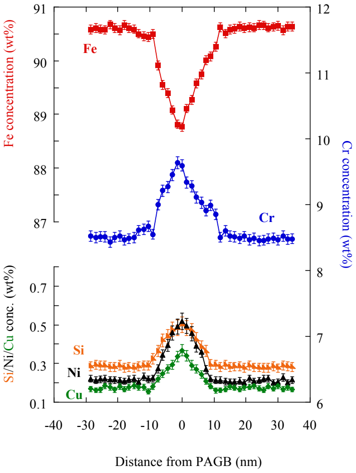
T91_7dpa_400C_01-12_M_3-2-F

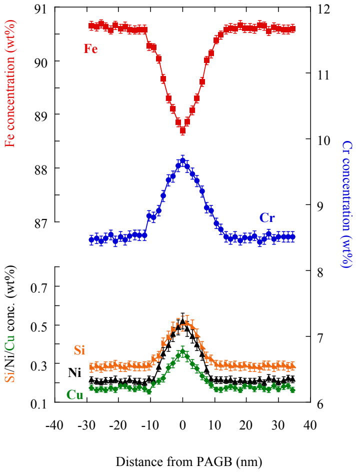
T91_7dpa_400C_01-12_M_3-3-F

T91_10dpa_400C_01-08

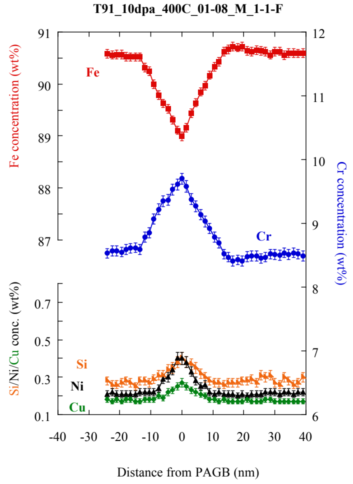
T91_10dpa_400C_01-08_M_1-1-F

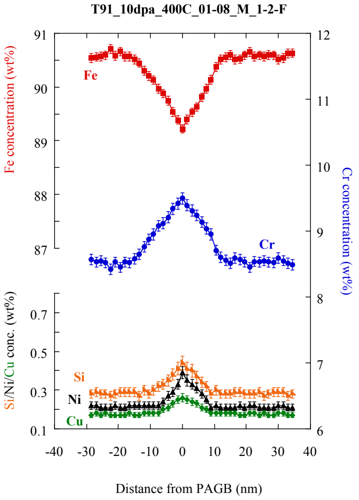
T91_10dpa_400C_01-08_M_1-2-F

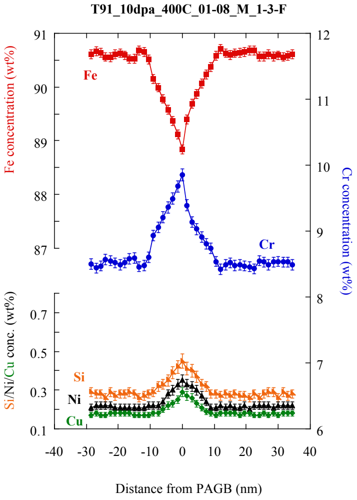
T91_10dpa_400C_01-08_M_1-3-F

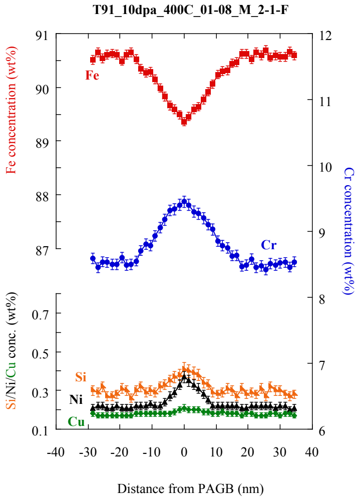
T91_10dpa_400C_01-08_M_2-1-F

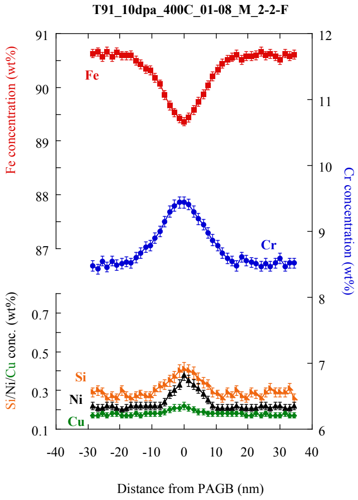
T91_10dpa_400C_01-08_M_2-2-F

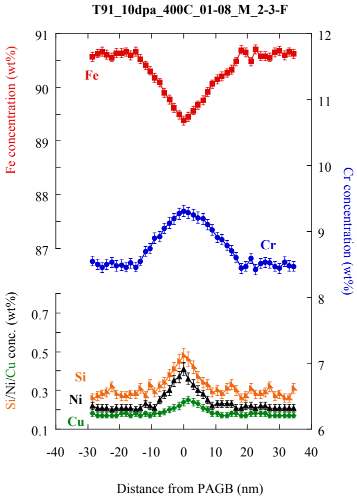
T91_10dpa_400C_01-08_M_2-3-F

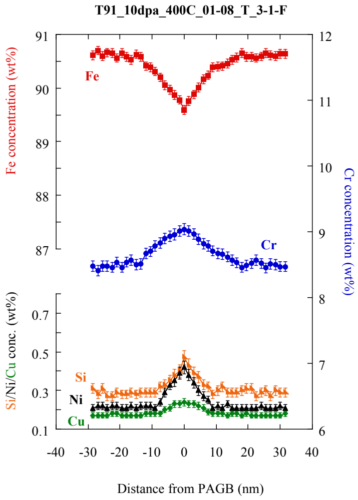
T91_10dpa_400C_01-08_T_3-1-F

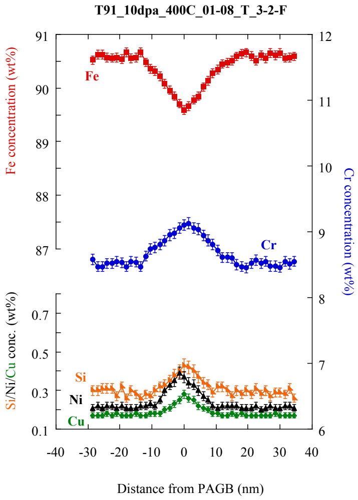
T91_10dpa_400C_01-08_T_3-2-F

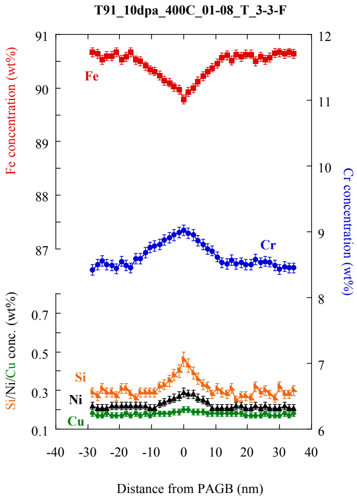
T91_10dpa_400C_01-08_T_3-3-F

T91_10dpa_400C_01-08_T_4-1-F

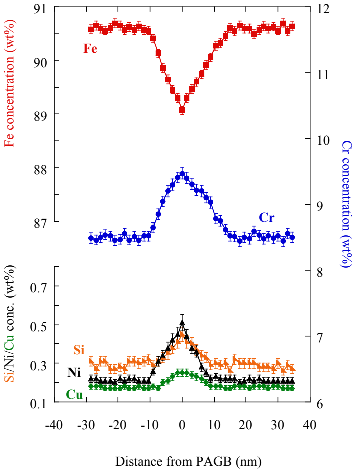

T91_10dpa_400C_01-08_T_4-2-F

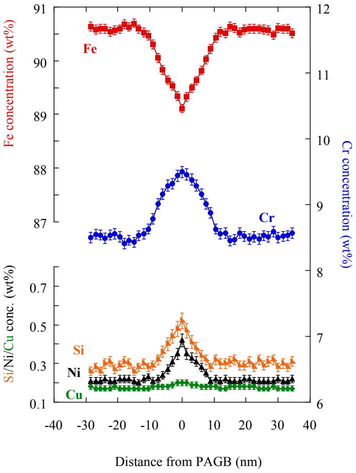

T91_10dpa_400C_01-08_T_4-3-F

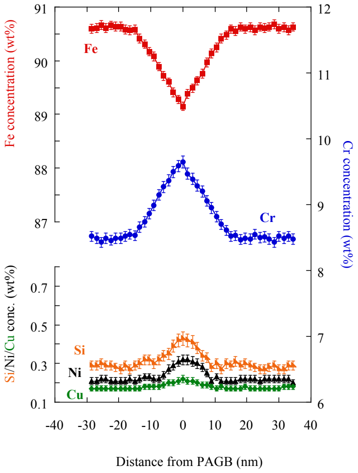

T91_10dpa_400C_01-08_T_5-1-F

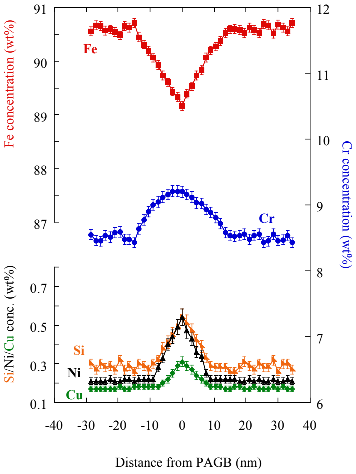

T91_10dpa_400C_01-08_T_5-2-F

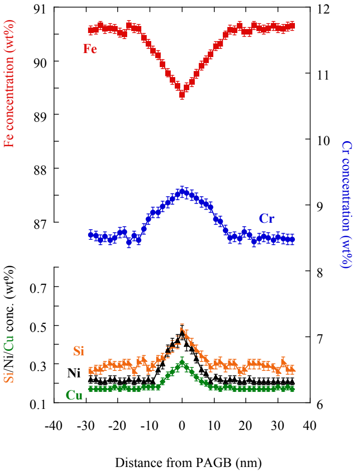

T91_10dpa_400C_01-08_M_5-3-F

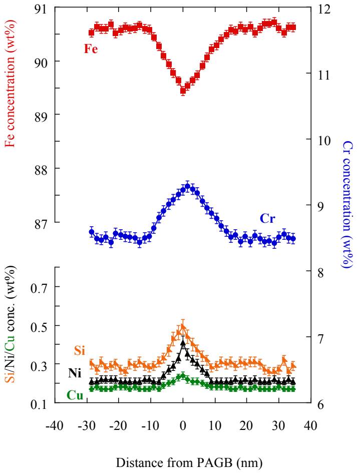

T91_3dpa_450C_10-11

T91_3dpa_450C_10-11_M_1-1-F

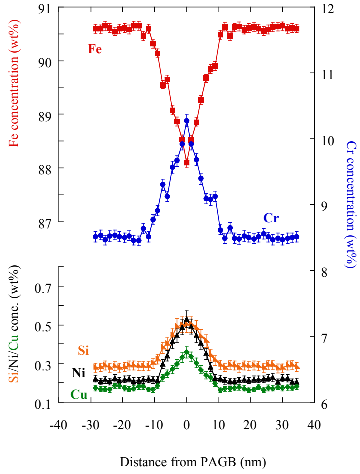

T91_3dpa_450C_10-11_M_1-2-F

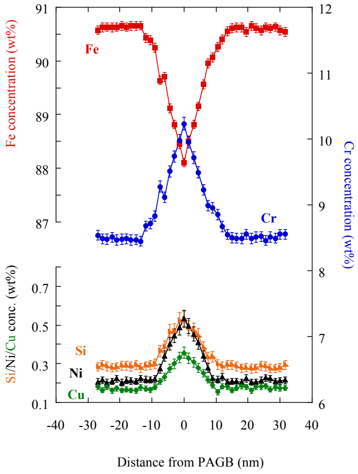

T91_3dpa_450C_10-11_M_1-3-F

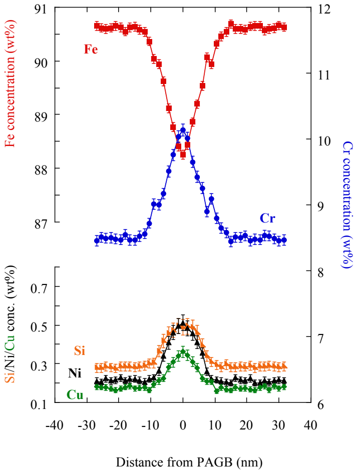

T91_3dpa_450C_10-11_M_1-4-F

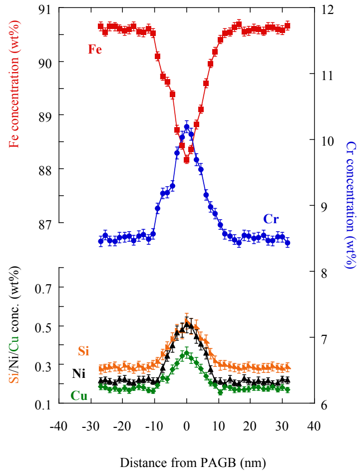

T91_3dpa_450C_10-11_M_1-5-S

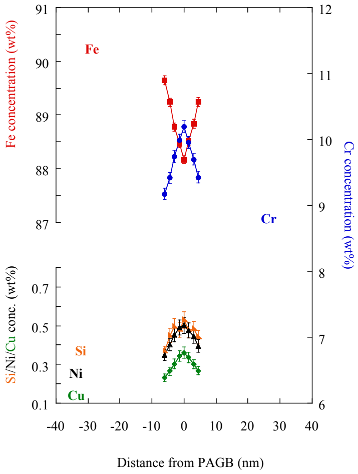

T91_3dpa_450C_10-11_M_1-6-S

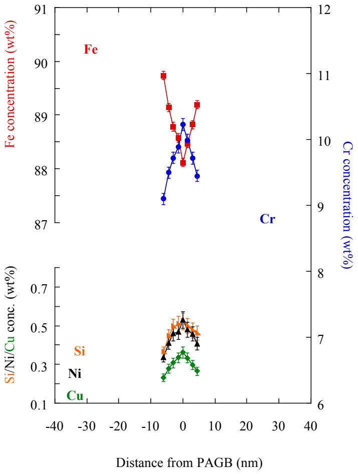

T91_3dpa_450C_10-11_M_1-7-S

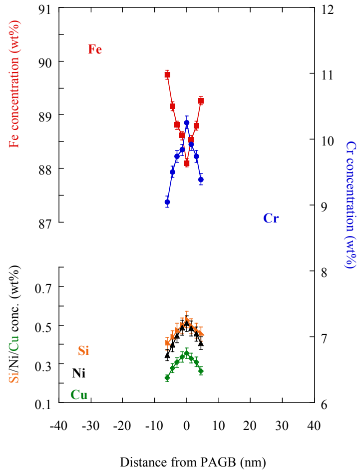

T91_3dpa_450C_10-11_M_1-8-S

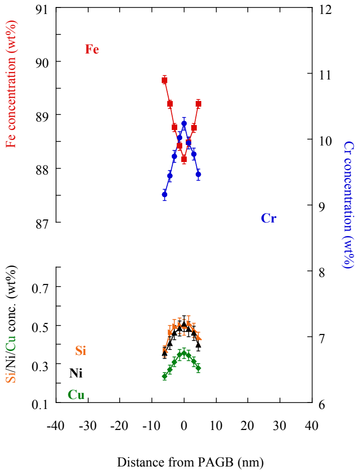

T91_3dpa_450C_10-11_M_1-9-S

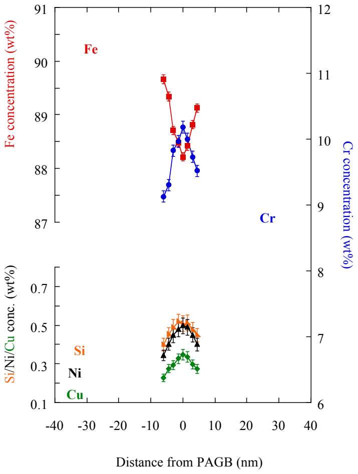

T91_3dpa_450C_10-11_M_2-1-F

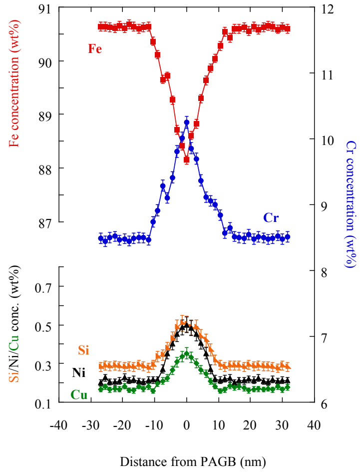

T91_3dpa_450C_10-11_M_2-2-F

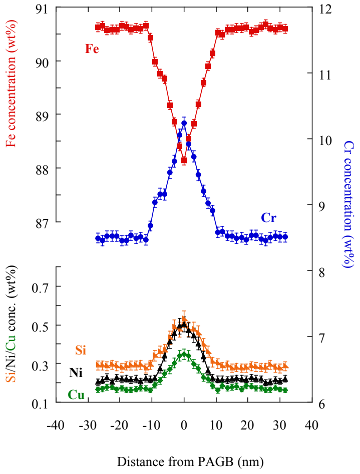

T91_3dpa_450C_10-11_M_2-3-S

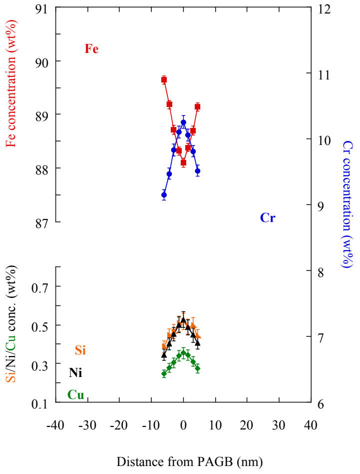

T91_3dpa_450C_10-11_M_2-4-S

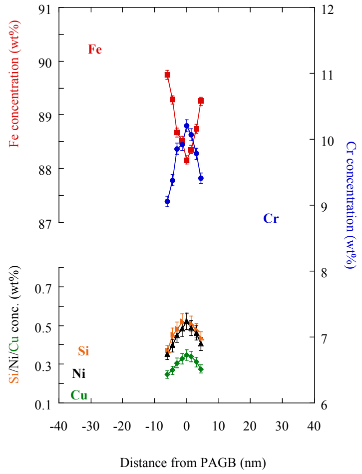

T91_3dpa_450C_10-11_M_2-5-S

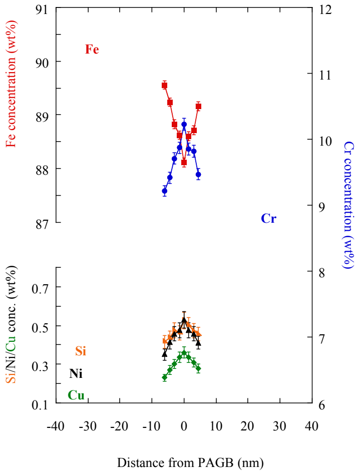

T91_3dpa_450C_10-11_M_2-6-S

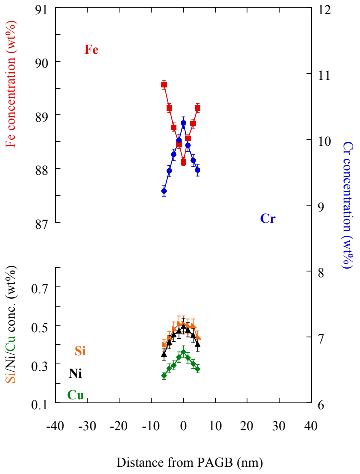

T91_3dpa_500C_07-08

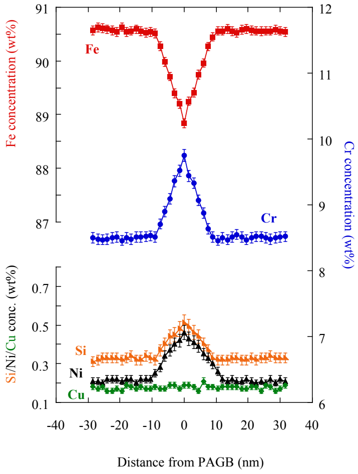
T91_3dpa_500C_07-08_B_1-1-F

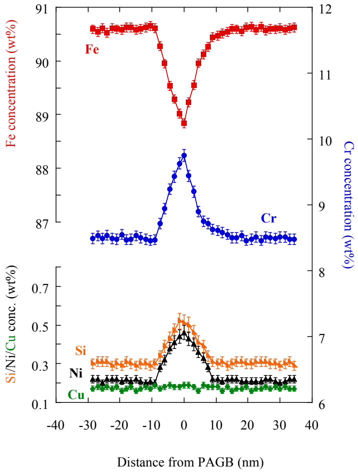
T91_3dpa_500C_07-08_B_1-2-F

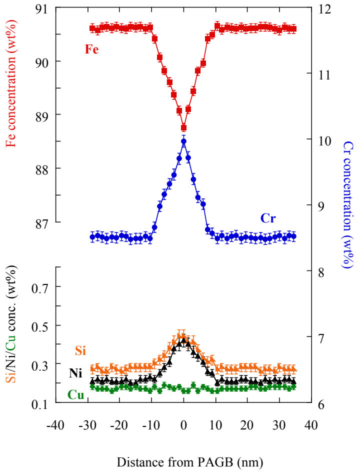
T91_3dpa_500C_07-08_T_2-1-F

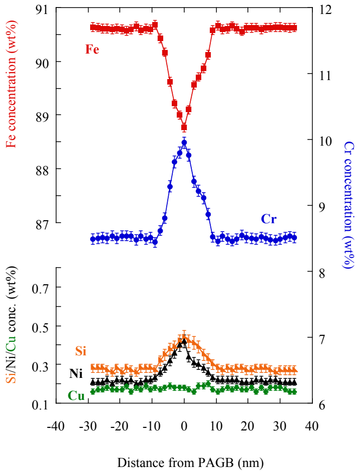
T91_3dpa_500C_07-08_T_2-2-F

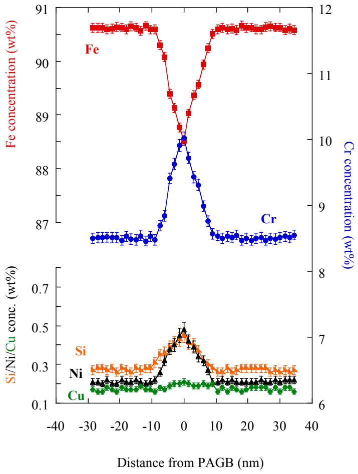
T91_3dpa_500C_07-08_T_2-3-F

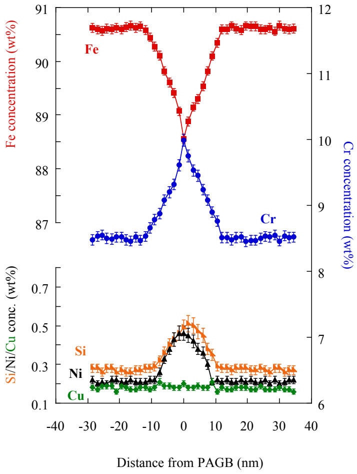
T91_3dpa_500C_07-08_T_2-4-F

T91_3dpa_600C_01-12

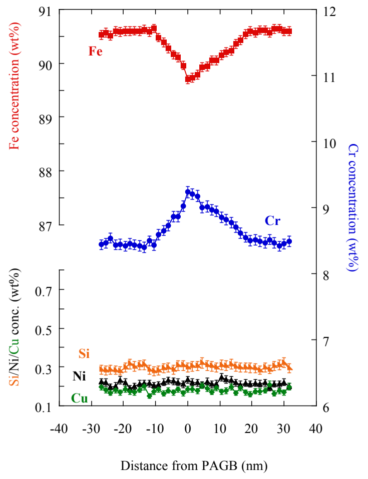
T91_3dpa_600C_01-12_B_1-1-F

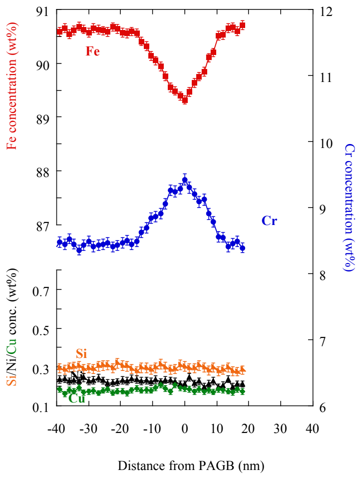
T91_3dpa_600C_01-12_B_1-2-F

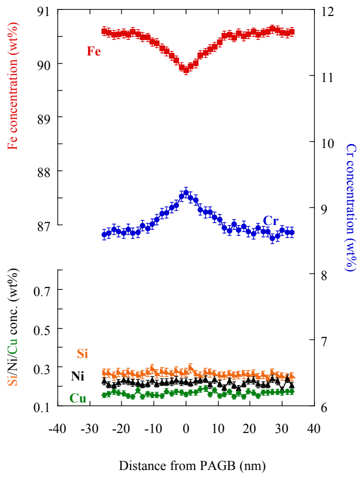
T91_3dpa_600C_01-12_B_1-3-F

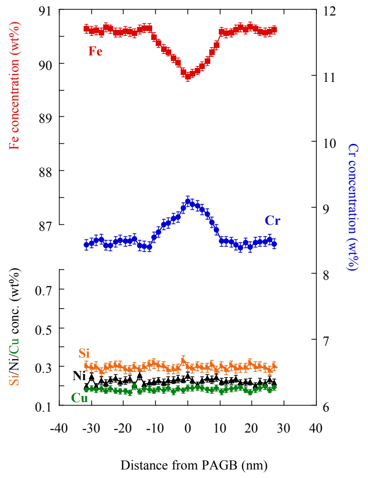
T91_3dpa_600C_01-12_B_2-1-F

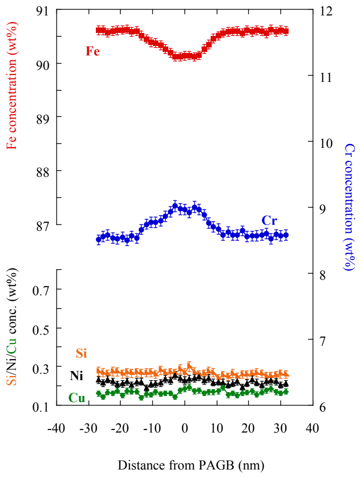
T91_3dpa_600C_01-12_B_2-2-F

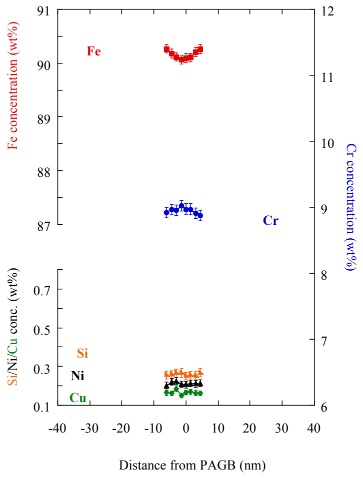
T91_3dpa_600C_01-12_B_2-3-S

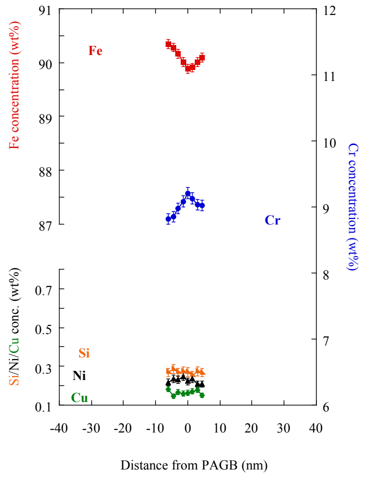
T91_3dpa_600C_01-12_B_2-4-S

T91_3dpa_700C_05-12

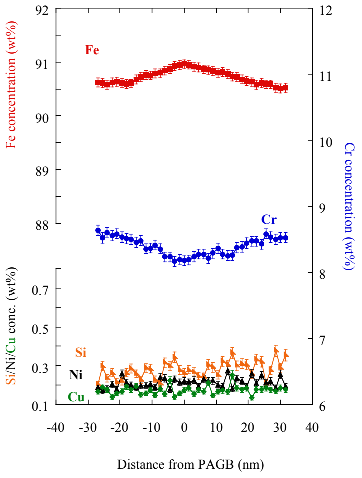

T91_3dpa_700C_05-12_MM_1-1-F

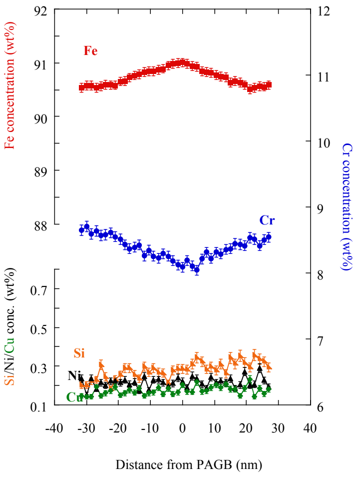

T91_3dpa_700C_05-12_MM_1-2-F

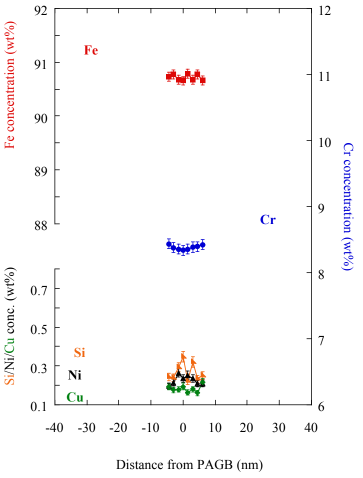

T91_3dpa_700C_05-12_MM_1-3-S

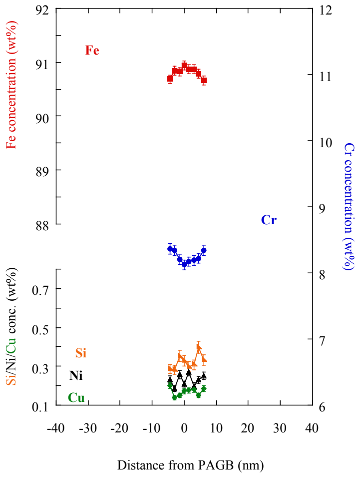

T91_3dpa_700C_05-12_MM_1-4-S

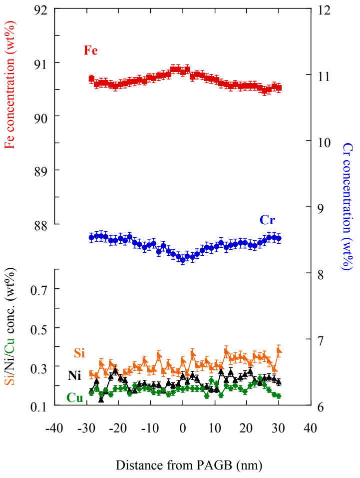

T91_3dpa_700C_05-12_MM_2-1-F

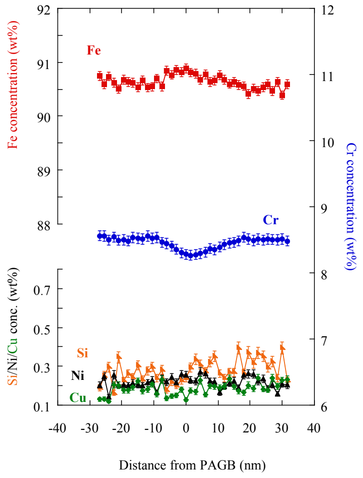

T91_3dpa_700C_05-12_MM_2-2-F

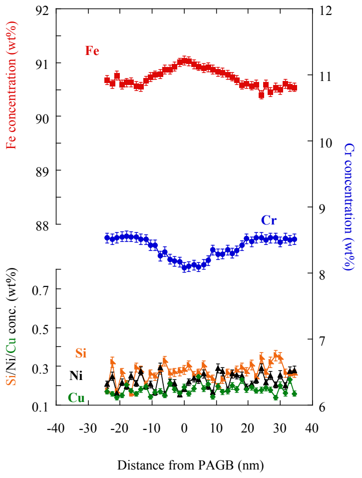

T91_3dpa_700C_05-12_MM_2-3-F

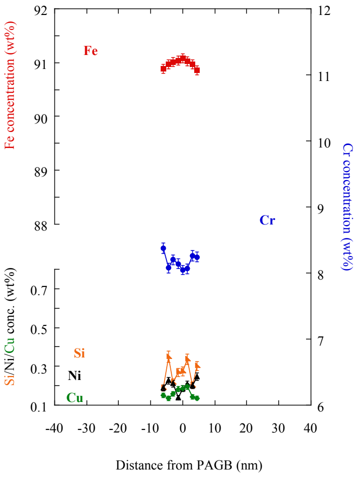

T91_3dpa_700C_05-12_MM_2-4-S

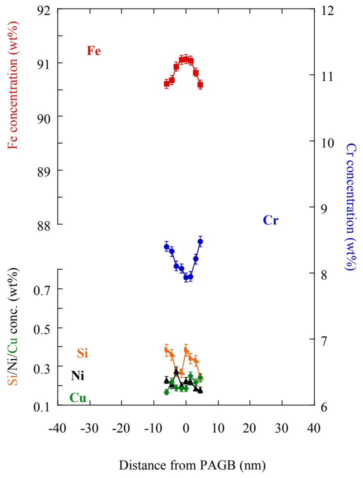

T91_3dpa_700C_05-12_MM_2-5-S

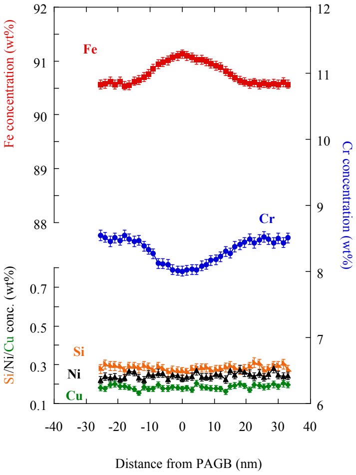

T91_3dpa_700C_05-12_MM_3-1-F

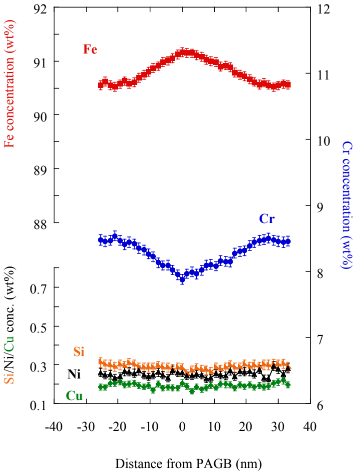

T91_3dpa_700C_05-12_MM_3-2-F

9Cr_1dpa_400C_04-09

9Cr_1dpa_400C_04-09_M_1-1-F

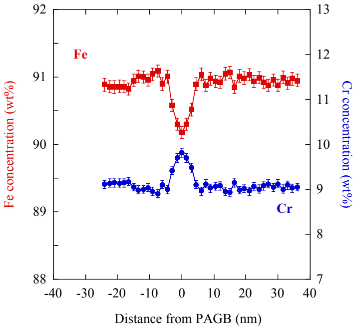

9Cr_1dpa_400C_04-09_M_1-2-F

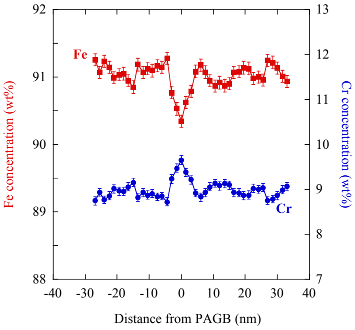

9Cr_1dpa_400C_04-09_M_1-3-F

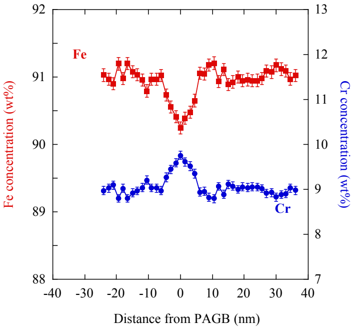

9Cr_1dpa_400C_04-09_M_2-1-F

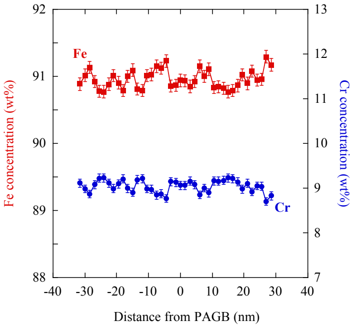

9Cr_1dpa_400C_04-09_M_2-2-F

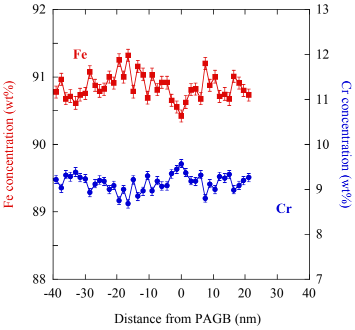

9Cr_1dpa_400C_04-09_M_2-3-F

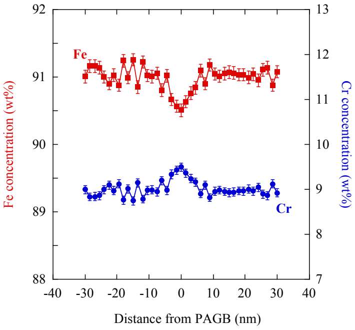

9Cr_1dpa_400C_04-09_M_3-1-F

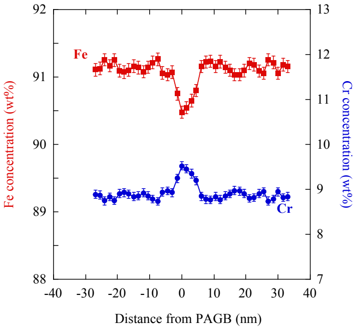

9Cr_1dpa_400C_04-09_M_3-2-F

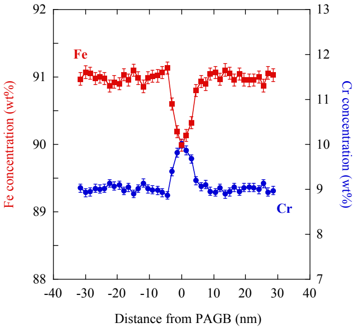

9Cr_1dpa_400C_04-09_M_3-3-F

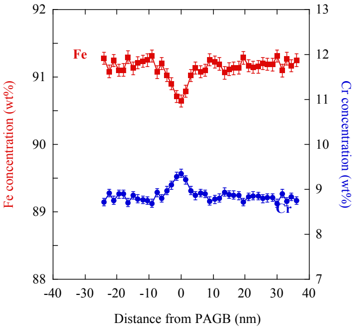

9Cr_3dpa_400C_01-12

9Cr_3dpa_400C_01-12_B_1-1-F

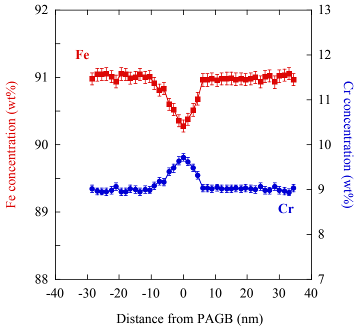

9Cr_3dpa_400C_01-12_B_1-2-F

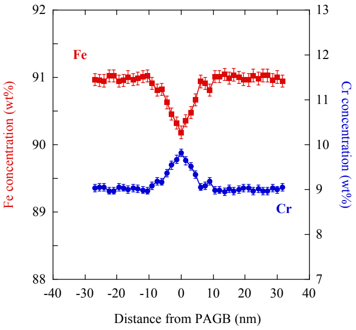

9Cr_3dpa_400C_01-12_B_1-3-F

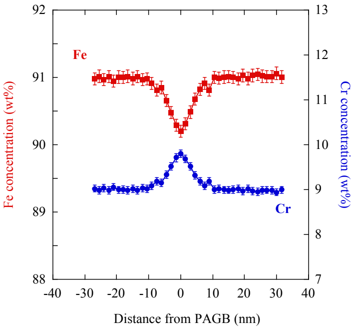

9Cr_3dpa_400C_01-12_B_1-4-F

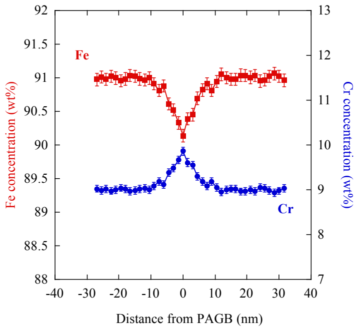

9Cr_3dpa_400C_01-12_B_1-5-S

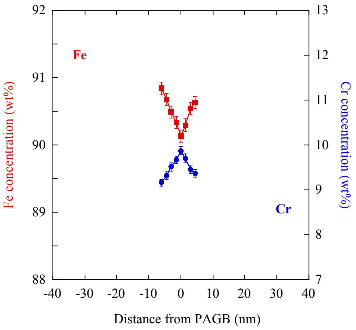

9Cr_3dpa_400C_01-12_B_1-6-S

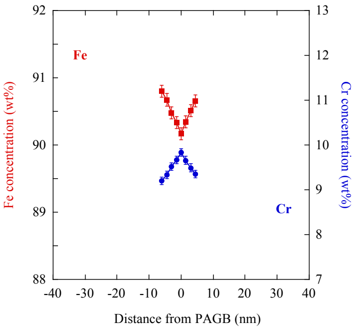

9Cr_3dpa_400C_01-12_B_1-7-S

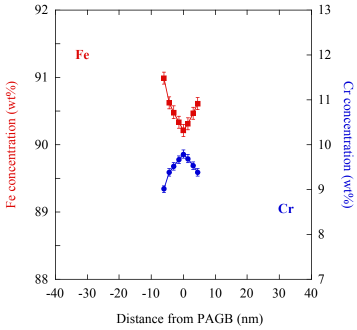

9Cr_3dpa_400C_01-12_B_1-8-S

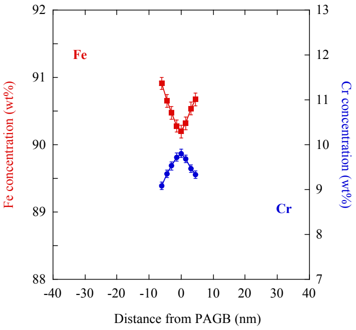

9Cr_3dpa_400C_01-12_B_1-9-S

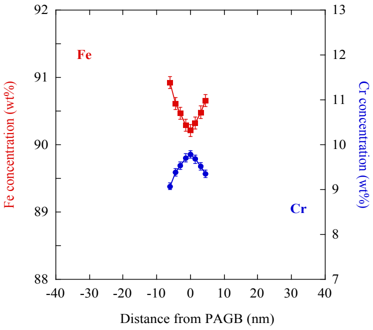

9Cr_3dpa_400C_01-12_B_2-1-F

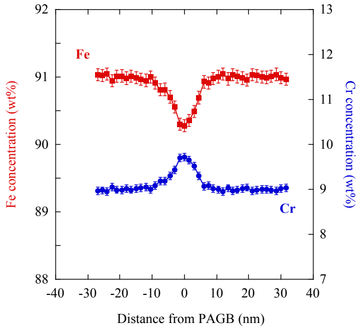

9Cr_3dpa_400C_01-12_B_2-2-F

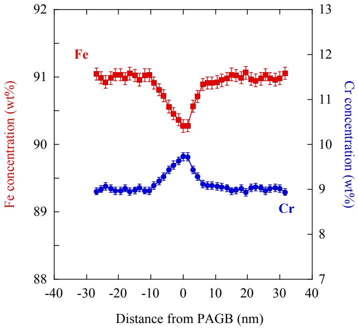

9Cr_3dpa_400C_01-12_B_2-3-S

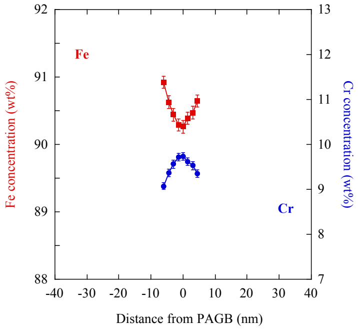

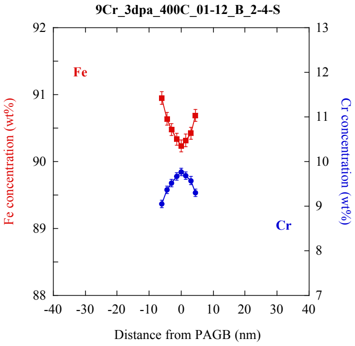
9Cr_3dpa_400C_01-12_B_2-4-S

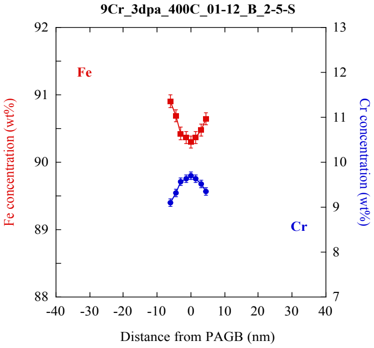
9Cr_3dpa_400C_01-12_B_2-5-S

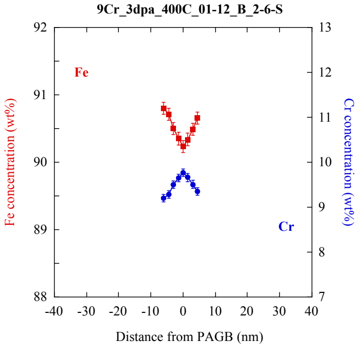
9Cr_3dpa_400C_01-12_B_2-6-S

9Cr_7dpa_400C_04-09

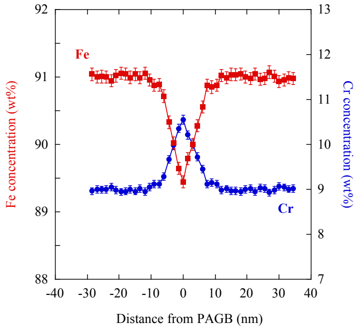
9Cr_7dpa_400C_04-09_T_1-1-F

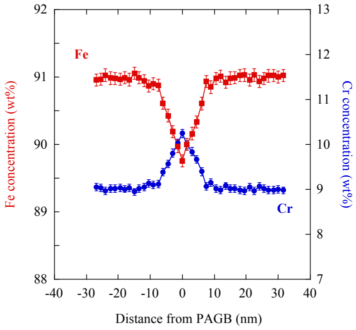
9Cr_7dpa_400C_04-09_T_1-2-F

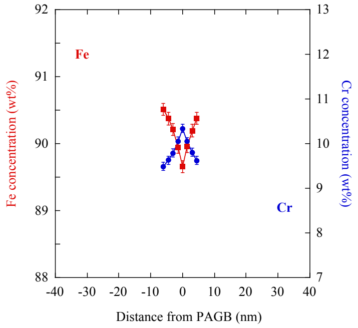
9Cr_7dpa_400C_04-09_T_1-3-S

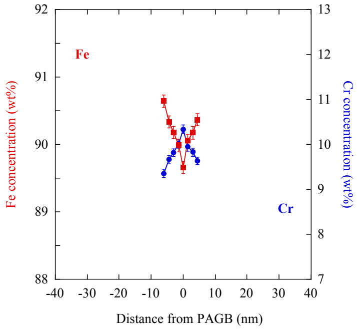
9Cr_7dpa_400C_04-09_T_1-4-S

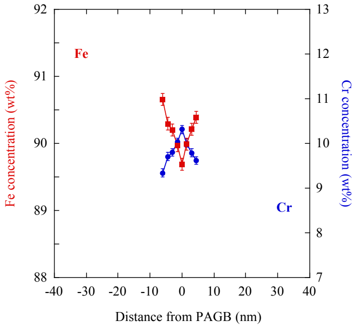
9Cr_7dpa_400C_04-09_T_1-5-S

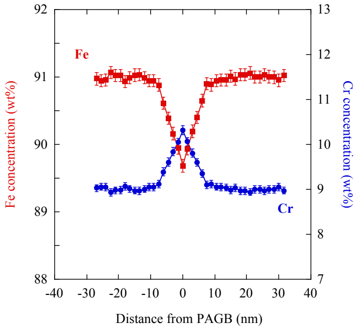
9Cr_7dpa_400C_04-09_T_2-1-F

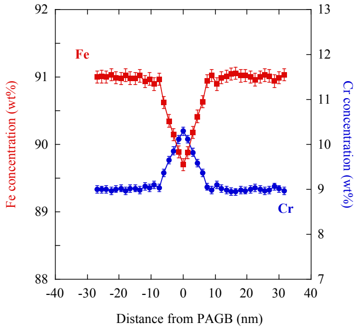
9Cr_7dpa_400C_04-09_T_2-2-F

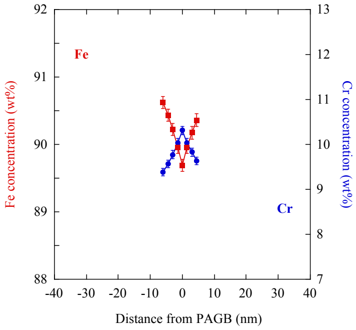
9Cr_7dpa_400C_04-09_T_2-3-S

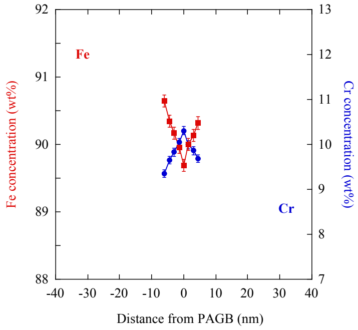
9Cr_7dpa_400C_04-09_T_2-4-S

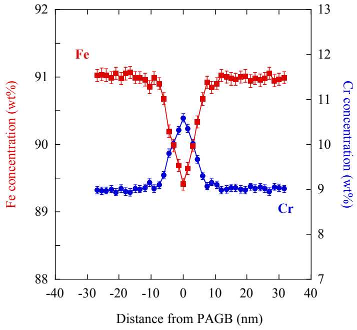
9Cr_7dpa_400C_04-09_T_3-1-F

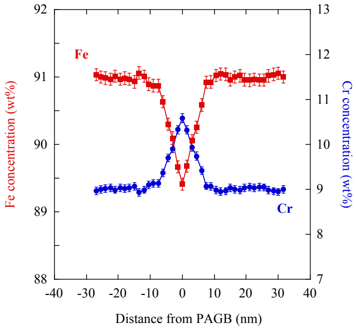
9Cr_7dpa_400C_04-09_T_3-2-F

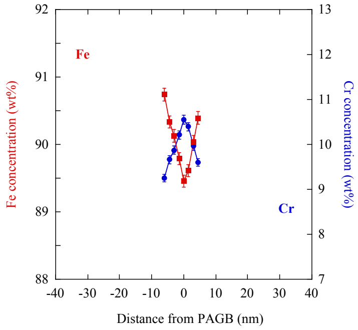
9Cr_7dpa_400C_04-09_T_3-3-S

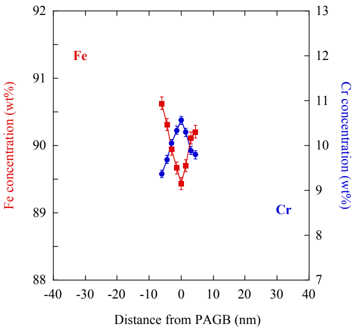
9Cr_7dpa_400C_04-09_T_3-4-S

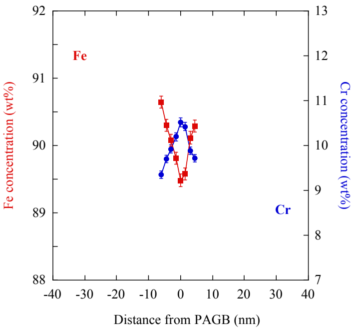
9Cr_7dpa_400C_04-09_T_3-5-S

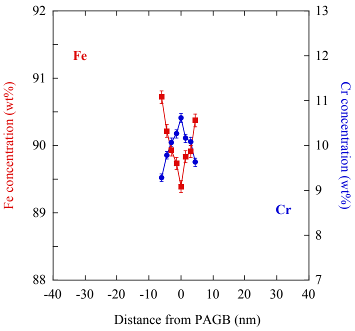
9Cr_7dpa_400C_04-09_T_3-6-S

9Cr_10dpa_400C_01-12

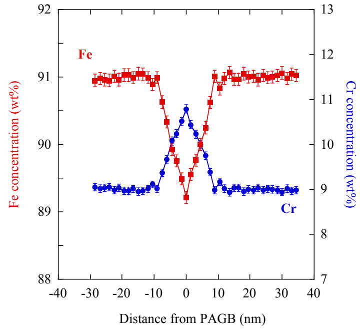
9Cr_10dpa_400C_01-12_T_1-1-F

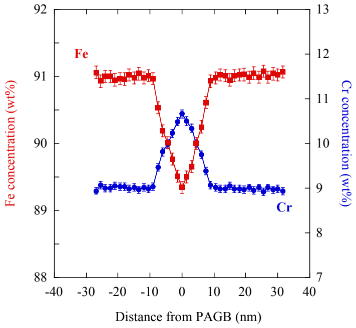
9Cr_10dpa_400C_01-12_T_1-2-F

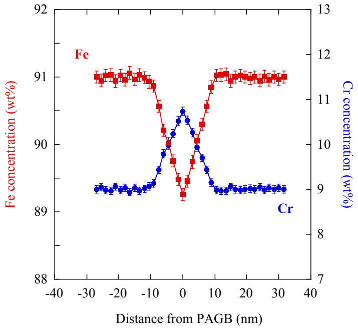
9Cr_10dpa_400C_01-12_T_1-3-F

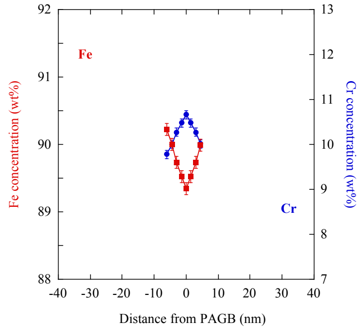
9Cr_10dpa_400C_01-12_T_1-4-S

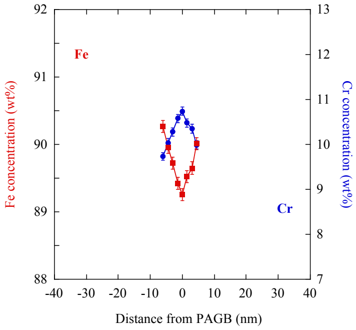
9Cr_10dpa_400C_01-12_T_1-5-S

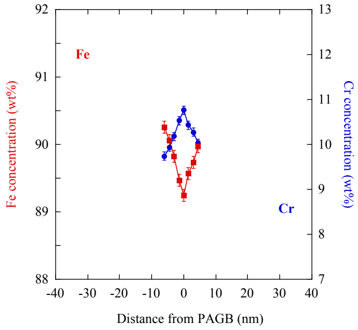
9Cr_10dpa_400C_01-12_T_1-6-S

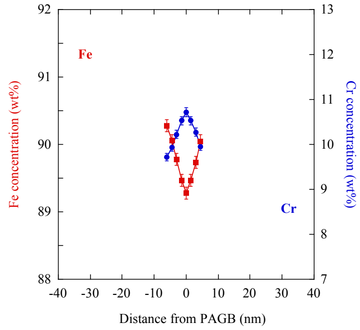
9Cr_10dpa_400C_01-12_T_1-7-S

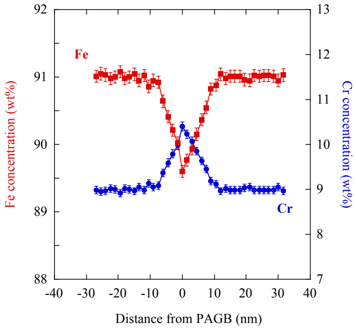
9Cr_10dpa_400C_01-12_T_2-1-F

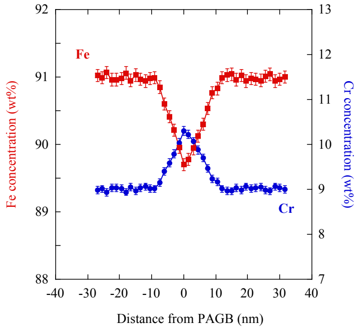
9Cr_10dpa_400C_01-12_T_2-2-F

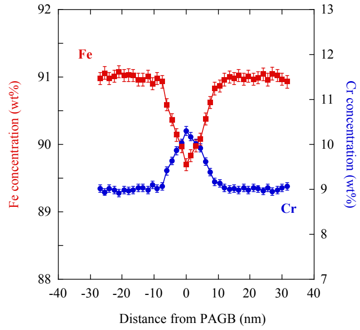
9Cr_10dpa_400C_01-12_T_2-3-F

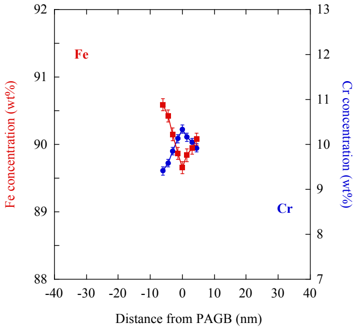
9Cr_10dpa_400C_01-12_T_2-4-S

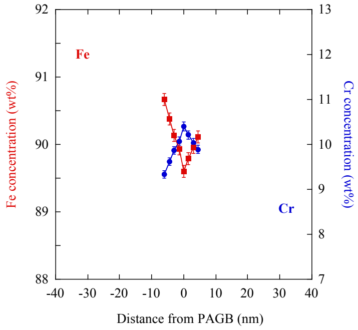
9Cr_10dpa_400C_01-12_T_2-5-S

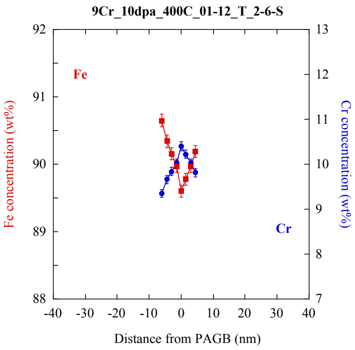
9Cr_10dpa_400C_01-12_T_2-6-S
Fe
Cr
Fe concentration (wt%)
Cr concentration (wt%)
Distance from PAGB (nm)
92
91
90
89
88
13
12
11
10
9
8
7
-40
-30
-20
-10
0
10
20
30
40

HT9_3dpa_400C_12-07

HT9_3dpa_400C_12-07_M_1-1-F

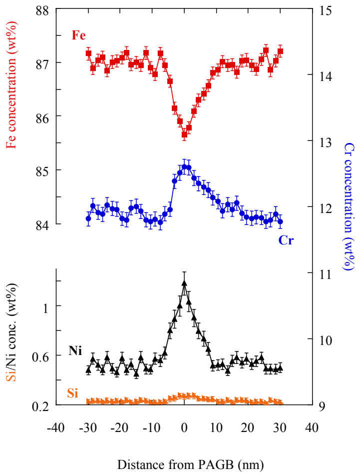

HT9_3dpa_400C_12-07_M_1-2-F

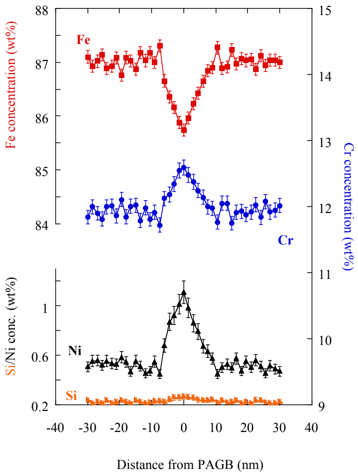

HT9_3dpa_400C_12-07_M_2-1-F

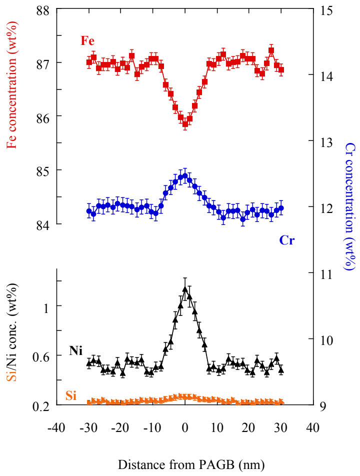

HT9_3dpa_400C_12-07_M_2-2-F

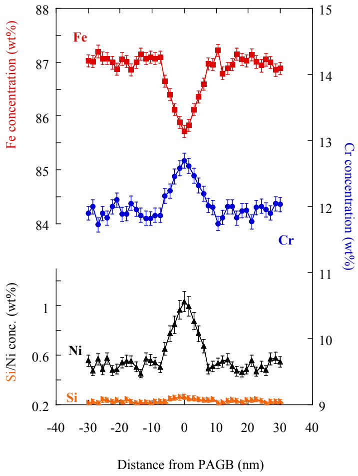

HT9_3dpa_400C_12-07_B_3-1-F

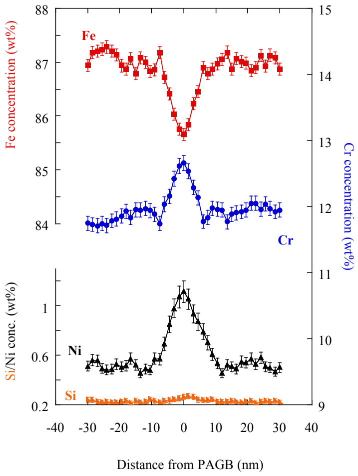

HT9_3dpa_400C_12-07_B_3-2-F

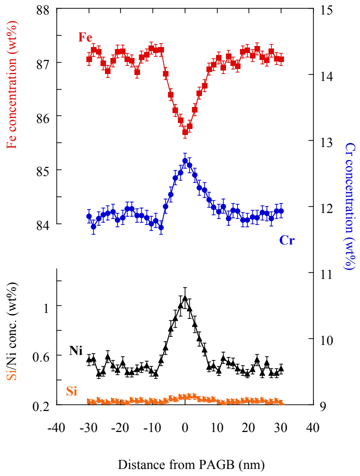

HT9_3dpa_400C_12-07_B_4-1-F

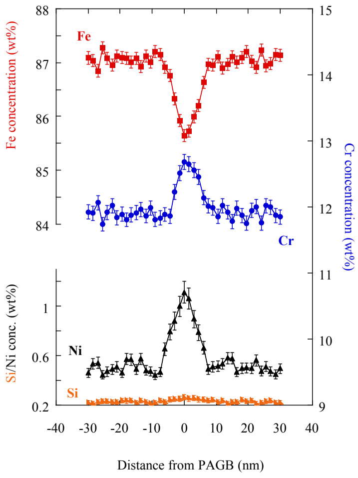

HT9_3dpa_400C_12-07_B_4-2-F

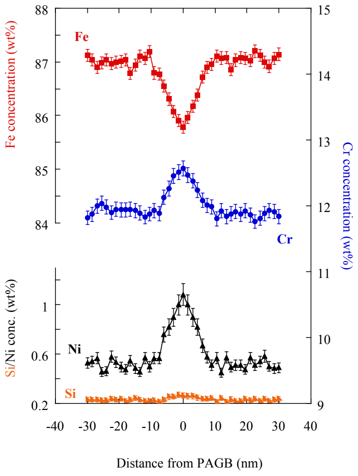

HCM12A_3dpa_400C_12-07

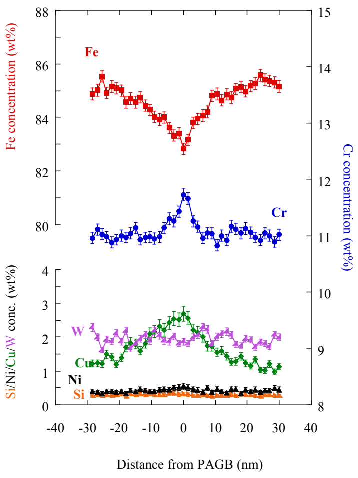
HCM12A_3dpa_400C_12-07_M_1-1-F

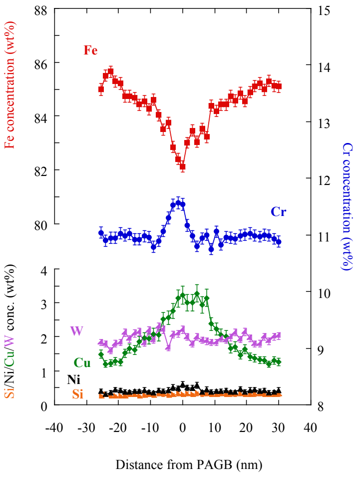
HCM12A_3dpa_400C_12-07_M_1-2-F

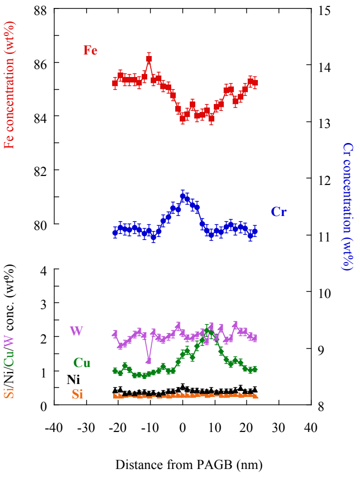
HCM12A_3dpa_400C_12-07_M_1-3-F

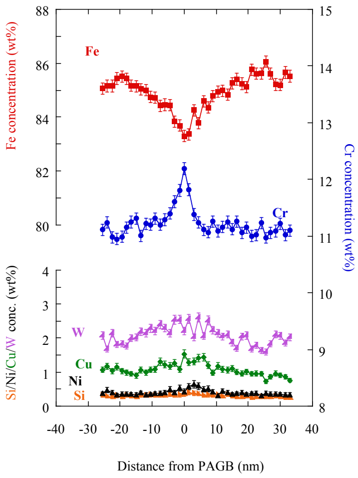
HCM12A_3dpa_400C_12-07_M_2-1-F

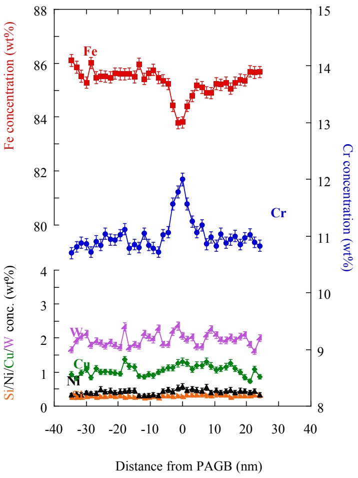
HCM12A_3dpa_400C_12-07_M_2-2-F

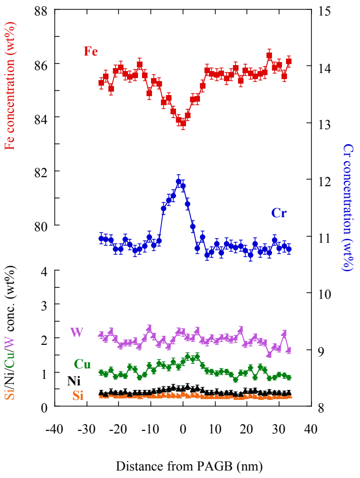
HCM12A_3dpa_400C_12-07_M_2-3-F

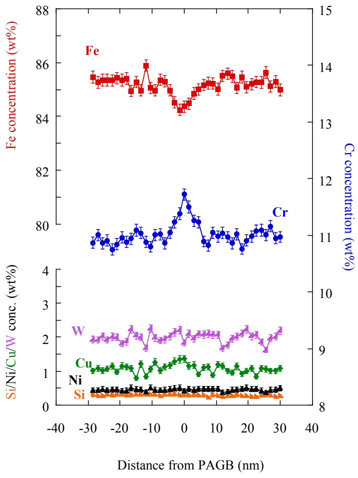
HCM12A_3dpa_400C_12-07_M_2-4-F

BIBLIOGRAPHY

[1] R. L. Klueh and D. R. Harries, *High-Chromium Ferritic and Martensitic Steels for Nuclear Applications*. ASTM, 2001.

[2] A. Kostka, K. Tak, R. Hellmig, Y. Estrin, and G. Eggeler, "On the contribution of carbides and micrograin boundaries to the creep strength of tempered martensite ferritic steels," *Acta Materialia*, vol. 55, no. 2, pp. 539–550, Jan. 2007.

[3] H. Takahashi, S. Ohnuki, and T. Takeyama, "Radiation-induced segregation at internal sinks in electron irradiated binary alloys," *Journal of Nuclear Materials*, vol. 103–104, pp. 1415–1420, 1981.

[4] T. Kato, H. Takahashi, S. Ohnuki, K. Nakata, and J. Kuniya, "The effect of solute content on grain boundary in electron-irradiated Fe-Cr-Mn alloys," *Journal of Nuclear Materials*, vol. 179–181, pp. 623–625, 1991.

[5] S. Ohnuki, H. Takahashi, and T. Takeyama, "Void swelling and segregation of solute in ion-irradiated ferritic steels," *Journal of Nuclear Materials*, vol. 103–104, pp. 1121–1125, 1981.

[6] R. E. Clausing, L. Heatherly, R. G. Faulkner, A. F. Rowcliffe, and K. Farrell, "Radiation-induced segregation in HT-9 martensitic steel," *Journal of Nuclear Materials*, vol. 141–143, pp. 978–981, 1986.

[7] E. A. Little, T. S. Morgan, and R. G. Faulkner, "Microchemistry of neutron irradiated 12%CrMoVNb martensitic steel," *Materials Science Forum*, vol. 97–99, pp. 323–328, 1992.

[8] Y. Hamaguchi, H. Kuwano, H. Kamide, R. Miura, and T. Yamada, "Effects of proton irradiation on the hardening behavior of HT-9 steel," *Journal of Nuclear Materials*, vol. 133–134, pp. 636–639, 1985.

[9] I. Neklyudov and V. Voyevodin, "Features of structure-phase transformations and segregation processes under irradiation of austenitic and ferritic-martensitic steels," *Journal of Nuclear Materials*, vol. 212–215, pp. 39–44, Sep. 1994.

[10] R. Schaeublin, P. Spatig, and M. Victoria, "Chemical segregation behavior of the low activation ferritic / martensitic steel F82H," *Journal of Nuclear Materials*, vol. 263, pp. 1350–1355, 1998.

[11] G. Gupta, Z. Jiao, A. N. Ham, J. T. Busby, and G. S. Was, "Microstructural evolution of proton irradiated T91," *Journal of Nuclear Materials*, vol. 351, no. 1–3, pp. 162–173, Jun. 2006.

[12] Z. Lu, R. Faulkner, N. Sakaguchi, H. Kinoshita, H. Takahashi, and P. Flewitt, "Effect of hafnium on radiation-induced inter-granular segregation in ferritic steel," *Journal of Nuclear Materials*, vol. 351, no. 1–3, pp. 155–161, Jun. 2006.

[13] E. a. Marquis, S. Lozano-Perez, and V. D. Castro, “Effects of heavy-ion irradiation on the grain boundary chemistry of an oxide-dispersion strengthened Fe–12wt.% Cr alloy,” *Journal of Nuclear Materials*, vol. 417, pp. 257–261, Oct. 2011.

[14] E. a. Marquis, R. Hu, and T. Rousseau, “A systematic approach for the study of radiation-induced segregation/depletion at grain boundaries in steels,” *Journal of Nuclear Materials*, vol. 413, no. 1, pp. 1–4, Jun. 2011.

[15] T. R. Allen, J. T. Busby, G. S. Was, and E. A. Kenik, “On the mechanism of radiation-induced segregation in austenitic Fe–Cr–Ni alloys,” *Journal of Nuclear Materials*, vol. 255, pp. 44–58, 1998.

[16] J. T. Busby, G. S. Was, and E. A. Kenik, “Isolating the effect of radiation-induced segregation in irradiation-assisted stress corrosion cracking of austenitic stainless steels,” *Journal of Nuclear Materials*, vol. 302, pp. 20–40, Apr. 2002.

[17] J. M. Perks and S. M. Murphy, “Modelling the major element radiation-induced segregation in concentrated Fe-Cr-Ni alloys,” in *Materials for Nuclear Reactor Core Applications, Vol. 1, Bristol, UK*, pp. 165–169.

[18] T. R. Allen and G. S. Was, “Modeling radiation-induced segregation in austenitic Fe–Cr–Ni alloys,” *Acta Materialia*, vol. 46, no. 10, pp. 3679–3691, Jun. 1998.

[19] G. S. Was, *Fundamentals of Radiation Materials Science: Metals and Alloys*. Springer, 2007.

[20] G. S. Was and S. M. Bruemmer, “Effects of irradiation on intergranular stress corrosion cracking,” *Journal of Nuclear Materials*, vol. 216, pp. 326–347, Oct. 1994.

[21] G. S. Was and T. R. Allen, “Radiation-Induced Segregation in Multicomponent Alloys: Effect of Particle Type,” *Materials Characterization*, vol. 32, pp. 239–255, Jun. 1994.

[22] J. H. Westbrook and K. T. Aust, “Solute hardening at interfaces in high-purity lead - I. Grain and twin boundaries,” *Acta Metallurgica*, vol. 11, p. 1151, 1963.

[23] K. T. Aust and J. H. Westbrook, *Lattice Defects in Quenched Metals*. Academic Press, 1965, p. 771.

[24] K. T. Aust, A. J. Peat, and J. H. Westbrook, “Quench-hardening gradients near vacancy sinks in crystals of zone refined lead,” *Acta Metallurgica*, vol. 14, p. 1469, 1966.

[25] K. T. Aust, R. E. Hanneman, P. Niessen, and J. H. Westbrook, “Solute induced hardening near grain boundaries in zone refined metals,” *Acta Metallurgica*, vol. 16, p. 291, 1968.

[26] R. E. Howard and A. B. Lidiard, “The annealing of vacancies in dilute alloys,” *Philosophical Magazine*, vol. 11, pp. 1179–1188, 1965.

[27] T. R. Anthony and R. E. Hanneman, “Non-Equilibrium Segregation of Impurities in Quenched Dilute Alloys,” *Scripta Metallurgica*, vol. 2, pp. 611–614, 1968.

[28] T. R. Anthony, “Solute segregation in vacancy gradients generated by sintering and temperature changes,” *Acta Materialia*, vol. 17, p. 603, 1969.

[29] T. R. Anthony, “Solute segregation and stresses generated around growing voids in metals,” in *Radiation-induced voids in metals*, 1972, vol. 15, pp. 630–646.

[30] P. R. Okamoto and H. Wiedersich, “Segregation of alloying elements to free surfaces during irradiation,” *Journal of Nuclear Materials*, vol. 53, pp. 336–345, 1974.

[31] R. A. Johnson and N. Q. Lam, "Solute segregation in metals under irradiation," *Physical Review B*, vol. 13, no. 10, pp. 4364–4375, 1976.

[32] P. R. Okamoto and L. E. Rehn, "Radiation-induced segregation in binary and ternary alloys," *Journal of Nuclear Materials*, vol. 83, pp. 2–23, 1979.

[33] P. G. Shewmon, "Surface Diffusion from a Point Source," *Journal of Applied Physics*, vol. 34, no. 4, p. 755, 1963.

[34] A. D. Marwick, "Segregation in irradiated alloys: the inverse Kirkendall effect and the effect of constitution on void swelling," *J. Phys. F: Metal Phys.*, vol. 8, no. 9, pp. 1849–1961, 1978.

[35] H. Wiedersich, P. R. Okamoto, and N. Q. Lam, "A theory of radiation-induced segregation in concentrated alloys," *Journal of Nuclear Materials*, vol. 83, pp. 98–108, 1979.

[36] N. Q. Lam, A. Kumar, and H. Wiedersich, "Kinetics of radiation-induced segregation in ternary alloys," in *Effects of Radiation on Materials: Eleventh Conference*, 1982, vol. 15, pp. 985–1007.

[37] J. M. Perks, A. D. Marwick, and C. A. English, "A Computer Code to Calculate Radiation-Induced Segregation in Concentrated Ternary Alloys," *Materials Development Division, Harwell Laboratory, AERE-R 12121*.

[38] S. Watanabe, N. Sakaguchi, N. Hashimoto, and H. Takahashi, "Quantitative studies of irradiation-induced segregation and grain boundary migration in FeCrNi alloy," *Journal of Nuclear Materials*, vol. 224, no. 2, pp. 158–168, Aug. 1995.

[39] S. Watanabe and H. Takahashi, "Discriminant of RIS in multi-component alloys," *Journal of Nuclear Materials*, vol. 208, no. 1–2, pp. 191–194, Jan. 1994.

[40] M. J. Hackett, "Mechanism for Suppression of Radiation-Induced Segregation by Oversized Solute Addition in Austenitic Stainless Steel," University of Michigan, 2008.

[41] M. J. Hackett, R. Najafabadi, and G. S. Was, "Modeling solute-vacancy trapping at oversized solutes and its effect on radiation-induced segregation in Fe–Cr–Ni alloys," *Journal of Nuclear Materials*, vol. 389, no. 2, pp. 279–287, May 2009.

[42] J. R. Manning, "Correlation factors for diffusion in nondilute alloys," *Physical Review B*, vol. 4, no. 4, pp. 1111–1121, 1971.

[43] L. E. Rehn, P. R. Okamoto, D. I. Potter, and H. Wiedersich, "Effect of solute misfit and temperature on irradiation-induced segregation in binary Ni alloys," *Journal of Nuclear Materials*, vol. 74, pp. 242–251, 1978.

[44] R. Faulkner, N. Waite, E. Little, and T. Morgan, "Radiation-induced grain boundary segregation in dilute alloys," *Materials Science and Engineering: A*, vol. 171, no. 1–2, pp. 241–248, Nov. 1993.

[45] R. G. Faulkner, S. Song, and P. E. J. Flewitt, "A Model Describing Neutron Irradiation-Induced Segregation to Grain Boundaries in Dilute Alloys," *Metallurgical and Materials Transactions A*, vol. 27A, pp. 3381–3390, 1996.

[46] R. Faulkner, "Radiation-induced grain boundary segregation in nuclear reactor steels," *Journal of Nuclear Materials*, vol. 251, pp. 269–275, Nov. 1997.

[47] R. G. Faulkner, S. Song, P. E. J. Flewitt, M. Victoria, and P. Marmy, "Grain boundary segregation under neutron irradiation in dilute alloys," *Journal of Nuclear Materials*, vol. 255, pp. 189–209, 1998.

[48] R. . Faulkner, S. Song, and P. E. . Flewitt, "Radiation-induced inter-granular segregation in first wall fusion reactor materials," *Journal of Nuclear Materials*, vol. 283–287, pp. 147–151, Dec. 2000.

[49] R. G. Faulkner, R. B. Jones, Z. Lu, and P. E. J. Flewitt *, "Grain boundary impurity segregation and neutron irradiation effects in ferritic alloys," *Philosophical Magazine*, vol. 85, no. 19, pp. 2065–2099, Jul. 2005.

[50] H. Watanabe, T. Muroga, and N. Yoshida, "The effects of oversized solute addition on microstructural evolution in Fe-Cr-Ni alloys during electron irradiation," *Journal of Nuclear Materials*, vol. 239, pp. 95–98, Dec. 1996.

[51] N. Sakaguchi, S. Watanabe, and H. Takahashi, "Effect of additional minor element on radiation-induced grain boundary segregation in austenitic stainless steel under electron irradiation," *Nuclear Instruments and Methods in Physics Research Section B: Beam Interactions with Materials and Atoms*, vol. 153, no. 1–4, pp. 142–146, Jun. 1999.

[52] D. I. R. Norris, C. Baker, C. Taylor, and J. M. Titchmarsh, "Radiation-induced segregation in 20Cr/25Ni/Nb stainless steel," in *Effects of Radiation on Materials: 15th International Conference*, 1992, pp. 603–620.

[53] K. Wong, J. Shim, and B. Wirth, "Molecular dynamics simulations of point defect interactions in Fe–Cr alloys," *Journal of Nuclear Materials*, vol. 367–370, pp. 276–281, Aug. 2007.

[54] K. L. Wong, H.-J. Lee, J.-H. Shim, B. Sadigh, and B. D. Wirth, "Multiscale modeling of point defect interactions in Fe–Cr alloys," *Journal of Nuclear Materials*, vol. 386–388, pp. 227–230, Apr. 2009.

[55] S. Choudhury et al., "Ab-initio based modeling of diffusion in dilute bcc Fe–Ni and Fe–Cr alloys and implications for radiation induced segregation," *Journal of Nuclear Materials*, vol. 411, no. 1–3, pp. 1–14, Apr. 2011.

[56] J. Pešička, R. Kužel, a. Dronhofer, and G. Eggeler, "The evolution of dislocation density during heat treatment and creep of tempered martensite ferritic steels," *Acta Materialia*, vol. 51, no. 16, pp. 4847–4862, Sep. 2003.

[57] R. Klueh, N. Hashimoto, M. Sokolov, K. Shiba, and S. Jitsukawa, "Mechanical properties of neutron-irradiated nickel-containing martensitic steels: I. Experimental study," *Journal of Nuclear Materials*, vol. 357, no. 1–3, pp. 156–168, Oct. 2006.

[58] J. Pešička, A. Dronhofer, and G. Eggeler, "Free dislocations and boundary dislocations in tempered martensite ferritic steels," *Materials Science and Engineering A*, vol. 387–389, pp. 176–180, Dec. 2004.

[59] G. Eggeler, J. C. Earthman, N. Nilsvang, and B. Ilschner, "Microstructural study of creep rupture in a 12% Chromium ferritic steel," *Acta Metallurgica*, vol. 37, no. 1, pp. 49–60, Jan. 1989.

[60] R. Klueh, K. Shiba, and M. Sokolov, "Embrittlement of irradiated ferritic/martensitic steels in the absence of irradiation hardening," *Journal of Nuclear Materials*, vol. 377, no. 3, pp. 427–437, Jul. 2008.

[61] X. Jia and Y. Dai, "Microstructure in martensitic steels T91 and F82H after irradiation in SINQ Target-3," *Journal of Nuclear Materials*, vol. 318, pp. 207–214, May 2003.

[62] J. J. Kai and R. L. Klueh, “Microstructural analysis of neutron-irradiated martensitic steels,” *Journal of Nuclear Materials*, vol. 230, pp. 116–123, 1996.

[63] M. J. Hackett, J. T. Busby, M. K. Miller, and G. S. Was, “Effects of oversized solutes on radiation-induced segregation in austenitic stainless steels,” *Journal of Nuclear Materials*, vol. 389, no. 2, pp. 265–278, May 2009.

[64] K. Field, J. Bentley, C. Parish, J. T. Busby, and T. R. Allen, “Dependence of Radiation Induced Segregation on Grain Boundary Structure in a 9 wt.% Cr Model Ferritic/Martensitic Steel,” in *The Minerals, Metals, and Materials Society 140th Annual Meeting & Exhibition*, 2011.

[65] E. A. Little, R. Bullough, and M. H. Wood, “On the Swelling Resistance of Ferritic Steel,” *Proceedings of the Royal Society of London: Series A, Mathematical and Physical Sciences*, vol. 372, no. 1751, pp. 565–579, 1980.

[66] J. Marian, B. Wirth, and J. Perlado, “Mechanism of Formation and Growth of <100> Interstitial Loops in Ferritic Materials,” *Physical Review Letters*, vol. 88, no. 25, pp. 1–4, Jun. 2002.

[67] D. S. Gelles, “Microstructural examination of commercial ferritic alloys at 200 dpa,” *Journal of Nuclear Materials*, vol. 233–237, pp. 293–298, 1996.

[68] R. R. Bullough, M. H. Wood, and E. A. Little, “Microstructural explanation for the low swelling of ferritic steels,” in *Effects of Radiation on Materials: Tenth Conference*, 1981, pp. 593–609.

[69] T. Muroga, A. Yamaguchi, and N. Yoshida, “Effects of Radiation on Materials: 14th International Symposium,” in *Volume 1*, 1989, p. 396.

[70] D. S. Gelles, S. Ohnuki, H. Takahashi, H. Matsui, and Y. Kohno, “Electron irradiation experiments in support of fusion materials development,” *Journal of Nuclear Materials*, vol. 191–194, pp. 1336–1341, 1992.

[71] D. Terentyev and L. Malerba, “Interaction of <100> and 1/2<111> dislocation loops with point defects in ferritic alloys,” *Journal of Nuclear Materials*, vol. 377, no. 1, pp. 141–146, Jun. 2008.

[72] Z. Jiao, N. Ham, and G. Was, “Microstructure of helium-implanted and proton-irradiated T91 ferritic/martensitic steel,” *Journal of Nuclear Materials*, vol. 367–370, pp. 440–445, Aug. 2007.

[73] N. Hashimoto and R. L. Klueh, “Microstructural evolution of nickel-doped 9Cr steels irradiated in HFIR,” *Journal of Nuclear Materials*, vol. 305, pp. 153–158, 2002.

[74] K. Asano, Y. Kohno, A. Kohyama, and G. Ayrault, “Microstructural evolution of HT9 under dual-beam charged particle irradiation,” *Journal of Nuclear Materials*, vol. 155–157, pp. 912–915, 1988.

[75] P. Dubuisson, D. Gilbon, and J. L. Seran, “Microstructural evolution of ferritic-martensitic irradiated in the fast breeder reactor Phenix,” *Journal of Nuclear Materials*, vol. 205, pp. 178–189, 1993.

[76] S. A. Maloy et al., “The mechanical properties of 316L/304L stainless steels , Alloy 718 and Mod 9Cr-1Mo after irradiation in a spallation environment,” *Journal of Nuclear Materials*, vol. 296, pp. 119–128, 2001.

[77] C. Deo, C. Tome, R. Lebensohn, and S. Maloy, “Modeling and simulation of irradiation hardening in structural ferritic steels for advanced nuclear reactors,” *Journal of Nuclear Materials*, vol. 377, no. 1, pp. 136–140, Jun. 2008.

[78] R. L. Klueh and J. M. Vitek, “Tensile Behavior of Irradiated 12Cr-1MoVW Steel,” *Journal of Nuclear Materials*, vol. 137, pp. 44–50, 1985.

[79] R. L. Klueh and J. M. Vitek, “Elevated-temperature tensile properties of irradiated 9Cr-1MoVNb steel,” *Journal of Nuclear Materials*, vol. 132, pp. 27–31, 1985.

[80] Z. Lu, R. G. Faulkner, G. Was, and B. D. Wirth, “Irradiation-induced grain boundary chromium microchemistry in high alloy ferritic steels,” *Scripta Materialia*, vol. 58, no. 10, pp. 878–881, May 2008.

[81] J. F. Ziegler, “The Stopping and Range of Ions in Matter (SRIM),” .

[82] *Standard Practice for Neutron Radiation Damge Simulation by Charged-Particle Irradiation*. E 521-96, ASTM International, 2003.

[83] C. C. Herrick, “Vapor Pressure of Liquid Indium,” in *Transactions of the Metallurgical Society of AIME - Institute of Metals Division*, 1964.

[84] “Experimental Nuclear Reaction Data,” *Brookhaven National Laboratory*. [Online]. Available: http://www.nndc.bnl.gov/exfor7/exfor00.htm.

[85] G. Cliff and G. W. Lorimer, “No Title,” *Journal of Microscopy*, vol. 103, p. 203, 1975.

[86] D. B. Williams and C. B. Carter, *Transmission Electron Microscopy*. New York, NY: Plenum Press, 1996.

[87] J. Wiley, *Table of Isotopes*, 8th ed. New York: Wiley-Interscience, 1996.

[88] A. D. Brailsford and R. Bullough, “The rate theory of swelling due to void growth in irradiated metals,” *Journal of Nuclear Materials*, vol. 44, pp. 121–135, 1972.

[89] A. D. Brailsford and R. Bullough, “The rate theory of swelling due to void growth in irradiated metals,” *Journal of Nuclear Materials*, vol. 44, pp. 121–135, 1972.

[90] “Alloy Data Sheet for T91 Heat #C2269 Slab 7B from Bethlehem Lukens Plate Mill, Plate #A9532.”

[91] “Alloy Data Sheet for HCM12A Heat #F114206.”

[92] “Alloy Data Sheet for HT9 Heat #9-607.”

[93] “Alloy Data Sheet for Fe-9Cr.”

[94] Z. Jiao and G. S. Was, “Segregation behavior in proton- and heavy-ion-irradiated ferritic–martensitic alloys,” *Acta Materialia*, vol. 59, no. 11, pp. 4467–4481, Jun. 2011.

[95] Z. Jiao, V. Shankar, and G. S. Was, “Phase stability in proton and heavy ion irradiated ferritic–martensitic alloys,” *Journal of Nuclear Materials*, vol. 419, no. 1–3, pp. 52–62, Dec. 2011.

[96] R. Klueh, N. Hashimoto, M. Sokolov, P. Maziasz, K. Shiba, and S. Jitsukawa, “Mechanical properties of neutron-irradiated nickel-containing martensitic steels: II. Review and analysis of helium-effects studies,” *Journal of Nuclear Materials*, vol. 357, no. 1–3, pp. 169–182, Oct. 2006.

[97] A. Alamo, M. Horsten, X. Averty, E. I. Materna-Morris, M. Rieth, and J. C. Brachet, “Mechanical behavior of reduced-activation and conventional martensitic steels after neutron irradiation in the range 250-450°C,” *Journal of Nuclear Materials*, vol. 283–287, pp. 353–357, 2000.

[98] R. L. Klueh and D. J. Alexander, “Embrittlement of Cr-Mo steels after low fluence irradiation in HFIR,” *Journal of Nuclear Materials*, vol. 218, pp. 151–160, 1995.

[99] A. C. Hindmarsh, “Ordinary Differential Equation System Solver,” *UCID-30001 Rev. 3, Lawrence Livermore National Laboratory*, 1974.

[100] A. C. Hindmarsh, “Linear Multistep Methods for Ordinary Differential Equations: Method Formulations, Stability, and the Methods of Nordiseck and GEAR,” *UCRL-51186 Rev. 1, Lawrence Livermore National Laboratory*, 1972.

[101] A. C. Hindmarsh, “Construction of Mathematical Software, Part III: The Control of Error in the GEAR Package for Ordinary Differential Equations,” *UCID-30050 Part 3, Lawrence Livermore National Laboratory*, 1972.

[102] “SilverFrost FTN95.” [Online]. Available: http://www.silverfrost.com/11/ftn95/overview.aspx. [Accessed: 05-May-2012].

[103] A. L. Nikolaev, V. L. Arbuzov, and A. E. Davletshin, “On the effect of impurities on resistivity recovery, short-range ordering, and defect migration in electron-irradiated concentrated Fe–Cr alloys,” *J. Phys.: Condens. Matter*, vol. 9, p. 4385, 1997.

[104] A. L. Nikolaev, “Stage I of recovery in 5 MeV electron-irradiated iron and iron-chromium alloys: the effect of small cascades, migration of di-interstitials and mixed dumbbells,” *J. Phys.: Condens. Matter*, vol. 11, p. 8633, 1999.

[105] S. Takaki, J. Fuss, H. Kugler, U. Dedek, and H. Schultz, “The resistivity recovery of high purity and carbon doped iron following low temperature electron irradiation,” *Radiation Effects*, vol. 79, pp. 87–122, Jan. 1983.

[106] H. Abe and E. Kuramoto, “Interaction of solutes with irradiation-induced defects of electron-irradiated dilute iron alloys,” *Journal of Nuclear Materials*, vol. 271–272, pp. 209–213, May 1999.

[107] H.-E. Schaefer, K. Maier, M. Weller, D. Herlach, A. Seeger, and J. Diehl, “Vacancy formation in iron investigated by positron annihilation in thermal equilibrium,” *Scripta Metallurgica*, vol. 11, pp. 803–809, 1977.

[108] L. De Schepper et al., “Positron annihilation on pure and carbon-doped α-iron in thermal equilibrium,” *Physical Review B*, vol. 27, no. 9, p. 5257, 1983.

[109] Y. Shirai, “No Title,” in *Annual Meeting of the Physical Society of Japan*, 1987.

[110] Y. Iijima, K. Kimura, and K. Hirano, “Self-diffusion and isotope effect in α-Iron,” *Acta Metallurgica*, vol. 36, no. 10, pp. 2811–2820, 1988.

[111] D. Nguyen-Manh, M. Y. Lavrentiev, and S. L. Dudarev, “The Fe–Cr system: atomistic modelling of thermodynamics and kinetics of phase transformations,” *Comptes Rendus Physique*, vol. 9, pp. 379–388, Apr. 2008.

[112] P. Olsson, C. Domain, and J. Wallenius, “Ab initio study of Cr interactions with point defects in bcc Fe,” *Physical Review B*, vol. 75, no. 1, pp. 1–12, Jan. 2007.

[113] C.-C. Fu, F. Willaime, and P. Ordejón, “Stability and Mobility of Mono- and Di-Interstitials in α-Fe,” *Physical Review Letters*, vol. 92, no. 17, pp. 1–4, Apr. 2004.

[114] D. Terentyev, P. Olsson, T. P. C. Klaver, and L. Malerba, “On the migration and trapping of single self-interstitial atoms in dilute and concentrated Fe–Cr alloys: Atomistic study and comparison with resistivity recovery experiments,” *Computational Materials Science*, vol. 43, no. 4, pp. 1183–1192, Oct. 2008.

[115] P. Olsson, “Ab initio study of interstitial migration in Fe–Cr alloys,” *Journal of Nuclear Materials*, vol. 386–388, pp. 86–89, Apr. 2009.

[116] A. D. LeClaire, “Physical Chemistry,” *Philosophical Magazine*, vol. 21, p. 819, 1970.

[117] A. D. LeClaire, “No Title,” *Journal of Nuclear Materials*, vol. 69, p. 70, 1978.

[118] R. A. Johnson, "Interstitials and vacancies in α Iron," *Physical Review*, vol. 134, no. 5A, pp. A1329–A1336, 1964.

[119] T. Diaz de la Rubia, N. Soneda, M. J. Caturla, and E. A. Alonso, "Defect production and annealing kinetics in elemental metals and semiconductors," *Journal of Nuclear Materials*, vol. 251, pp. 13–33, Nov. 1997.

[120] C. M. Walter and N. L. Peterson, "Isotope effect in self-diffusion in iron," *Physical Review*, vol. 178, no. 3, pp. 922–929, 1969.

[121] D. Graham, "Mass Dependence of Self-Diffusion in Iron," *Journal of Applied Physics*, vol. 40, no. 6, p. 2386, 1969.

[122] V. Irmer and M. Feller-Kniepmeier, "Isotope effect for self-diffusion in single crystals of α Iron and correlation factor of solute diffusion in α Iron," *Journal of Applied Physics*, vol. 43, no. 3, pp. 953–957, 1972.

[123] Y. N. Osetsky and A. Serra, "Vacancy and interstitial diffusion in bcc-Fe," *Defect and Diffusion Forum*, vol. 143–147, pp. 155–160, 1997.

[124] C. Tuijn, H. Bakker, and G. Neumann, "The correlation factor of impurity diffusion in body-centered cubic metals for mixed nearest- and next-nearest-neighbour monovacancy jumps," *J. Phys.: Condens. Matter*, vol. 4, p. 4801, 1992.

[125] G. Neumann and C. Tuijn, "Impurity diffusion in metals," in *Diffusion and Defect Data Part B: Solid State Phenomena, Volume 88*, 2002.

[126] S. J. Rothman, L. J. Nowicki, and G. E. Murch, "Self-diffusion in austenitic Fe-Cr-Ni alloys," *J. Phys. F: Metal Phys.*, vol. 10, pp. 383–398, 1980.

[127] H. Matter, J. Winter, and W. Triftshiiuser, "Phase transformations and vacancy formation energies of transition metals by positron annihilation," *Applied Physics*, vol. 20, pp. 135–140, 1979.

[128] J. L. Campbell and C. W. Schulte, "Positron trapping and self-diffusion activation energies in Chromium," *Applied Physics*, vol. 19, pp. 149–152, 1979.

[129] M. A. Tschopp, K. N. Solanki, F. Gao, X. Sun, M. A. Khaleel, and M. F. Horstemeyer, "Probing grain boundary sink strength at the nanoscale: Energetics and length scales of vacancy and interstitial absorption by grain boundaries in α-Fe," *Physical Review B*, vol. 85, no. 6, pp. 1–21, Feb. 2012.

[130] R. D. Carter, D. L. Damcott, M. Atzmon, G. S. Was, S. M. Bruemmer, and E. A. Kenik, "Quantitative analysis of radiation-induced grain-boundary segregation measurements," *Journal of Nuclear Materials*, vol. 211, pp. 70–84, 1994.

[131] L. K. Mansur, "Correlation of neutron and heavy-ion damage: II. The predicted temperature sift of swelling with changes in radiation dose rate," *Journal of Nuclear Materials*, vol. 78, pp. 156–160, 1978.

[132] L. K. Mansur, "Theory of transitions in dose dependence of radiation effects in structural alloys," *Journal of Nuclear Materials*, vol. 206, no. 2–3, pp. 306–323, Nov. 1993.

[133] R. A. Johnson and N. Q. Lam, "Solute segregation under irradiation," *Journal of Nuclear Materials*, vol. 69 & 70, pp. 424–433, 1978.

[134] J. Wallenius, P. Olsson, C. Lagerstedt, N. Sandberg, R. Chakarova, and V. Pontikis, "Modeling of chromium precipitation in Fe-Cr alloys," *Physical Review B*, vol. 69, no. 9, pp. 1–9, Mar. 2004.

[135] D. Farkas, C. G. Schon, M. S. F. De Lima, and H. Goldenstein, “Embedded atom computer simulation of lattice distortion and dislocation core structure and mobility in Fe□Cr alloys,” *Acta Materialia*, vol. 44, no. 1, pp. 409–419, Jan. 1996.

[136] M. Matijasevic and a Almazouzi, “Effect of Cr on the mechanical properties and microstructure of Fe–Cr model alloys after n-irradiation,” *Journal of Nuclear Materials*, vol. 377, no. 1, pp. 147–154, Jun. 2008.

[137] R. Schaeublin, T. Leguey, P. Spätig, N. Baluc, and M. Victoria, “Microstructure and mechanical properties of two ODS ferritic/martensitic steels,” *Journal of Nuclear Materials*, vol. 307–311, pp. 778–782, Dec. 2002.

[138] R. Schaeublin, D. Gelles, and M. Victoria, “Microstructure of irradiated ferritic/martensitic steels in relation to mechanical properties,” *Journal of Nuclear Materials*, vol. 307–311, pp. 197–202, Dec. 2002.

[139] Y. Hosoi, N. Wade, T. Urita, M. Tanino, and H. Komatsu, “Change in microstructure and toughness of ferritic-martensitic stainless steels during long-term aging,” *Journal of Nuclear Materials*, vol. 133–134, pp. 337–342, 1984.

[140] Z. Liu and X. Huang, “Factors that affect activation energy for Li diffusion in LiFePO4: A first-principles investigation,” *Solid State Ionics*, vol. 181, no. 19–20, pp. 907–913, Jul. 2010.

[141] R. L. Fleischer, “Substitutional solutes in AlRu: I. Effects of solute on moduli, lattice parameters, and vacancy production,” *Acta Metallurgica Materialia*, vol. 41, no. 3, pp. 863–869, 1993.

[142] R. Fleischer, “Substitutional solutes in AlCo: I. Effects of solute on moduli, lattice parameters, and vacancy production,” *Journal of Materials Research*, vol. 8, no. 1, pp. 49–58, 1993.

[143] J. P. Wharry, Z. Jiao, V. Shankar, J. T. Busby, and G. S. Was, “Radiation-induced segregation and phase stability in ferritic–martensitic alloy T91,” *Journal of Nuclear Materials*, vol. 417, no. 1–3, pp. 140–144, Oct. 2011.

[144] C. R. Hubbard, H. E. Swanson, and F. A. Mauer, “A silicon powder diffraction standard reference material,” *Journal of Applied Crystallography*, vol. 8, pp. 45–48, 1975.

[145] A. Taylor, “Lattice parameters of binary nickel-cobalt alloys,” *Journal of the Institute of Metals*, vol. 77, pp. 585–594, 1950.

[146] M. E. Straumanis and L. S. Yu, “Lattice parameters, densities, expansion coefficients and perfection of structure of Cu and of Cu-In α phase,” *Acta Crystallographica, Section A (Crystal Physics, Diffraction, Theoretical and General Crystallography)*, vol. A25, no. 6, pp. 676–682, 1969.

[147] R. G. Ross and W. Hume-Rothery, “High temperature x-ray metallography, I. A new Debye-Scherrer camera for use at very high temperatures, II. A new parafocusing camera, III. Applications to the study of chromium, hafnium, molybdenum, rhodium, ruthenium, and tungsten,” *Journal of the Less-Common Metals*, vol. 5, no. 2, pp. 258–270, 1963.

[148] N. Schmitz-Pranghe and R. Kohlhaas, “X-ray diffraction investigation of liquid iron, cobalt and nickel,” *Zeitschrift fur Naturforschung A (Astrophysik, Physik und Physikalische Chemie)*, vol. 25, no. 11, p. 1752, 1970.